University of Nevada, Reno

Plasma Formation and Evolution on Cu, Al, Ti, and Ni Surfaces Driven by a Mega-Ampere Current Pulse

A dissertation submitted in partial fulfillment of the requirements for the degree of Doctor of Philosophy in Physics

by

Kevin C. Yates

Dr. B. S. Bauer/Dissertation Advisor

December, 2015

THE GRADUATE SCHOOL

We recommend that the dissertation
prepared under our supervision by

KEVIN C. YATES

Entitled

Plasma Formation And Evolution On Cu, Al, Ti, And Ni Surfaces Driven By A Mega-Ampere Current Pulse

be accepted in partial fulfillment of the
requirements for the degree of

DOCTOR OF PHILOSOPHY

Bruno S. Bauer, Advisor

Stephan Fuelling, Committee Member

Radu Presura, Committee Member

David M. Leitner, Committee Member

Henry Fu, Graduate School Representative

David W. Zeh, Ph. D., Dean, Graduate School

December, 2015

Dissertation Abstract

Plasma Formation And Evolution On Cu, Al, Ti, And Ni Surfaces Driven By A Mega-Ampere Current Pulse

by

Kevin C. Yates

Doctor of Philosophy in Physics

Department of Physics

University of Nevada, Reno 2015

Professor Bruno S. Bauer Chair, Advisor

Metal alloy mm-diameter rods have been driven by a 1-MA, 100-ns current pulse from the Zebra z-pinch. The intense current produces megagauss surface magnetic fields that diffuse into the load, ohmically heating the metal until plasma forms. Because the radius is much thicker than the skin depth, the magnetic field reaches a much higher value than around a thin-wire load. With the "barbell" load design, plasma formation in the region of interest due to contact arcing or electron avalanche is avoided, allowing for the study of ohmically heated loads. Work presented here will show first evidence of a magnetic field threshold for plasma formation in copper 101, copper 145, titanium, and nickel, and compare with previous work done with aluminum. Copper alloys 101 and 145, titanium grade II, and nickel alloy 200 form plasma when the surface magnetic field reaches 3.5, 3.0, 2.2, and 2.6 megagauss, respectively. Varying the element metal, as well as the alloy, changes multiple physical properties of the load and affects the evolution of the surface material through the multiple phase changes. Similarities and differences between these metals will be presented, giving motivation for continued work with different material loads.

During the current rise, the metal is heated to temperatures that cause multiple phase changes. When the surface magnetic field reaches a threshold, the metal ionizes and the plasma becomes pinched against the underlying cooler, dense material. Diagnostics fielded have included visible light radiometry, two-frame shadowgraphy (266 and 532 nm wavelengths), time-gated EUV spectroscopy, single-frame/2ns gated imaging, and multi-frame/4ns gated imaging with an intensified CCD camera (ICCD). Surface temperature, expansion speeds, instability growth, time of plasma formation, and plasma uniformity are determined from the data. The time-period of potential plasma formation is scrutinized to understand if and when plasma forms on the surface of a heated conductor. When photodiode signals of visible light surface emission reach values indicating temperatures consistent with plasma formation, a sharp increase in signal is observed, which can be interpreted as related to an abrupt increase in conductivity when plasma forms, as has been observed experimentally as well as in Quantum Molecular Dynamic simulations[1,2,3,4]. The increase in conductivity, in the context of an overall rising current, causes an abrupt increase in current density in the plasma-forming layer, leading to an increase in temperature that reinforces the increase in conductivity. Laser shadowgaphy images allow for the observation of expansion as well as the development and evolution of surface instabilities. The sudden expansion of the surface of a heated conductor is not sufficient to claim plasma formation. The development of late-time surface instabilities does indicate surface plasma formed, although it does not pinpoint the moment of plasma formation. The self-emission images captured by ICCD cameras provide a third indicator of plasma formation. The images first show non-uniform dots begin to glow, then show bright filaments in the direction of current flow, and eventually show a uniform surface emission. The early dots are believed to be plasma; however, the filamentation occurs near the time of the abrupt increase in the visible diode signal. The

filaments are likely caused by electrothermal instabilities,[5,6,7,8,9,10] a formation attributed to a plasma.

The interplay between an ohmically heated conductor and a magnetic field is important for the field of Magnetized Target Fusion (MTF). MTF compresses a magnetized fuel by imploding a flux-conserving metal liner. During compression, fields reach several megagauss, with a fraction of the flux diffusing into the metal liner. The magnetic field induces eddy currents in the metal, leading to ionization and potential mixing of metal contaminant into the fusion fuel.

Acknowledgements

I would like to thank Bruno Bauer and Stephan Fuelling for their advisement over the past 6 years. Their patience and willingness to have endless discussions about our research has allowed me to develop a greater understanding of our research and the experiments.

I would also like to thank Tom Awe and Trevor Hutchinson who both helped tremendously in designing and implementing recent experiments with both experimental contributions and analysis.

I would like to thank the NTF technical staff, in particular Alexey Astanovitskiy and Oleg Dmitriev for help in designing and developing several diagnostics and infrastructure over the years. Also, thanks to Vidya Nalajala for the years of help with the electrical systems and data acquisition systems. I would also like to thank Aaron Covington and Tim Darling for the many conversations we have had over the years as it pertains to material science. And thank you to Vladimir Ivanov, Radu Presura, and their many students over the years for helping with the optical diagnostics in the Zebra lab.

Finally, I would like to thank Glen Wurden, Chris Grabowski, and James Degnan for the wonderful research experience I had working at Kirtland AFB on the FRCHX experiment. It was not only a valuable experience, it was also one of the most exciting projects that I have been fortunate enough to be a part of.

Table of Contents

Table of Contents (continued)

Table of Contents (continued)

List of Tables

List of Figures

List of Figures (continued)

List of Figures (continued)

List of Figures (continued)

List of Figures (continued)

List of Figures (continued)

List of Figures (continued)

List of Figures (continued)

List of Figures (continued)

List of Figures (continued)

List of Figures (continued)

List of Figures (continued)

List of Figures (continued)

List of Figures (continued)

Introduction

If, when, and how plasma forms on the surface of a metal conductor is an important question for both fundamental science as well as applications. The question of the conductivity and phase state of a metal surface under multi-megagauss conditions has been posed for many decades.[11] Intense current pulses can ohmically heat metal surfaces to plasma conditions. Such pulses drive magnetized target fusion systems,[12,13] flyer plate experiments,[14] recyclable transmission lines,[15] and ultra-high magnetic field generators.[16] Recent experiments[17,18,19,20,21] have investigated the phase transitions of metal into plasma in the "current skinning" regime (also referred to as the "liner" or "thick wire" regime), in which the current initially flows in a skin layer, but then propagates into the conductor as a nonlinear diffusion wave.[22] Plasma forms at a much higher surface magnetic field (B_s) than for a thin wire, because of the continuous presence of cold underlying metal conductor.

There is limited predictive capability in determining the resultant state of a metal surface when pulsed by an intense current. The conductivity of metals in different states -- solid, liquid, warm dense matter, vapor, plasma, or some mix of these -- is not completely known.[23,24,25,26,27] Modeling the properties of a system using radiation-magnetohydrodynamics (R-MHD) can be difficult due to the rapid variations in material properties and is complicated by the complex interplay of magnetic diffusion, hydrodynamics, and radiative energy transfer.[28,29,30,31,32]

When a thick metal conductor is heated by an intense current pulse, the surface heats and becomes more resistive, accelerating the diffusion of current into the hundreds of microns of cold, highly conductive material under the surface. The diffusion of the current into the conductor leads to a reduced ohmic heating of the surface and can lead to marginal surface plasma formation.

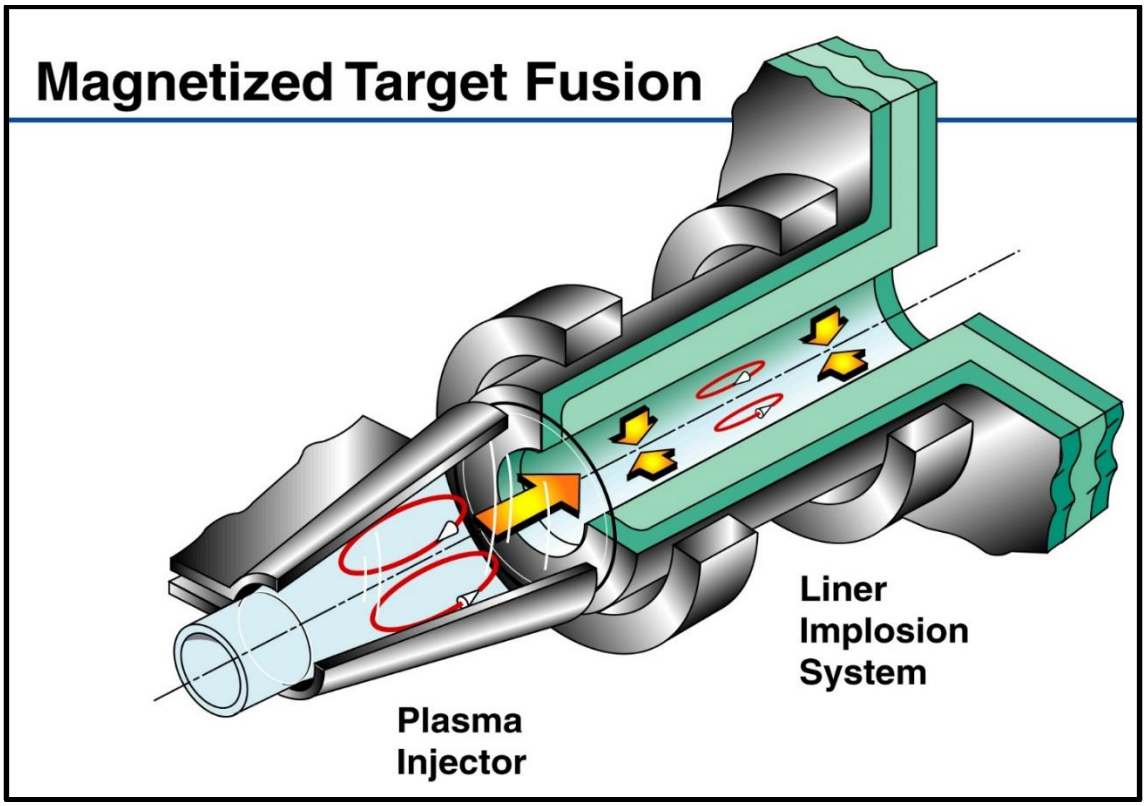

Figure Intro. 1: A schematic shows a Magnetized Target Fusion (MTF) configuration with the target plasma being injected into the liner implosion system shortly before compression. (Figure courtesy of R. Siemon, LANL)

An immediate application for understanding these processes is found in the case of Magnetized Target Fusion (MTF) and is illustrated in Figure Intro. 1. The MTF concept of fusion is a form of magneto-inertial fusion (MIF) that compresses a metal liner around a magnetized plasma fuel by pulsing the metal liner with a multi-mega-ampere current pulse. The target plasma is a Field Reversed Configuration (FRC) with closed magnetic field lines to insulate the electrons and ions from the walls of the metal liner. The MTF concept is illustrated in Figure Intro.1. The FRC is formed and then translated into a metal liner and captured using magnetic mirrors. After trapping of the target plasma, a large current pulse is sent through the liner. The current pulse compresses the flux-conserving metal liner and adiabatically heats the plasma. The goal of MTF is to seed a strong enough magnetic field such that the increase in field strength reduces the electron and ion thermal conductivity across the magnetic field lines and to the metal liner. As the magnetic flux

is compressed, a portion of the flux will diffuse into the metal liner. The diffusion of this flux will create eddy currents that will heat the metal surface and may lead to phase changes. The heating of the metal liner can lead to the formation of metal vapor and metal plasma that can diffuse across the magnetic field lines and penetrate the fusion fuel as illustrated in Figure Intro. 2. The diffusion process that leads to the heating, phase transformations, and eventual development of instabilities, is dictated by the conductivity of the metal liner. The amplitude of these hydrodynamic instabilities determines to what extent the contaminants mix with the fuel. Severe high-Z contamination can lead to radiative cooling of the plasma to temperatures and pressures that are far below those needed for high fusion yield.

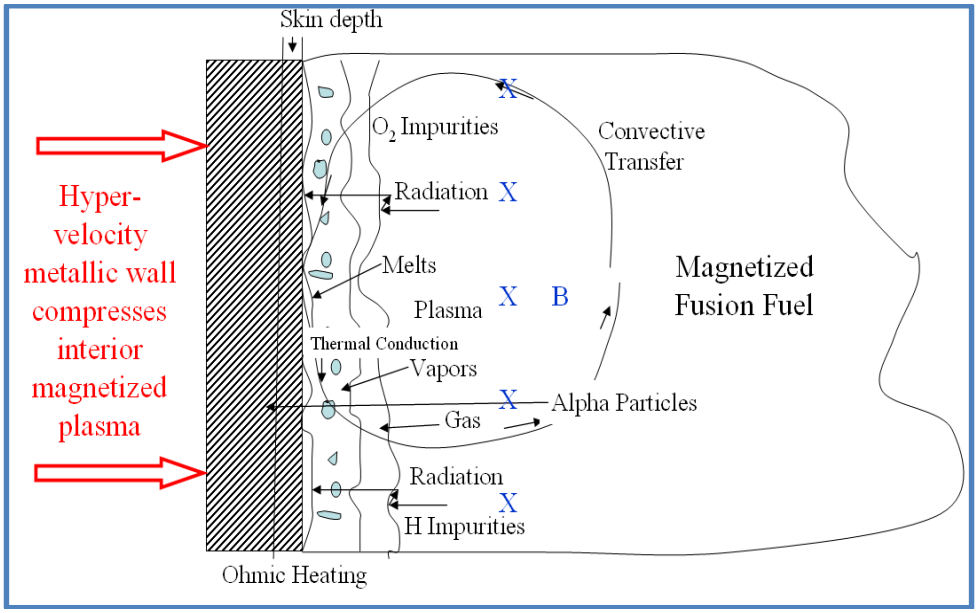

Figure Intro 2: A metallic wall compressing a magnetic field will lead to diffusion of the magnetic flux into the metal wall, leading to melting, vaporization, and ionization of the surface. The metal material may cross the magnetic field lines and contaminate the fusion fuel, causing radiative cooling (Figure courtesy of V Makhin and R.E. Siemon).

Several hypotheses have been developed to explain the interaction of a metal conductor with a pulsed MG magnetic field and have been summarized by Garanin et al.[33,34] Garanin simulated the formation of surface plasma when a megagauss magnetic field diffuses into a copper surface. Effects of thermal conductivity, radiative transfer, and dynamic electric conductivity were

included in the theory and simulation. For copper, Garanin calculated that for a smoothly rising magnetic field of 5 MG/μs, plasma would form at a surface magnetic field of 3 MG. For an instantaneous turn on of the surface magnetic field, surface plasma formed at a magnetic threshold of 1.6 MG.

To study the effects of pulsing a metal surface with a multi-megagauss magnetic field similar to that produced in MTF, a single wire experiment was designed to study the same parameters in a z-pinch configuration. By pulsing a thick metal rod to a peak current of 1 mega-ampere, a surface magnetic field can reach several megagauss. While the geometry may be different, the thick rod pulsed by a mega-ampere current experiences the same surface heating as the megagauss magnetic field diffusion of MTF. The radius of curvature of the MTF liners and the z-pinch thick rods are large enough that the diffusion properties of the magnetic field can be treated such as that for a flat surface. As stated by Knoepfel, this can be done for a rod with a skin depth that is much smaller than the radius.

While data exist for metal rods heated in the skinning regime,[35,36,37,38,39] data comparing different alloys of copper rods are unavailable. In addition, many papers do not distinguish between a surface explosion (the time at which the sublimation energy has been deposited onto the surface of the material), and the time of plasma formation. However, Awe[40] observed plasma formation from ohmically heated Al-6061 rods when pulsed by a linear rising current and showed that the surface of the aluminum rod could explode without forming plasma.

In the work reported here, several diagnostics are used to determine and confirm the presence or absence of plasma. The first is visible light radiometry, using a diagnostic that images the load surface to a photodiode array. When plasma starts to form, the diode signals indicate surface temperatures too high for the material to be entirely in the solid, liquid, or gas phase. In

addition, with the overall current rising, the photodiodes show a sharp increase in signal. In this case, we can identify an initiation "time" of bulk surface plasma formation as the instant at the start of the abrupt increase in optical photodiode signal. The diode signals are used to calculate a lower bound for the average surface temperature, by applying a blackbody approximation. At the time of bulk surface plasma formation, the blackbody application shows the lower bound of the surface temperature to be in the range of 0.5 to 1.0 eV. The abrupt increase in surface emission can be interpreted as related to an abrupt increase in conductivity when plasma forms.[41,42,43,44] The increase in conductivity, in the context of an overall rising current, causes an abrupt increase in current density in the plasma-forming layer, leading to an increase in plasma temperature that reinforces the increase in conductivity. Laser shadowgaphy images allow for the observation of expansion, with resistive vapor initially expanding across magnetic field lines. After plasma forms, the conductive plasma layer will feel a radially inward force that will lead to surface instabilities. The sudden expansion of the surface of a heated conductor is not sufficient to claim plasma formation; on the other hand, the eventual development of surface instabilities is an indicator of plasma formation, though it does not pinpoint the moment of plasma formation. The self-emission images captured by ICCD cameras provide a third indicator of plasma formation. Early non-uniform dots filament in the direction of current near the time of the abrupt increase in the visible diode signal and indicate positive feedback of electrothermal instabilities, a formation attributed to a plasma. Awe observed surface plasma and a threshold for plasma formation for aluminum 6061 utilizing several diagnostics, including visible radiometry, extreme ultraviolet spectroscopy, and surface instabilities observed via laser shadowgraphy. Chaikovsky et al.[9] observed a threshold for plasma formation on copper with solid cylinders with diameters of 2, 3, and 4 mm pulsed by 1.5-2.0 MA, with only the 2-mm-diameter rod forming plasma. X-ray

photodiodes (XRDs) sensitive in the 10-15 eV range were fielded and were used to determine the temperature by assuming the surface radiated as a blackbody. Time of plasma formation was determined to be when the surface temperature reached 2 eV, sufficient to ensure the signal was out of the noise. The nominal threshold surface magnetic field was calculated using the initial rod radius. Continued work was done using aluminum and titanium rods as reported by Labeskaya et al.[45] The aluminum and titanium rods observed plasma formation in the range of 2.5-4.0 and 3.0-4.0 MG nominal surface magnetic field respectively. Cu-101 and Al-5052 rods have also been studied at Sandia's 20-MA Z facility. Images of instability growth were observed using 2-frame x-ray radiography with 6.151 keV and 1.865 keV monochromatic backlighting. The development and evolution of surface instabilities on aluminum matched well with 2D MHD simulations. However, the copper rods showed much less agreement with simulations. The discrepancy could be due to the need for refinement of conductivity, equation of state, and opacity models utilized in the modeling.

The immediate difficulty of studying the interaction of the trapped magnetic flux with the metal liner was the inability to easily access the liner with diagnostic tools. Another drawback of studying the liner physics directly was the cost of such experiments on the larger facility machines such as Atlas, Shiva Star, or the Z machine. Figure Intro. 3 illustrates the idea behind designing a simple wire experiment on the Zebra z-pinch machine that would allow for the study of the interaction between a MG magnetic field with a metal conductor. The first goal in conducting a wire experiment to study these effects was to design a load configuration that allowed for benchmarking R-MHD simulations. This required ensuring that the heating and subsequent changes in state were caused by ohmically heating the wire material and not through some non-thermal process such as contact arcing or electron avalanche.

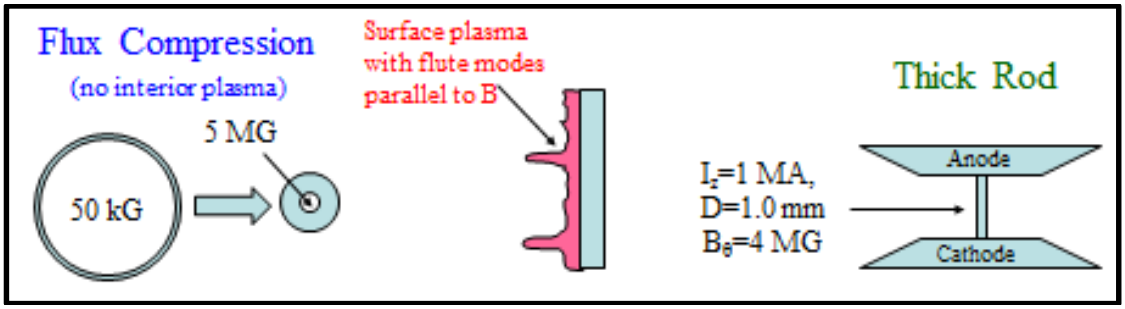

Figure Intro 3: The physics of magnetic flux conserving driven liners can be studied using a thick rod in a z-pinch configuration using the Zebra mega-ampere pulsed power machine. (figure courtesy of R. Siemon)

The "Zebra Megagauss Experiments" (labeled as MG-I to MG-IX) have been successfully designed to benchmark R-MHD simulations. The metal rods are pulsed by the Zebra generator with a reproducible 1 MA current pulse with a rise time of 100 ns. Measurements have been made to infer the surface magnetic field (B_s), the time of plasma formation, the surface temperature (T_{BB}), the uniformity of surface emission, expansion rate, and spectral emission. A parametric study was done of aluminum 6061, copper 101, copper 145, nickel 200, and titanium type II. The diameters were varied from 0.5-mm to 2.0-mm to study the effects of varying surface dB/dt. Experiments with aluminum 6061 were conducted by Awe and were used to benchmark simulations performed by Lindemuth[46] using MHDR and Garanin[47] using UPMHD. It was observed that for aluminum, plasma formation occurred when the surface magnetic field reached a threshold of 2.2 MG. Work presented here will show that a threshold was observed for plasma formation on the surface of copper 101, copper 145, titanium II, and nickel 200 when pulsed by a linear rising magnetic field of 30-80 MG/μs. Plasma formed on the surface of copper 101, copper 145, titanium II, and nickel 200 when the surface magnetic field reached 3.5, 3.0, 2.2, and 2.6 MG respectively.

Chapter I: Fundamental Physics of the Z-Pinch Experiment

The UNR Megagauss experiments conducted at the NTF study the interaction of a multi-megagauss magnetic field with a mega-ampere current carrying conductor. The experiments are conducted on the Zebra pulsed power machine using a z-pinch configuration to pulse a metal load with a mega-ampere current pulse. The loads used are conductive rods with a diameter much larger than the conductive and magnetic skin depth (δ_B).

The z-pinch configuration has been used on wire arrays and single wire experiments for many years.[48,49] An incredible amount of research has been done in the area of pulsed power physics with the wire diameters being small enough for the current to diffuse entirely through the load radius. These thin wire ($D \leq 100\mu m$) experiments have been shown to form plasma at magnetic field strength less than a megagauss. It is not well understood what causes plasma formation under these conditions, however, it is likely due to non-thermal processes such as electrical breakdown.

The MG experiments were designed to study the formation of plasma on pulsed metal surfaces via thermal processes. It was theorized that a metal conductor would form plasma when the surface magnetic field reaches 1.5 to 3.0 MG.[50] It was observed in experiments that aluminum forms plasma at a surface magnetic field threshold of 2.2 MG.[51] Along with the threshold for broad surface plasma formation, the expansion speed, time of vapor formation (referred to as the explosion or expansion time), instability growth, blackbody temperature, surface emission, and extreme ultraviolet temperature were observed. To understand the design of the experiment this chapter will develop and utilize simple models that will then be used to understand the z-pinch physics. With these models at hand, it will be easy to understand the design of the hardware as well as the choice of materials to be pulsed.

Section I.A: Electric and Magnetic Fields of a Z-Pinch Configuration

The z-pinch configuration of the MG experiments is illustrated in Figure I.1 below. The current carrying conductor is axial to the flow of current. The current flows through a thick return conductor to the anode plate, then through the axial conductor to the cathode plate. The current flowing through the conducting rod creates an azimuthal magnetic field. The current density (J_z) and the azimuthal magnetic field (B_θ) create a $J \times B$ force that acts radially inward on the material. This inward force is what is commonly known as a z-pinch.

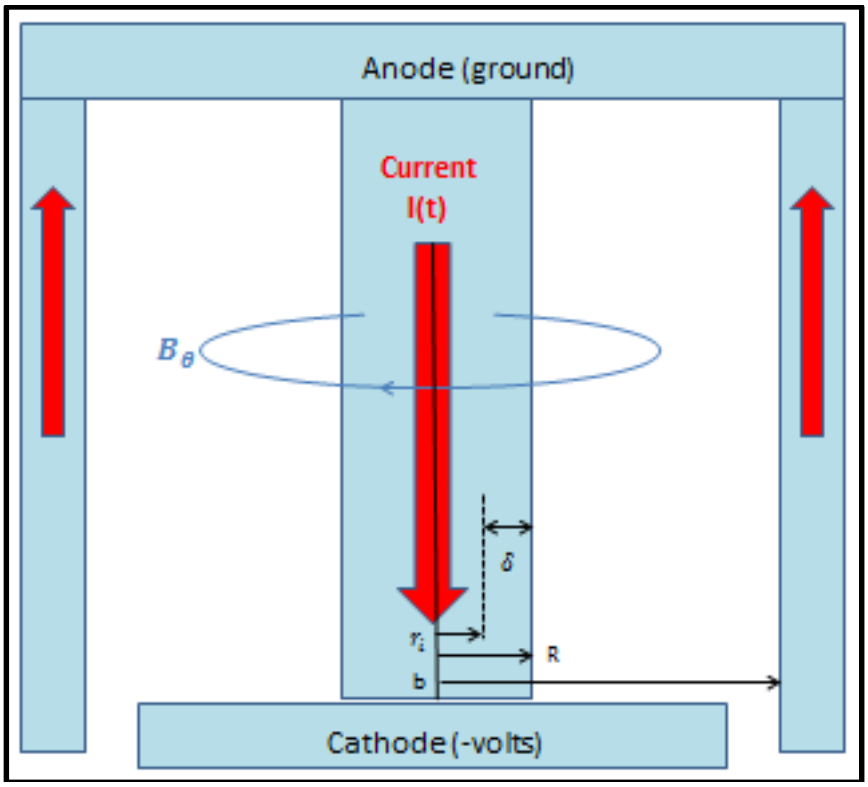

Figure I.1 Z-pinch configuration at the Nevada Terawatt Facility. Figure shows the current, magnetic field and subsequent skin effect that will be derived in this chapter.

To simplify the derivation of the field equations, a steady state equilibrium ($\vec{v}$=0) will be assumed. This implies no bulk fluid flow. Next, the current shall be taken to be uniformly distributed within a thin metallic shell of the conductor. This shell will cover the volume from inner radius r_i to the outer radius *R*. The current density can therefore be written as,

$$J = \frac{I}{\pi(R^2 - r_i^2)} \quad \text{for } r_i < r < R \tag{I.1}$$

$$J = 0 \quad \text{for } r < r_i \text{ or } R < r$$

As $r_i \to 0$ the current density becomes uniform throughout the entire conducting wire and is referred to as the thin wire limit. The condition $r_i \sim R$ leads to the current density being contained in a thin skin layer of depth $R - r_i$ and is referred to as the thick rod limit. The diffusion of the current into the conductor is determined by the resistive properties of the metal and shall be discussed in more detail later in this chapter. The resistivity (η) will be taken as a constant in order to simplify the equations. Using Ohm's Law ($E = \eta J$) the axial electric field can be written as,

$$E_z = \eta J_z = \frac{\eta I}{\pi(R^2 - r_i^2)} \quad \text{for } r_i < r < R \tag{I.3}$$

Using Ampere's Law, the azimuthal magnetic field can be written as

$$B_\theta(r > R) = \frac{\mu_0 I}{2\pi r}$$

$$B_\theta(r_i < r < R) = \frac{\mu_0 I(r^2 - r_i^2)}{2\pi r(R^2 - r_i^2)} \tag{I.4}$$

$$B_\theta(r < r_i) = 0$$

The field equation above describes the fields due to a current flowing through a skin layer. By setting r_i=0 the field equations become valid for a wire with uniform current density.

The importance of the fields in the MG experiments is to be determined below. It is important to understand what effect the fields have on the surface of the rod in order to help in designing hardware that ensures that plasma formation is due entirely to ohmic heating of the material and not due to a non-thermal process such as electric field emission. To determine the effect, a separable solution of Laplace's equation is solved in the vacuum between the surface of the axial conductor (r=R) and the return conductor (r=b). The cathode will be labeled as z=-z_c and

the anode/return current conductor z=0. The potential at the return conductor shall be set to zero (*V(r,z=0)=0* and *V(b,z)=0*) and the axial electric field at the surface of the rod is

$$E_z(R) = \frac{\eta I}{\pi(R^2 - {r_i}^2)} \tag{I.5}$$

The potential is then,

$$V(R,z) = -\int_z^0 E_{es,z}(R)dz \tag{I.6}$$

E_{es} in Equation I.6 is the electrostatic electric field only. It is considerably bigger than the total electric field given by Equation I.5, because it must overcome the Faraday electric field created by the inductance of the rod. The inductance and the induced EMF of our rod in a z-pinch configuration can be written as

$$L = \frac{\mu_0 z_c}{2\pi} ln\left(\frac{b}{R}\right) \Rightarrow EMF = -L\frac{dI}{dt} \tag{I.7}$$

Where $\frac{dI}{dt} = 11\frac{kA}{ns}$ at $500kA$. The potential along the rod is then

$$V(R,z) = \frac{\mu_0 z}{2\pi}\frac{dI}{dt} ln\left(\frac{b}{R}\right) + \frac{\eta I z}{\pi(R^2 - {r_i}^2)} \tag{I.8}$$

Using Laplace's equation

$$\nabla^2 V = \frac{1}{r}\frac{\partial}{\partial r}\left[r\frac{\partial V}{\partial r}\right] + \frac{1}{r^2}\frac{\partial^2 V}{\partial \theta^2} + \frac{\partial^2 V}{\partial z^2} = 0 \tag{I.9}$$

Applying the boundary conditions for *V(r,z)*, the potential can be found. Since there is no theta dependence, equation I.9 simplifies to

$$\nabla^2 V = \frac{1}{r}\frac{\partial}{\partial r}\left[r\frac{\partial V}{\partial r}\right] + \frac{\partial^2 V}{\partial z^2} = 0 \tag{I.10}$$

It shall be assumed that the potential has the separable form

$$V(r,z) = z \cdot f(\mathrm{r}) \tag{I.11}$$

Substituting this into equation I.10 results in

$$\frac{1}{r}\frac{\partial f}{\partial r} + \frac{\partial^2 f}{\partial r^2} = 0 \Rightarrow f(r) = Aln(B \cdot r) \tag{I.12}$$

Applying boundary condition *V(b)=0*

$$V(b,z) = 0 = z \cdot Aln(B \cdot b) \Rightarrow B = \frac{1}{b} \tag{I.13}$$

And for boundary condition set by the rod surface *(r=R)*

$$V(R,z) = \frac{\mu_0 z ln\left(\frac{b}{R}\right)}{2\pi}\frac{dI}{dt} + \frac{\eta I z}{\pi(R^2 - {r_i}^2)} = z \cdot Aln\left(\frac{R}{b}\right) \tag{I.14}$$

$$\Rightarrow A = \frac{\mu_0 ln\left(\frac{b}{R}\right)}{2\pi}\frac{dI}{dt}\ln\left(\frac{R}{b}\right)^{-1} + \frac{\eta I}{\pi(R^2 - {r_i}^2)}\ln\left(\frac{R}{b}\right)^{-1} \tag{I.15}$$

Which gives

$$V(r,z) = z\left[\frac{\eta I}{\pi(R^2 - {r_i}^2)} + \frac{\mu_0 ln\left(\frac{b}{R}\right)}{2\pi}\frac{dI}{dt}\right]\frac{\ln\left(\frac{r}{b}\right)}{\ln\left(\frac{R}{b}\right)} \tag{I.16}$$

As the Faraday electric field is purely axial (upwards) in this geometry, the radial component of the electric field is just that of the electrostatic component of the electric field, which can now be determined as

$$E_r(r,z) = E_{es,r}(r,z) = -\frac{\partial V}{\partial r} = -\frac{z}{r}\left[\frac{\eta I}{\pi(R^2 - {r_i}^2)} + \frac{\mu_0 ln\left(\frac{b}{R}\right)}{2\pi}\frac{dI}{dt}\right]\frac{1}{\ln\left(\frac{R}{b}\right)} \tag{I.17}$$

If r$\rightarrow R$ and $r_i \rightarrow 0$ for uniform current distribution, then the effects of the radial electric field can be determined with equation I.18

$$E_r(R,z) = \frac{z}{R}\left[\frac{\eta I}{\pi R^2} + \frac{\mu_0 ln\left(\frac{b}{R}\right)}{2\pi}\frac{dI}{dt}\right]\frac{1}{\ln\left(\frac{b}{R}\right)} \tag{I.18}$$

The design of the MG hardware was intended to keep the radial electric field smaller than the threshold for plasma formation by explosive electron emission (10^8 V/m for Al). The radial field is tabulated (Table I.1) below, for typical experimental parameters.

I=1.0 MA, $z=z_c$=0.007m, r=R=0.5mm, b=0.3m		
Element	**Resistivity [Ω*m]**	$E_r(r,z)$ **[V/m]**
Aluminum	2.8×10^{-8}	-3.09×10^{7}
Copper	1.68×10^{-8}	-3.08×10^{7}
Nickel	6.93×10^{-8}	-3.10×10^{7}
Titanium	42×10^{-8}	-3.20×10^{7}

Table I.1 Radial electric field in Zebra z-pinch configuration

This radial electric field calculation does not take into account the inductance of the 6.25-mm-diameter, ~7-mm-long portion of the barbell load above the central thin rod section. Adding in this extra inductance increases the maximum radial electric field by an amount less than the tabulated estimates.

Section I.B: Magnetic Diffusion

The magnetic field diffusion into a current carrying conductor will be considered here and follows closely the method used by Knoepfel[52]. The diffusion equation will help to describe the distribution of current as well as the radial electric field as shown above. The loads in our experiments have a large radius of curvature to allow us to assume a planar geometry in deriving the following equations. The fluid velocity will also be taken to be zero. By using Maxwell's equations and Ohm's Law, this section will derive the equation for magnetic diffusion that will further be used to describe the joule heating of our loads for different metal materials.

Maxwell's Equations

$$\nabla \cdot E = \frac{\rho}{\epsilon_0} \tag{I.22}$$

$$\nabla \times E = -\frac{\partial B}{\partial t} \tag{I.23}$$

$$\nabla \cdot B = 0 \tag{I.24}$$

$$\nabla \times B = \mu_0 J + \mu_0 \epsilon_0 \frac{\partial E}{\partial t} \tag{I.25}$$

Ohm's Law

$$E = \eta J \tag{I.26}$$

Equation I.22 can be rewritten as $\nabla \cdot E = 0$ because we can assume charge neutrality. Substituting Ohm's Law into equation I.25 and comparing the two terms on the right, it can be shown that $\frac{1}{\eta}$ is much greater than $\frac{\epsilon_0}{\tau}$, where τ is on the order of 100ns for our experiment. Equation I.25 can now be simplified to $\nabla \times B = \mu_0 J = \frac{\mu_0 E}{\eta} \Rightarrow E = \frac{\eta}{\mu_0} \nabla \times B$

Substituting this into equation I.23

$$\nabla \times E = \frac{\eta}{\mu_0} \nabla \times \nabla \times B \tag{I.27}$$

Using the triple scalar product and $\nabla \cdot B = 0$

$$\nabla \times \nabla \times B = \nabla(\nabla \cdot B) - \nabla^2 B \Rightarrow \frac{\partial B}{\partial t} = \frac{\eta}{\mu_0} \nabla^2 B \tag{I.28}$$

This diffusion equation is a three-dimensional equation but can be simplified to one dimension through the planar approximation. This approximation gives

$$\frac{\partial B}{\partial t} = \frac{\eta}{\mu_0} \frac{\partial^2 B}{\partial x^2} \tag{I.29}$$

The differential equation can be solved using the Laplace Transform method and has been done elsewhere[53,54]. The Laplace Transform method is explained in detail in many college books[55]. The boundary conditions for the equation are as follows:

Initial condition *B(x,t=0)=0*

Boundary condition *B(x=0,t)=f(t)*

The boundary condition will be set such that the magnetic field is a step function at the boundary. The function will be set to a constant, f(t)= B_0 for $t > 0$. These conditions are used to solve equation I.29 to give

$$B(x,t) = B_0 \text{erfc}\left[\sqrt{\frac{\mu_0}{\eta}}\frac{x}{2\sqrt{t}}\right] \quad \text{(I.30)}$$

Where erfc is the complementary error function defined as

$$erfc(z) = 1 - \frac{2}{\sqrt{\pi}}\left(z - \frac{z^3}{3} + \frac{z^5}{10} - \frac{z^7}{42} + \right) \quad \text{(I.31)}$$

Figure I.2 illustrates the magnetic field penetration in time into an aluminum load with the surface magnetic field held at a constant B_0 =100 Tesla at the surface. The surface magnetic field is a step function and is held at a constant 100 Tesla. Figure I.3 illustrates the magnetic field penetration at 20ns for several different materials for the same boundary condition.

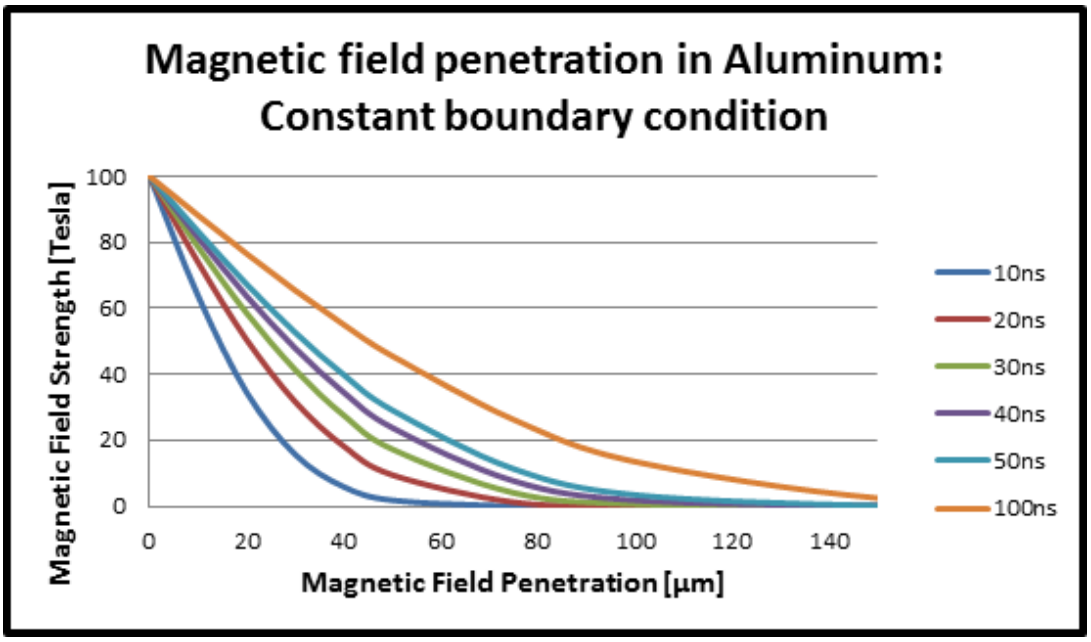

Figure I.2 The magnetic field diffusion into an aluminum conduction rod with a constant surface magnetic field of 100 T at times ranging from 0 to 100ns.

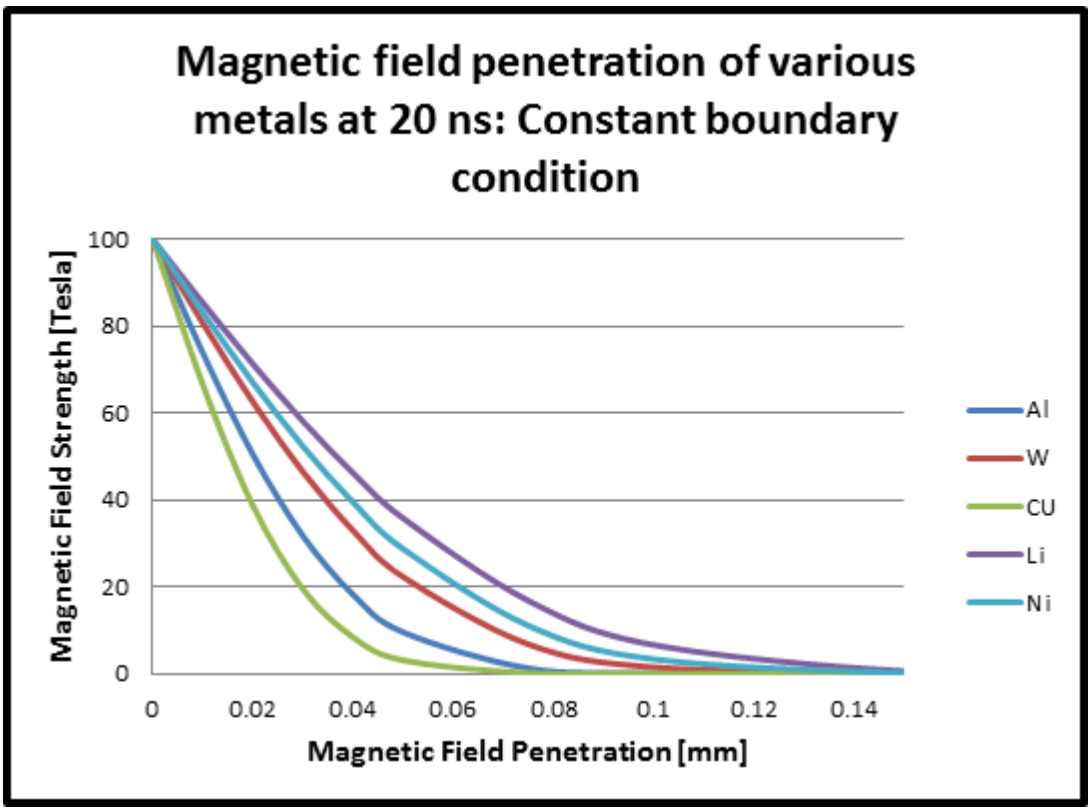

Figure I.3 The magnetic field penetration with a constant surface magnetic field for different metals at 20ns.

With an equation for the magnetic field, the current density can now be found using

$$J = \frac{1}{\mu_0}\frac{\partial B}{\partial x} \tag{I.32}$$

The differentiation is easier to perform if equation I.30 is rewritten as

$$B(x,t) = B_0\text{erfc}[ux] = B_0[1 - \frac{2}{\sqrt{\pi}}\left(ux - \frac{u^3x^3}{3} + \frac{u^5x^5}{10} - \cdots\right)] \tag{I.33}$$

In this form, differentiation is much easier and gives the current density as

$$J = \frac{-2B_0}{\mu_0\sqrt{\pi}}\left(u - u^3x^2 + \frac{u^5x^4}{2} - \frac{u^7x^6}{6} + \cdots\right) = \frac{-2B_0}{\mu_0\sqrt{\pi}}\sum_{n=0}^{\infty}(-1)^n\frac{u(t)^{2n+1}x^{2n}}{n!} \tag{I.34}$$

The power density can be found once again using $P=\eta J^2$

$$P(x,t) = \frac{4\eta B_0^2}{\mu_0^2\pi}\left(\sum_{n=0}^{\infty}(-1)^n\frac{u(t)^{2n+1}x^{2n}}{n!}\right)^2 \tag{I.35}$$

The temperature can be determined by assuming the specific heat is constant and gives

$$T(t) = \int_0^t \frac{P(x,t')}{C_v} dt' = \frac{4\eta B_0^2}{\mu_0^2 \pi} \frac{1}{C_v} \int_0^t \left(\sum_{n=0}^{\infty} (-1)^n \frac{u(t')^{2n+1} x^{2n}}{n!} \right)^2 dt' \quad \text{(I.36)}$$

The solution of the diffusion equation presented here assumed a step function for the surface magnetic field. For greater realism, the boundary condition would need to be replaced with a function that properly matches the current profile of Zebra. The assumption of constant material resistivity must also be modified if the diffusion equation is to be realistic. As the temperature of aluminum, copper, nickel and titanium is increased (in the solid, liquid, and vapor states), the resistivity increases. This is not true for a metal in the plasma state and will be discussed in detail later in this chapter. The resistivity of a conductor can be written as[56]

$$\eta(T) = \eta_0 \left(1 + \frac{Q}{\rho C_v \eta_0} \frac{\partial \eta}{\partial T} \right) \quad \text{(I.37)}$$

Where $\eta(T)$ is the temperature dependent resistivity, Q is the heat energy density, Cv is the specific heat, and ρ is the mass density. Substituting equation I.37 into I.29 and numerically solving for the magnetic field results in a non-linear magnetic diffusion wave propagating towards the center of the cylindrical wire. Results of this nonlinear diffusion wave can be found in Knoepfel[57].

Section I.C: Z-Pinch Equilibrium

The stability of a conductor in a z-pinch configuration can be understood with the use of magneto-hydrodynamic equations (MHD). The equations and derivations in this section are taken from[58,59]. The equations used to study MHD are the following:

Mass continuity equation:

$$\frac{\partial \rho}{\partial t} + \vec{\nabla} \cdot (\rho \vec{u}) = 0 \quad \text{(I.38)}$$

Charge continuity equation:

$$\frac{\partial \sigma}{\partial t} + \vec{\nabla} \cdot \vec{j} = 0 \quad \text{(I.39)}$$

Single fluid equation of motion:

$$\rho \frac{d\vec{u}}{dt} = \rho \left(\frac{\partial \vec{u}}{\partial t} + \vec{u} \cdot \vec{\nabla} u \right) = \sigma \vec{E} + \vec{j} \times \vec{B} - \vec{\nabla} p \quad \text{(I.40)}$$

Generalized Ohm's law:

$$\vec{E} + \vec{u} \times \vec{B} = \eta \vec{j} + \frac{\vec{j} \times \vec{B} - \vec{\nabla} p_e}{ne} \quad \text{(I.41)}$$

MHD is the specific case where charge neutrality is approximated. For charge neutrality to be assumed, the electric force σE and the charge separation $\frac{d\sigma}{dt}$ must be small enough to justify omitting them from the equation above. This approximation is justified when $\frac{\rho}{\varepsilon_0 B^2}$>>1. Using parameters similar to those in the MG Zebra experiments (ρ=0.3g/cm^3, B=200Telsa) the ratio is several orders of magnitude greater than 1, justifying the charge neutrality approximation.

Ideal MHD and the Magnetic Reynolds Number

The second and third terms on the right side of the Generalized Ohm's Law will drop out when the scale length of the fluid motion of the plasma is much larger that the ion Larmor radius. This approximation holds if the ∇p and $\vec{j} \times \vec{B}$ forces cause the $\vec{E} \times \vec{B}$ drift to dominate over the weaker drifts such as the diamagnetic drift, ∇B or curvature drift. The small Larmor radius approximation leads the General Ohm's Law to be written simply as:

$$\vec{E} + \vec{u} \times \vec{B} = \eta \vec{j} \quad \text{(I.42)}$$

In a high-temperature plasma, the resistivity is very small. With small resistivity, large conductivity, the term on the right side of the General Ohm's Law can be approximated to be zero giving the following:

$$\vec{E} + \vec{u} \times \vec{B} = 0 \qquad \text{(I.43)}$$

This approximation that leads to this homogenous equation is referred to as Ideal MHD. It should be noted that the result of infinite conductivity means that the plasma fluid velocities arise largely from the $\vec{E} \times \vec{B}$ drift and not from diamagnetic or guiding-center drifts. With infinite conductivity and zero resistivity, the collisional frequencies must be zero, leading to zero diffusion of particles across magnetic field lines. The consequence of this is that the plasma will be "tied" to the magnetic field lines. The plasma being "tied" to the magnetic field lines gives rise to the conservation of magnetic flux through any closed contour that moves with the plasma. As an example, let us imagine a cylindrical plasma as shown in Figure I.4 where the magnetic field lines are parallel and axial. If the B-field of the cylindrical plasma were to increase (decrease), then the plasma would compress (expand) to conserve flux according to the magnetic flux equation:

$$\varphi = B \cdot A \qquad \text{(I.44)}$$

Where φ is the magnetic flux, B is the usual magnetic field and A is the area that the flux line penetrates.

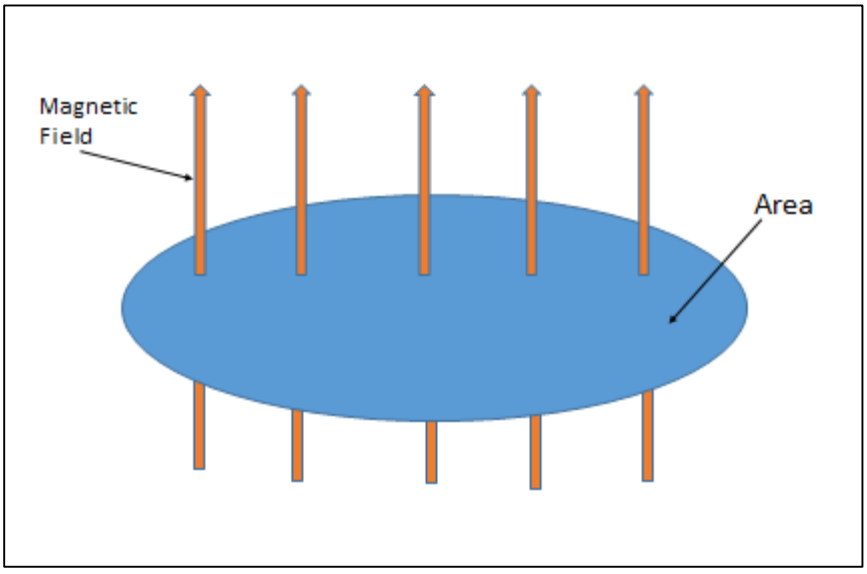

Figure I.4 Cylindrical plasma where the magnetic field lines are parallel and axial

Along with the bulk plasma conserving flux, the individual ions and electrons also conserve flux through their gyro-orbits. As the B-field is ramped up (down) the gyro-orbits are also compressed (expanded) so as to increase (decrease) the perpendicular energy and hence heat (cool) the plasma. This form of heating and cooling plasma is referred to as adiabatic compression and expansion.

The question should be asked: when is infinite conductivity a valid approximation? To determine this we shall start with Faraday's Law,

$$\frac{d\vec{B}}{dt} = -\vec{\nabla} \times \vec{E} = \vec{\nabla} \times \left(\vec{u} \times \vec{B}\right) - \vec{\nabla} \times (\eta \vec{j}) \tag{I.45}$$

Now using Ampere's Law,

$$\vec{\nabla} \times \vec{B} = \mu_0 \vec{j} \tag{I.46}$$

And the triple vector product,

$$\vec{\nabla} \times \vec{\nabla} \times \vec{B} = \vec{\nabla}\left(\vec{\nabla} \cdot \vec{B}\right) - \nabla^2 \vec{B} \tag{I.47}$$

We arrive at the following,

$$\frac{\mathrm{d}\vec{\mathrm{B}}}{\mathrm{dt}} = \vec{\nabla} \times \left(\vec{\mathrm{u}} \times \vec{\mathrm{B}}\right) + \left(\frac{\eta}{\mu_0}\right)\nabla^2 \vec{\mathrm{B}} \tag{I.48}$$

Where I have used $\nabla \cdot \vec{B} = 0$. The first term on the right describes the convection of the magnetic field with the plasma while the second term represents the resistive diffusion of the magnetic field across the plasma. The ratio of the two terms can be taken where *L* is the characteristic scale length of the plasma and u is the characteristic fluid velocity:

$$\frac{term\ 1}{term\ 2} = \frac{\vec{\nabla} \times (\vec{u} \times \vec{B})}{\left(\frac{\eta}{\mu_0}\right)\nabla^2 \vec{B}} = \frac{\frac{1}{L} u B \mu_0}{B \eta \frac{1}{L^2}} = \frac{L u \mu_0}{\eta} \equiv R_M \tag{I.49}$$

Where R_M is called the Magnetic Reynolds number. If this number is sufficiently large, then the infinite conductivity approximation is valid. With the parameters of the MG experiments ($L \sim 10^{-6},\ u \sim 10^{3}, \eta \sim 10^{-8}, \mu_0 \sim 10^{-6}$ in mks units) the Magnetic Reynolds number is on the

order of 0.01 to 1, depending on the chosen metal, such that the plasma in this work is not Ideal MHD.

MHD Equilibrium

When the magnetic and pressure gradients are equal, the system is said to be in steady state. Assuming local charge neutrality and the fluid velocity being zero everywhere (*u=σ=0*) then the single fluid equation becomes

$$\vec{\nabla}p = \vec{j} \times \vec{B} \tag{I.50}$$

Using Maxwell's equations

$$\vec{\nabla} \times \vec{B} = \mu_0 \vec{j} \tag{I.51}$$

$$\vec{\nabla} \cdot \vec{B} = 0 \tag{I.52}$$

Along with the single fluid equations, we can derive an equilibrium equation.

$$\vec{\nabla}p = \vec{j} \times \vec{B} = \frac{1}{\mu_0}\left(\vec{\nabla} \times \vec{B}\right) \times \vec{B} = \frac{1}{\mu_0}\left[\left(\vec{B} \cdot \vec{\nabla}\right)\vec{B} - \vec{\nabla}\left(\frac{B^2}{2}\right)\right]$$

$$\vec{\nabla}p = -\frac{1}{2\mu_0}\vec{\nabla}B^2 + \frac{1}{\mu_0}(\vec{B} \cdot \vec{\nabla})\vec{B} \tag{I.53}$$

$$\Rightarrow \vec{\nabla}\left(p + \frac{B^2}{2\mu_0}\right) = \frac{1}{\mu_0}(\vec{B} \cdot \vec{\nabla})\vec{B}$$

Equation I.53 is known as the "pressure balance condition." The left hand side shows the plasma pressure and magnetic pressure whereas the right hand side comes from the bending and compression of the magnetic field lines. There are some cases where the right hand side can be taken to be zero so that the field lines are approximately straight and parallel. This gives the pressure-balance equation as,

$$p + \frac{B^2}{2\mu_0} = constant \tag{I.54}$$

The ratio of the plasma pressure to the magnetic pressure is referred to as the β of the plasma,

$$\beta \equiv \frac{2\mu_0 p}{B^2} \tag{I.55}$$

An applicable situation would be a cylindrical plasma with the field lines running along the cylindrical axis. In the MTF configuration, the FRC follows this pressure balance equation and has a β=1. The MG experiments do not have the luxury of setting the right hand side to zero because our field lines are curved. Therefore, we solve the differential equation,

$$\frac{\partial}{\partial r}\left(p + \frac{B_\theta^2}{2\mu_0}\right)\hat{r} = \frac{1}{\mu_0}(\vec{B}\cdot\vec{V})\vec{B} \tag{I.56}$$

$$\frac{1}{\mu_0}(\vec{B}\cdot\vec{V})\vec{B} = \frac{1}{\mu_0}\left(B_\theta\hat{\theta}\cdot\vec{V}\right)B_\theta\hat{\theta} = \frac{1}{\mu_0}B_\theta\nabla_\theta B_\theta\hat{\theta}$$

$$= \frac{1}{\mu_0}B_\theta\frac{1}{r}\frac{\partial(B_\theta\hat{\theta})}{\partial\theta} = \frac{1}{\mu_0}\frac{B_\theta}{r}\left(\frac{\partial B_\theta}{\partial\theta}\hat{\theta} + \frac{\partial\hat{\theta}}{\partial\theta}B_\theta\right) = -\frac{1}{\mu_0 r}B_\theta^2\hat{r} \tag{I.57}$$

$$\Rightarrow \frac{\partial}{\partial r}\left(p + \frac{B_\theta^2}{2\mu_0}\right) = -\frac{1}{\mu_0 r}B_\theta^2 \tag{I.58}$$

Integrating equation I.58 gives

$$p + \frac{B_\theta^2}{2\mu_0} = -\int\frac{1}{\mu_0 r}B_\theta^2 dr \tag{I.59}$$

The solution to this differential equation is valid for any magnetic field profile so I will choose to use the following equation:

$$B_\theta = \frac{\mu_0 I}{2\pi r}\frac{(r^2 - r_i^2)}{(R^2 - r_i^2)} \tag{I.60}$$

Substituting into equation I.59 gives,

$$p(r) = p_0 - \frac{\mu_0^2 I^2 (r^2 - r_i^2)^2}{2\mu_0 4\pi^2 r^2 (R^2 - r_i^2)^2} - \frac{1}{\mu_0}\int_{r_i}^{r}\frac{\mu_0^2 I^2 (r^2 - r_i^2)^2}{4\pi^2 r^3 (R^2 - r_i^2)^2}dr \tag{I.61}$$

In the thin wire limit, this reduces to,

$$p(r) = p_0 - \frac{\mu_0 I^2 r^2}{4\pi^2 R^4} \tag{I.62}$$

To solve for p_0 it can be noted that $p(r) = 0$ at $r = R$. Therefore,

$$p_0 = \frac{\mu_0 I^2}{4\pi^2 R^2} \tag{I.63}$$

Which allows us to write,

$$p(r) = \frac{\mu_0 I^2}{4\pi^2 R^2}(1 - \frac{r^2}{R^2}) \tag{I.64}$$

Equation I.64 is known as the "pinch condition" and reveals the parameters for a self-constricting current-carrying plasma.

Z-pinch stability

Plasma instabilities are a common phenomenon observed in laboratory and astrophysical plasmas. For example, one type of plasma instability that also occurs with ordinary fluids is the Rayleigh-Taylor instability.[60] It occurs at the interface between two fluids, when a higher density fluid is accelerated by a lower density fluid. In a fusion plasma, instabilities can occur due to the magnetic pressures that constrict the plasma fuel. It was first thought that the high pressures in a z-pinch configuration would allow for the design of an energy source. It was quickly realized that the configuration was unstable. Any radial perturbation leads to the growth of instabilities. Such a perturbation could be due to machining artifacts or impurities on the surface of a material. What seeds these instabilities as well as determining ways to mitigate their growth is of great interest to the z-pinch community. To determine what affects the late time surface instabilities, a clear understanding of the evolution of the surface from the solid to liquid to vapor to plasma must be determined. To understand some of these effects, the conductivity through these states will first be discussed.

Section I.D: Conductivity and Phase Transitions

The conductivity of solid metal conductors is discussed in detail in Croxton[61] with the conductivity scaling as the inverse square root of the temperature.

$$\sigma = \frac{N_e e^2 l}{(3mkT)^{\frac{1}{2}}} \tag{I.65}$$

The conductivity of a plasma can be written as

$$\sigma = \frac{(4\pi\epsilon_0)^2 (kT_e)^{\frac{3}{2}}}{\pi Z e^2 \sqrt{m} ln\Lambda} \tag{I.66}$$

And is commonly known as the Spitzer conductivity of a plasma. The conductivity of a solid conductor has a negative response to an increase in temperature with the plasma having a positive response to an increase in temperature. The conductivity of a metal in the vapor and plasma states is not an easy parameter to determine. Experiments have been conducted in recent years to determine the conductivity of aluminum, copper, titanium, and nickel in the vapor and plasma states. The results of these experiments will be discussed next.

Electrical Conductivity of Metals

The conductivity of copper plasmas was studied by DeSilva and Kunze[62] by exploding 99.9% copper wires of diameters 125 μm and 250 μm in a capillary tube. The plasmas produced are characterized by a coupling constant

$$\Gamma = \frac{z^2 e^2}{kT} \left(\frac{4\pi n}{3}\right)^{\frac{1}{3}} \tag{I.67}$$

For which $\Gamma \geq 1$ is labeled as strongly coupled. The coupling constant is a mathematical ratio of the potential energy to the kinetic energy per particle. This means that for large Γ, the plasma would need to be a high density and low temperature plasma. The plasma discharges conducted by DeSilva and Kunze yielded coupling constants between 3 and 100, corresponding to temperatures from 8,000 to 30,000 K and densities in the range of 0.3-3 g/cm^3. When the

conductivity is plotted versus Γ, the data converges to a line at values of Γ >10, suggesting that at these higher coupling constants, the conductivity is a function of Γ only.

The experiments were repeated with 99.9% copper and 99% aluminum with diameters of 125 μm by DeSilva and Katsouros[63] with the wires confined by a water bath instead of a glass capillary. This limited the ability to make measurements at high density and high temperatures due to the inability of water to inhibit the thermal expansion. However, lower densities were achieved, reaching approximately 0.01 g/cm^3 and showed the breakdown of the Γ dependence of the conductivity that had been observed previously. The copper and aluminum wires acted similarly with the plots of the conductivity versus density for aluminum being slightly shifted to lower densities due to aluminum's lower mass density. For both metals the conductivity fell with decreasing density at a rate of approximately ρ^3 until the conductivity reached a minimum near 0.1 g/cm^3 where the conductivity begins to rise with decreasing density. This had been observed previously with hydrogen plasmas by Reinholtz[64]. The minimum is thought to be at the transition point of the metal-nonmetal phase that has been shown to occur when $\left(\frac{R_a}{R_s}\right)^3 \approx \frac{1}{3}$, where $R_a=\frac{e^2}{I}$, I is the ionization potential and $R_s=\left(\frac{4\pi n_i}{3}\right)^{-3}$ is the Wigner-Seitz radius given by Likalter[65].

Ab initio molecular dynamic calculations were performed to determine the conductivity of aluminum in the warm dense matter regime. The Kubo-Greenwood expression was used to calculate the conductivity directly by taking into account electron-electron, electron-ion, and electron-neutral interactions. This approach has been successful in low density plasma when the Debye screening can be applied[66] but fails in high density plasmas where Debye screening can no longer be approximated[67]. It appears that at higher densities, the conductivity converges to a line. For a given temperature, the density at which the conductivity converges to this line changes; at higher temperature it converges at higher densities. To understand the departure of

the conductivity curve at a given temperature from this line, a brief discussion of degenerate and partial degenerate (partially ionized) plasmas must be discussed.

Calculations were performed[68] for the dense degenerate regime as well as the partially degenerate regime. The density was taken to be 2 g/cm^3 which is characteristic of expanded liquid aluminum. The results for the density as well as the conductivities at this density in the temperature range from 1,000 K to 15,000 K illustrated the metallic-like character of this regime. The plots followed the Drude model of free electron gas. For the partially degenerate regime, a density of 0.3 g/cm^3 was taken for temperature ranging from 7,600 K to 16,400 K. The density and temperature range is characteristic of the partially ionized plasma produced in the experiments. The plots of the density of states in the regime illustrates a departure from a free-electron-like curve. The plots of conductivity were no longer following a trend similar to a Drude metal as had been observed with the degenerate case. Instead, the electrical conductivities are similar to those observed in calculations of hydrogen[69] as well as metal-molten-salt solutions[70]. With this discussion in mind, Figure I.5 can now be understood more clearly. The departure from the conductivity line occurs for higher temperature as the density decreases. The point at which it departs, the metal is beginning to transform from a degenerate dense regime to a partially degenerate regime. This is consistent with partially ionized plasma. Conductivity measurements of copper along with quantum molecular dynamics calculations were done by Clerouin[71] with the warm dense matter copper ranging in densities of 0.5-0.3g/cm^3 and temperatures of $6{,}000\ \mathrm{K} < T < 30{,}000\ \mathrm{K}$. The results of the experiment and QMD simulations for temperatures of 10,000 and 30,000K are shown in Figure I.5. The red data points represent QMD simulations while the green are the experimental data. The triangles are for the 30,000K copper and the circles are the 10,000K copper.

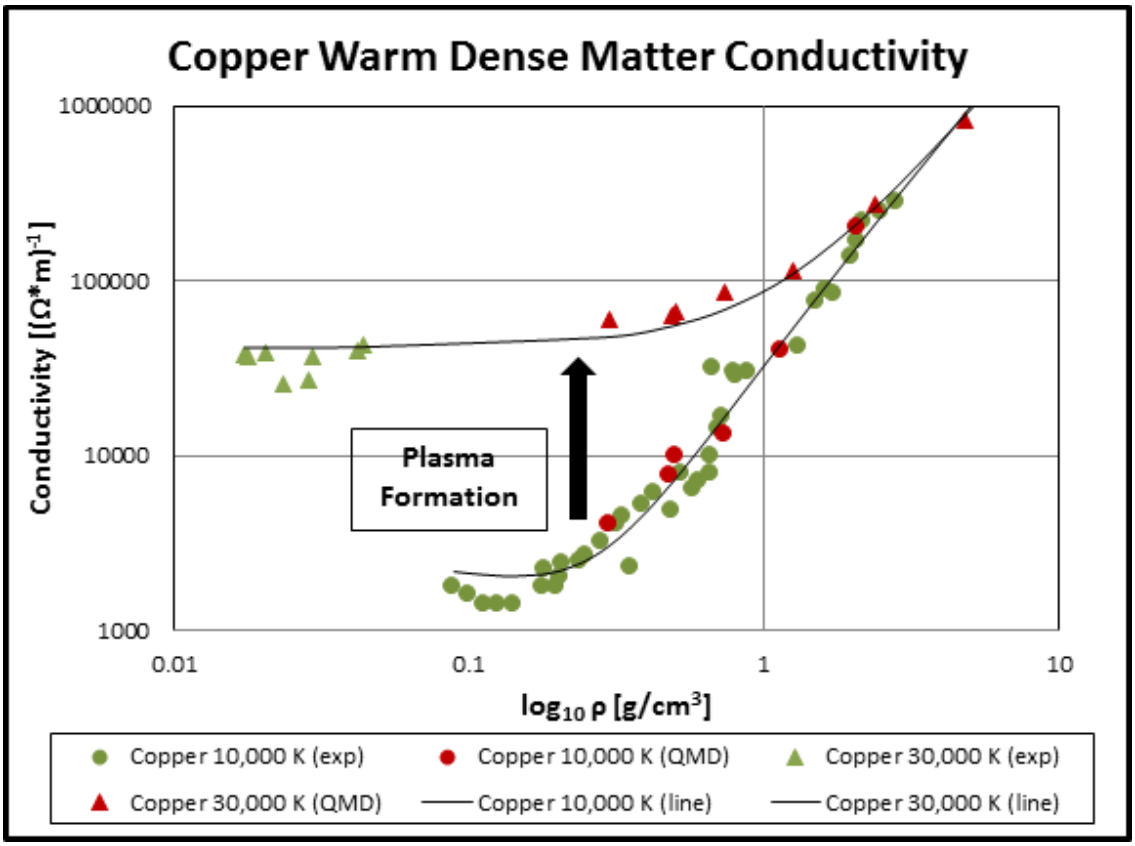

Figure I.5 Plot of experimental (green) and Quantum Molecular Dynamic (QMD) simulation (red) results for the conductivity of copper as a function of density. Plots are for temperatures of 10,000K and 30,000K.

The results for copper, aluminum, nickel and titanium are plotted in Figure I.6. A clear similarity is observed for the nickel and copper at both 10,000K and 30,000K temperatures. The aluminum shows a difference at 10,000K but has similar results to copper and nickel at 30,000K. Only a few data points exist for titanium, with the 28,000K data point converging on the other metals at 30,000K. This suggests that the metals may converge to a similar conductivity as the metals are ionized, whereas, in the vapor or bi-phase state, the metals may differ by an order of magnitude for the same densities and temperatures.

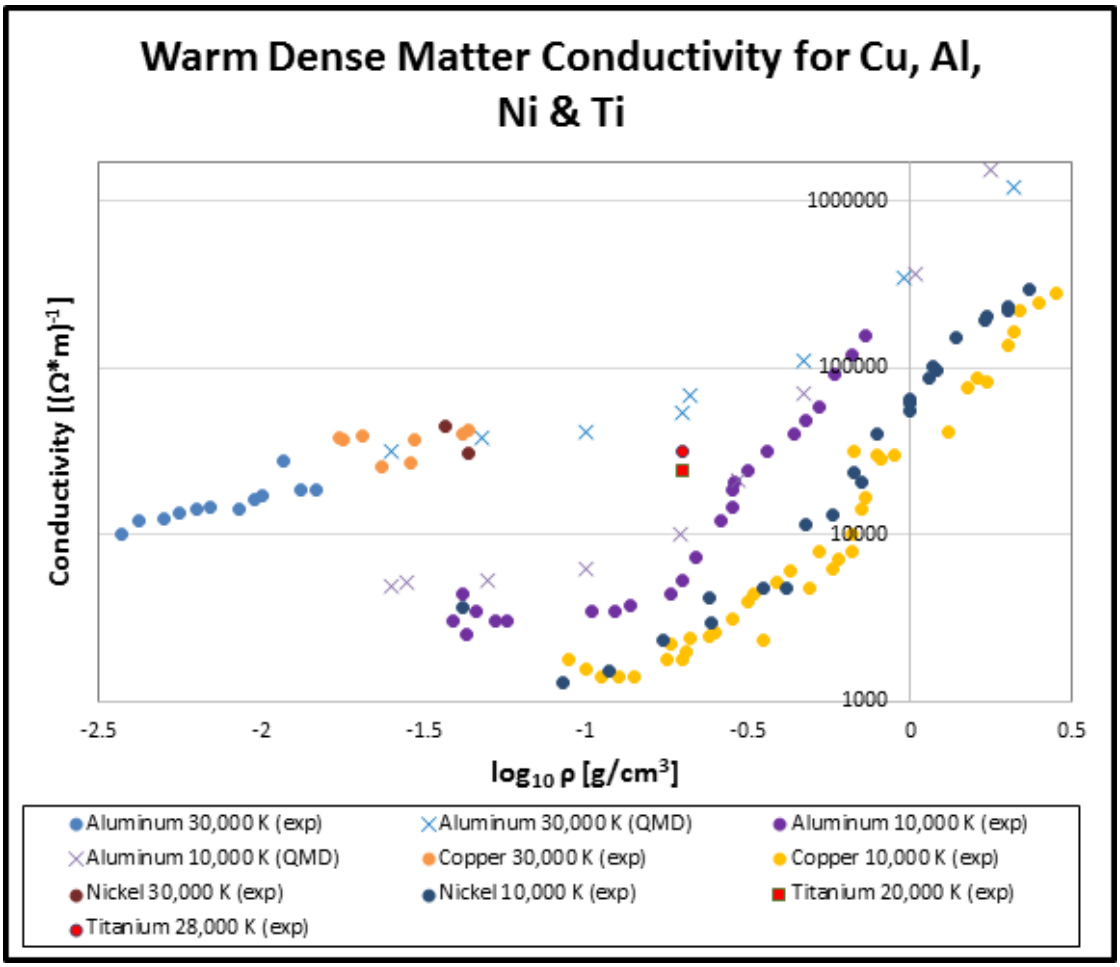

Figure I.6 Plot of experimental and Quantum Molecular Dynamic (QMD) simulation results for the conductivity of copper, aluminum, nickel and titanium as a function of density.

Understanding the conductivity of metals in the warm dense matter regime is important for benchmarking simulations to understand the evolution of the surface of the metal[72]. It is also important to understand the role of the conductivity of the metal in the solid and liquid states and how this affects the heating process. Figures I.7 and I.8 plot the conductivities of aluminum, copper, and nickel in the solid and liquid states respectively. A reliable source for titanium in this regime could not be found.

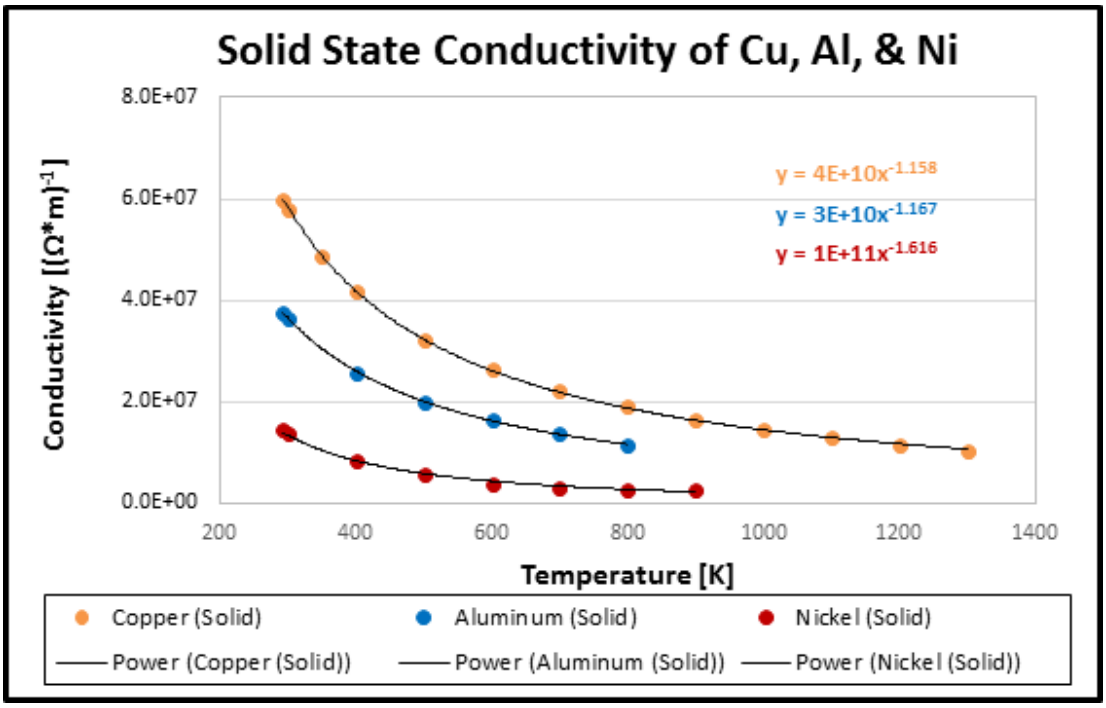

Figure I.7 The conductivity as a function of temperature for copper, aluminum and nickel in the solid state.

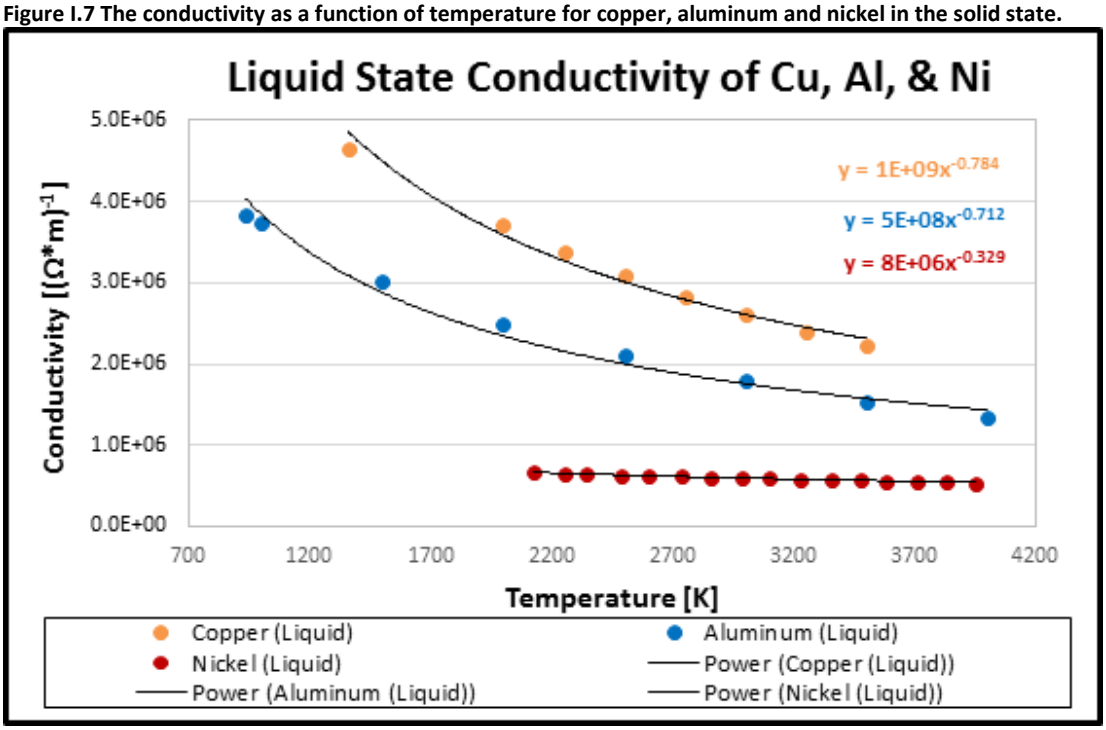

Figure I.8 The conductivity as a function of temperature for copper, aluminum and nickel in the liquid state.

Emissivity of Metals

Emissivity is a metric describing a material's ability to radiate away thermal energy. The emissivity is the efficiency of a material to emit thermal energy and is defined as the fraction of emitted radiation compared to that of a thermal black body. A material with an emissivity of 1 is a perfect thermal blackbody while a material with an emissivity of 0 is a perfect thermal reflector. A perfect blackbody in thermal equilibrium with its surroundings will absorb all incident light and emit thermal radiation according to the Planck distribution,

$$I(\nu, T) = \frac{2\pi h\nu^3}{c^2} \frac{1}{\exp\left(\frac{h\nu}{kT}\right) - 1} \quad \text{(I.68)}$$

Where $I(\nu, T)$ is the intensity of the radiating light, ν is the frequency of the radiating light, and *T* is the temperature of the blackbody. The ability for an object to absorb incident light can be described by the coefficient of absorption (absorptivity). The absorptivity is the fraction of incident photons absorbed by an absorbing and radiating object in thermal equilibrium. In contrast, the emissivity is the fraction of light emitted by an object to that of a blackbody at the same temperature. If the body is in thermal equilibrium with its surroundings, the absorptivity is equal to the emissivity. This statement is a corollary to Kirchhoff's law of thermal radiation.

An objects emissivity determines how it will radiate at a particular temperature and wavelength. However, the emissivity of an object may change based on several factors such as surface roughness, oxidation, temperature, and wavelength. Several studies have been conducted to understand these effects for aluminum, copper, nickel, and titanium. A difference in aluminum from solid to liquid was observed by Hanstrom [73]. Aluminum in the solid state, constant temperature of 300K, has an emissivity that ranges from 0.07 to 0.12 in the wavelength range of 400 to 1000nm with it peak at about 850nm. Liquid aluminum, constant temperature of 1550K, has an emissivity ranging from 0.11 to 0.07 in the wavelength range of 400 to 1000nm. The effect

of surface roughness was studied[74] by adding a surface roughness of 0.08μm to 0.2μm to the aluminum surface. The emissivity in the wavelength range of 300 to 800nm was measured to be 0.4 to 0.2 and 0.3 to 0.15 across the wavelengths for the 0.08μm and 0.2μm surface roughness respectively. The temperature was held at 323K, so the effect of melting a rough surface was not studied and compared to an initially smooth surface. An effect of alloy on the emissivity of aluminum as well as the surface roughness of aluminum alloys was observed in several studies[75,76,77,78], however, the wavelength range was in the 1 to several micron wavelength. This range is outside the range of our diagnostics, but gives credence to the concern that the same effects may exist in the visible and near IR as well. The study of aluminum alloys and the level of surface oxidation show an effect of oxidation in the wavelength range of 3 to 4μm. The alloys with no oxide had similar emissivities at ~0.1 in the temperature range 600 to 800K. The alloys with an oxide layer had a greater effect on the emissivity that ranged from 0.1 to 0.3.

The emissivity of copper in the visible range from solid to liquid was studied by Watanabe[79,80]. Figure I.9 is a plot of the emissivity of copper in the solid and liquid state. The emissivity of solid and liquid copper decrease with increasing wavelength, with the values diverging between 550 and 600nm wavelength. This phase dependence on the emissivity of a metal has been observed for several metals, including nickel, cobalt, gold and silver, just to name a few.

The emissivity of nickel across the solid/liquid boundary was first studied by Burgess[81] in 1915. At a wavelength of 550nm the emissivity in solid and liquid nickel was determined to be 0.44 and 0.46 respectively. More recently, the emissivity of liquid nickel was found to range from 0.34 to 0.38 in the wavelength range of 650 to 920nm[8283] while solid nickel ranged from 0.33 to

0.34. A reliable source for the emissivity for titanium across the solid/liquid boundary was not found, however, the effects of adding titanium to an aluminum alloy was studied by Krishnan[84].

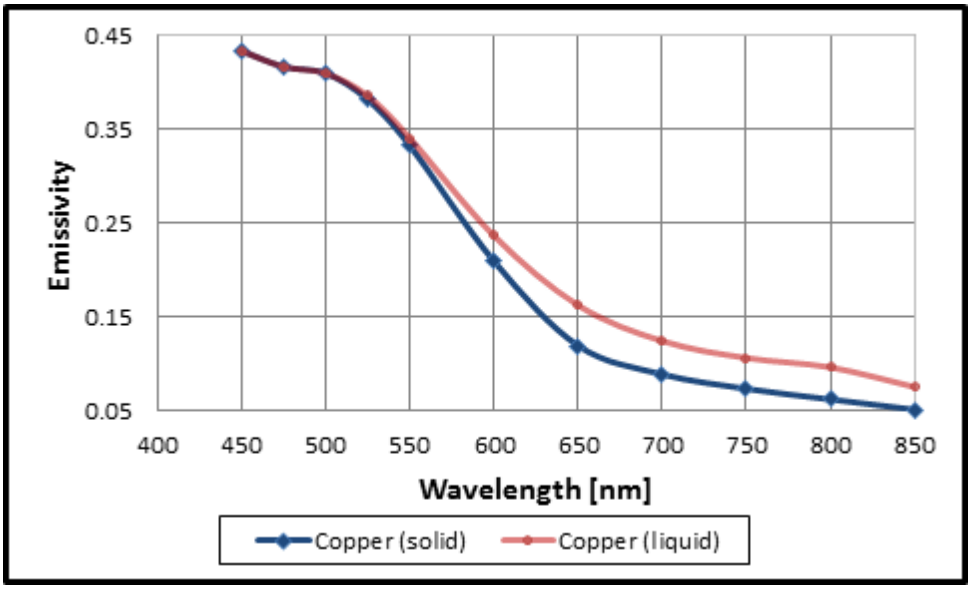

Figure I.9 The emissivity of copper in the solid and liquid state as a function of wavelength in the visible range.

Figure I.10 plots the results from the Krishnan study will the zero percent aluminum alloy (pure titanium) has an emissivity of 0.39. The emissivity stays approximately flat until the percentage swings to greater than 50% for aluminum where it steadily declines to ~0.1 at 100% aluminum.

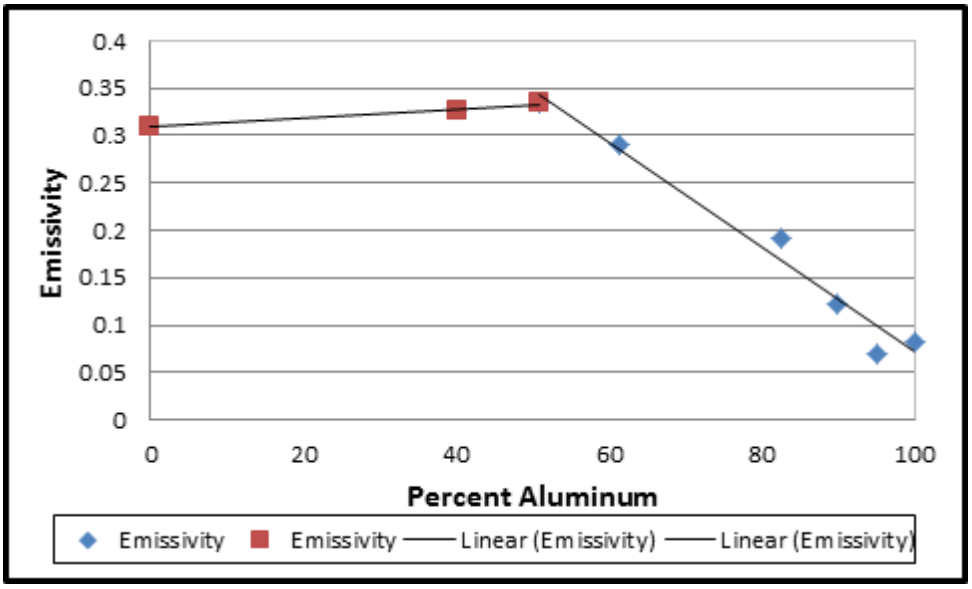

Figure I.10 The emissivity of titanium-aluminum alloy as a function of percent aluminum.

Electrothermal Instabilities (ETI)

When a metal conductor is driven by a large pulsed power current, the surface can be driven through multiple stages of heating and phase changes. As discussed earlier in this chapter, when a conductor is pulsed in a cylindrical configuration, a pinch effect will lead to the development of instabilities. The seeds of the late time surface instabilities may be caused by an electrothermal process. Electrothermal instabilities (ETI) are an effect that occur when the resistivity of a material depends on temperature and may play a crucial role in z-pinch experiments such as ours. There are two forms of ETI that will be discussed here. The first can be written mathematically as:

$$\frac{\partial \eta}{\partial T} < 0 \qquad \text{(I.69)}$$

This form illustrates the classic Spitzer resistivity of plasma and leads to filamentation and current channels along the axis of current flow. The second form of ETI can be written mathematically as

$$\frac{\partial \eta}{\partial T} > 0 \qquad \text{(I.70)}$$

This form is best recognized in condense matter and is classically referred to as the overheat instability[85]. The overheat instability leads to the formation of strata perpendicular to the flow of current.

This form is best recognized in condense matter and is classically referred to as the overheat instability.[86] The overheat instability leads to the formation of strata perpendicular to the flow of current.

Striations were first observed in gas puff experiments [87] and later in thin wire experiments. [88] The striations observed in thin wire experiments occur in the core of the conductor and have been modeled using 2D PIC simulations by Oreshkin et al. [89,90] It was

concluded that the striations are formed early in the conductor explosion when the material is in a liquid or bi-phase state. This process occurs when the liquid increases in temperature and decreases in density, leading to a decrease in metal conductivity. A current flowing along the z-axis of a conductor can be influenced by random density fluctuations that lead to random temperature fluctuations. The overheated region forces the current to flow in the surrounding material located along the same radial position. The increased current density causes the surrounding areas to overheat. The process continues and leads to a strata formation. The striations contain regions of higher temperature and lower density alternating with regions of lower temperature and higher density. These alternating layers of high and low temperatures are perpendicular to the direction of current flow. The formation of strata is not due to the evolution of sausage instabilities (*m=0*) as suggested by Abramova.[91] Oreshkin's simulations show a small magnetic field pressure (~0.5 kbar) compared to the thermal pressure. The thermal pressure is determined by the two-phase nature of the system and is given by the pressure at the critical point. The EOS used by Oreshkin has a critical point pressure of 4.5 kbar, approximately 10 times larger than the magnetic field pressure. Therefore, it was concluded that the striations were not caused by the electromagnetic forces but rather by the overheat instabilities.

The simulations were compared to experiments conducted by Sinars et al[92] and showed similar results. It must be noted that in the thin wire experiments the wire explosion were due to electrical breakdown in the metal vapors. These effects cannot be simulated using MHD, however, it is reasonable to compare the thin wires with MHD because the striation effect originates from the matter inside the core.

To understand the results of Oreshkin's simulations, the mathematical details must be visited. The processes simulated by Oreshkin utilized the MHD approximation:

$$\frac{\partial \rho}{\partial t} + \nabla \cdot (\rho \vec{u}) = 0 \tag{I.71}$$

$$\rho \frac{\partial \vec{u}}{\partial t} + \rho(\vec{u} \cdot \nabla)\vec{u} = -\nabla p + \frac{1}{c}\vec{j} \times \vec{H} \tag{I.72}$$

$$\rho \frac{\partial \varepsilon}{\partial t} + \rho(\vec{u} \cdot \nabla)\varepsilon = -p\nabla \cdot \vec{u} + j^2\eta + \nabla \cdot (\kappa \nabla T) \tag{I.73}$$

Disregarding motion allows equation I.73 to be rewritten as

$$\rho c_v \frac{\partial T}{\partial t} = j^2\eta + \nabla \cdot (\kappa \nabla T) \tag{I.74}$$

We shall now introduce a temperature perturbation and solve for T, seeking a solution in the form

$$T_1(t, z) = C * exp(\int \gamma dt + ik_z z) \tag{I.75}$$

Where T_1 is the temperature perturbation, *C* is a constant, $k_z = 2\pi/\lambda$ is the azimuth wavevector, λ is the wavelength, and γ is the instantaneous instability buildup increment. This can be solved to give the dispersion equation

$$\gamma = \frac{j^2 \frac{\partial \eta}{\partial T} - k_z^2 \kappa}{\rho c_v} \tag{I.76}$$

For all negative values of γ the temperature perturbations are stable. For positive values, the perturbations are unstable and will grow. The first term on the right in the numerator of equation I.76 is positive for most metals in the solid and liquid states, therefore, unstable modes will occur for wavelengths greater than a minimum wavelength defined as

$$\lambda_{min} = \frac{2\pi}{j}\sqrt{\kappa \left(\frac{\partial \eta}{\partial T}\right)^{-1}} \tag{I.77}$$

For all wavelengths greater than the minimum wavelength, the instability amplitude will grow exponentially. All wavelengths smaller than the minimum wavelength will be suppressed due to thermal conductivity.

When motion is allowed, the diffusion equation for *γ* leads to three roots, two complex, one real for the range of parameters of interest to thermal instabilities. The complex roots represent damped oscillations while the real root represents either a buildup or suppression, depending on the sign of the root, of the instability growth. The MHD calculations showed that the fastest growing mode of thermal instability had a wavelength of 1-20μm.

The role of thermal instabilities in a thick copper and aluminum wires was studied by Peterson[93] using a series of 1D RMHD simulations using HYDRA[94] and 2D RMHD simulations using LASNEX[95]. Cu-101 and Al-5052 rods were pulsed at Sandia's 20-MA Z facility for comparison in this study. Images of instability growth were observed using 2-frame x-ray radiography with 6.151 keV and 1.865 keV monochromatic backlighting. The development and evolution of surface instabilities on aluminum matched well with the 2D MHD simulations. However, the copper rods showed much less agreement with simulations. The discrepancy could be due to the need for refinement of conductivity, equation of state, and opacity models utilized in the modeling.

One of the possible reasons for the experiment not matching well with the simulations is the application of a positive feedback for instability growth seeded by density and temperature variations in the conductor. Unlike the thin wire experiments and simulations presented by Oreshkin et al, where the current density is uniform across the radial cross section of the wire, the thick wires utilized by Peterson in both simulation and experiment are in a skinning mode. The current is non-uniform, allowing for the diffusion of the current "away" from perturbations in density and temperature, causing a negative feedback. The effects of electrothermal instabilities in the skinning mode were studied by Oreshkin and Chaikovsky.[96] Oreshkin's simulations showed that the propagation of a non-linear diffusion wave into a metal liner did not form long wavelength mode surface instabilities as was observed in the thin wire simulations and

experiments. The diffusion wave propagates inward, reaching the inner surface of the liner, where it is reflected back on itself. This localized increase in current density on the inner surface of the liner leads to the formation of thermal instabilities. In a thick wire experiments, such as the one conducted by Peterson and the one presented here, the nonlinear diffusion wave propagates to the center of the rod, where it will be reflected upon itself and form thermal instabilities at the center of the rod. The effects, if any, of electrothermal instabilities when a wire in the "liner" regime is pulsed by a mega-ampere current is not understood. One goal of the research presented here was to determine if electrothermal instabilities have a role in the evolution of the metal surface from solid to plasma states.

Section I.E: Radiation Transport

Radiation transport is of great importance in the fields of warm dense matter and high energy density physics. The radiation transport is described by the emission and absorption of photons in a medium. Solving the equation for radiation transport can be difficult due to the complexity of the processes involved. The reciprocal of the absorption coefficient is referred to as the mean free path of a photon and determines the medium optical thickness. When a plasma is optically thick (a short mean free path) at all photon frequencies, the equation for transport can be written as a diffusion equation. This is due to the small spatial steps between the emission and absorption of a photon leading to a diffusion process. Care must be taken in determining when to apply a diffusion equation to radiation transport. Plasma that consists of low and medium atomic numbered elements tend to be dominated by emission lines that are well separated. Many of these emission lines are optically thick and can therefore be described by diffusion. One must be careful however because only the core of these lines is thick, with the

wings of the profile having a lower optical thickness and not well described by diffusion. If the lines overlap or if the continuum is optically thick, then diffusion becomes a good approximation. The state of LTE occurs when the rates of collisions exceed the rate associated with radiation processes. In this case a Maxwellian distribution can be applied to represent the plasma and the ionization population can be reasonably understood by the Saha and Boltzmann equation. The radiation source function in LTE is given by the blackbody equation

$$I(\nu, T) = \frac{2\pi h\nu^3}{c^2} \frac{1}{\exp\left(\frac{h\nu}{kT}\right)-1} \tag{I.78}$$

There is a minimum density required for a plasma of a particular charge state to be in LTE. As the charge state increases, the density necessary for LTE increases. This is due to the increase in the radiation transition rates.

At lower density, aluminum plasma will radiate emission line spectra. As the density increases the lines approach the Planck limit. Absorption coefficients are determined by three types of transitions: bound-bound, bound-free and free-free. The bound-bound transitions are the most dominant in determining the optical properties of a plasma with the oscillator strength approximately scaling as the inverse of the transition energy. The cores of lines have large absorption cross section. This means that any radiation from these lines that escape the plasma must originate near the surface of the plasma. If the plasma located at the outer edge is cooler than the interior, then the continuum originates from deeper inside the plasma and exceeds the line radiation. When this occurs absorption lines are observed. In the MG experiments presented here, the spectra will be compared to computer code PrismSPECT. In using this code, care must be taken to ensure the code is being run in a regime that represents (or an approximation that is suitable) the plasma parameters of the experiment properly.

Section I.F: Benchmarking MHD Conditions

The equations of MHD can and have been utilized in running simulations of the MG experiments. As discussed earlier in this chapter, MHD is the specific case where charge neutrality is approximated. Charge neutrality is assumed when the electric force and the charge separation are small enough to be omitted from the MHD equations. This is achieved with a high density (1/10 solid density) plasma as is the case for the thick rod Zebra experiments. The density provides collisionality that leads to a resistive MHD regime. The vacuum-plasma interface cannot be modeled well with MHD due to the lower density interface; a problem that has not yet been solved appropriately with hybrid or kinetic modeling. The 1D MHD simulations of copper and aluminum run by Garanin took into account hydrodynamic motion, magnetic diffusion, electronic heat conduction, and radiative heat transfer in the "back and forth" approximation. The equation of state, conductivity, electron heat conductivity, and radiation transport for copper and aluminum were utilized with the formulary described elsewhere[97,98]. Simulations were also run by Lindemuth[99] using a 1D MHD code to simulate the aluminum 6061 rods pulsed on Zebra, with comparisons made between different formulary. Tables in SESAME format of EOSs 3719 and 3799, along with Planckian and Rosseland opacities 13716 from Los Alamos National Laboratory, were used in the simulations. Resistivities and thermal conductivities were implemented using SESAME formatted versions of both Lee-More-DesJarlais 29371 and 29373 as well as models developed at the All-Russian Scientific Research Institute of Experimental Physics (VNIIIEF). The variations in SESAME tables varied the time of plasma formation and the peak plasma temperatures for three different initial diameters of aluminum rods. The design of the MG experiments is to benchmark these simulations by studying different metals and alloys to

determine the effect on the time of plasma formation, time of surface explosion, expansion rate, and blackbody-estimated surface temperatures. These experiments will provide a unique and valuable data set that can be implemented in modifying electrical conductivity, thermal conductivity, opacities, and equation of state.

Chapter II: Nevada's Zebra Facility

The Megagauss experiments conducted at UNR's Nevada Terawatt facility uses the Zebra z-pinch 1 MA current pulse to produce multi-megaguass magnetic fields on the surface of thick metal rods. The machine is used in the short-pulse mode with the currrent rising lineraly from 100 kA to 900 kA in 70 ns at a rate of 1.1×10^{13}A/s. Zebra has a high-impedance of 1.9 Ω, allowing for small variation in the initial rod diameter without having any effect on the current profile. Due to this impedance mismatch, load variation is possible so that a study of dB/dt on the surface of a metal rod can be performed.

Section II.A: Zebra Machine

Zebra's 1 MA current pulse is delivered by a Marx generator composed of (32) 1.3 µF capacitors with a total capacitance of 41.6 µF. The capacitors are rated for a maximum voltage of 100 kV but are charged to only 85 kV to extend their lifetime. The energy stored in the Zebra capacitor bank is ($E=CV^2/2$) 150 kJ. The 32 capacitors discharge to deliver a 2.7 MV pulse through

a self-breaking gas switch to a 28 nF, 3.5 MV coaxial capacitor. The capacitor discharges through an SF_6-insulated Rimfire switch and delivers its energy to a 50 ns, 1.9 Ω, vertical transmission line. An eight channel self-breaking water switch is used in the open configuration to deliver the short pulse to the load. If the water switch is closed, the machine is operating in the long-pulse mode and has a current pulse that is 200 ns. Only the short-pulse mode was used in the experiments discussed here. The high impedance of Zebra allows for a large radius metal rod to act as a short circuit, making the current waveform insensitive to initial rod diameter. The high voltage applied to the cathode has a negative potential with respect to the grounded anode plate.

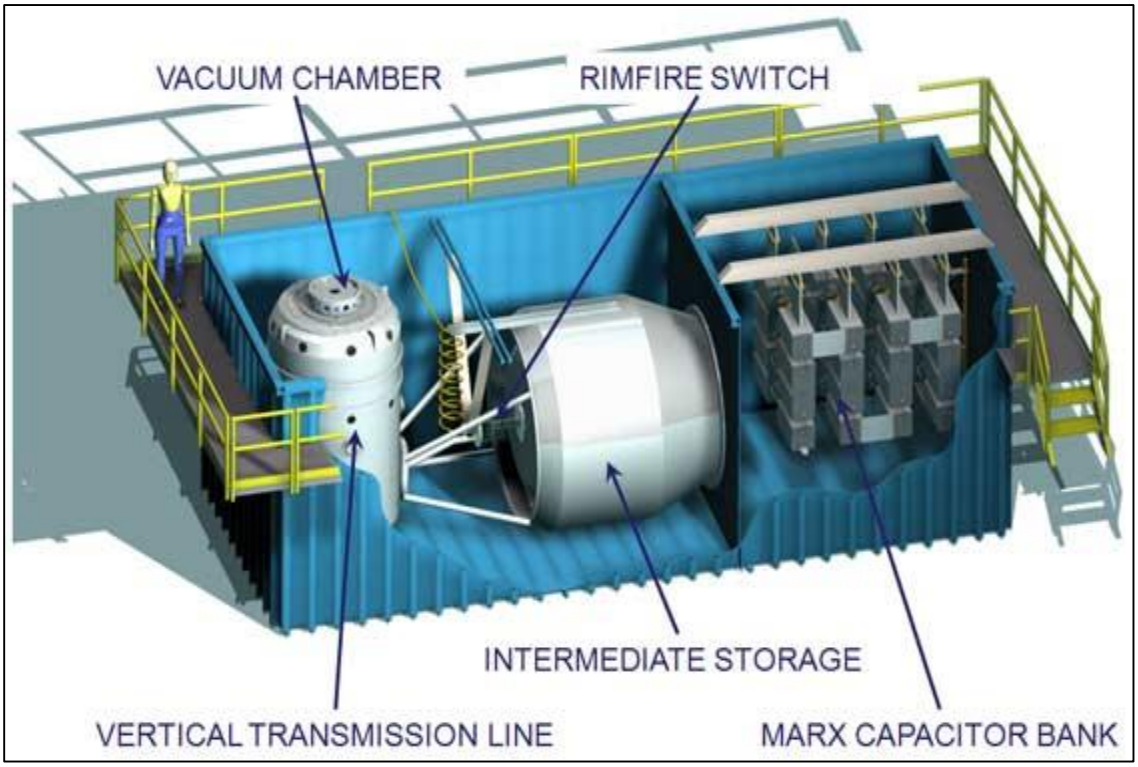

Figure II.1 Drawing of the Zebra facility with person in the top left corner for scaling. (Figure courtesy of the A. Astanovitskiy, UNR)

The conducting load is placed along the vacuum chamber axial center with the wall of the vacuum chamber acting as the return conductor. The walls of the chamber consist of 16 diagnostic ports equally spaced by 22.5° intervals. The viewing ports consist of 8 ports of 2” diameter, 7 ports of

3” diameter, and one port that is 4” for coupling the Leopard laser to the z-pinch. The ports are named for their geometrical positoning.

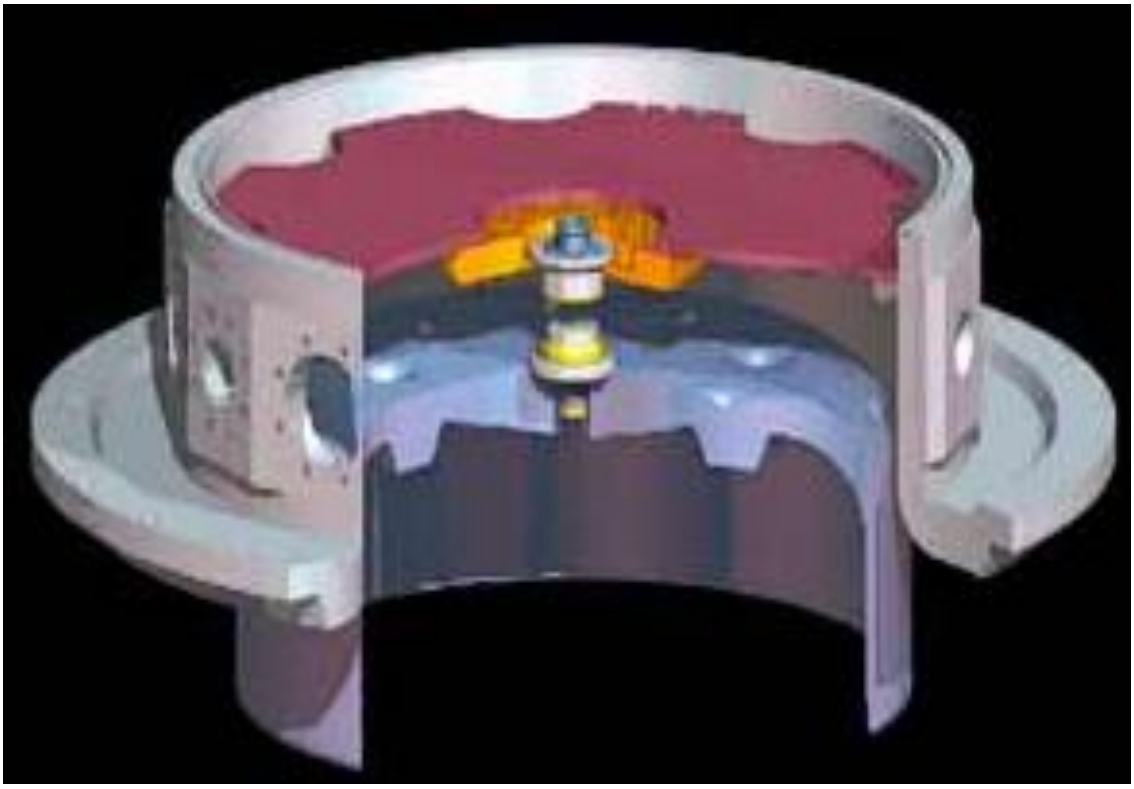

Figure II.2 The chamber configuration with the low high mesa and high anode plate. This configuration uses the wall of the chamber as the return current path. (Image courtesy of A Astanovitskiy and V. Nalajala, UNR)

Figure II.2 is a schematic of the chamber configuration with the high mesa and the high anode plate as used in the MG VI, MG VII, MG VIII and MG IX experiments. Figure II.3 is a schematic showing the different ports that were used in MG V, MG VI, MG VII, MG VIII and MG IX along with the diagnostics that were attached to each. Most ports use BK-7 windows with small glass debris slides inserted to protect the windows from load debris during a shot. The ports that were used for the UV laser shadowgraphs and interferometery used quartz windows as well as quartz slides. The electrical and optical signals collected through the view ports are relayed to digitizers located in mulitple screen enclosures throughout the lab. Around the Zebra vacuum chamber is an

assembly of steel rails called the “space frame” that is used as mechanical support for optics and other diagnostics. The space frame is connected to the concrete floor of the building and is used to decouple the optical elements from the vacuum chamber. The decoupling of the optics from the vacuum structure ensures that the vibrations from a shot does not effect the optical alignment. However, from shot to shot, the mesa will move enough for the load to drift out of the view of the optical line making shot to shot alignment of the optics to the target chamber center necessary. There is also a slight drift that occurs as the chamber goes under vacuum which can have enough of an effect that the cameras used for imaging must be realigned. This effect is not dramatic and takes a short time to account for.

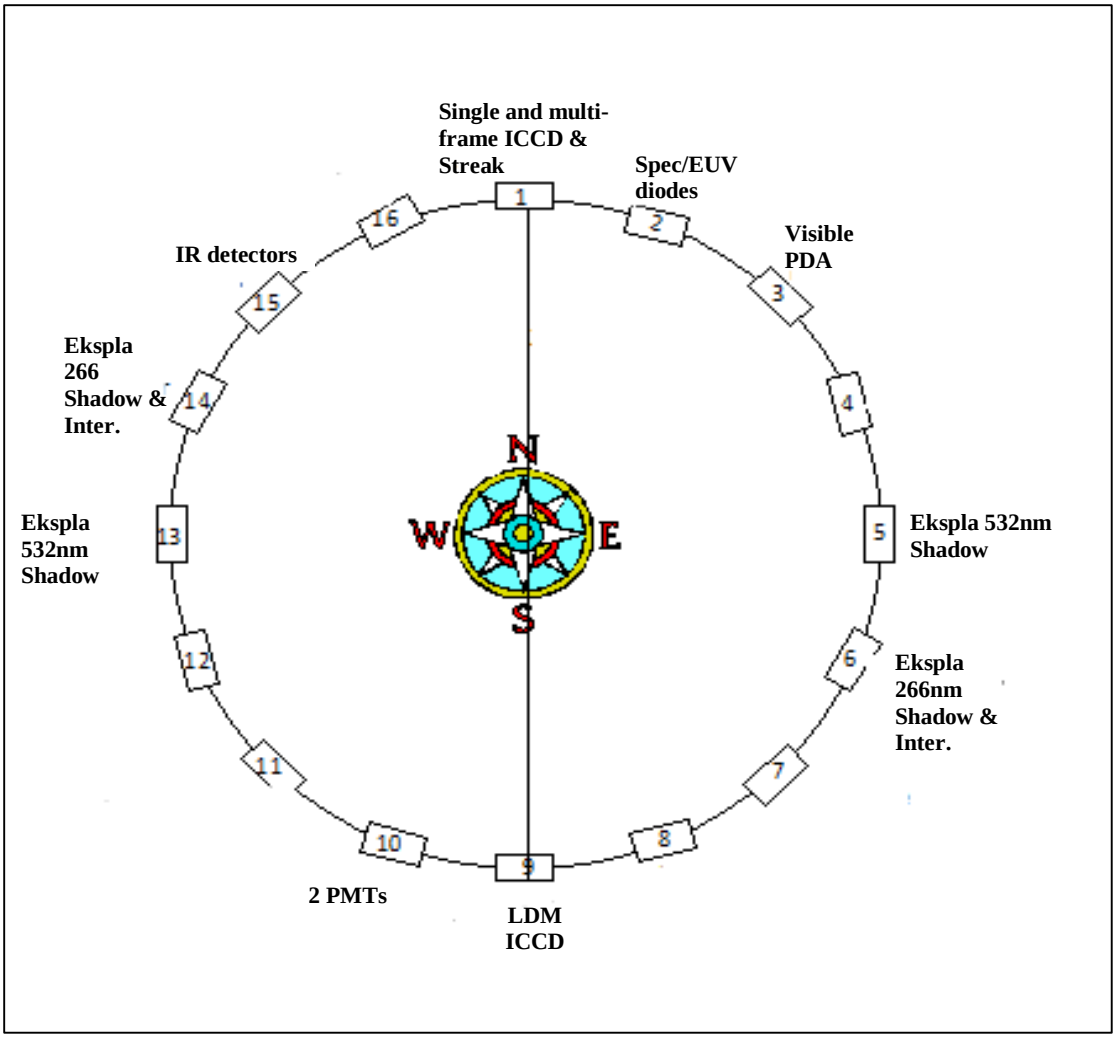

Figure II.3 Illustration of chamber ports with corresponding diagnostics for MG VI-IX.(Figure of ports courtesy of A Astanovitskiy, UNR)

Prior to a shot, the chamber must be evacuated to a pressure of 10^{-5} Torr to reduce the risk of the insulator stack flashing over. The chamber is pumped out using two mechanical pumps, one turbo pump, and one cryo pump.

Section II.B: Zebra Current

The current profile of Zebra is determined by the use of differerntial B-dots. Three B-dots are placed in the anode plate spaced at 120° intervals at a distance of 6.5 inches from the chamber axis as shown in Figure II.4. The one exception to this was the anode plate used in MG V which had the B-dots at a distance of 5.5 inches from the chamber axis. Each probe consists of two flux loops coiled in opposite directions and marked so that the probes are placed in the same orientation every time to match the orientation in which they were calibrated. The B-dots are calibrated using a pulser in which the loops are placed at 3.3 inches from the current pulse. This ratio of chamber distance, 6.5 inches, to calibration distance, 3.3 inches, must be taken into consideration when determining the current of the zebra pulse. The flux loops were coiled in opposite directions to change the polarity of each signal. If noise is added to the system, it causes a d.c. offset that shifts both signals in the same direction. The signals from B-dot 2, shot 2863 are shown in Figures II.5 and II.6. To determine the offset, an average is taken from -400 ns to -200 ns and then subtracted from the entire signal. Figure II.5 shows both polarties, P (postive) and N (negative), and the result of subtracting the offset and averaging the two signals. The voltage signals are then summed to determine the current profile. If the offset were not removed, the current profile would be superimposed on top of a line with a slope equal to the offset.

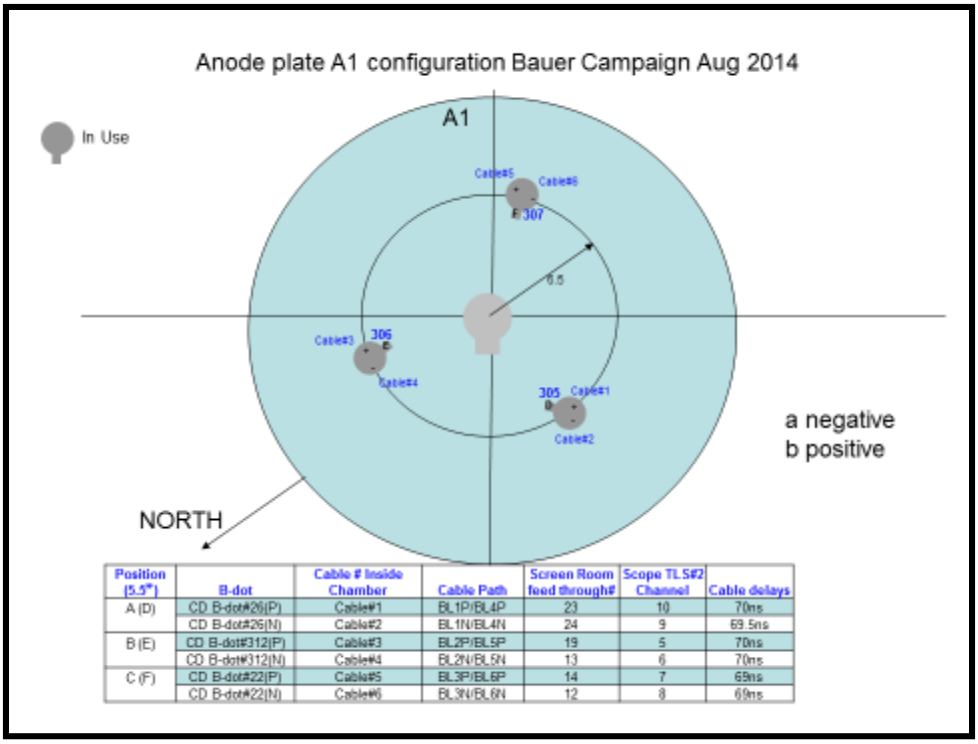

Position (5.5")	B-dot	Cable # Inside Chamber	Cable Path	Screen Room feed through#	Scope TLS#2 Channel	Cable delays
A (D)	CD B-dot#26(P)	Cable#1	BL1P/BL4P	23	10	70ns
	CD B-dot#26(N)	Cable#2	BL1N/BL4N	24	9	69.5ns
B (E)	CD B-dot#312(P)	Cable#3	BL2P/BL5P	19	5	70ns
	CD B-dot#312(N)	Cable#4	BL2N/BL5N	13	6	70ns
C (F)	CD B-dot#22(P)	Cable#5	BL3P/BL6P	14	7	69ns
	CD B-dot#22(N)	Cable#6	BL3N/BL6N	12	8	69ns

Figure II.4 Anode plate configuration showing placement of bdot probes. (Drawing courtesy of V. Nalajala)

Figure II.6 shows all three B-dot probes overlayed with only small deviations among the signals that will add an insignificant error to the current profile. The current profile from summing the voltage signals is time shifted so that the current of 500 kA occurs at 100 ns ($I(100ns)=500$ kA).

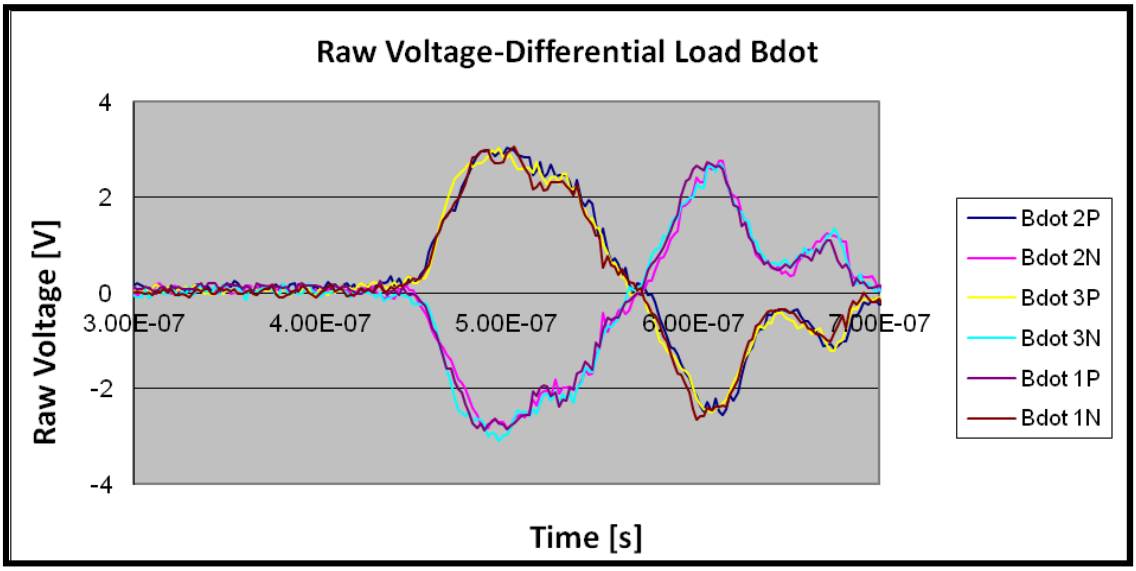

Figure II.5 Raw signals from all three bdots showing the polarity of each flux loop.

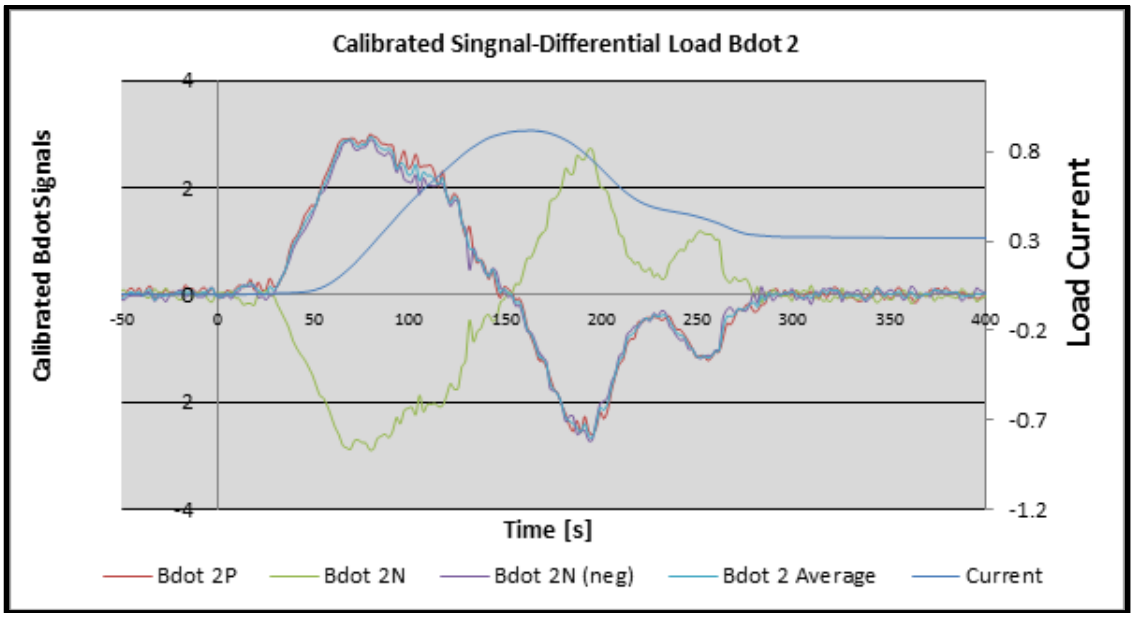

Figure II.6 Raw signals (red and green) were averaged and integrated to get a current profile (blue).

The current profiles for MG VI and MG IX are plotted in Figures II.7 through II.10 for all the shots, except for a few unsuccessful ones.

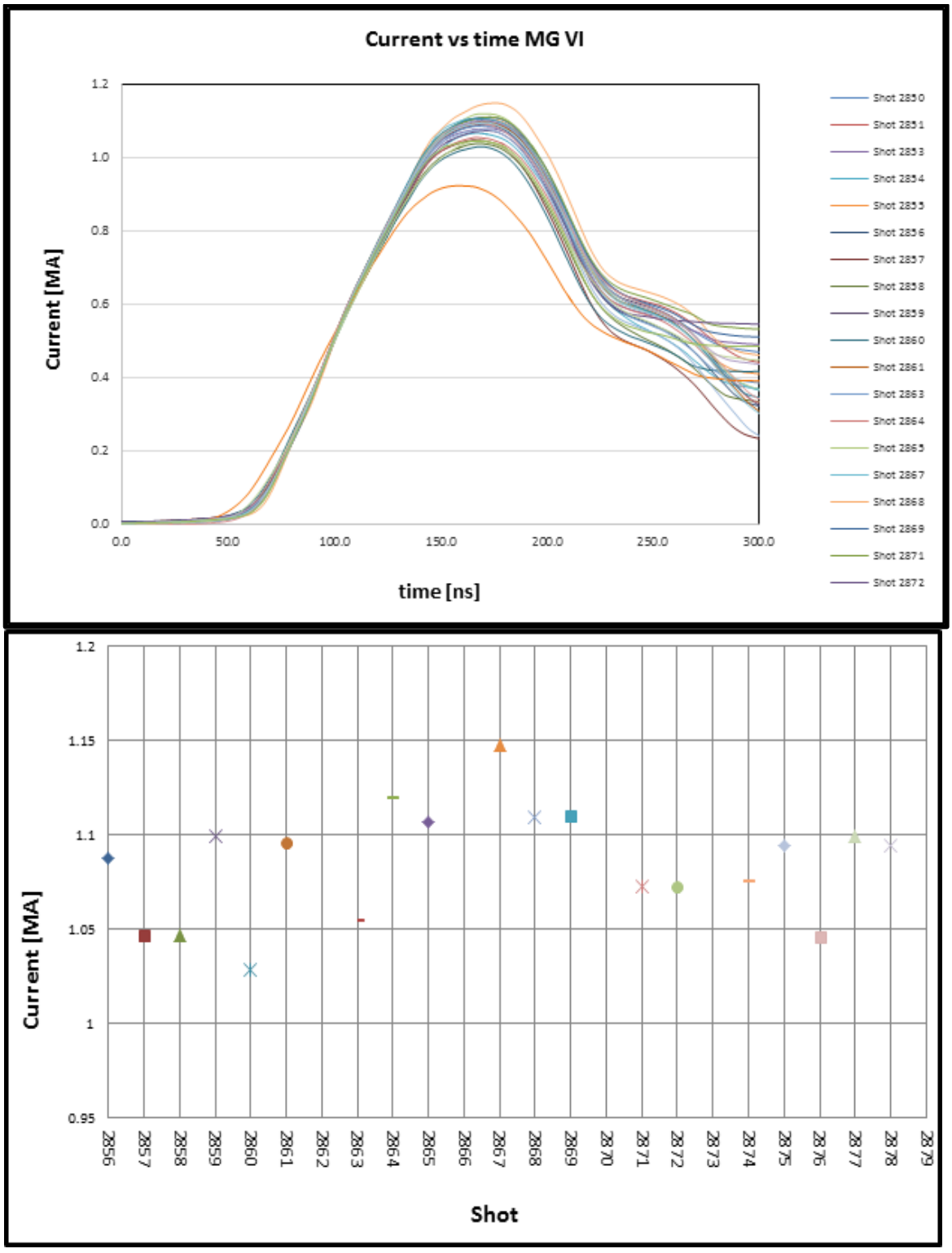

Figure II.7 Current profiles of the MG VI shots with the peak current for each shot displayed to show small variations from shot to shot.

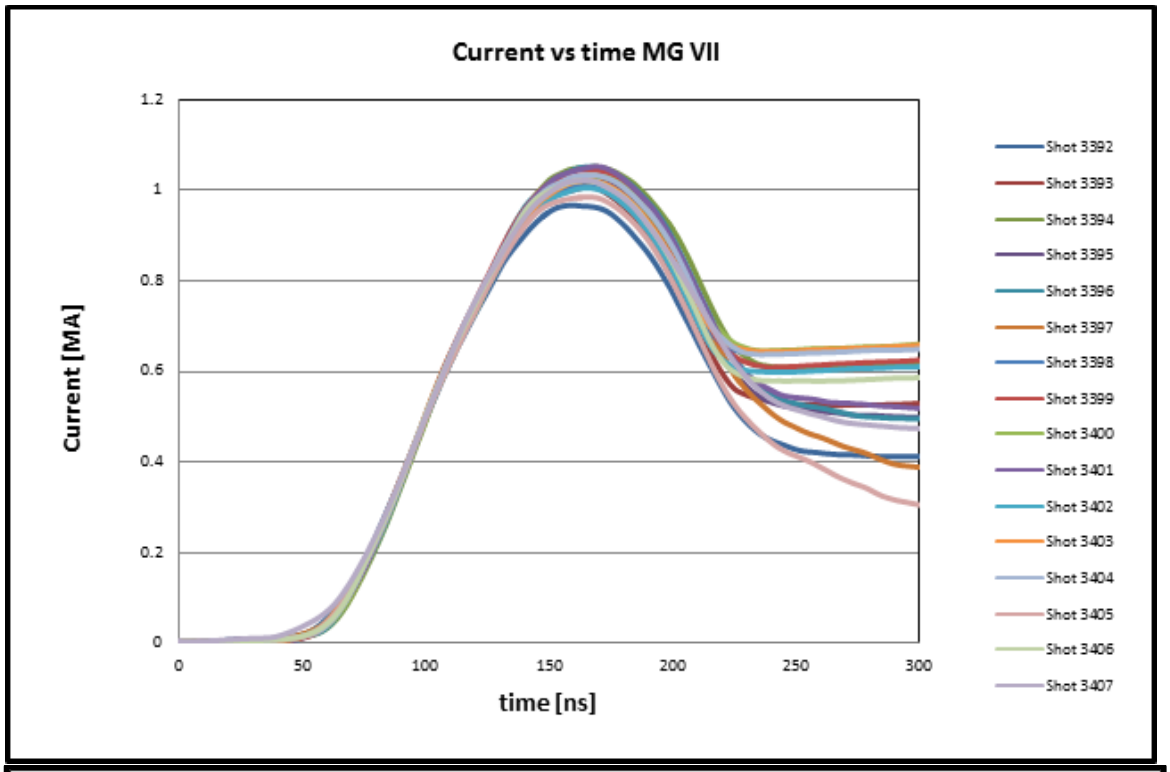

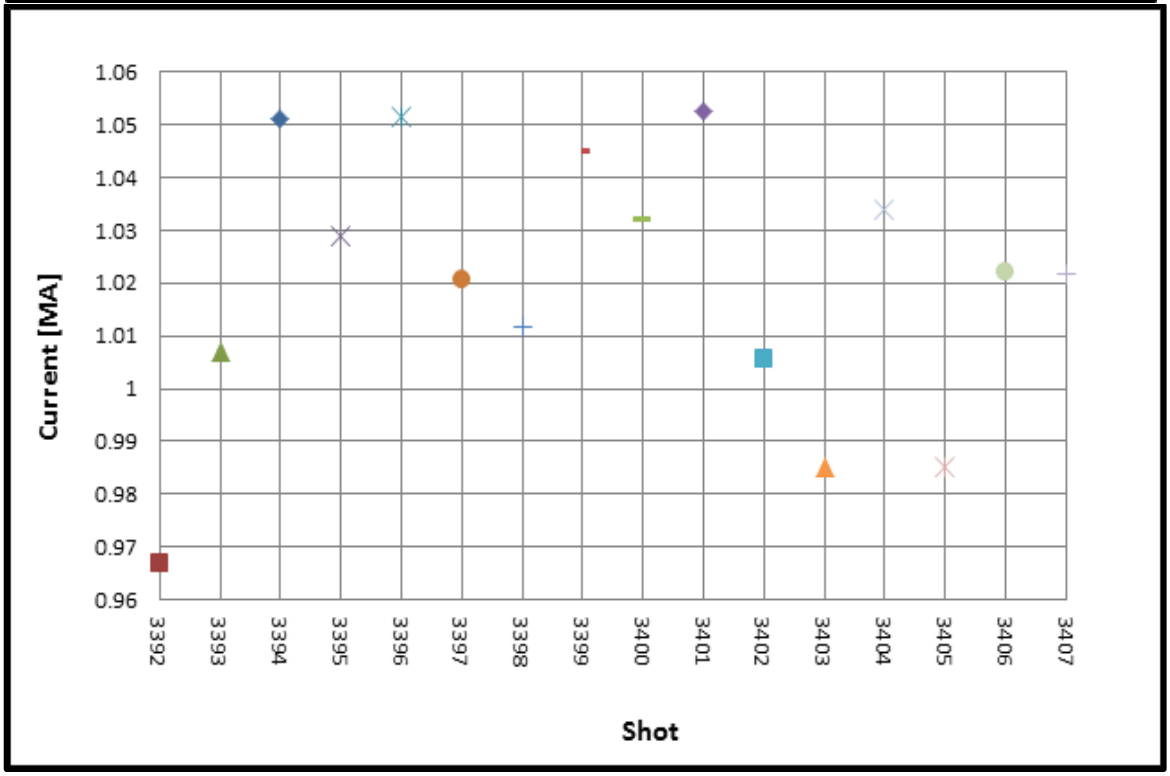

Figure II.8 Current profiles of the MG VII shots with the peak current for each shot displayed to show small variations from shot to shot.

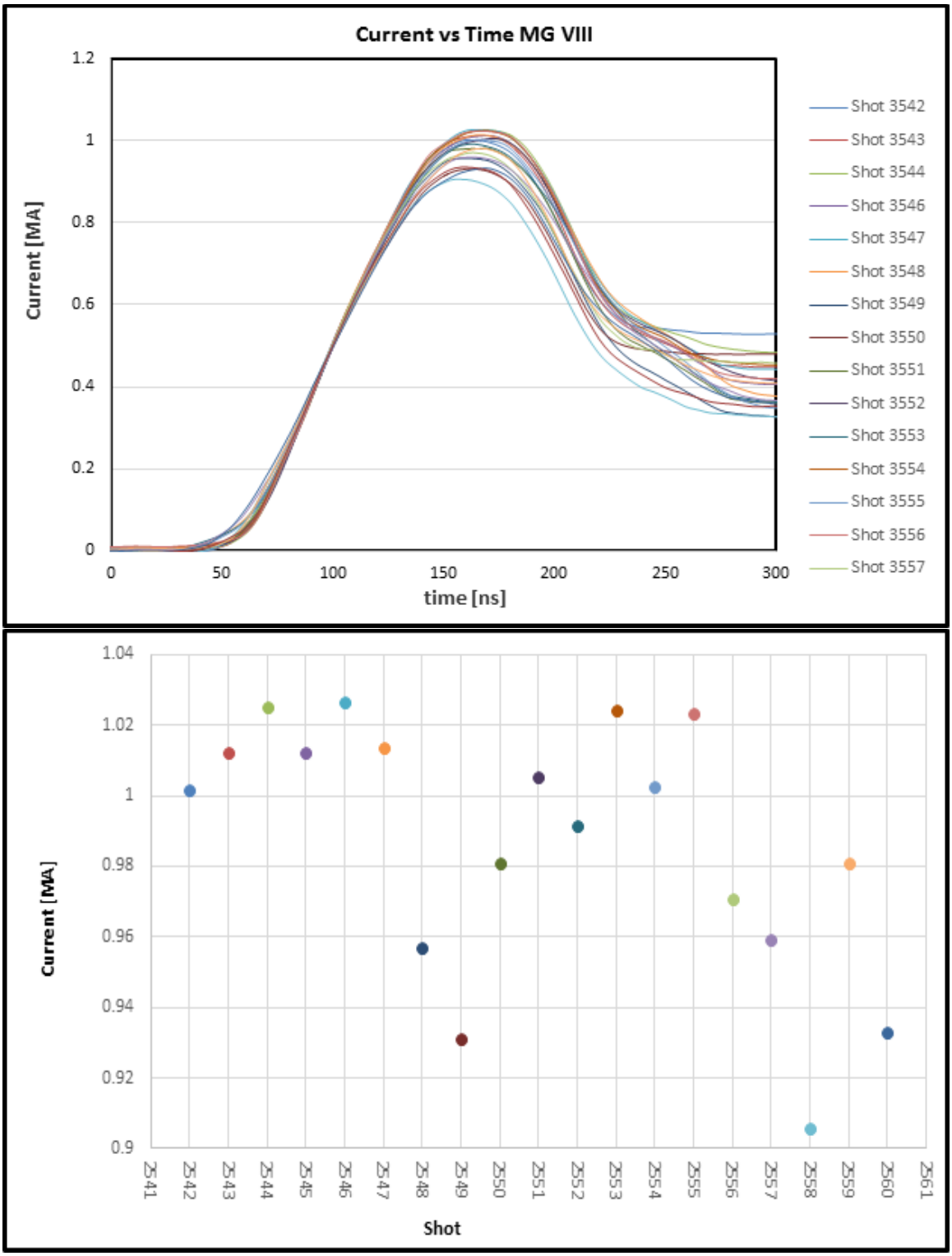

Figure II.9 Current profiles of the MG VIII shots with the peak current for each shot displayed to show small variations from shot to shot.

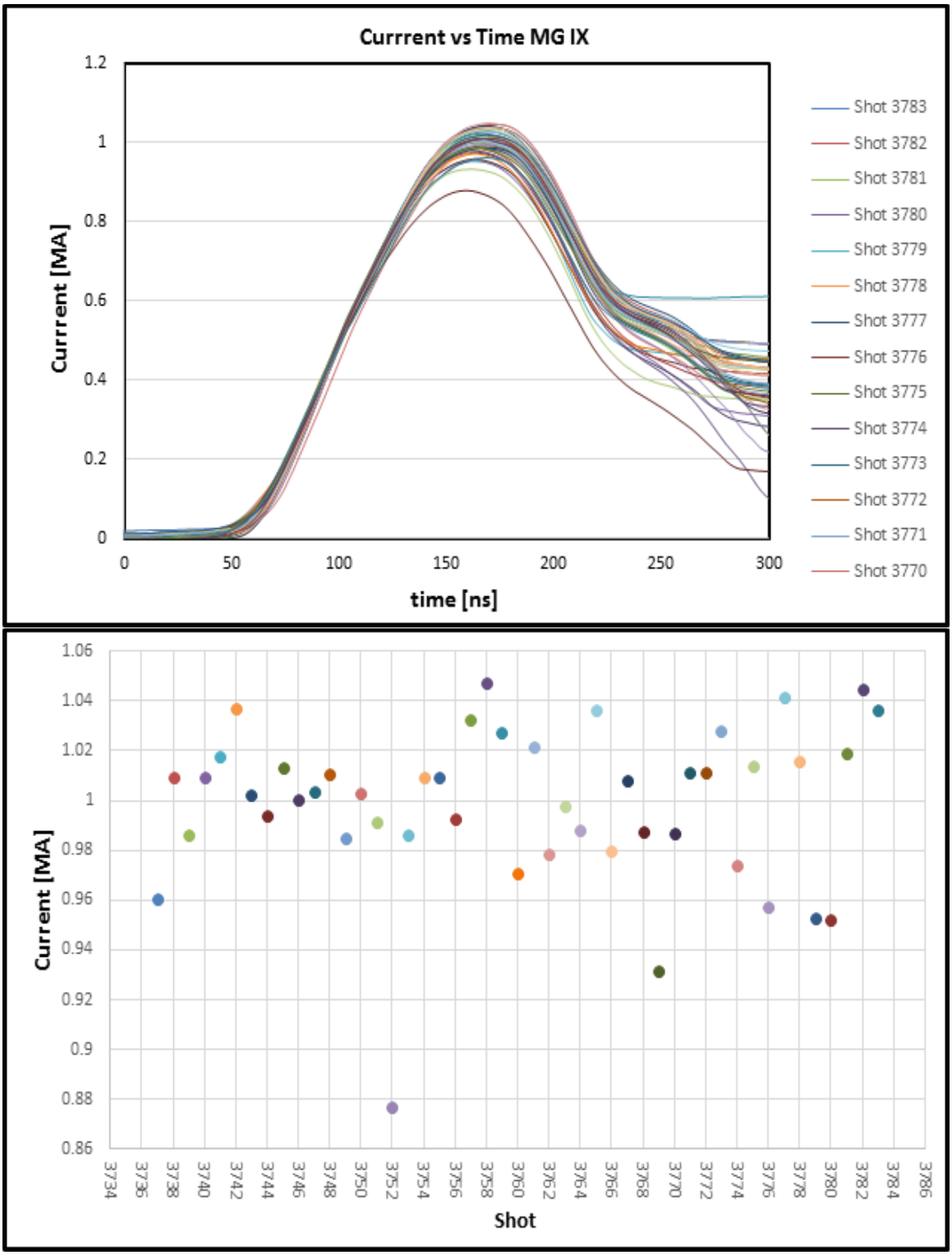

Figure II.10 Current profiles of the MG IX shots with the peak current for each shot displayed to show small variation from shot to shot.

Section II.C: Triggering of the Diagnostics

To determine the results of the MG experiments accurately, the timing of the diagnostics with respect to the current pulse must be well characterized. The time base was arbitrarily defined as *I*(t)=100 ns=500 kA for the Zebra current pulse. All of the diagnostic's triggering was done using a pulse generated from a Low Water Vdot (LWVD) probe that is located in the Zebra water tank. The delay between the triggering of the LWVD and the current pulse at the load reaching 500 kA is 300 ns with a standard deviation of 4.5 ns. The LWVD pulse is relayed with cables to the diagnostic screen boxes where they are then relayed to digital scopes, delay generators and diagnostic triggering. The imaging optics use a DG535 pulse generator to vary the timing of the diagnostic trigger. The cable delays that relay the trigger pulse to each diagnostic must be known. A schematic illustrating the delay cables that go from the LWVD to the various screen boxes is shown in Figure II.11.

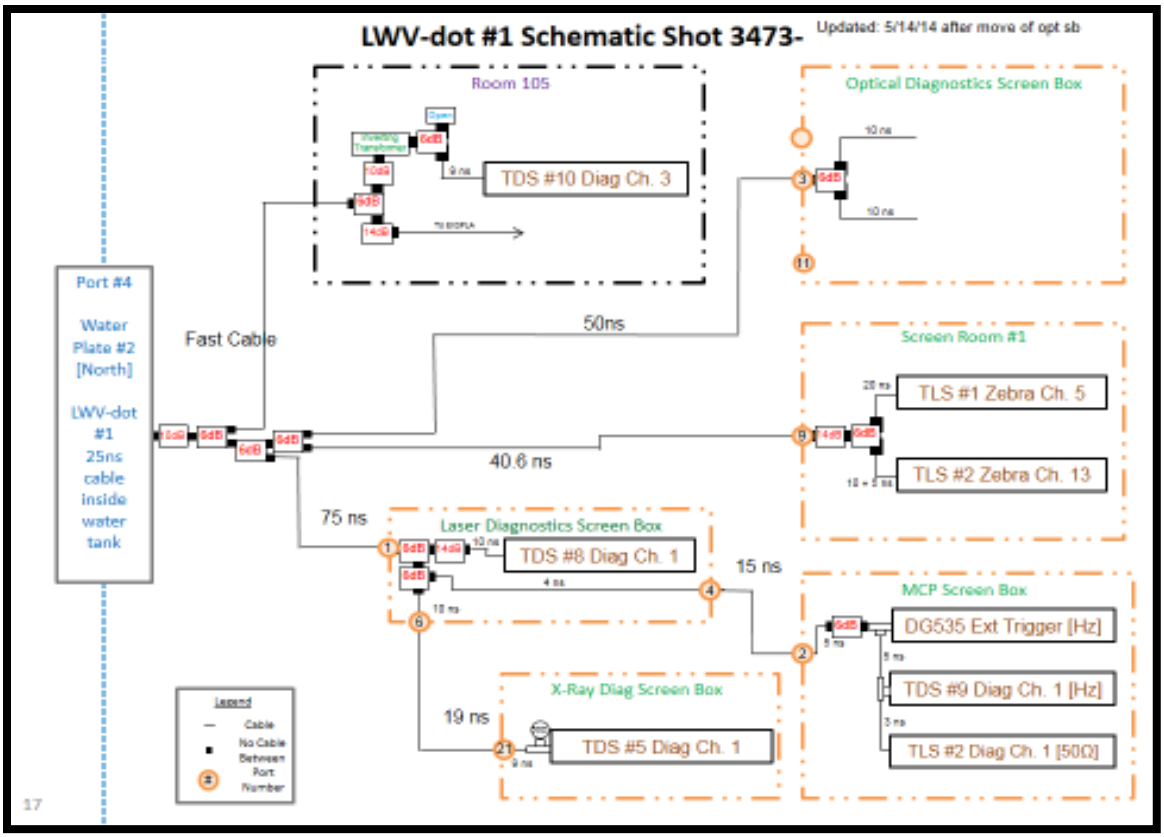

Figure II.11 Schematic of the LWVD trigger signals that are sent to the diagnostic screen boxes for triggering as well as timing fiducials. (Schematic courtesy of B. Le Galloudec and V. Nalajala, UNR)

The timing of all scope signals and the timing of the captured images can be correlated with the current profile by taking into account all the delays in the cables, delay generators, fibers, and the time of flight of any optically relayed image. To ensure the diagnostics are properly cross-correlated, timing fiducials were delivered to many of the diagnostics. This was done by splitting off a fraction of light from the Ekspla laser and fiber-coupling the light to fast photodiodes. The photodiodes utilized were high-speed detectors from Thorlabs (Item# DET10A). The light was coupled into the digitizers of each diagnostic as a timing fiducial.

Chapter III: Load Hardware

The Megagauss experiments at Nevada Terawatt Facility were designed to study the physical parameters related to liner experiments such as Magnetized Target Fusion (MTF) and Magneto-Liner Inertial Fusion (MagLIF) in collaboration with Los Alamos, AFRL, and Sandia national laboratories. The MTF and MagLIF experiments are currently under development at AFRL, Los Alamos and Sandia. The design of the loads was driven mostly by the physical parameters involved with the MTF experiment with some consideration of load material taken into account by the MagLIF experiment . During the compression of a metal liner, in the case of MTF this is aluminum, the state of the inner liner is not well understood. The interaction of the inner wall of the liner with the plasma during compression will ultimately determine the time duration in which the plasma can not only keep its high temperature, but also how much and how long the magnetic flux stays trapped within the plasma fuel. The thick rod experiments presented here allow for the study of the same physical parameters as those in the liner experiments. For the rod experiment to simulate the physics involved in the liner experiments, the following conditions must be met:

1. The evolution of the phase state of the metal surface via ohmically heating the metal rods as opposed to other, non-MHD, processes such as arcing electrical contacts or electron avalanche.
2. The metal rod surface magnetic field must reach megagauss magnitudes ($B_s > 1MG$).
3. The rod thickness must be large enough such that the current is non-uniform in a skin layer ($\delta < R$).
4. Rods must be smooth enough to avoid extreme non-uniform heating or hydrodynamic jetting.
5. The surface must sustain stability until formation of plasma.

The initial work done in designing a load to study these parameters was done by Awe and is discussed in more detail in his dissertation. The diagnostics used to determine performance of the load hardware included a 38 element photodiode array, a 2 ns-gated intensified CCD camera,

a 12-frame 5ns gated intensified CCD camera, and a 16-frame 4ns gated intensified CCD camera. The experiments are conducted to study different materials, alloys, surface finish, and chamber configuration i.e., a new transmission line. A list of these variations is listed below:

Materials:

Aluminum 6061

Copper 101

Copper 145

Nickel 200

Titanium II

Chamber configuration:

Large AK gap

Small AK gap with cage configuration and transmission line

Surface finish:

Turned on a lathe

Turned on a lathe and electropolished

Surface cleaning was required for all rods that were machined on a lathe and not electropolished in order to remove any machining grease. The rods were cleaned with acetone followed by alcohol. This process was done by filling a small bowl with acetone, placing the rod in a small strainer, and then dipping it into the bowl and moving it around to allow for "sloshing." The alcohol was then sprayed across the surface of the rod with a laboratory bottle to remove

residual acetone. The rod was then left out to dry on Kimwipes. This process was done for all rods except for those that were electropolished. The one exception to this process was the MG VI experiment. The copper and aluminum rods shot in that campaign were also put into a sonic bath with soap to remove the grease. This procedure was not continued in future experiments because it is believed to be unnecessary.

Section III.A: Diagnostics to Determine Hardware Performance

Optical imaging

To observe the effects of alloy, surface finish, load design, and transmission line design, multiple diagnostics are fielded to monitor the behavior of the load material during a Zebra shot. An Andor intensified CCD (ICCD) camera was fielded to image the visible surface emission of the loads. A diagram of the camera is shown in Figure III.1.

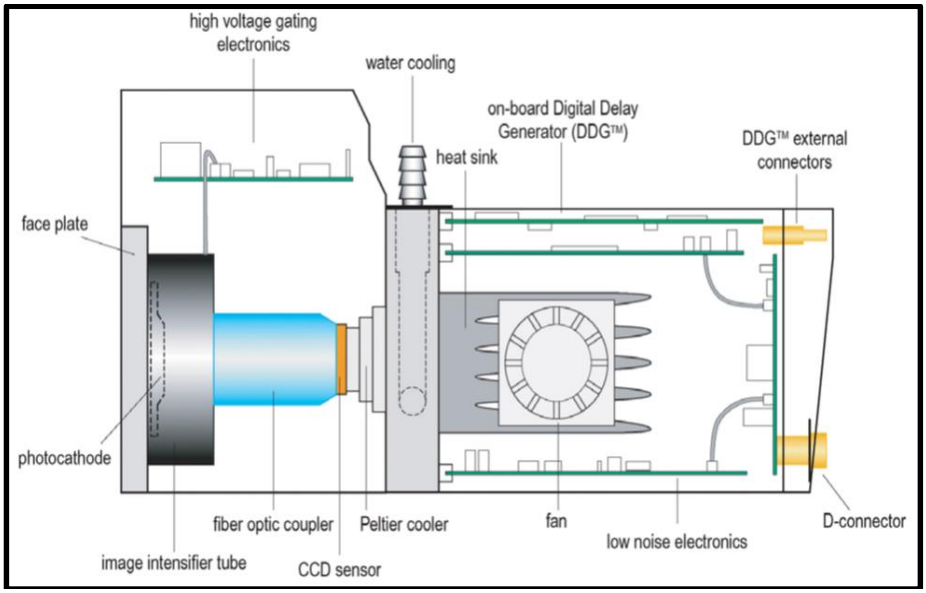

Figure III.1 Schematics of the Andor ICCD camera that was fielded to capture 2 ns gates images of the surface emission of the rods. (schematic courtesy of Andor Technology)

An image of the load is relayed by a multi-lens system to the face of the camera. The image plane is placed at the photocathode where the light produces photoelectrons. These electrons are swept away by an electric field into a honeycomb shaped structure called a multichannel plate (MCP). The function of the MCP is to magnify the number of photoelectrons. This is done by placing a large voltage across the MCP and situating the channels such that they are at an angle to the incoming electrons. This guarantees the electrons will strike the walls of the channels where they will create secondary electron emissions. This process occurs multiple times as the electrons travel across the MCP honeycomb channels. The voltage setting on the MCP determines the magnification of the number of electrons. The electrons are then accelerated toward a phosphor anode plate where they are converted back into photons. A fiber optic coupler transfers this image to the CCD chip where the image is then recorded. The gain setting of the MCP can be set from 0 to 255 with the gain curve approximately fitting the function: (counts/photoelectron)=$2^{(gain/30)}$. The MCP limits the spatial resolution of the image to about 40μm but can be manipulated by magnifying the image as it is relayed to the ICCD camera as will be discussed shortly. The CCD chip has 1024×1024 pixels that are $13\mu m \times 13\mu m$ squares. The imaging system used to relay the image to the camera for MG-V is shown in Figure III.2.

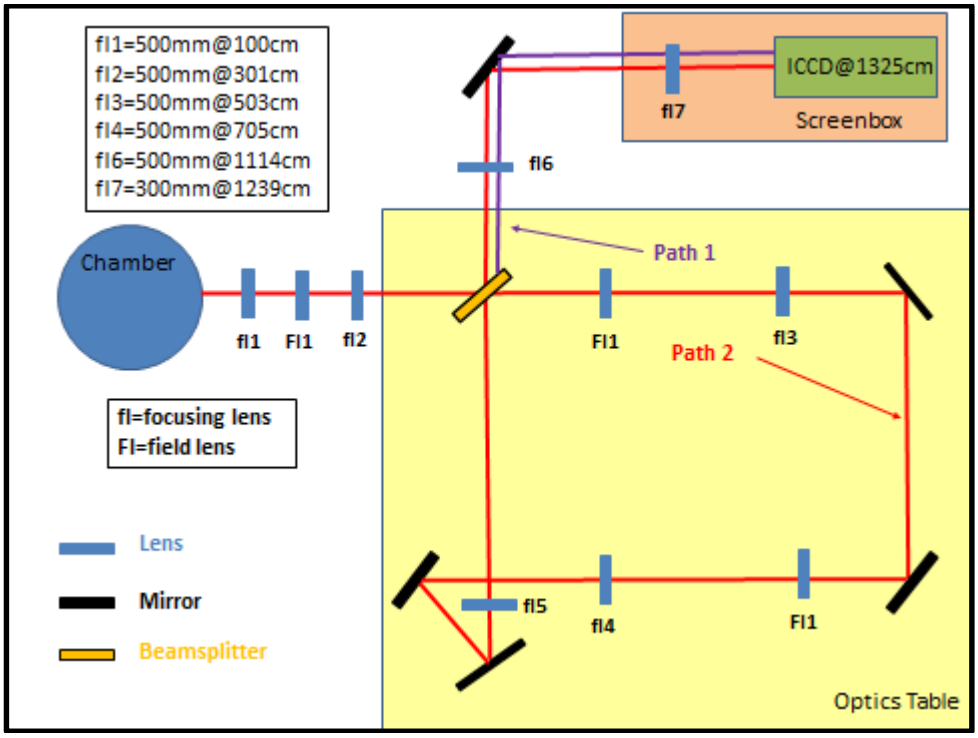

Figure III.2 Optical imaging system used in MG-V to relay the rod image from target chamber center to the ICCD camera.

The image was captured by the first lens at 100 cm and relayed using both focusing lenses as well as field lenses. The long distance that the image was relayed required the use of field lenses to reduce the effect of vignetting. Without the field lenses, off-axis rays would be lost as they propagate through the system. A pellicle beamsplitter was used to split the image beam into two paths. One path was sent directly to the ICCD while the other beam was relayed an additional six meters before being sent to the ICCD. This was done so that two images separated in time by 20 ns could be collected on the CCD chip on every shot. Care must be taken when attempting to do this. With a time difference of 20 ns between the two images, there is a significant difference between the intensity of the two images as the load is initially non-uniform and dim, and evolves into a more uniform and bright object. The dynamic range of the CCD must provide high contrast

images. As the timing of the ICCD was changed from shot to shot, the gain applied to the MCP must be carefully chosen. An image that is taken early in the plasma formation would need more gain than an image that is take later in time, especially for the loads of smaller radius that form plasma earlier on the current profile. A Thorlabs 532±10 nm filter was placed directly in front of the ICCD to narrow the bandwidth of the image. This was done to reduce the chromatic aberration and improve the image resolution.

The MG-VI optical line was different from all other systems that had been fielded previously. Two multi-element lenses were borrowed from Dr. Glen Wurden at Los Alamos National Laboratory. These two lenses were used to capture and relay the load image to the ICCD camera as well as a visible spectrometer and a 12-frame Hadland visible camera. Unlike previous campaigns, only one image was captured by the ICCD camera. The optical layout for MG-VI is illustrated in Figure III.3.

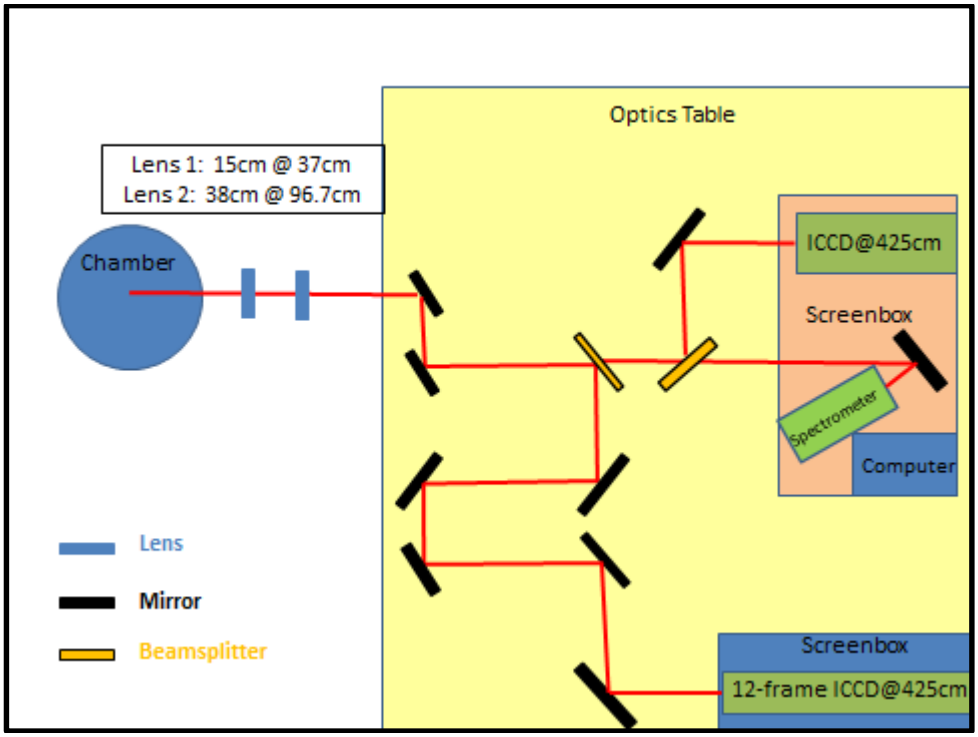

Figure III.3 Optical imaging system for MG VI with two lenses up close to the chamber to relay the rod image to the 12-frame Hadland ICCD and the single-frame Andor ICCD.

It was thought that the large lenses on loan from Los Alamos would help with two important aspects of the optical path:

1. The large diameter and short focal length lenses (small f#) allowed the first lens to be placed close to the vacuum chamber port window. This increased the light collection in hopes of observing earlier light emission.
2. The two lenses were sufficient to relay the load image to the cameras and visible light spectrometer. This reduces the problems associated with alignment of many lenses over a long distance.

Despite what appeared to be clear advantages to the new optical setup, other problems arose. The most important of these problems was the effect seen by using multi-element lenses. The alignment of the optical system was done by routing the Ekspla laser through the south port. To ensure that the laser was going through the chamber straight each time an alignment was done, an iris was placed at the entrance to the south port along with two irises along the optical path outside of the north port. The laser was sent through target chamber center (TCC), through multiple irises, and finally to the cameras and spectrometer. This was done with no lens in the system, only mirrors and irises. Then the first lens was placed in position. The lens was moved to place the laser in the center of the optic. The optics did not have anti-reflection coatings, so part of the laser light reflected back on itself. This effect can be used to align the rotational degree of freedom. If the laser light does not reflect back on itself, then the optic would need to be rotated until it lined up with its reflection. Since the optical elements being used had several lenses inside, each lens had a partial reflection. It was noticed that the reflections did not all line up with the incoming beam. This suggests that the lenses are slightly off axis from one another inside the

assembly. There was nothing that could be done with this problem and it was determined that the optical resolution was good enough to justify continuing with their use.

The light from this optical line was sent to the optical table where it was split into two paths using a pellicle beamsplitter. One path sent the image into a set of mirrors that were mounted on a translational stage and then into the Hadland 12-frame ICCD camera. The lenses on the translational stage were designed to help with focusing the image onto the Hadland CCD chip. The Hadland camera is a large camera that is housed inside a large metal box. The size prevented the camera from being mounted onto a translational stage in the way the ICCD is. The mirrors were used to vary the optical path length to optimize the focusing of the image.

The other path of light that was split at the pellicle was sent through a second pellicle beamsplitter. The two optical paths from this beamsplitter were both sent into the same screen box. One path was sent directly into the ICCD camera while the other was bounced off of a mirror and sent into the visible spectrometer. The size of the screen box limited the options for how our diagnostics could fit into the box and still be accessible. This is the reason for the placement of the mirror for the visible spectrometer.

The resolution of the imaging system needed to be optimized and determined. This was done by placing a cactus needle at TCC and moving the cameras into place of the best resolution according the human eye. The cactus needle was backlit using a white light source and a diffuser. This procedure was done to capture a rough estimate of the best placement of the cameras. To determine the image resolution a 4-40 bolt was placed at TCC and imaged to the ICCD. The separation between teeth is 635 μm with the image showing 335 pixels between adjacent teeth. This gave a camera resolution of ~1.9 μm/pixel and a magnification of about 7. To determine the image resolution a knife edge was placed at TCC. Figure III.4 shows images of both the 4-40 bolt

and the knife edge. A line-out can be taken of the knife-edge and the edge width can be used to determine the resolution. This was done using multiple filters to determine the effect of using the Wratten #58 green filter as well as the Thorlabs FG900 IR rejection filter which were to be used on the imaging of the Hadland camera. Images were taken with both filters, no filters, and the IR rejection filter alone.

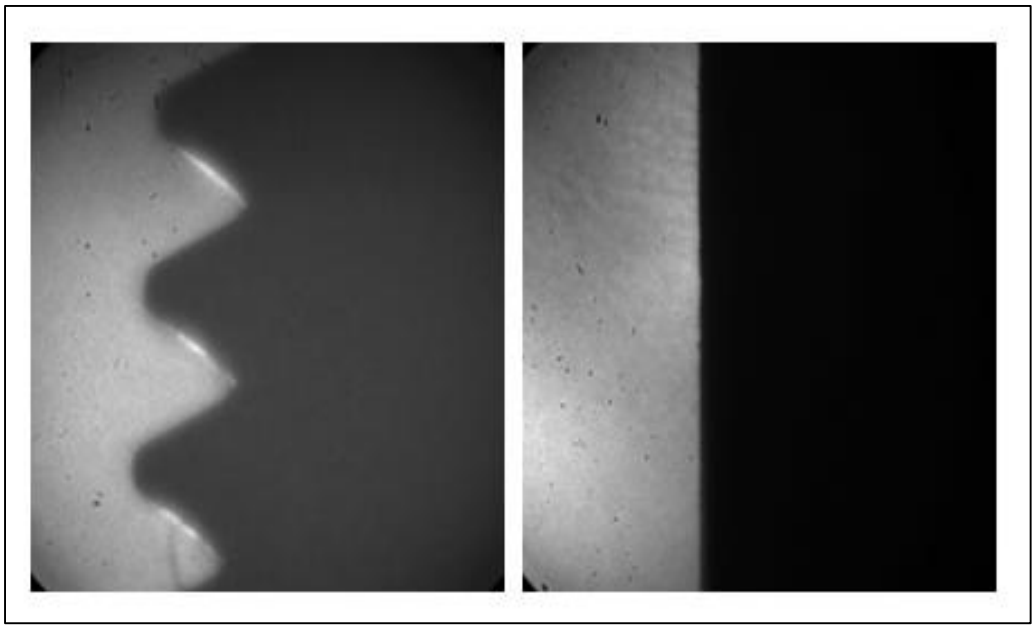

Figure III.4 An image captured by the ICCD camera of a 4-40 bolt (left) and a razor's edge (right) placed at TCC to determine the optical resolution of our collection optics and camera in the MG VI experiment.

Determining the differentiated edge width and using the camera resolution of 1.9 μm/pixel, an image resolution is found. Figures III.5-III.7 show the line-outs for the three filter sets as well as the differentiated edge for each. The image with both the Wratten #58 green filter and the IR rejection filter had a differentiated edge with a FWHM of 6 pixels, giving a resolution of 11 μm. The image with the IR rejection filter only had a differentiated edge with a FWHM of 8 pixels, giving a resolution of 15 μm. The image with no filters had a FWHM of 13 pixels, giving a resolution of 25 μm. The results above motivated us to use both the green filter as well as the IR rejection filter in the optical system.

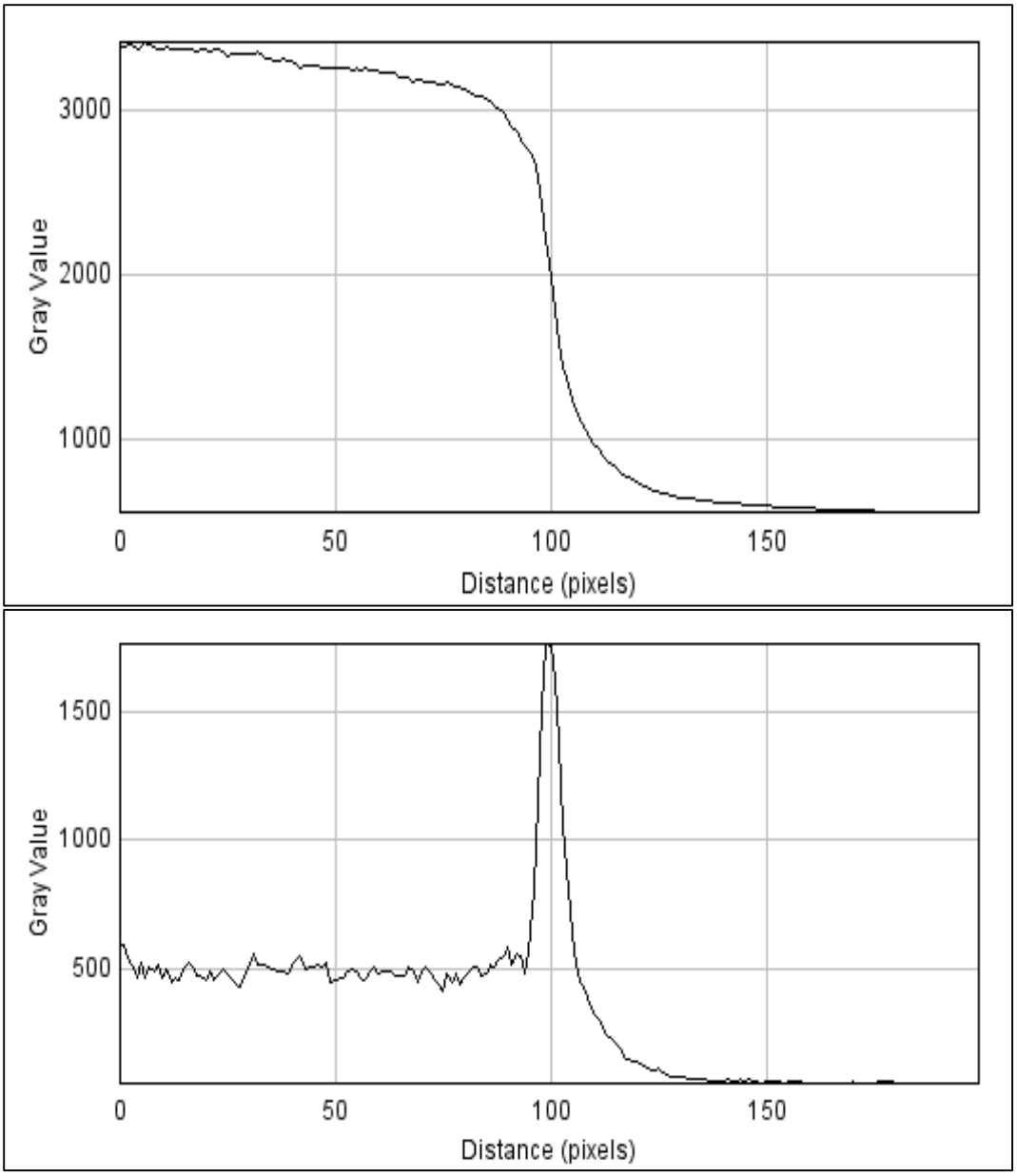

Figure III.5 Line-out of razor edge showing edge width (top) with the corresponding differentiated edge width (bottom) with both Wratten #58 green filter and IR rejection filter. The optics produced a resolution of 11µm.

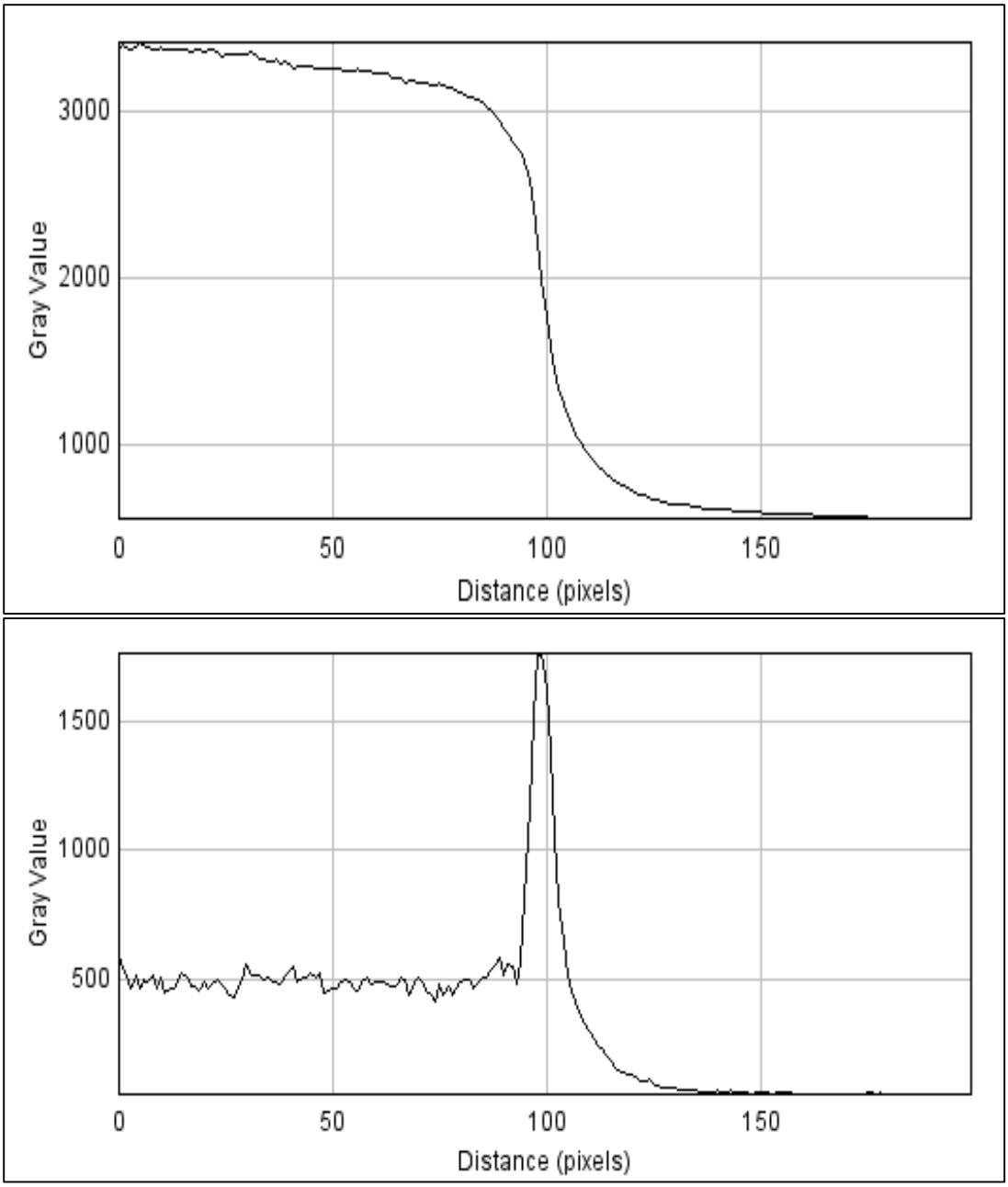

Figure III.6 Line-out of razor edge showing edge width (top) with the corresponding differentiated edge width (bottom) with IR rejection filter only. The optics produced a resolution of 15µm.

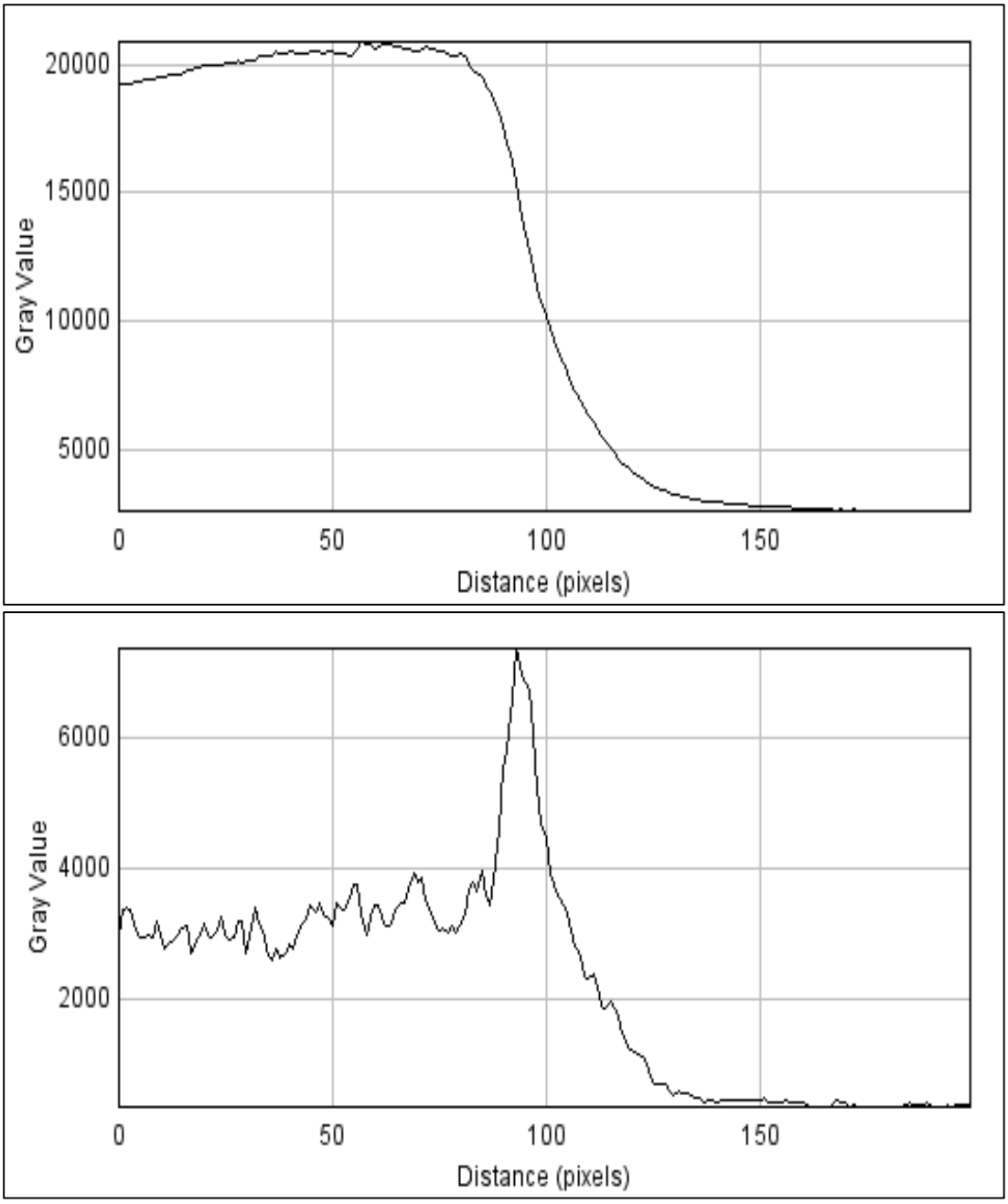

Figure III.7 Line-out of razor edge showing edge width (top) with the corresponding differentiated edge width (bottom) with no filtering. The optics produced a resolution of 25μm.

A multi-frame Hadland camera was fielded on loan from Los Alamos National Laboratory. The Hadland Ultra UHSi Model 12/24 camera allowed for 12 frame optical imaging of the load. The Hadland camera is capable of 24 frame imaging with 10 μs time delay between the 12th and 13th frame. This long delay between the two sets of 12 frames made the second set of no use to

the MG experiments. The camera has a max frame rate of 200 million frames per second allowing for a range of gate times of 5 ns to 1 ms. The inter-frame time could be set from 0 to 10 ms. The camera was equipped with an MCP that allowed for high gain which was recommended to be kept at a max setting of 100. The gain curve could be set by entering a desired gain curve into the program with minimal gain setting being 0 and max gain setting being 100 with the 100 setting having a gain of 5000. The camera was equipped with an S25 photocathode (range of 400 nm to >850 nm). The camera has a Nikon F-mount with a viewfinder that can be used for rough alignment when the camera is not armed. The viewfinder works by having a mirror reflect the light 90 degrees from the CCD chip when the camera is not armed. When arming the camera, the mirror slowly rotates out of position allowing for a gated image to being taken by the camera. The CCD has a 12 bit dynamic range and has 4872×3248 pixels. Figure III.8 shows a picture of the Hadland camera.

Figure III.8 The 12-frame Hadland camera with a Nikkor lens attached to the front (image courtesy of Hadland Imaging LLC).

To improve the light collection and the spatial resolution of the images, a long distance tele-microscope (LDM) was purchased. The Questar QM100 is designed to allow for 1 µm resolution with a working distance of 15cm to 35cm using a Cassegrain optical design. This allows

the LDM to be placed up against the chamber port. Figure III.9 is an image of the LDM. The south port of the Zebra chamber was used for imaging with the LDM because it is the largest diameter port at 4 inches. With the high quality optics of the LDM, high quality optical windows as well as debris shields were used to reduce the effects of these being in the optical path. The purpose of the debris shield is to protect the expensive windows from the debris during a shot with the debris shield being replaced between each shot. The windows are 4 inch diameter, 15mm thickness, BK7 with a surface quality of λ/10 and were purchased from Optosigma. Soda lime cover slips from Ted Pella were used as the debris shields with a thickness of 0.2mm allowing for minimal effect on the image quality. A special holder for the debris shield as well as the window was made by Alexey Astanovitskiy.

The LDM was placed within an inch of the port window by hanging it from the space frame using an aluminum frame. Translation stages allowing for movement in the x, y, and z directions were used along with a tip/tilt mount to adjust the pitch, a rotational stage, and a lab jack for adjusting the height. The image was relayed using the LDM with a 28mm Nikkor lens attached to back to magnify and relay the image several inches to an ICCD. The image was split with a 50/50 beamsplitter after passing through the 28mm lens, allowing for two ICCD cameras to be fielded. A design of the optical path is shown in Figure III.10, with the ICCD cameras housed in aluminum boxes shown perpendicular to one another. The two cameras used were Andor ICCD cameras. One of the cameras uses a USB link and can be linked fiber optically making it easy to control the camera from several meters away with the computer in a protected screen box. The other Andor camera utilizes a cable bundle that runs from the camera to a protected screen box that houses the computer, requiring an EMI braid wrapped around it to protect it during a shot. Each aluminum box that held the Andor cameras had a power filter built into the back so that the power

used to power the cameras would be clean from noise as well as any power spikes. With the two cameras, each shot was able to collect two images allowing the timing of the two images to be separated by just a few ns to observe the short time evolution of the surface emissions.

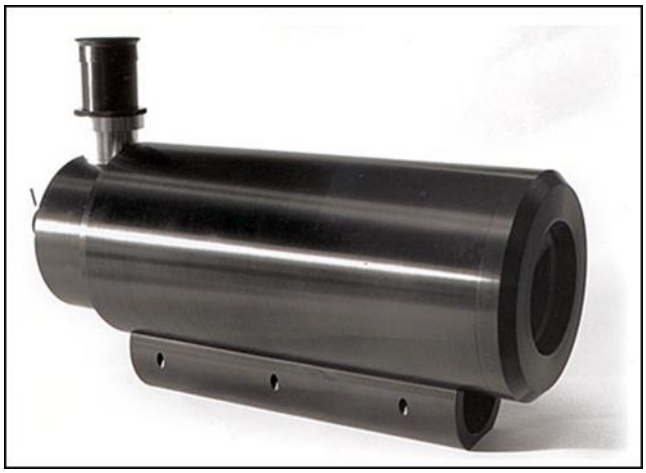

Figure III.9 The Questar QM100 Long Distance Microscope (LDM) has ~2.5" entrance aperture with a length of ~12". (image courtesy of Questar Corporation)

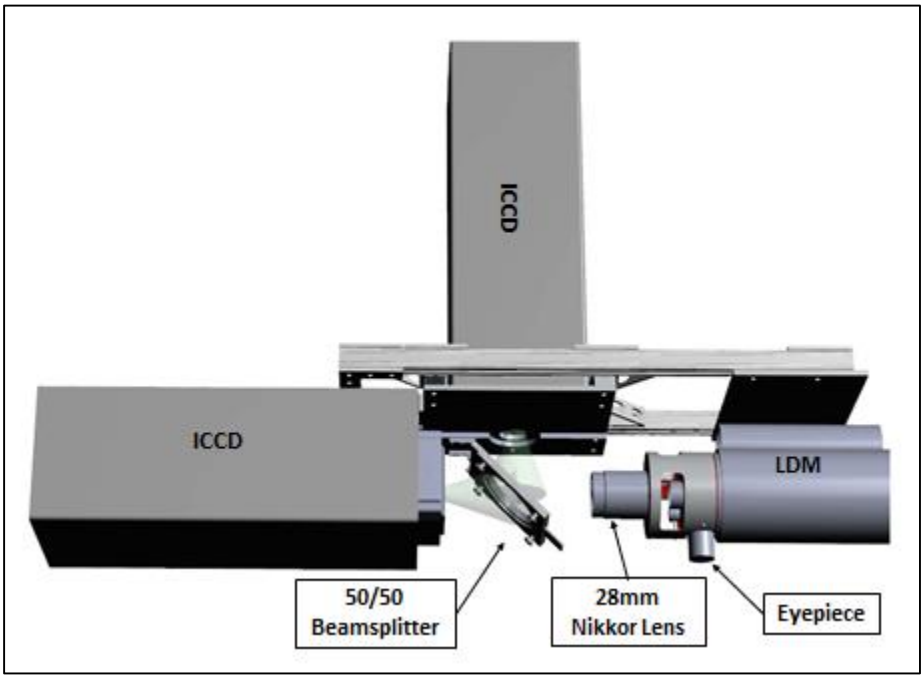

Figure III.10 The design of the optics system and manifold that held the LDM, 28mm Nikkor lens, pellicle beamsplitter, and two EMI shielded Andor ICCD cameras as one piece to be hung from the space frame and placed within 1" of the Zebra port. (Image courtesy of T.J. Awe, SNL)

With the higher collection and resolution optics, a much better image could be captured. An Air Force 1951 resolution target purchased from Thorlabs was placed at TCC and illuminated to determine the optical resolution and magnification. Figure III.11 shows an image taken with the single-frame ICCD camera of the target. A lineout of the smallest group (group 7) was taken using ImageJ and exported into Microsoft Excel. Figure III.12 shows a lineout of the group 7 elements with the elements decreasing in size from left to right in the lineout image. The first two group elements are resolved with the third, fourth, fifth, and sixth elements getting progressively worse. The resolution is determined using the line pair per mm scale provided by Thorlabs and is shown in Figure III.13. The resolution of the two ICCD cameras were 0.6μm/pix with a spatial resolution of 2-5μm. The resolution of the SIMX camera was 1.78μm/pix with a spatial resolution of 11μm. Because of the curvature of the rod face and shot to shot variations, the images can vary in resolution. This is why the μm/pix of the imaging system is determined for each camera, such that for each image, the number of pixels resolved determines the shot resolution in microns.

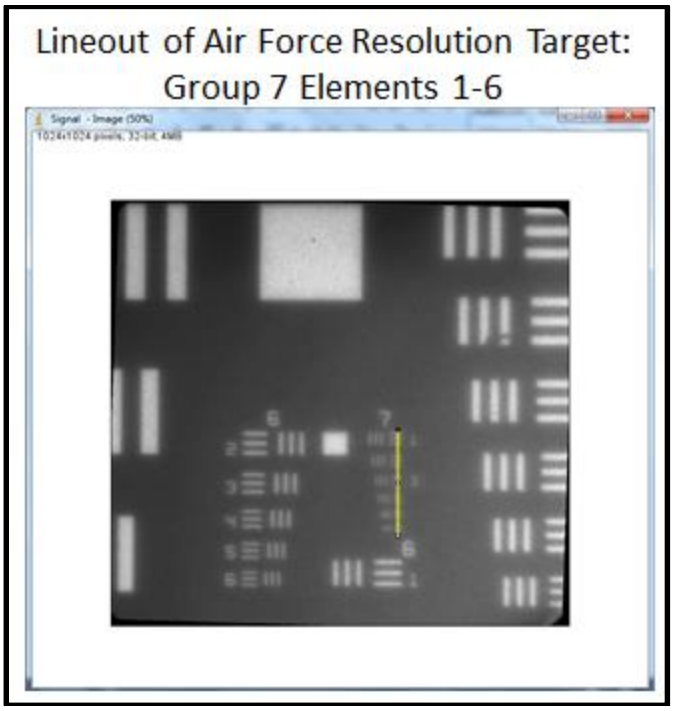

Figure III.11 An ImageJ lineout is taken of the smallest group of the Air Force Resolution Target and exported into Excel.

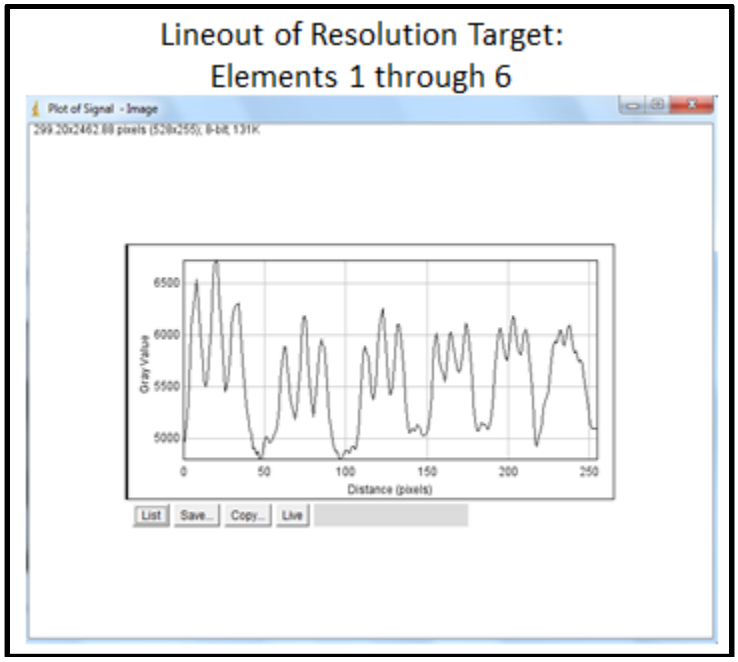

Figure III.12 A lineout of the Group 7 Elements 1 through 6 of the Air Force Resolution Target illustrating the limit in resolving ability as the line pairs become less resolved moving left to right. The second set from the right is Element 2 and is used to determine the limiting resolution of the system and the magnification.

Air Force Resolution Target Group Number and Element Size
(line pair per mm)

Element	Group Number									
	-2	-1	0	1	2	3	4	5	6	7
1	0.250	0.500	1.00	2.00	4.00	8.00	16.00	32.0	64.0	128.0
2	0.280	0.561	1.12	2.24	4.49	8.98	17.95	36.0	71.8	144.0
3	0.315	0.630	1.26	2.52	5.04	10.10	20.16	40.3	80.6	161.0
4	0.353	0.707	1.41	2.83	5.66	11.30	22.62	45.3	90.5	181.0
5	0.397	0.793	1.59	3.17	6.35	12.70	25.39	50.8	102.0	203.0
6	0.445	0.891	1.78	3.56	7.13	14.30	28.50	57.0	114.0	228.0

Figure III.13 An Air Force Resolution Target was utilized in the MG IX experiment to determine magnification and resolution of the Andor and SIMX ICCD imaging systems.

For one week of the MG IX experiment, a 16-frame SIMX ICCD camera was fielded on loan from National Security Technologies out of the Nevada Test Site. The north port was used with an LDM placed up close to the chamber. The LDM was hung from the space frame with the same translation stages and mounts that were used for the Andor ICCD cameras on the opposite side of the chamber. Since the camera was too large and too expensive to put up close to the chamber, three relay lenses were used to relay the image from the back of the LDM to a screen box on the optics table that was housing the SIMX camera. A 50mm Nikkor lens was attached to the front of the SIMX for resolving the images. The optical layout is illustrated in Figure III.14. The SIMX camera allowed for 16 images to be captured with a gate of 4 and 5ns (depending on shot).

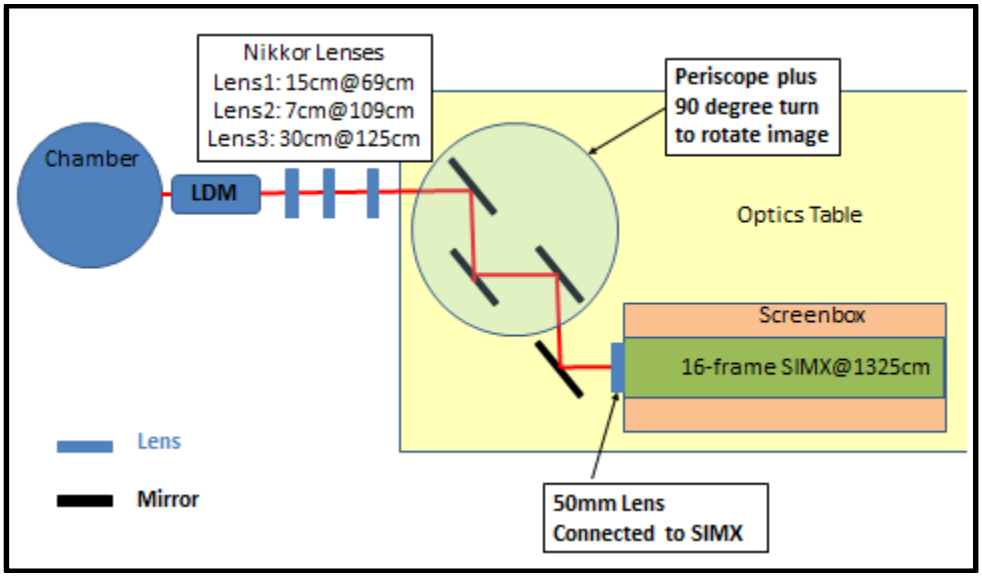

Figure III.14 The optical layout for the 16-frame SIMX ICCD camera fielded on MG-IX experiment.

The SIMX camera was aligned before each shot by backlighting the rod with the LDM that was located on the opposite side of the chamber. This is possible by attaching a white light source to the LDM through the eye piece and utilizing the LDM like a focusing flashlight. The LDM was placed out of focus so the light source did not converge onto the target and get blocked completely by the rod. This backlighting procedure allowed the rod to be centered on the CCD of

the SIMX. It was observed that any small movement near the lenses after alignment, moved the image partly out of the field of view. This was observed by the clipping of the rod image during a shot. To get best resolution of the rod, the light source was used on the LDM that is used for the SIMX optical path. The light source front-lit the rod. As the image was moved into focus, the reflected line would become small and more crisp. Surface structure could occasionally be resolve. The process of centering and resolving the image was done before each shot.

Photodiode array

A 38-element photodiode array (PDA) was used to determine uniform emission of the loads. A lens attached to a port of the vacuum chamber imaged the load onto the photodiode array that was filtered using a green Wratten #58 green filter and an infrared filter to limit the spectral width that was observed. Only 16 elements were used with every other element being grounded to reduce noise from coupling between channels. An ND1.222 filter was placed over half of the elements to ensure that elements do not saturate or become nonlinear as the load evolves into the brighter, late time emission. The unfiltered elements were used to analyze the more sensitive early time emission with the filtered elements used to analyze late time emission. With the image of the load relayed onto the array, the time and amplitude of emission from different locations along the load can be observed. The array elements have a vertical height of 0.89mm, giving a vertical spatial resolution of 0.165mm with a 5.38 optical magnification.

Section III.B: Hardware Design and Performance

Current joint and transmission design

The design of the MG experiments began many years ago with MG-I under PhD student Tom Awe. The motivation in the design was to ensure that the heating that leads to phase transitions and ultimately to plasma formation was due to ohmic heating and not some non-thermal process such as electron avalanche or photoionization. One of the first challenges in designing load hardware was to mitigate non-thermal processes at the joints that couple the load hardware to the anode and cathode of the Zebra machine. Without clean contacts, early plasma formation was observed far from the location of arcing. A knife-edge design was implemented that used several screws to compress stainless steel knife-edge hardware into the aluminum anode and cathode plates, breaking through the aluminum oxide layer allowing for a better contact. A copper mesh was also used to carry current on the anode side to allow for compression of the anode-cathode gap which occurs when the chamber goes under vacuum. Figure III.15 shows the design of these contacts.

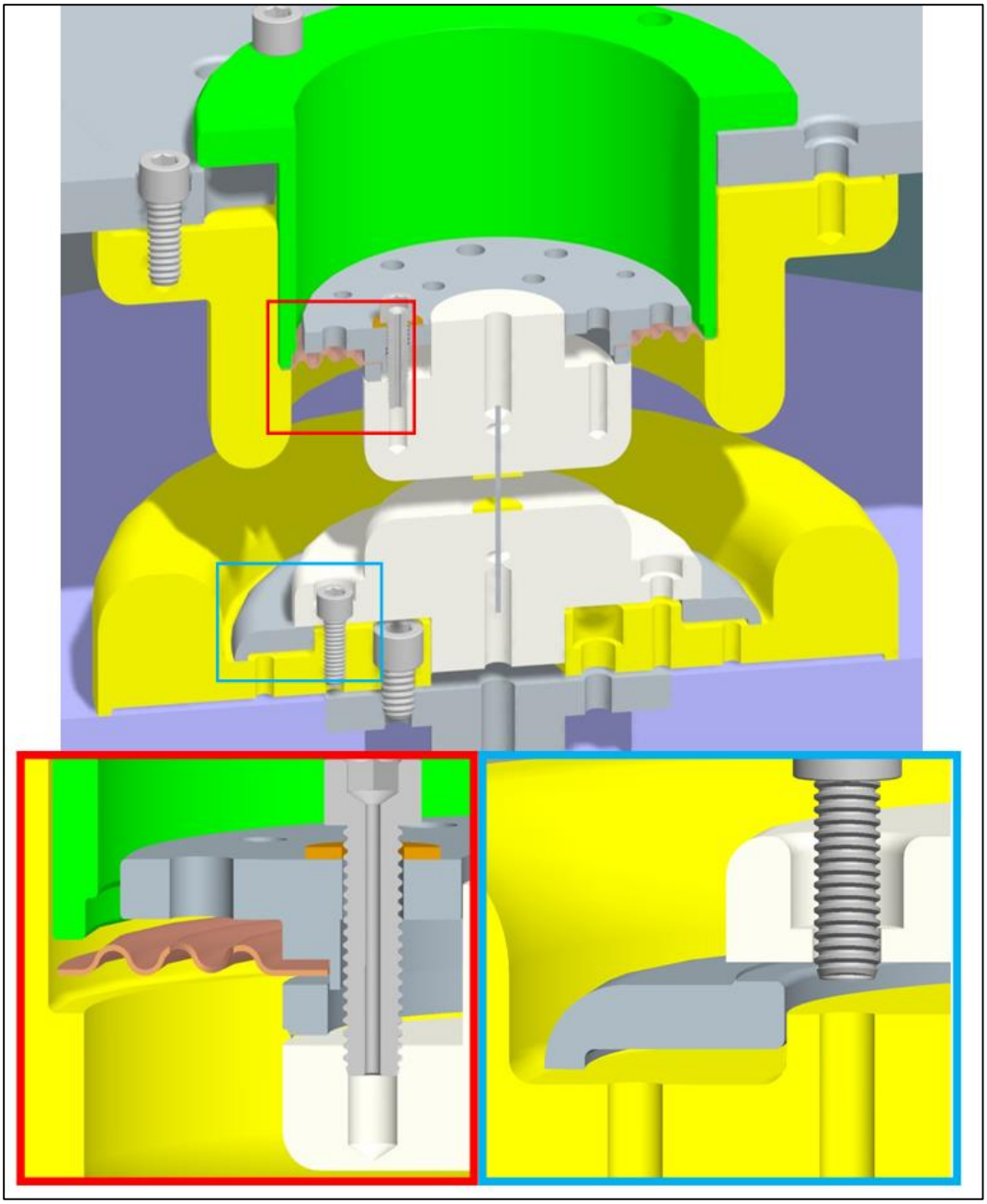

Figure III.15 A zoomed in image of the anode and cathode pieces of the load hardware. The anode (bottom left) shows the placement of the copper mesh used to form a clean contact while the chamber is placed under vacuum and the hardware is compressed. The cathode (bottom right) shows the double knife edge used to break through the aluminum oxide to produce a clean contact from the mesa to the load (images courtesy of S. Fuelling).

Prior to developing this knife-edge contact, a photomultiplier tube diagnostic showed a difference of approximately 40 ns in early light detection between the cathode contact and the center region of the load. With the implementation of the knife-edge and copper mesh, observed light emission at the two locations occurred at the same time. A novel load was designed to enhance the

mitigation of non-thermal processes by removing the direct line of sight of the central region of the load from the contacts. This was done by shaping the load in what is now referred to as the hourglass load and the barbell load. The hourglass load was machined from a single piece of aluminum and came with a high cost. The hourglass and barbell designs performed well with no signs of early plasma formation due to non-thermal processes. The hourglass and barbell design and loads are shown in Figure III.16.

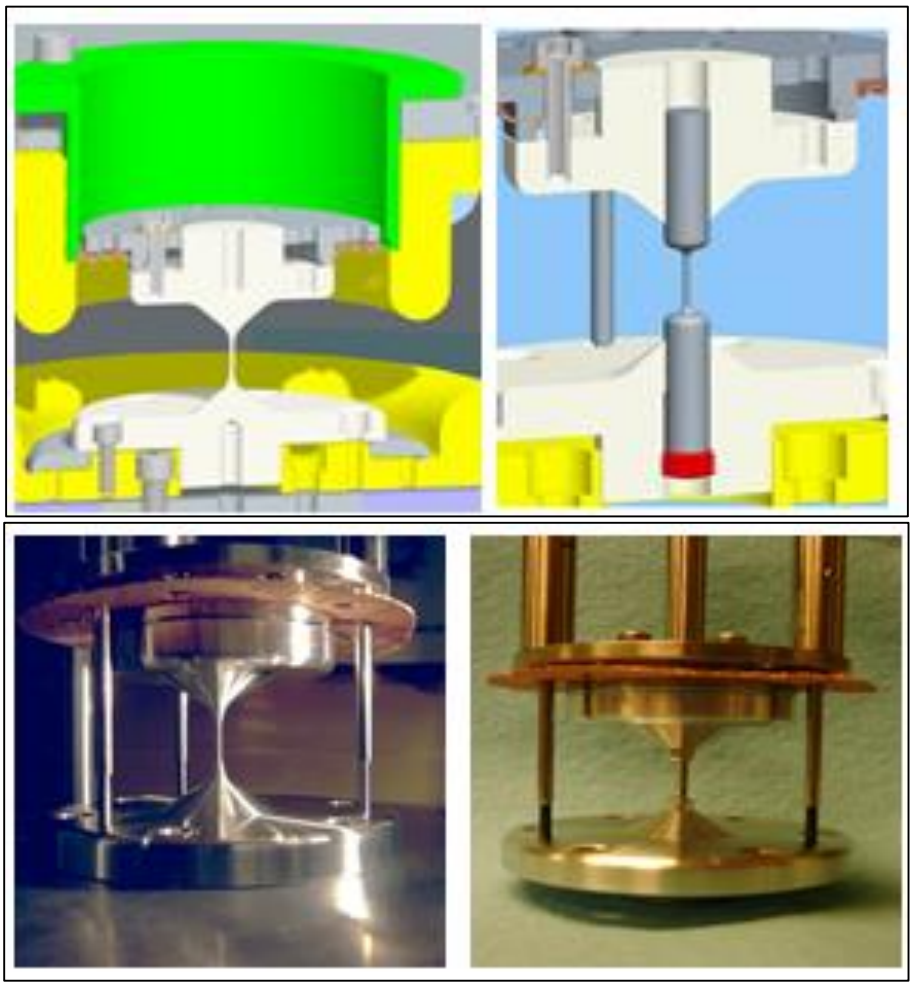

Figure III.16 Computer drawings (top images) and pictures (bottom images) of the hourglass (left images) and barbell (right images) aluminum rods (images courtesy of S. Fuelling).

The barbell load was used as the standard loads for all future MG experiments due to its ability to mitigate non-thermal plasma formation but also because of its lower cost of machining.

A desire to be able to put optics into the chamber during a shot motivated the design of a caged load system that would place the return current inside the chamber as opposed to being the walls of the vacuum chamber. This would make the AK gap smaller and provide an area of the vacuum chamber where there were no electric fields, allowing for the placement of optics. One purpose of placing optics into the chamber would be to have the ability to place collection optics closer to the load in order to be able to collect more light for optical imaging with the ICCD. This would allow for not only more light collection, but the F/# would no longer need to be limited by the aperture of the port window. Another purpose for placing optics into the chamber is for developing x-ray radiography. By placing an off-axis parabola into the chamber, the Leopard laser could be focused onto a foil and produce an x-ray emitting spot that would then radiograph the load.

A desing of the caged hardware is shown in Figures III.17 and III.18 with an illustration of its use in laser produced x-ray radiography in Figure III.19.

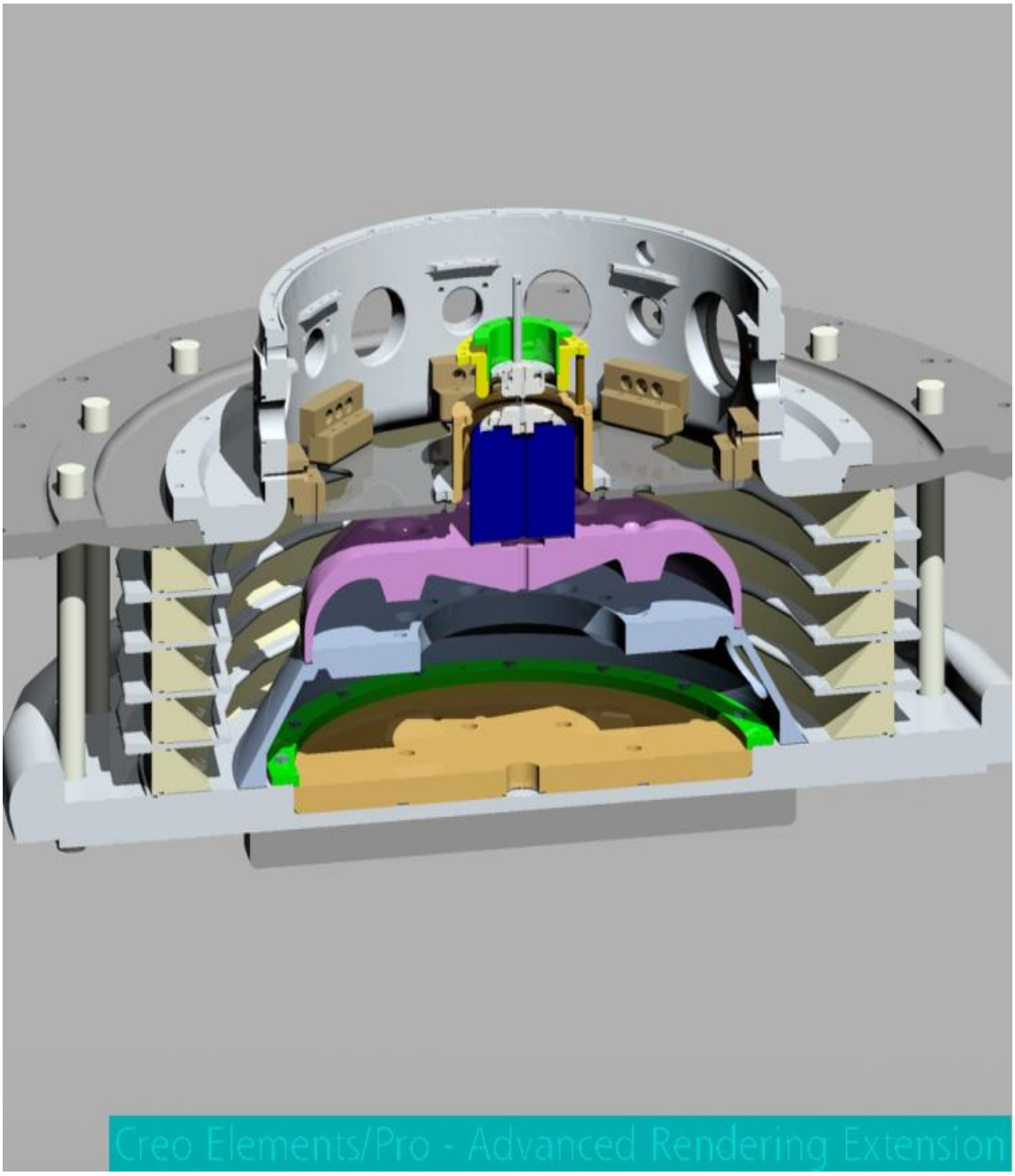

Figure III.17 An engineering schematic of the chamber configuration for the caged load. The illustration shows the Zebra transmission line (light blue) and the Mesa (dark pink). The transmission line (dark blue) designed to deliver the current to the caged load sat on top of the Mesa with the cages hardward bolted into the top. The drawing also shows the insulator stack (off-white) that protects from Zebra shorting to ground. (Schematic courtesy of A. Astanovitskiy and S. Fuelling)

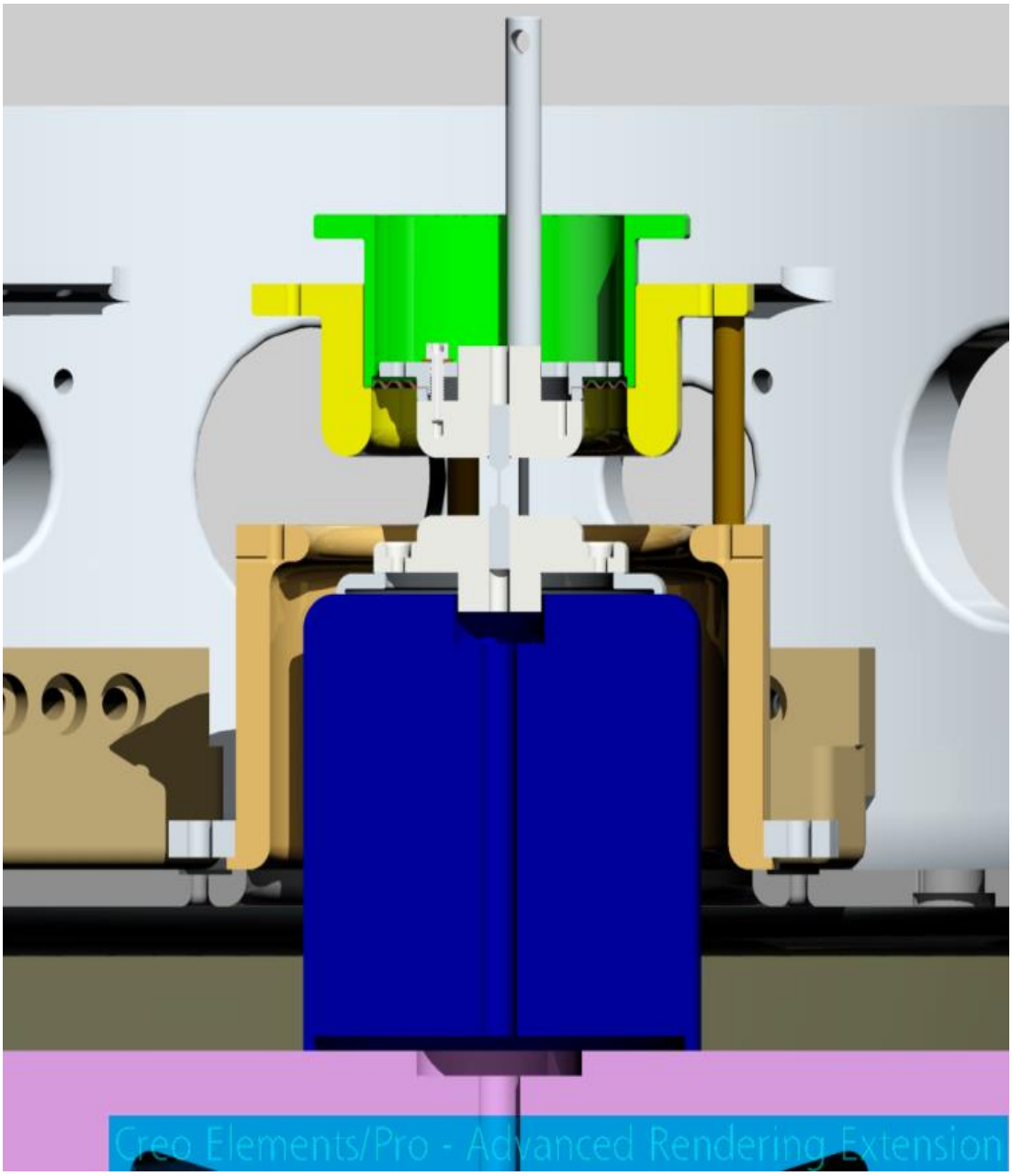

Figure III.18 Zoomed in image of schematic showing the transmission line (dark blue) and the caged hardware used to develop the ability to x-ray backlight the rods. (Schematic courtesy of A. Astanovitskiy and S. Fuelling)

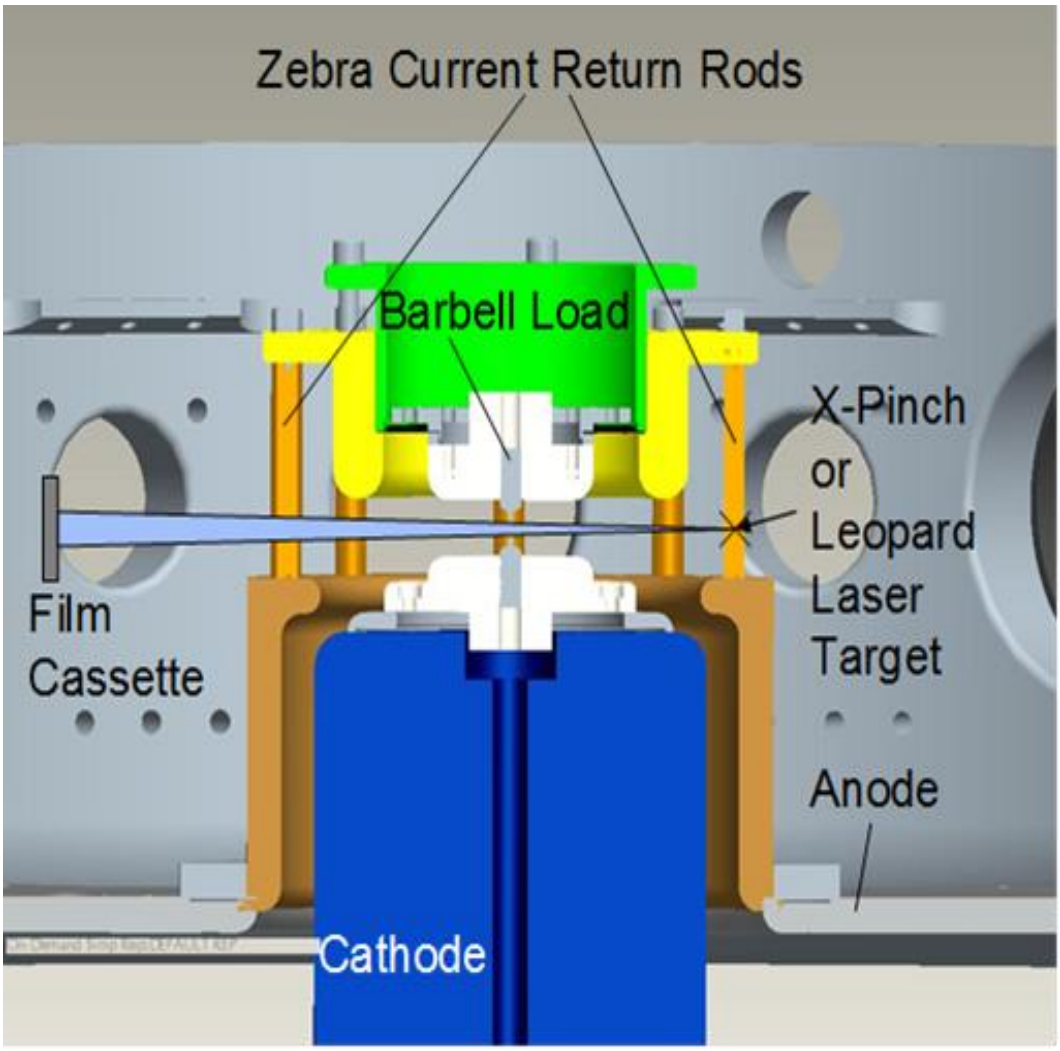

Figure III.19 Schematic illustrating the design and implementation of the caged hardware for xray backlighting. The caged hardware allows for placement of optics and materials into the chamber by decreasing the radius of the anode/cathode gap to not include the entire volume of the vacuum chamber. (Schematic courtesy of A. Astanovitskiy and S. Fuelling)

The new transmission line that was used in MG V was initially designed to be machined out of stainless steel, however, the final design was machined out of aluminum. This likely does not make a difference due to the fact that even if the transmission line was made out of stainless steel, after a number of shots, it would be coated with aluminum (or whatever other load material is being shot) from the loads vaporizing out from target chamber center. The hardware did not perform well with breakdown occurring somewhere along the transmission line, causing early

plasma formation along the load. Figure III.20 illustrates the early plasma formation that was seen with the ICCD.

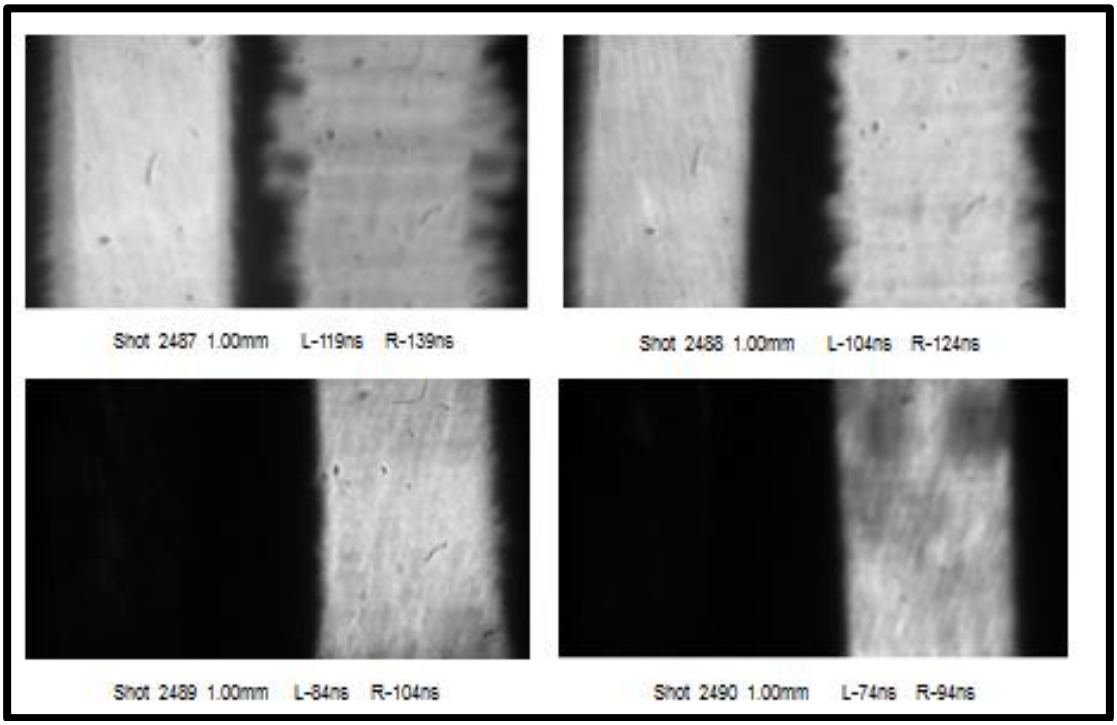

Figure III.20 The ICCD images from MG-V indicate early plasma formation that is likely due to the electric field emission caused by the small anode/cathode gap in the new transmission line design.

Figure III.21 shows the surface emission evolution that was observed in MG IV as the aluminum surface first emits non-uniform dots that transform into filaments along the direction of current flow, and then eventually evolves into a uniform surface emission. This was quite reproducible in previous campaigns along with the time of the evolution. Comparing these images with what was observed in MG V, there are two distinct differences. First, the timing of saturation of surface emission is clearly well before any time that was observed in MG IV. Second, MG V does not show evidence of the early spots and filamentation. There are signs of early plasma that is similar to what is observed along machining artifacts, but there is no clear evidence of the evolution that was previously seen. One possible cause for the failure of caged hardware is an un-optimized ratio of the anode to cathode radii[100].

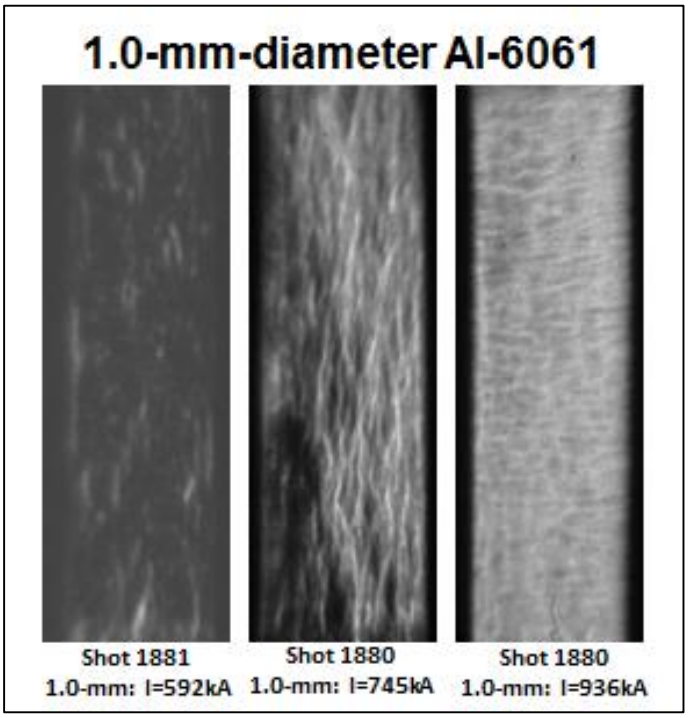

Figure III.21 ICCD images from MG-IV show clear signs of surface emission evolving from a non-uniform plasma to a uniform plasma via ohmic heating. The times of the uniform emission are much later than what is observed in MG-V (image courtesy of T.J. Awe).

With the failure of the caged hardware in MG V, it was decided to return to the previous design of the chamber that is illustrated in Figure III.22.

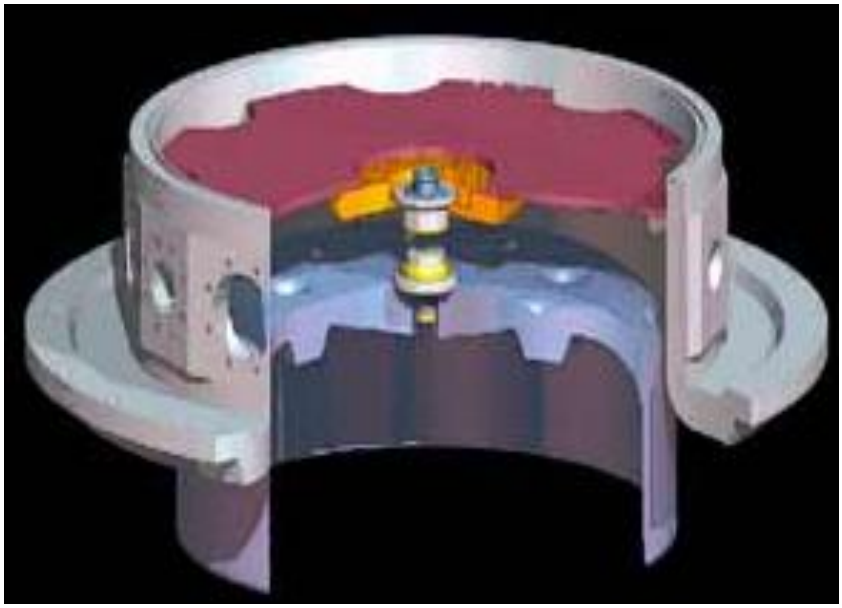

Figure III.22 The Zebra chamber with the cathode mesa (blue), anode plate (red) and the vacuum chamber (grey). (Image courtesy of V. Nalajala)

Section III.C: Surface Finish and Load Variation

Surface Finish

The first goal after returning to the old chamber configuration was to ensure that the hardware was performing the same as it had in MG IV. To do this, the first shots were done using 1.00 mm-diameter aluminum 6061. The first 13 shots of MG VI were all aluminum 6061. The hardware performed well which allowed a few variations to be made to the PDA and spectroscopy diagnostics which will be described in detail in later chapters.

To understand the effect of alloying and surface finish several rods were sent to Sandia National Laboratory for Scanning Electron Microscope (SEM) analysis as well as apply Energy Dispersive Xray Spectroscopy (EDS) to the surface. The rods in all the SEM and EDS images are on their side, such that during a Zebra shot, the current would be flowing left to right. Figure III.23 shows the SEM images of conventionally lathed aluminum 6061. There are machining marks left

by the lathe that look similar to the strata that have been observed in some of the visible self-emission. The zoomed in image (right image) shows inclusions on much of the surface with a large piece of debris in the upper left corner of the image.

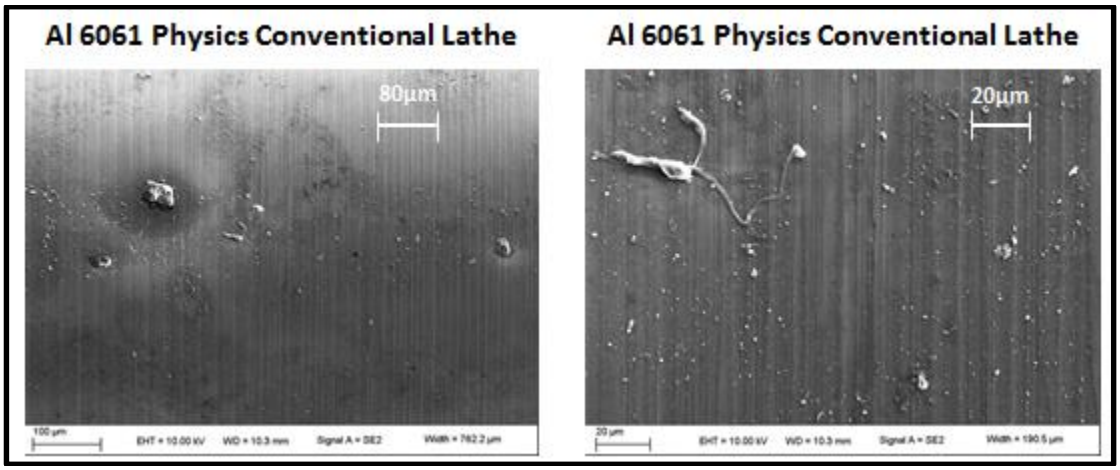

Figure III.23 The images of the conventionally lathed aluminum 6061 shows machining marks left by the lathe that would be perpendicular to the current during a shot (the load is on its side with current during experiment flowing left to right). Inclusions and what appears to be debris is clearly seen in the zoomed in image (right image).

Figure III.24 show the EDS of the conventionally lathed aluminum 6061. The first image, image "a", is the SEM image of the part of the rod that is analyzed with the EDS in the subsequent images "b-f". The color in each image represents the distribution and concentration of each respective element. Image "b" shows the distribution of carbon (blue surface) that correlate well with the darker marks in the SEM images. The carbon is likely left by the cutting tool on the lathe. Precipitates of silicon and copper can be seen in several images.

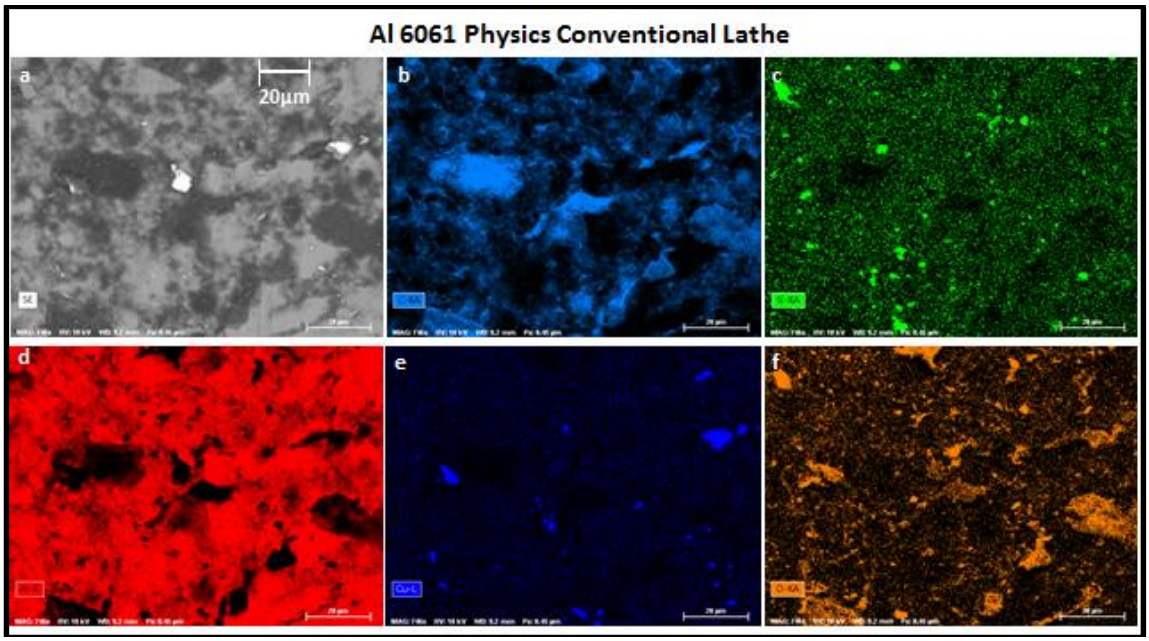

Figure III.24 Electron Dispersion Spectroscopy of the aluminum rod shows the chemical makeup of the surface color coded for each element. Image "a" is the SEM image with subsequent images showing carbon (blue surface features), silicon (green surface features), aluminum (red surface features), copper (violet surface features), and oxygen (gold surface features).

Figure III.25 shows the SEM images of aluminum 6061 that has been electropolished. The machining marks left by the lathe cutting tool have been removed with inclusions being left behind. There are pits in the surface that appear to be left by the electropolishing process removing some of the inclusions, leaving behind a "hole" in the metal. The zoomed in image (right image) appears to show surface grain structure. It is interesting to note the white precipitate in the right image that seem to line up left to right in straight lines. This effect is not understood, but may be a result of the extruding process of the aluminum "pulling" the silicon and magnesium inclusions into lines.

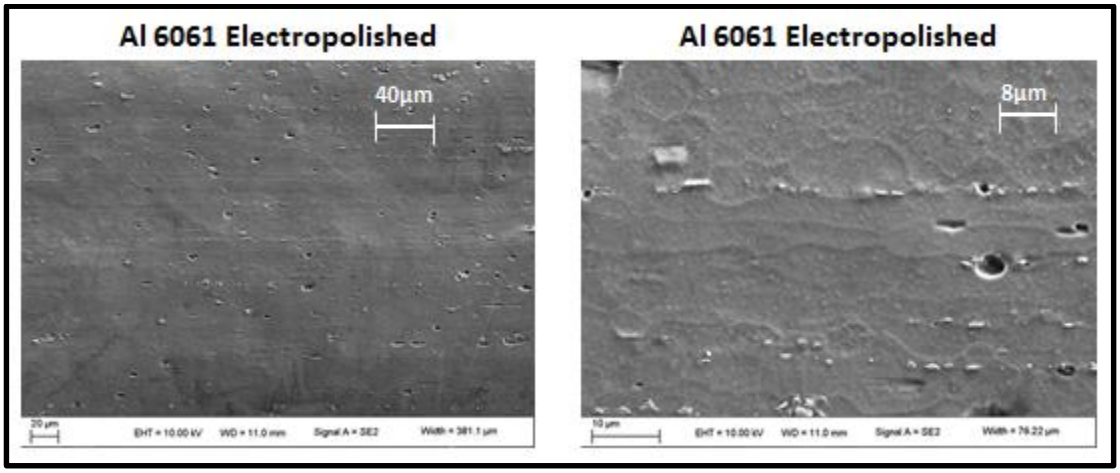

Figure III.25 Electropolished aluminum 6061 shows no signs of the lathe machining marks. It appears that some of the inclusions have been removed, leaving behind pits. The zoomed in image (right image) also appear to show surface grain structure.

The EDS of the electropolished aluminum 6061 is shown in Figure III.26. Precipitates are still observed on the surface, however, the surface is much cleaner with the different elements appearing more dispersed over the surface with fewer areas of high concentration.

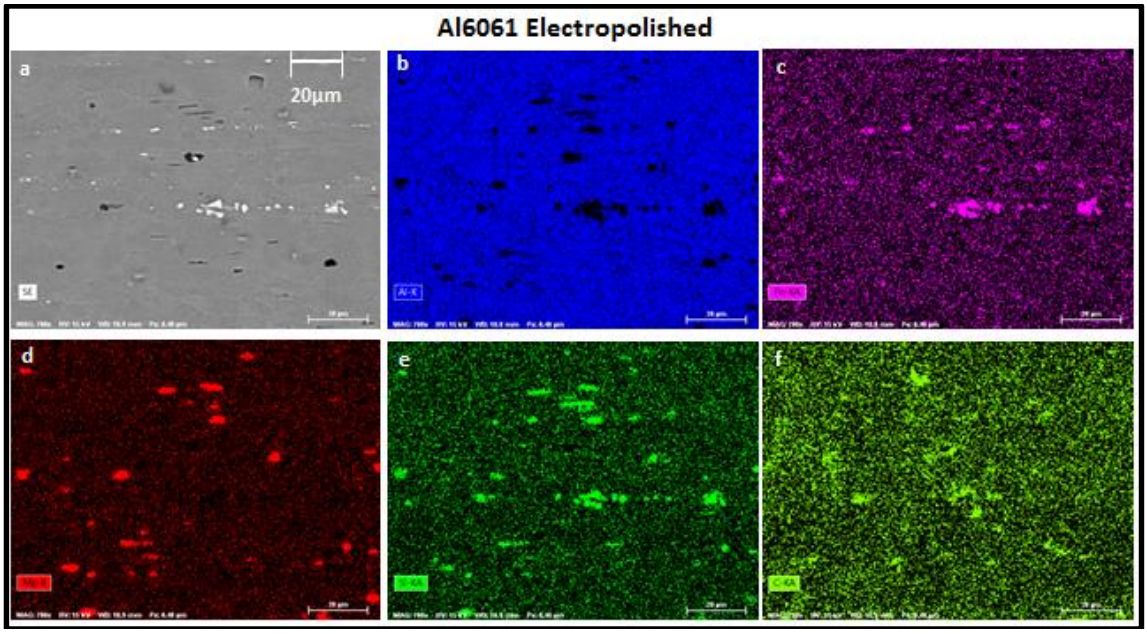

Figure III.26 Electron Dispersion Spectroscopy of the aluminum 6061 electropolished rod shows the chemical makeup of the surface color coded for each element. Image "a" is the SEM image with subsequent images showing aluminum (blue surface features), iron (pink surface features), magnesium (red surface features), silicon (dark green surface features), and carbon (light green surface features).

Figure III.27 shows SEM images of the copper 145 conventionally lathed rods from 2012 and 2015. Both images show distinct machining marks similar to the marks observed in the aluminum 6061 rods.

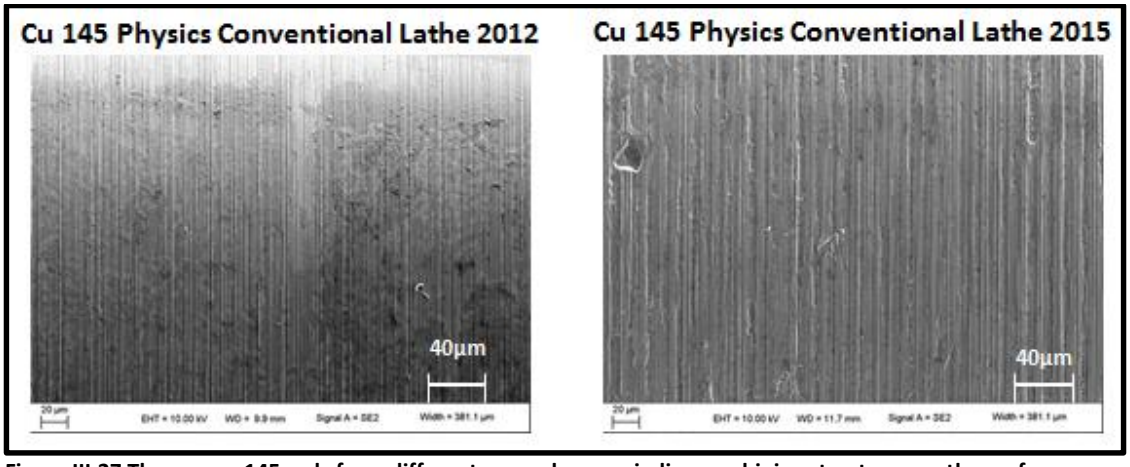

Figure III.27 The copper 145 rods from different years show perioding machining structures on the surface.

Figure III.28 shows the results of the EDS for the copper 145 with image "a" showing some white precipitates streaking left to right. The composition of these marks can be seen in image "e" with

the tellurium mapping (red). There are also carbon precipitates observed in the EDS (violet) with the oxygen well dispersed across the surface. There are several regions of the surface in the EDS image that have carbon in localized regions and have a pattern following the machining marks. The rods that have been fired have always had a black tarnish on the surface that was visible within a couple days of being machined on the lathe. Any surface showing signs of a green patina was several years old and was never shot on Zebra. For this reason, it is likely that the surface chemistry is dominated by a cuprous oxide layer. This is also in agreement with the EDS images in Figure III.28.

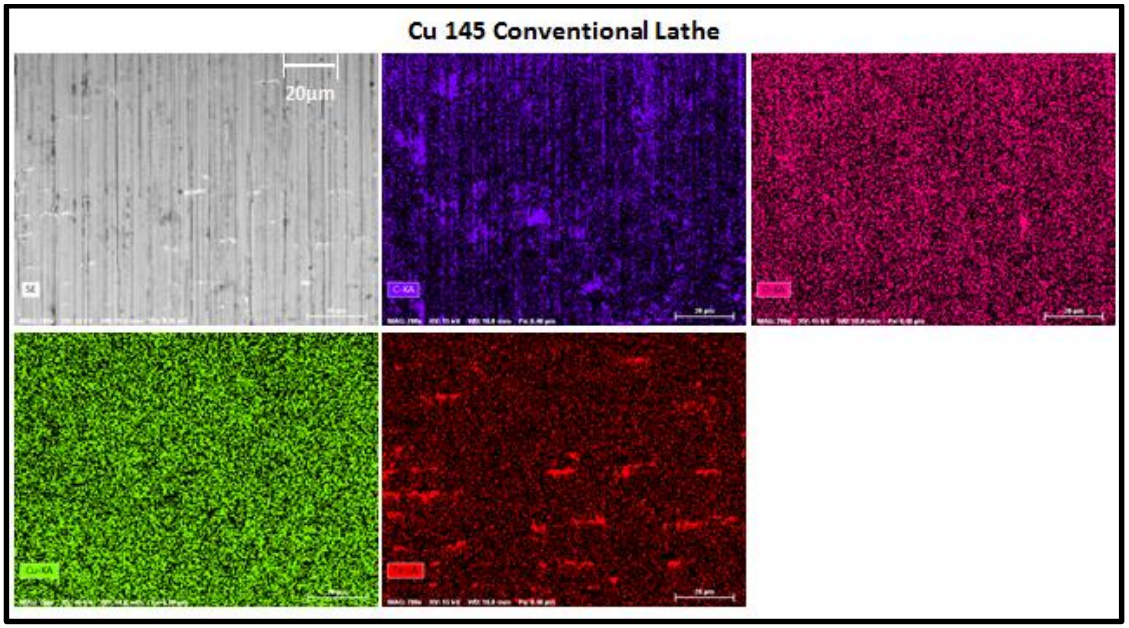

Figure III.28 Electron Dispersion Spectroscopy of the copper 145 rod shows the chemical makeup of the surface color coded for each element. Image "a" is the SEM image with subsequent images showing carbon (violet surface features), oxygen (pink surface features), copper (green surface features), tellurium (red surface features).

Figure III.29 shows the SEM images for copper 101 conventionally lathed and electropolished. The conventional lathe shows the common machining marks with the electropolished rod showing no machining marks, but surface inclusions throughout.

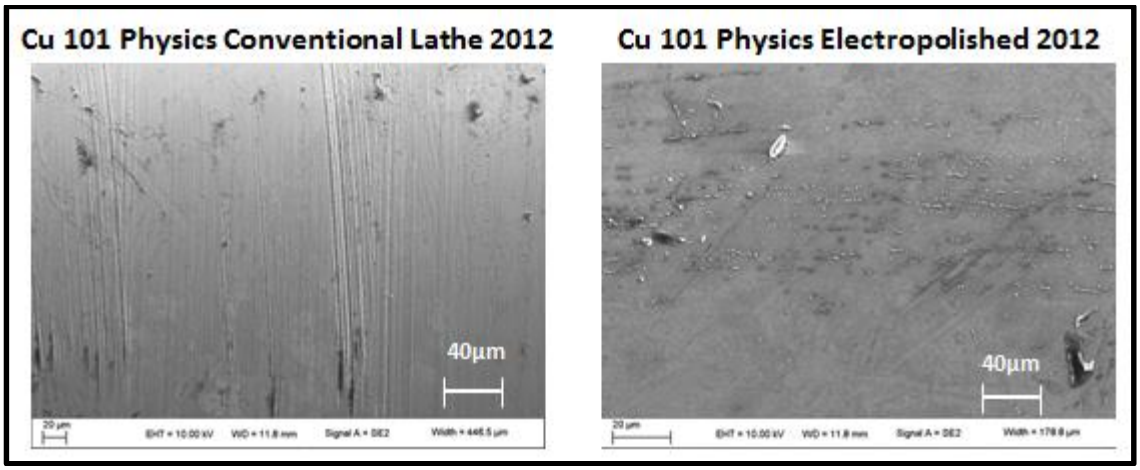

Figure III.29 Copper 101 conventional lathe (left) and electopolished (right). The conventionally lathed rods show machining marks while the electropolished has no machining marks, but shows some inclusions on the surface.

The EDS of the copper 101 electropolished rod shows precipitates of carbon and of chlorine. No tellurium streaks are observed in the copper 101 images.

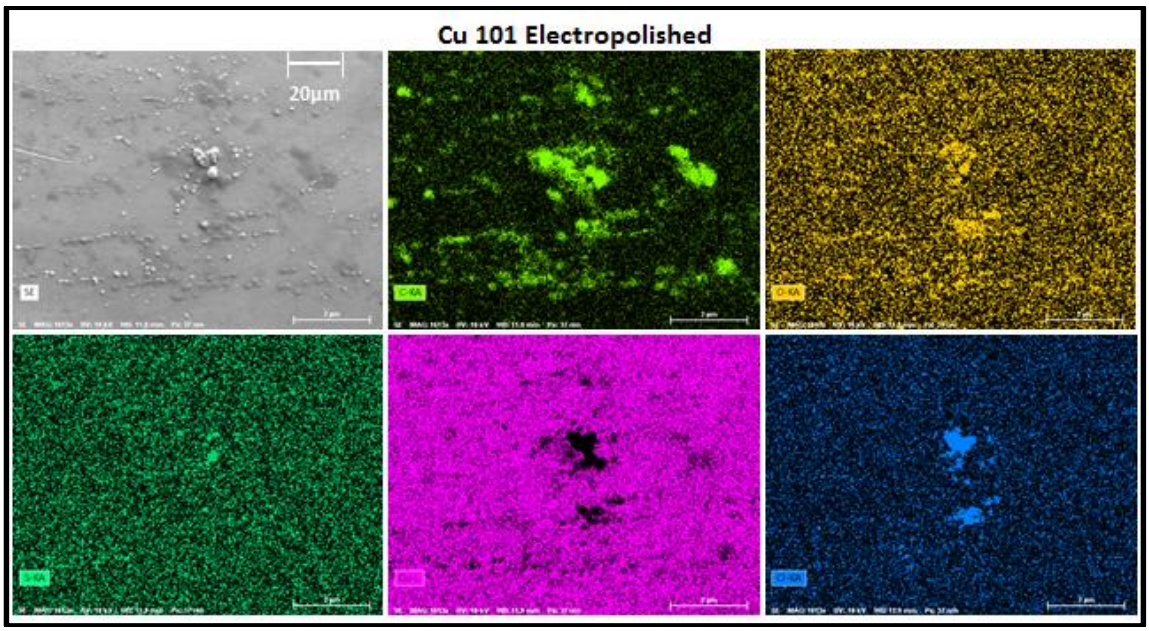

Figure III.30 Electron Dispersion Spectroscopy of the electropolished copper 101 rod shows the chemical makeup of the surface color coded for each element. Image "a" is the SEM image with subsequent images showing carbon (green surface features), oxygen (gold surface features), sulfur (dark green surface features), copper (pink surface features), and chlorine (blue surface features).

Some of the effects of surface finish and rod integrity have been observed by chance and systematic machining practices that leave surface artifacts for observation. Figure III.31 shows

ICCD images from multiple shots of 1.00 mm-diameter aluminum. Image “a” illustrates a failed shot where it is thought that there might have been some type of stress done to this load (several rods from this batch were bent from machining and poor handling) or perhaps a contact issue. The image shows very bright streaks of plasma light from the anode (top) and cathode (bottom) regions of the barbell. The cathode shows a bright non-uniform surface emission that could be a cascading effect of free electrons from a poor contact at the cathode. Shot 2850 shows a line of emission near the top of the ICCD image. This occurs near the edge of the barbell shape where it becomes more difficult for the cutter to make a smooth transition from the region of smaller radius to the region of larger radius. The rough machining marks left at these difficult points show up as early light emission in the ICCD but do not appear to have an effect on the evolution of the rest of the rod.

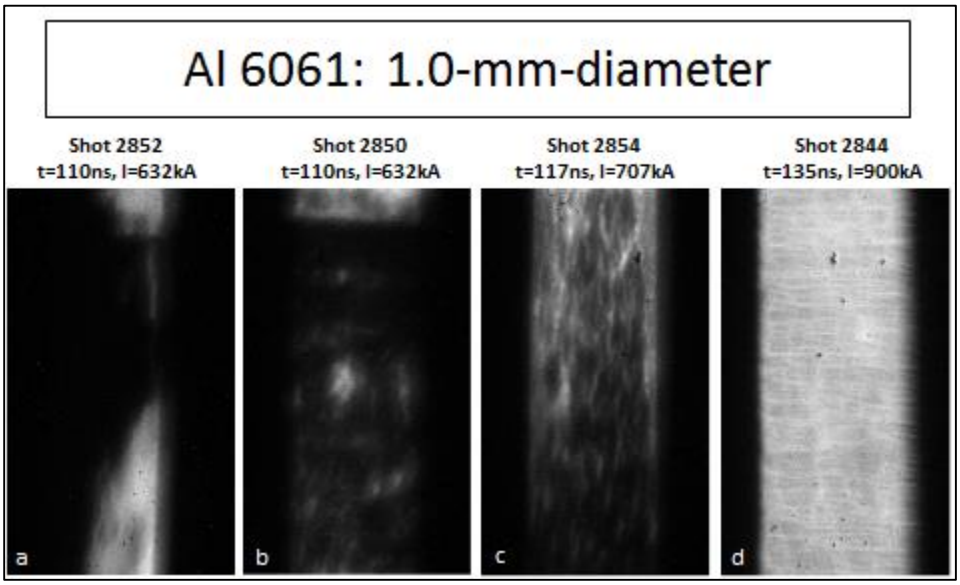

Figure III.31 The aluminum 6061 Andor ICCD images from MG VI illustrate similar surface evolution as was observed in the MG III & IV experiments indicating an ohmically heated surface. Image “a” is a shot that had poor contacts that caused an avalanche of electrons.

If a load behaves properly, the surface will first show signs of small spots of emission that evolve into filament-like features, and eventually evolve into a uniformly radiating surface. The other shots, images “b-d”, show this nice evolution from early non-uniform spots to a uniform surface

emission. With the ICCD images indicating an evolution of surface emission that is indicative of ohmically heating the rod, the experiment shifted to varying the load parameters.

To better understand the surface emissions, several rods of aluminum 6061 and copper 101 were electropolished. Figure III.32 shows the most illustrative results of the two surface finishes of copper 101. The electropolished (EP) rods, images “a” and “b”, have a uniform glow with several bright dots emitting across the surface. The non-electropolished (non-EP) rods, images “c” and “d”, show early (image “c”) and late time (image “d”) strata. This is not surprising from the SEM images of the EP and non-EP rods which showed machining marks on the non-EP rods similar to the glowing strata formation. Image “c” shows several dots, dots that are “widening” perpendicular to the current flow, and strata that is a fractional width and full width of the load diameter. The time gated image may only observe 2ns of the surface evolution, but the surface appears to show a larger time scale of the surface dynamics, with different parts of the surface being at different times in the evolution of phase. If this is correct, it suggests that the dots form strata that reach across the entire circumference of the rod. This is indicative of an electrothermal instability (ETI) as discussed in Chapter I. The strata observed in image “c” may seed the late time instabilities forming in image “d.” The absence of strata in the images of the rods with EP raise doubt in the strata being an ETI effect. The images in “a” and “b” show bright dots that show no signs of forming strata or growing in the direction perpendicular to the current flow. If ETI is driving the non-uniform emission in the EP surface, it would be expected that these bright dots would form strata.

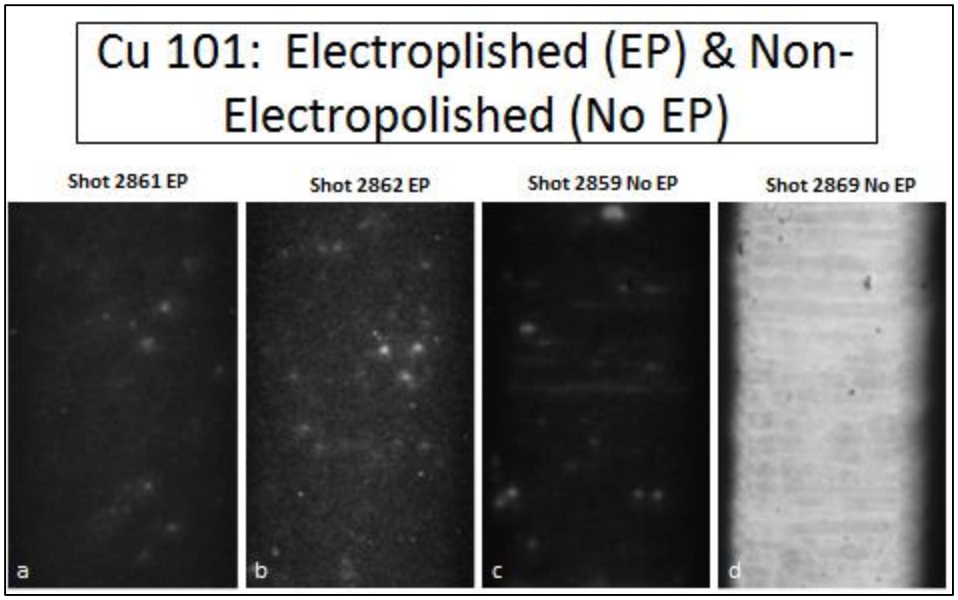

Figure III.32 Electropolished Cu 101 (images "a" and "b") show no signs of strata forming, only bright dots and a glowing background. The non-electropolished Cu 101 (images "c" and "d") show strata forming early in time ("c") and late time ("d"), possibly leading to the formation of late time MRT formation.

Figure III.33 show results for the EP and non-EP aluminum 6061 rods. Image "a" (EP surface) shows a glowing surface with a few bright dots beginning to form. The streak of light at the bottom right of the image is from a bulb that was flashing next to the camera at 60Hz and entered the optical path during the Zebra shot. The little bright dots that are spread all over the image are hard photons (likely x-rays) produced by the Zebra machine. Image "b" (EP surface) has surface filaments forming. Neither image of the EP surface rods shows signs of strata formation. The filamentation is likely ETI, with the formation of plasma leading to a reverse in the sign of the change in resistivity with respect to temperature. When plasma forms, the resistivity goes down with increasing temperature, leading to the formation of filaments in the direction of the current flow as discussed in Chapter I. The non-EP surfaces shown in images "c" and "d" both show signs of strata similar to the early and late time strata observed with the copper 101. With only a few shots with aluminum 6061 and copper 101, it appears evident that the electropolishing removes the observable strata from the surface emission due to the removal of much of the machining grooves as was shown by the SEM images.

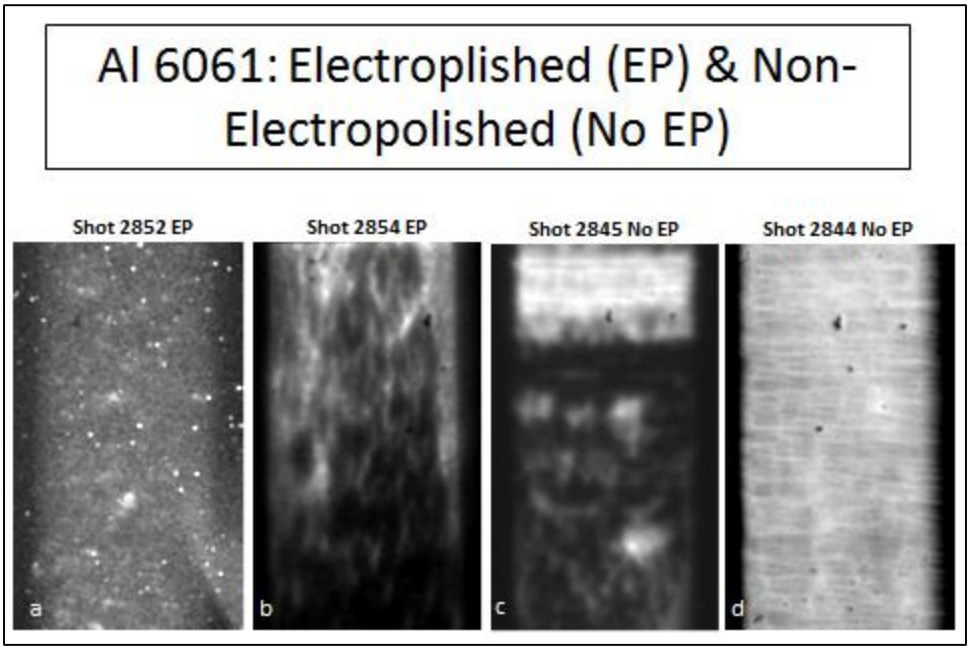

Figure III.33 Electropolished Al 6061 (images "a" and "b") show no signs of strata forming, only bright dots with a glowing background filaments forming in the direction of current flow. The non-electropolished Al 6061 (images "c" and "d") show strata forming early in time ("c") and late time ("d"), possibly leading to the formation of late time MRT formation.

Load material variation

The aluminum loads in multiple campaigns have given evidence to a surface magnetic field threshold for plasma formation to be approximately 2.2 MG. There were multiple questions about the observations and whether or not they were truly representative of aluminum or if the aluminum oxide was playing a significant role in the process. Some of these questions are as follows:

1. Was the aluminum oxide contributing to the ability for the metal surface to hold off non-thermal plasma formation by insulating the underlying metal?
2. What effect does the aluminum oxide have on the early visible light emission, i.e. do the early spots followed by filaments and then uniform emission depend on the oxide layer?

3. What effect will changing metals have on the behavior of the anode/cathode contacts?

We can begin to answer some of these questions by simply changing the metal. Copper was chosen for the MG-VI experiment for multiple reasons. First, there were simulations done by Garanin as to if and when plasma would form on the surface of a copper metal pulsed by megagauss magnetic fields. Garnain's simulations predicted that copper would form plasma for an instantaneous switching of the surface magnetic field at a threshold of ~1.6 MG. For a smooth increase of surface magnetic field at a rate of 5 MG/μs, the threshold for plasma formation was calculated to be ~3.0 MG. Copper is also relevant to experiments that have been and continue to be conducted at Sandia National Laboratory. Questions remain as to the expansion rate, time of plasma formation, and the effect electrothermal instabilities have on the late time magneto-Raleigh-Taylor instabilities.

The evolution of surface emission on aluminum 6061 was well documented in MG IV by Awe. The early bright spots observed evolved into filaments and eventually into a uniform surface emission. The uniqueness of this effect to aluminum is an important theory to justify or to discredit. The aluminum oxide could be playing a key role in the surface emission with a thin layer forming on the surface of aluminum when placed in air. The thin layer protects the aluminum from further oxidation. This passivation of aluminum can be increased through a process of anodizing. Anodizing is an electrolytic process used to increase the thickness of the oxide layer of metals. This was not done on our loads but has been contemplated for future experiments. Aluminum oxide is also an electric insulator and acts like a ceramic when it is heated such that it maintains its material strength. An early concern was that the oxide was protecting the aluminum surface in a way that a coating of oil will protect thin wires from initiating early plasma

formation[101]. It was also thought that the early non-uniform emission could be a result of the oxide layer. To study the effect the oxide has on the surface of aluminum when pulsed to high temperatures, other metals with different oxide properties could be tested. One of these metals tested was copper. The effect the copper oxide has on the evolution of the surface is likely to be negligible. The reason for this is because unlike aluminum oxide, the copper oxide is not a ceramic and will not strengthen as it begins to heat. Copper oxide is a semiconductor, meaning that as the temperature increases the conductivity increases. It is not understood what effect, if any, this oxide layer will have on the surface of the metal, but if oxide layers are to have an effect, it is thought that aluminum oxide and copper oxide would act differently.

The copper alloy chosen for MG VI was copper 101. Copper 101 is commonly known as oxygen free highly conductive (OFHC) copper. It is 99.99% pure copper. The diameters used for the experiment were 1.00-, 0.8- and 0.7-mm. A smaller diameter of 0.5-mm was attempted but it was only possible by making a double barbell shape. This type of rod was only shot once because it was difficult to machine and the effects of the double barbell shape was not understood at the time. Images from the ICCD of the 1.0-, 0.8-, and 0.7-mm-diameter loads are shown in Figures III.34-III.36.

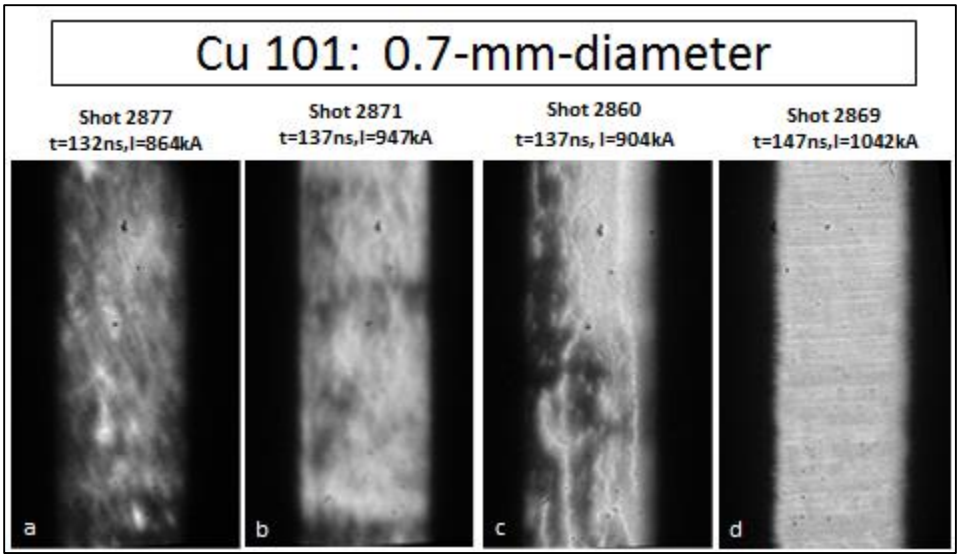

Figure III.34 Surface emission of copper 101 0.7-mm-diameter rods captured in MG VI with the Andor ICCD show qualitative similarities with aluminum 6061. Early non-uniform surface emission evolves into uniform emission with late time strata and formation of surface instabilities. Images "a" and "b" appear slightly out of focus, likely due to the rod shifting out of focus during vacuum pump down of the Zebra chamber.

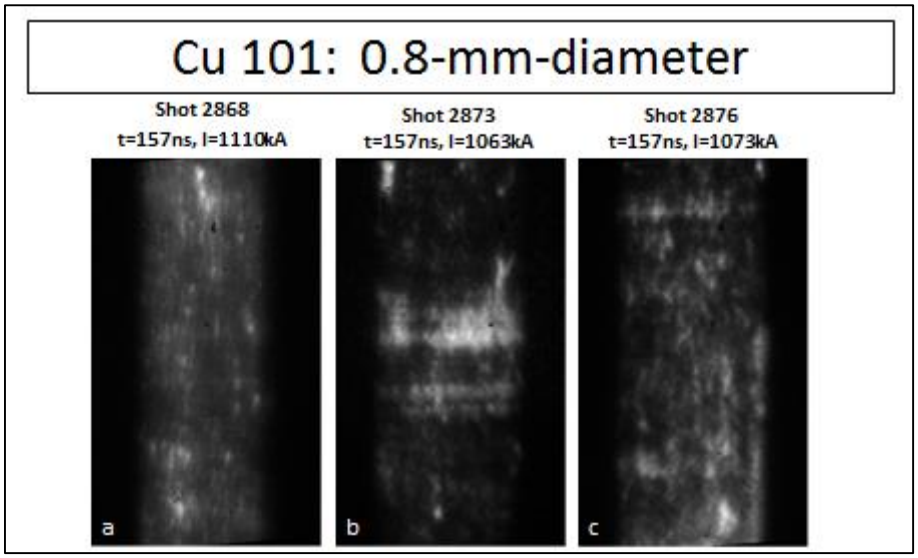

Figure III.35 Surface emission of copper 101 0.8-mm-diameter rods captured in MG VI with the Andor ICCD show early dots that appear to be forming filament. The strata-like structure in image "b" is likely a machining artifact, as has been observed in previous experiments.

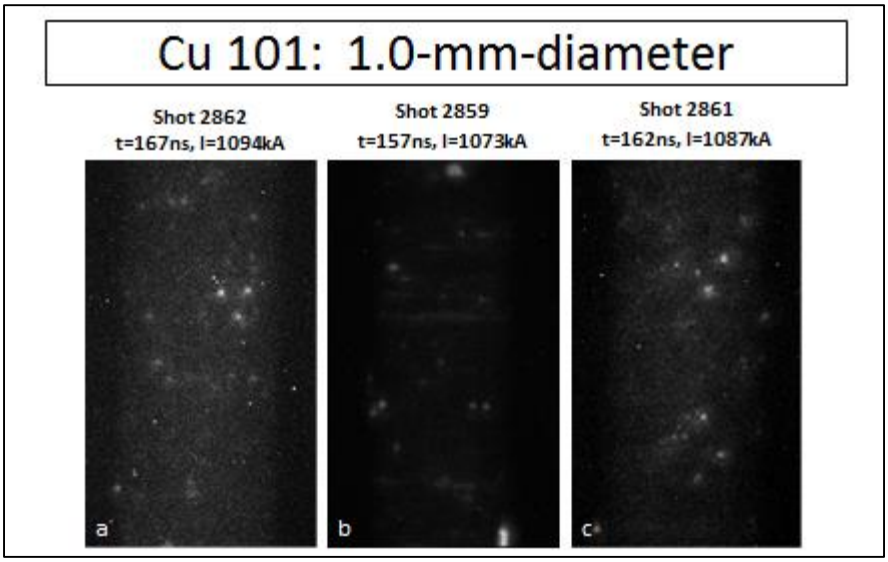

Figure III.36 Surface emission of copper 101 1.0-mm-diameter rods captured in MG VI with the Andor ICCD show early dots that appear with no signs of filamentation. The strata can be seen beginning to glow in image "b" which is likely due to machine marks, but also has a possibility of being the formation of ETI.

The 0.7-mm copper loads show clear signs of filamentation with emission becoming uniform before peak current. Images in Figure III.34 from shots 2877, image "a", and 2871, image "b", appear to have poor resolution quality but are still sufficient enough to indicate filamentation. Shot 2871 appears to be in the late stages of filamenation and is approaching a more uniform emission. The number of copper shots was limited but sufficient to conclude that the copper surface acts similar to the aluminum surface in terms of non-uniform surface emission evolving into filaments, followed by a uniform surface emission. Shot 2869, image "d", has surface instabilities forming, with a strata-like surface emission that is similar to what has been observed with aluminum 6061. The 0.8-mm copper loads show surface emission from dots that appear to be forming filaments in shot 2876 (image "c"). The image in Figure III.35 from shot 2873 shows early emission from a machining artifact similar to what has been seen with aluminum. The 1.0-mm copper loads never formed uniform surface plasma, however, early bright spots are observed

on all 1.0-mm-diameter rods. In image “b” of Figure III.36 there are dim structure of strata appearing that look like they could be from machining structures left behind by the lathe.

The optical design for the single frame ICCD’s was improved for the MG IX experiment. The light collection was greater with a light collection of f#/4 compared to previous f#/10, with the resolution improving to ~2 to 5 μm compared to ~40 μm previously. The results for the high resolution images of copper 101 are shown in Figure III.37. Shot 3752 shows an interesting glow with a few bright dots just beginning to appear on the surface. Shot 3757 shows dots that appear to be forming strata, perhaps electrothermal instabilities, with the later image having already evolved to filaments that have nearly become uniform. Shot 3765 clearly had an optical element bumped prior to the shot, with the edge of the load being visible and the load being shifted to one side. The image quality looks poor with the surface showing signs of strata forming filaments. Shot 3762 has nice image quality, but show large machining artifacts in the center of the image. There are some highly resolved strata above the large machining strata that look like spots forming strata, similar to what is observed in shot 3757.

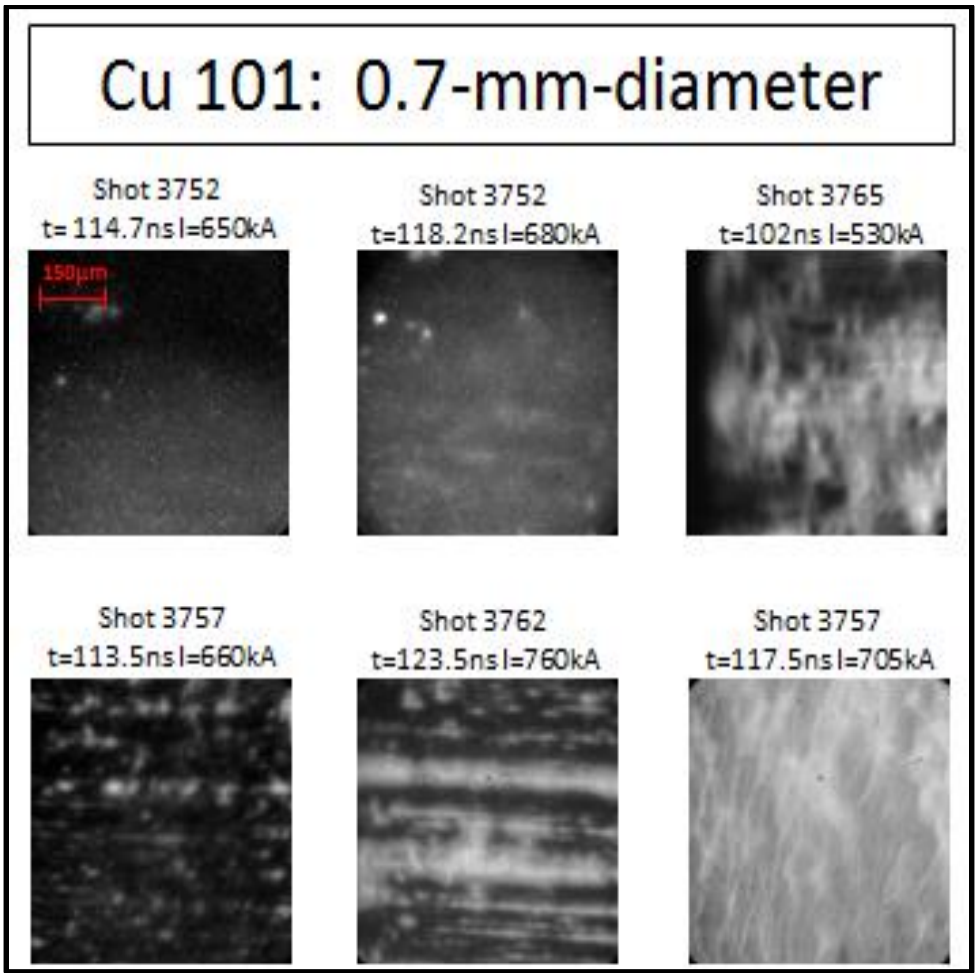

Figure III.37 High resolution images of copper 101 during the MG IX experiment using the LDM and two Andor ICCD cameras produced images with a 600µm field of view. Early images observed a glowing rod with dots that form strata and evolve into filaments.

The results for the high resolution images of copper 145 are shown in Figure III.38. Shot 3777 shows a non-uniform glow in the first image at 90.3ns with dots and clear strata formations observed 3ns later. Shot 3776 shows a large number of strata forming with no signs of dots and no indication of filamentation forming. Shot 3775 shows the strata forming filaments, with the later image of this shot showing the filamentation dominating the surface emission with a few areas of the image showing remnants of the strata. Shot 3751 shows what would appear to be a midpoint in the evolution of the surface between the formation of surface strata and the dominance of surface filamentation.

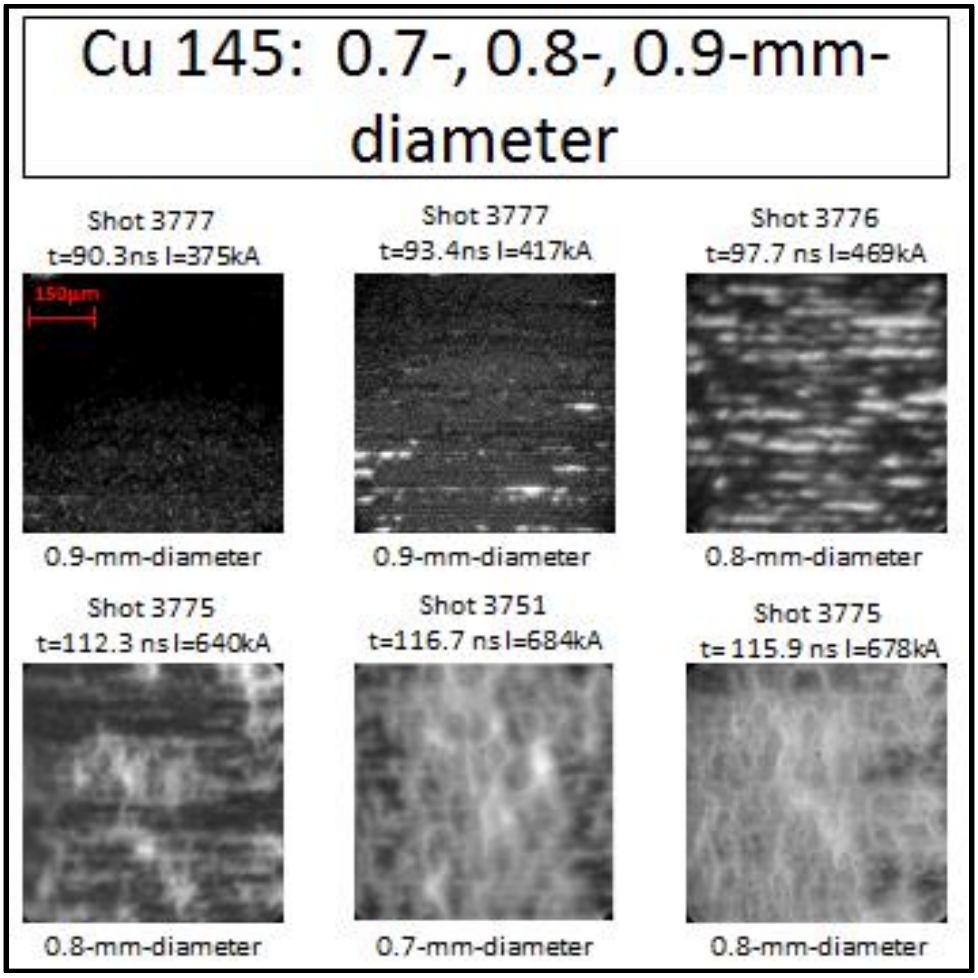

Figure III.38 Copper 145 images captured during the MG IX experiment using the LDM and two Andor ICCD cameras show strata that form filaments that become more uniform in time.

There was one shot taken of nickel 200 and titanium II in MG IX with the results of the high resolution imaging shown in Figures III.39 and III.40. The nickel images show a few dots, some remnants of strata, and large filaments. The filaments in the left image of the nickel shot appear to be larger than anything observed with the copper 101 or copper 145 images. This could be for more than one reason. If the resolution was poor on this shot, it could make the filaments look broader and also make several filaments look like one. There is also the possibility that when filaments first form, they are quickly pinched by the local $J \times B$ force, leading to smaller filaments. The nickel image could be capturing this small moment in time when the filaments are still large and have not been pinched down to a smaller size. The later image of the nickel surface shows uniform emission and what appears to be an image out of focus. This is likely due to the rod surface expanding enough to greatly reduce the resolution. Despite the possibility of poor resolution, the image still shows signs of MRT instabilities forming with large wavelength strata. It is interesting to note the dramatic difference between these two images with only ~4ns between them.

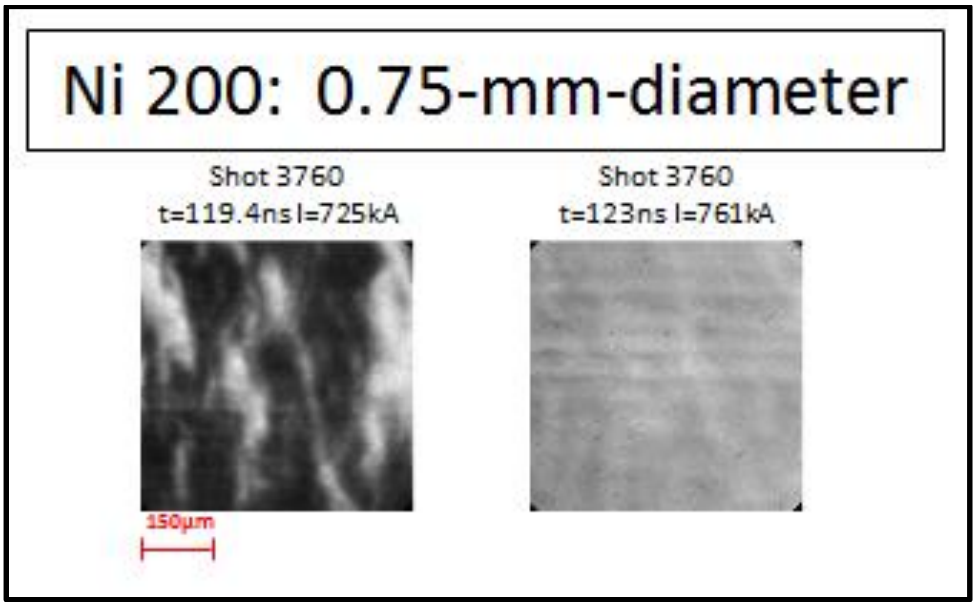

Figure III.39 The only nickel 200 shot on MG IX using the LDM and two Andor ICCD cameras show early filamentation with signs of small strata and a few dots that appear to be beginning to filament. The late time images shows a uniform surface with strata, indicating the late time MRT devolpment.

The titanium II results show less structure than the copper and nickel images. The first image of titanium has some structure that looks like it is in the late stages of filamentation and nearing a uniform surface emission. The second titanium image shows a uniform surface emission with a few areas of the images showing signs of strata that are likely to be late time MRT instability growth. Similar to the comments made about the nickel images above, the resolution has likely degraded due to expansion of the rod. With such a small amount of data for nickel and titanium, it is hard to develop a theory for why the images look different. This will be discussed again in chapter VII along with the results of the other diagnostics.

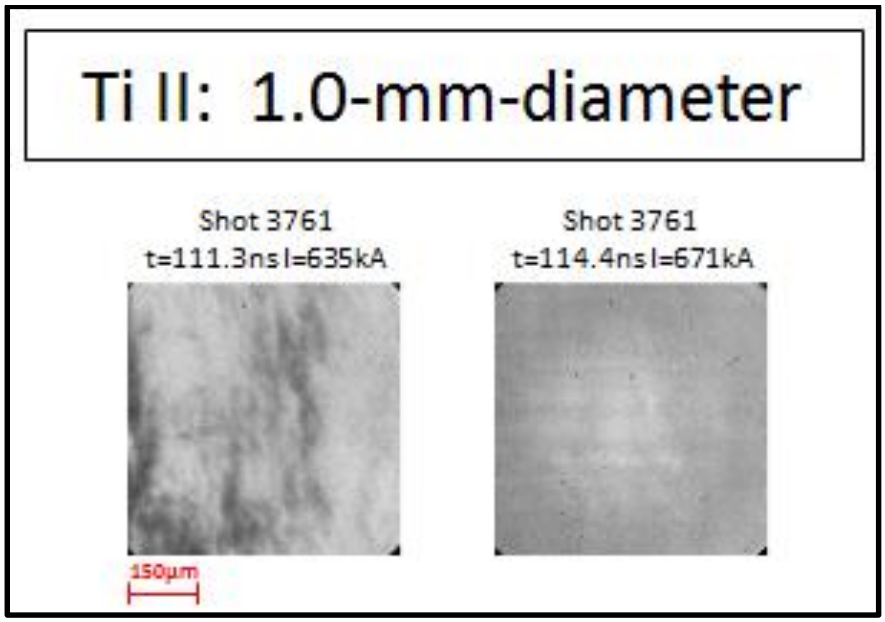

Figure III.40 The only titanium II shot on MG IX using the LDM and two Andor ICCD cameras show early non-uniform surface emission which may be late time filamentation that is out of focus due to expansion and nearly "filled in" on the surface. The late image show uniform surface emission with signs of strata indicating late time MRT development.

The evolution in time of dots to filaments to uniform surface emission is reproducible to within 10ns for copper and aluminum alloys for both EP and non-EP surfaces. The exception to this statement are those shots that have been concluded to have had a failure in the anode and cathode contacts. The reproducible timing suggests this effect is more likely to be caused by Joule heating of the surface metal (or inclusions) and not a result of electric field ionization or dominated by the surface oxide layer. This hypothesis is more evident by the shift in the timing of the surface emission features with change in the initial rod radius. There is a uniform glow that is observed on the copper and aluminum alloys that is believed to be the vapor or melted metal surface. This glow does not show the same non-uniform structure of the dots and filaments, with the intensity of the glow becoming less at a given current magnitude with an increase in the initial rod radius. If these observed effects were driven by electric field emission, it is predicted that electropolishing would have an observable effect by removing and reducing the "sharp" points on

the surface of the rod as well as removing and reducing the amount of surface oxide on the rod. No such effect have been observed.

12-Frame Hadland ICCD Camera

The single frame ICCD images of the surface emission of the rods hold tremendous value, however, without the ability to perform a lot of shots, understanding the evolution from the surface is difficult. Fielding the 12-frame Hadland camera in MG VI and the 16-frame SIMX camera in MG IX were done in the hope of better understanding the evolution and development of surface emissions. The Hadland camera in MG VI provided some useful images early in the experimental campaign. Figure III.41 shows the images from an aluminum 6061 rod with the images gated for 5ns and 0ns between the end of one frame and the beginning of the next. The gating was not changed during the experiment, however, the output pulse did not work properly, so the time with respect to current is not known for the images. Images “a-d” show a non-uniformly radiating surface becoming more uniform, with a machining artifact showing early brightness. The bright ring in image “a” can be followed through the images and shows surface instabilities forming there first.

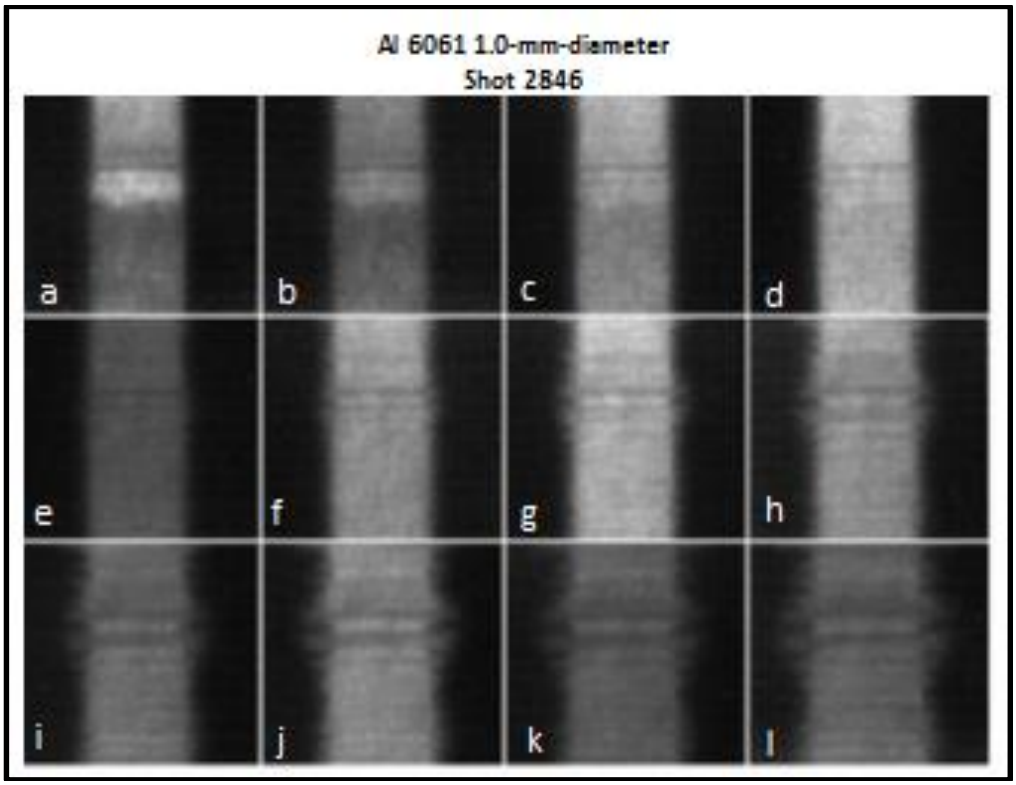

Figure III.41 The 12-frame Hadland ICCD camera fielded on MG VI shows the evolution of the surface of an Al 6061 rod. The early non-uniform surface emission is observed to initiate at what appear to be a machining artifact and evolve into early MRT development. The resolution was not sufficient to observe the fine surface structures.

Figure III.42 shows the results of shot 2852, the same aluminum shot that showed a failure in the rod in Figure III.31 with the single frame ICCD. The 12-frame camera shows the rod lighting up non-uniformly, with the surface becoming uniform and forming late time surface instabilities. These images suggests that it takes at least 15 to 20 ns for a rod that breaks down early due to a failure to evolve into a uniform surface emission.

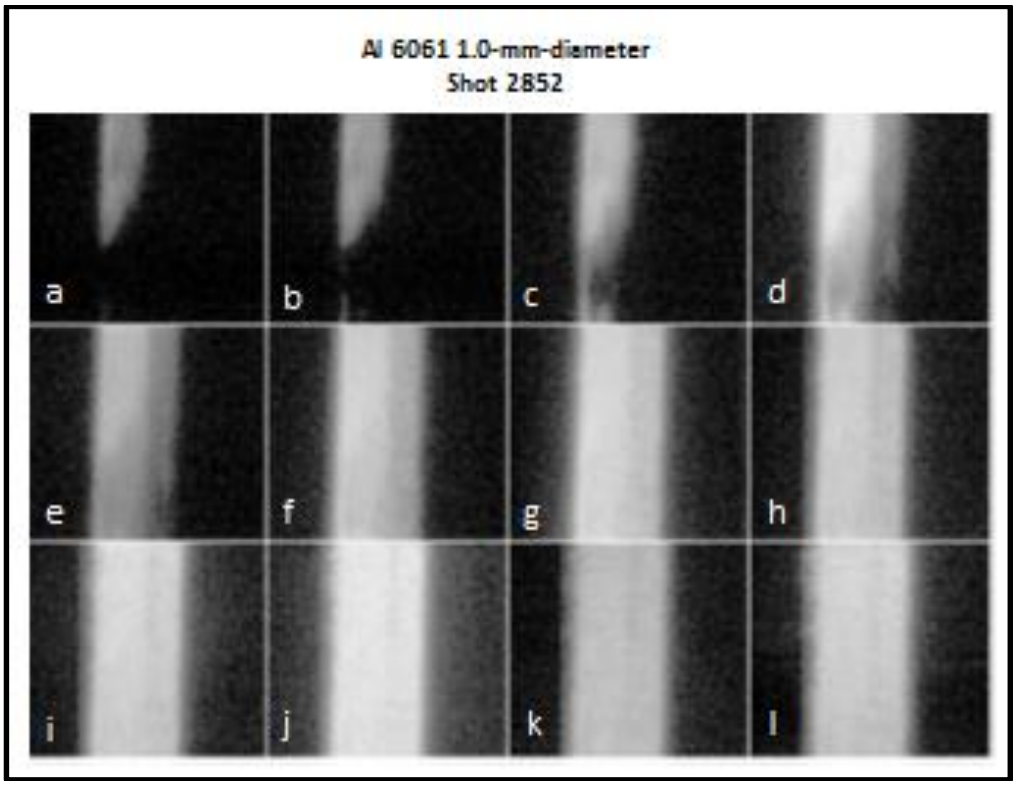

Figure III.42 The 12-frame Hadland camera was useful in determining load hardware performance, with Shot 2852 failing at the contacts. This failure is likely due to using refurbished anode and cathode hardware, provide poor contacts that lead to electron avalanche from the cathode.

The results for two copper 101 shots are shown in Figures III.43 and III.44 with shot 2860 observing non-uniform emission early in time that fills in and becomes uniform. This shot performed well, as was also shown by the single frame ICCD in Figure III.34. Figure III.44 shows the failure of a copper rod with shot 2874 have a cascading of emission down one side of the rod. This shot captured images before the surface breakdown, allowing for the time it takes a failed rod to become uniform. With 5 ns gating, the images show a time of 15 to 20 ns to go from early breakdown to uniform surface emission. This is similar to the time scales that have been observed for rods that behave well at the same diameter.

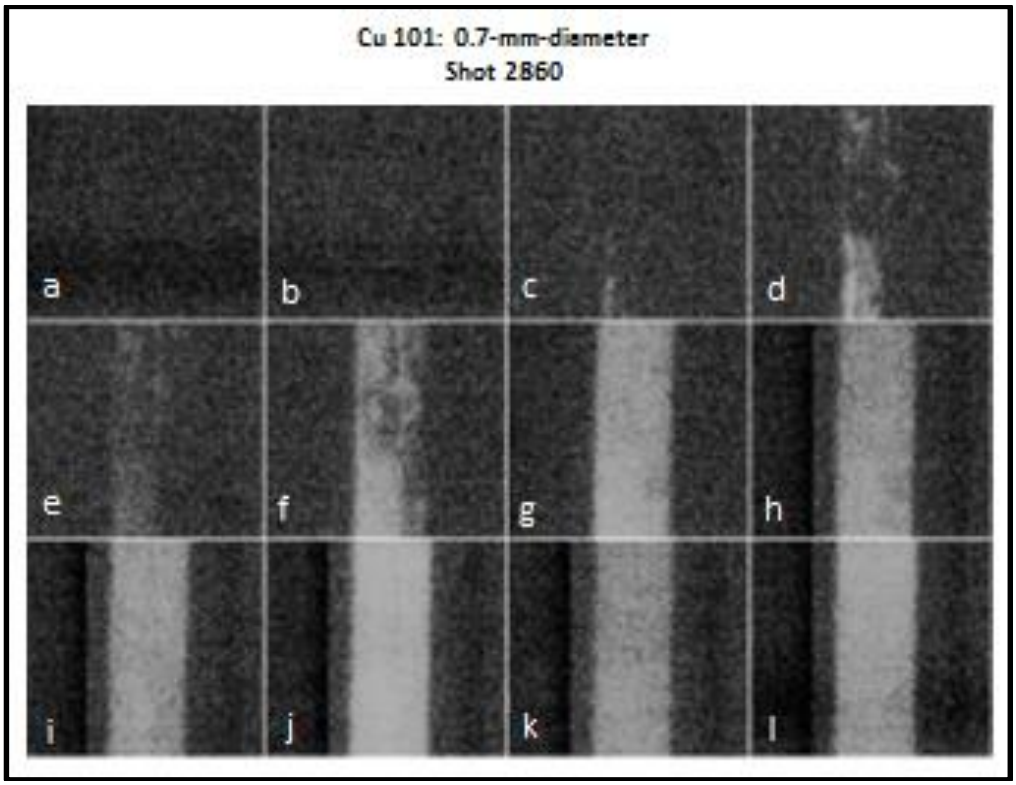

Figure III.43 The 12-frame Hadland camera showed an evolution from early non-uniform emission to uniform surface emission on the copper 101 0.7-mm-diameter rod. The camera did not provide high resolution images, but still provided qualitative information of performance on the copper 101 rod.

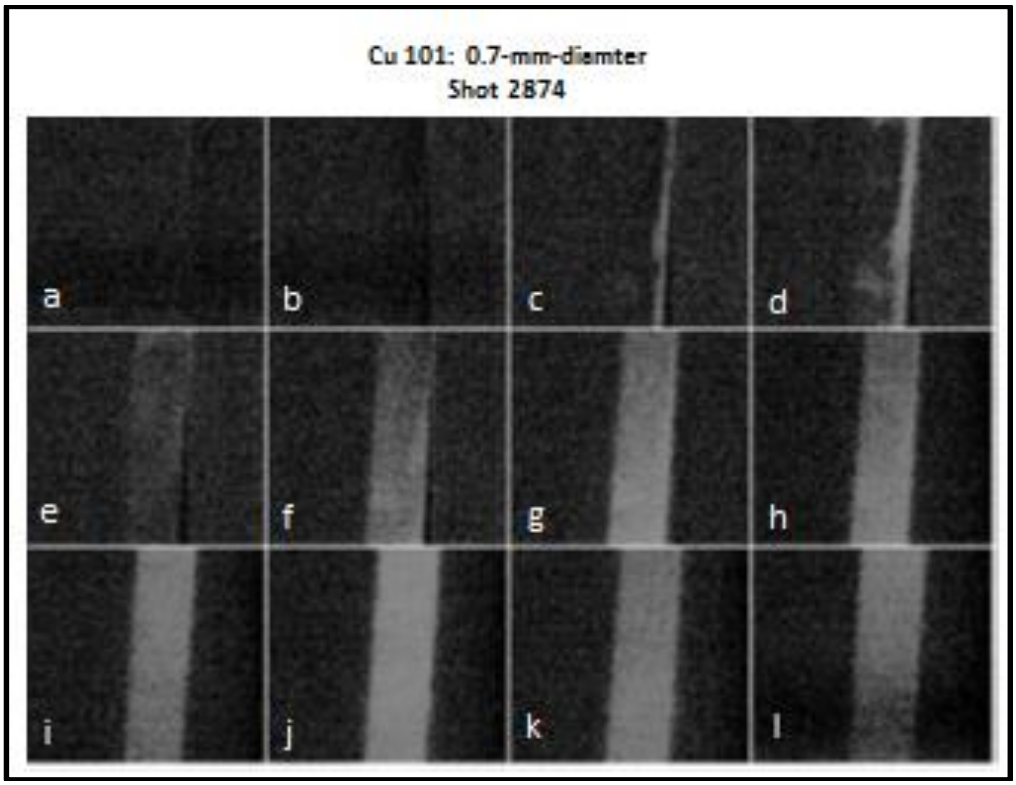

Figure III.44 Shot 2874 illustrate the usefulness of the 12-frame Hadland camera in observing hardware performance of copper 101. It is believed that this rod was not cleaned properly, leading to a flashover along the one side of the load.

16-Frame SIMX ICCD Camera

The 16-frame SIMX camera fielded in MG IX provided much better results. There was a timing issue with this camera as well, with the camera not triggering when expected. This will be discussed in more detail in Chapter V. The images below are gated for 4ns with 0ns between the end of one frame and the beginning of the next. The figures below do not show all 16 images for each shot. Only the images that observed light emission were included in the figures. Figure III.45 shows the results for aluminum 6061 that has been electropolished. Image "a" shows several dots that can be followed through the images with two dots filamenting together in image "b" and many filaments forming in the next few images. Each image was gated for 4ns. The timing

on the shots are not well known because there was a problem with the camera triggering when it was intended. There was also a malfunction in the cameras output trigger pulse that would give us the timing of each image. This will be discussed more in chapter V. It is interesting to note that no strata are observed in the imaging except for some strata-like structures that appear to be forming by image "g".

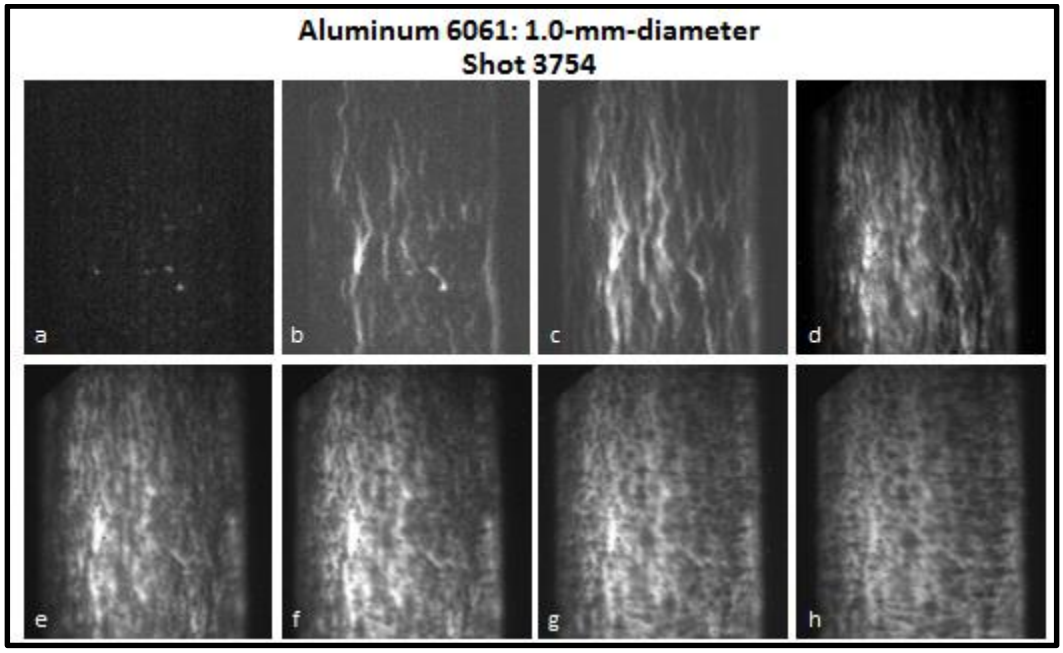

Figure III.45 The 16-frame SIMX ICCD camera fielded in MG IX provide high resolution images. The Al 6061 rod shows the surface dots early in time filament together and evolve in time to a more uniform surface. Image "a" show two early dots (bottom right) that filament together in image "b".

Figure III.46 shows the images from copper 101. Images "a-c" show a non-uniformly emitting surface with dots and strata forming on the surface. By image "d" the surface is uniformly radiating with instabilities beginning to form. Strata is observed on most of the images, with several images showing surface instabilities. The early images appear to be out of focus, with the dots and strata looking blurred. No filaments are observed, however, the resolution may be the cause of this or what appears to be a sudden jump in time between images "c" and "d", going from low emission with strata to uniform emission and small instability growth.

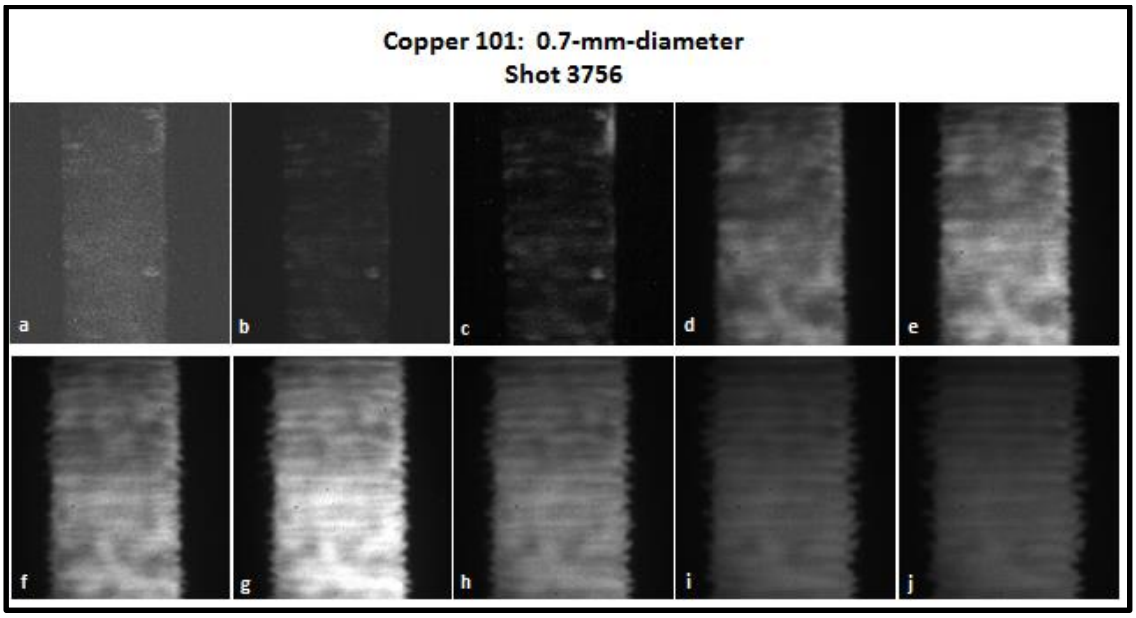

Figure III.46 The 16-frame SIMX ICCD camera in MG IX experiment shows the evolution of the copper 101 surface. Early dots form with strata developing. Late time MRT can be seen developing and evolving from image "d" through image "j". The resolution of this shot is poor compared to the aluminum data from shot 3754.

Figure III.47 shows the results for the copper 145 images. Early spots and strata can be seen in images "a-d" with the dots and strata forming filaments up the left side of the rod. A very nice evolution is captured with these first few images with late time strata and the initial formation of surface instabilities is nicely resolved in the later images.

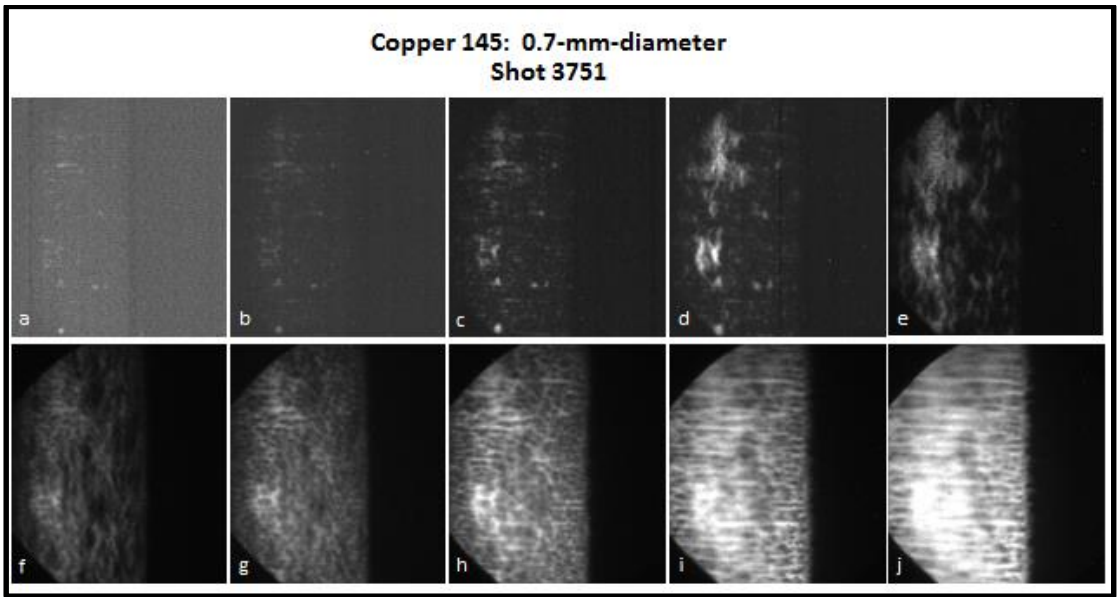

Figure III.47 The SIMX images of the copper 145 shot was highly resolved with early dots being observed on several images. The early dots are seen to evolve into filament that grow and become more uniform. The surface forms late time strata with images "i" and "j" showing the development of late time MRT.

Figure III.48 shows the results for the nickel 200 images. The first few images show a glowing rod with no signs of dots or strata appearing on the surface. By image "c" the surface has quickly begun to radiate over much of the surface area. The surface emission is non-uniform, however, the resolution on this shot appears poor so the dots and strata are likely blurred out. It is clear that there appears to be structure similar to the dots observed with copper and aluminum, with image "c" and "d" possibly having the dots begin to filament. Strata and the formation of surface instabilities can be observed in images "f-g". It is interesting to note that the resolution appears to be better in image "i" and "j".

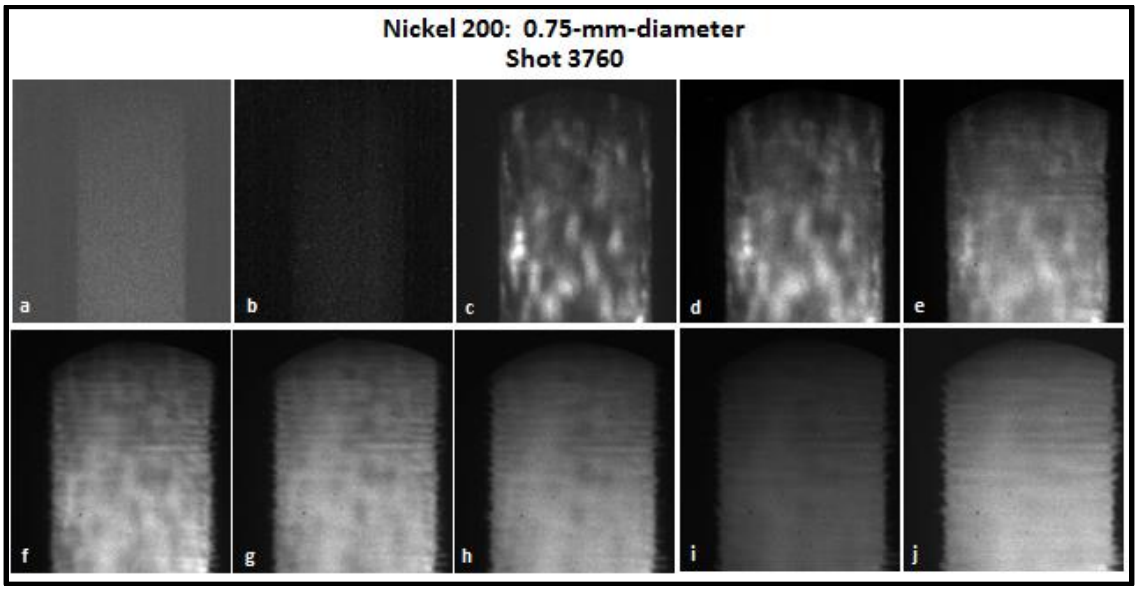

Figure III.48 The SIMX images of the nickel 200 shot show an early glowing load that forms a non-uniform surface emission that quickly evolves into a uniform surface emission. Images "f" through "j" show surface instabilities developing. The image resolution on this shot is poor compared to previous shots.

Figure III.49 shows the results for the titanium images. The first image of titanium shows a glowing rod with a couple small glowing dots with the bright spot in the bottom right corner appearing to be the beginning of a filament. All other images show the rod already uniformly radiating with instabilities forming and expanding outward. Without many early images of the titanium and the single frame images being so late, it is difficult to come to any conclusion about the surface emission of titanium compared to aluminum, copper, and nickel.

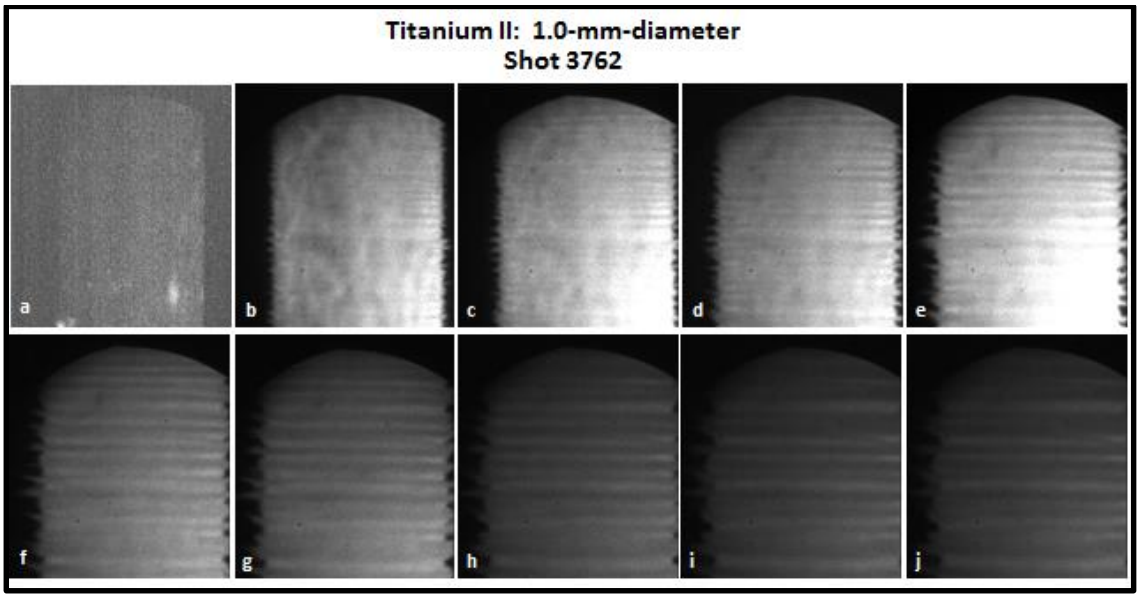

Figure III.49 The SIMX images of titanium II show one an image of a glowing load with a few dots forming and a possible filament forming in image "a". All proceeding images show surface instabilities forming and expanding.

Photodiode Array (PDA)

The PDA also shows signs of nice uniform emission from different parts of the varying loads, indicative of load hardware behaving properly. Figures III.50 to III.54 plot the array elements that are not covered by the ND filter and are therefore much more sensitive to early detection of light. The two shots in Figure III.50 show the effects of an aluminum 6061 shot that does not perform well (left plot) and one that performs well (right plot). The poor shot has a spread in the diode element signals of about 12 ns while the rod that performed well had a spread of about 2 ns. The ICCD images (not shown here) show a similar result with the surface emission. The leading theory for the cause of some shots of aluminum having poor results is that the anode and cathode pieces were not new, but were instead refurbished metal hardware from a previous experimental campaign. As stated earlier in this chapter, the refurbished hardware machines the used pieces and bores out the hole for the rod to fit into that has been filled in by a shot rod. This

provide poor contacts for the next rod by not having as clean of a surface on a re-bored hole. A thorough study of this effect was not performed, however, it is best to avoid this in the future to reduce the possible negative effect on the experimental results.

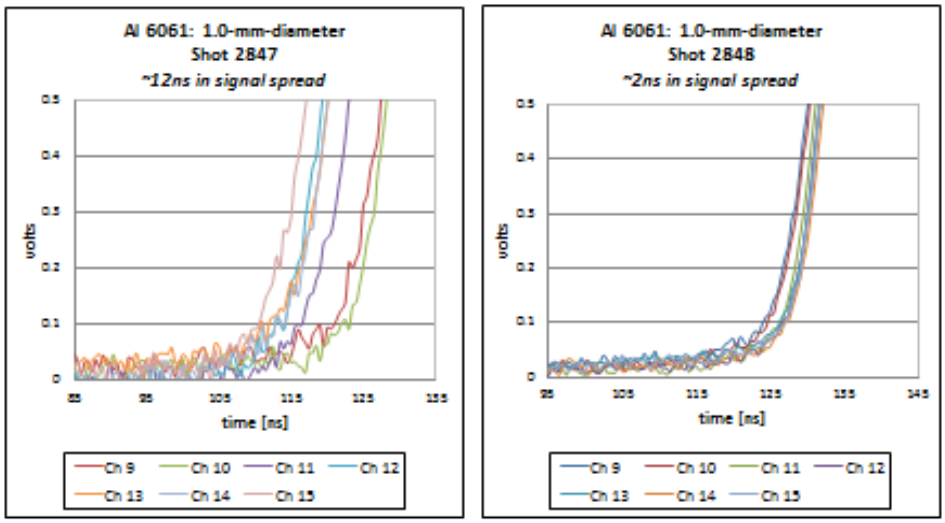

Figure III.50 The diode array show a spread in signal when the load hardware does not perform well (left image) and shows a small spread in diode signal when the load hardware performs well (right image).

The results of several copper 101 and 145 shots are shown in Figures III.51 and III.52. The left plot shows the worst spread in data from all the experiments with the right plot showing a result that was more common. The copper shots performed well as a whole, with none of the shots having a spread that reached 10 ns. Only two shots of nickel 200 were performed, with both results shown in Figure III.53. Both shots performed well with the two shots having different filtering placed in front of the diode array. This filtering effect will be discussed in detail in chapter IV. The results for titanium II are shown in Figure III.53 and indicate well-performed load hardware with the maximum spread reaching only 4 ns.

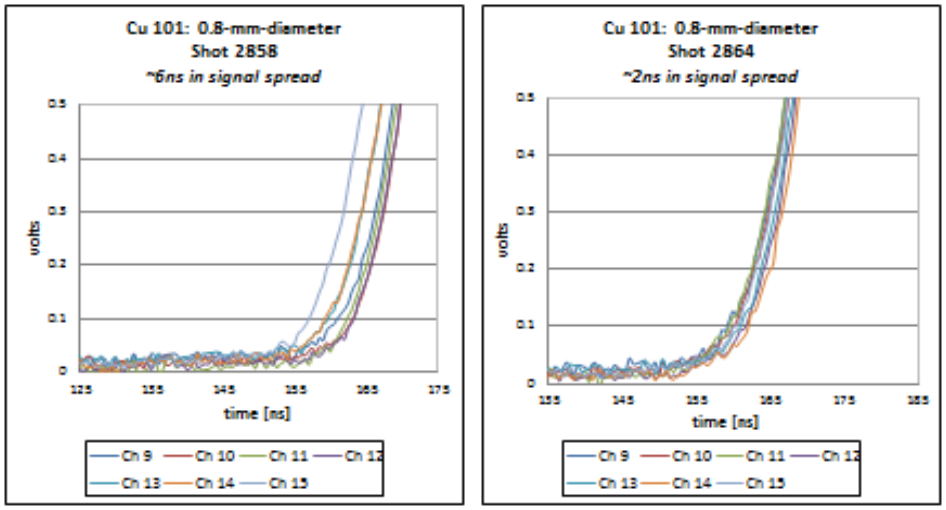

Figure III.51 Only two shots of copper 101 had a spread of ~6ns in diode signal, with most other shots having a spread of ~2ns.

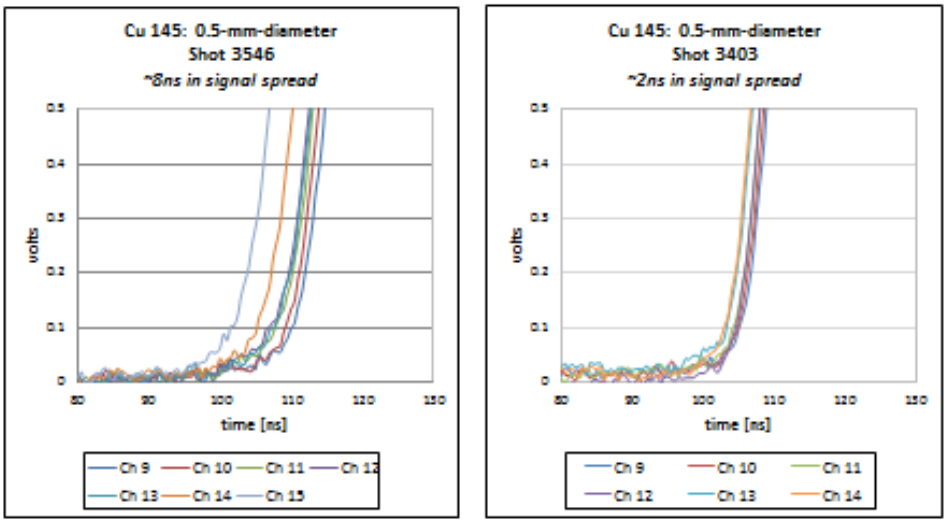

Figure III.52 Only one shot of copper 145 had a spread of ~8ns in diode signal, with most other shots having a spread of ~2ns.

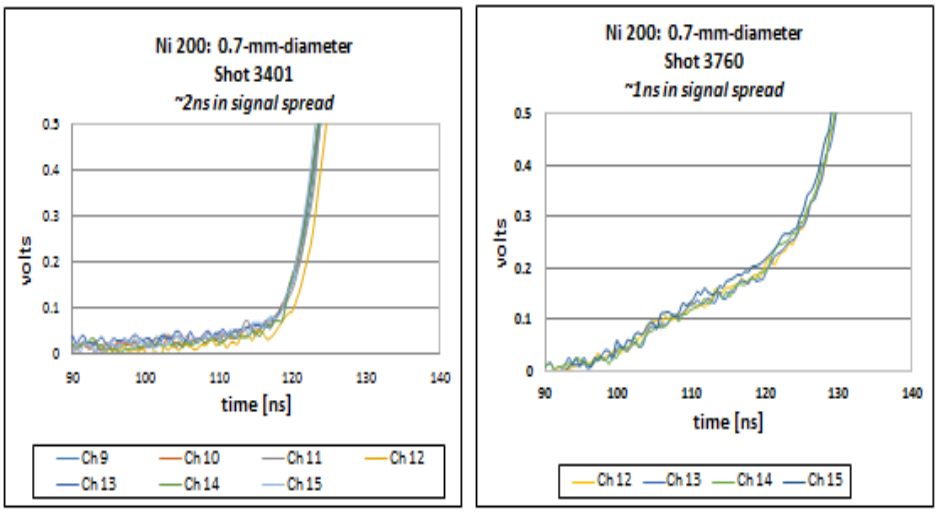

Figure III.53 Both shots of nickel 200 showed uniform emission of the surface with all diode signals lighting up together.

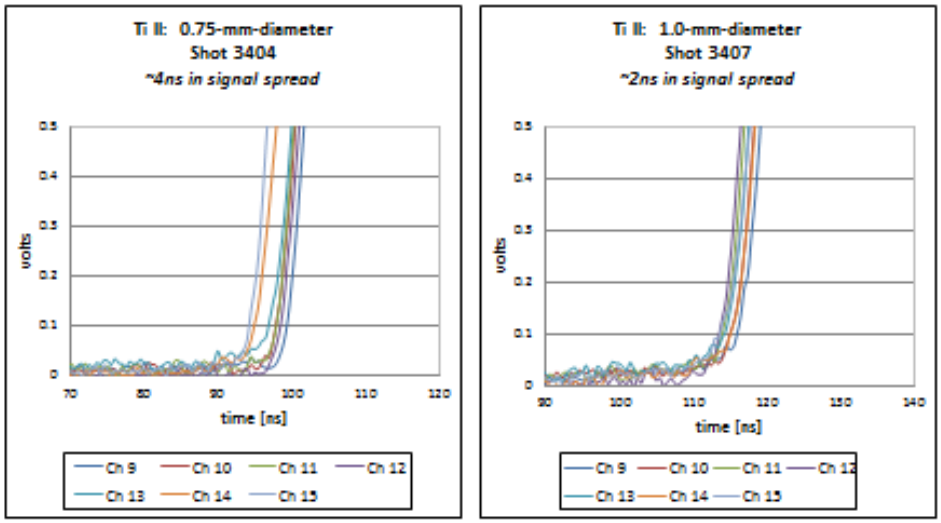

Figure III.54 All titanium shots show a spread in diode signal between 2 and 4ns.

The effect of surface finish and the alloying on the load hardware is not conclusive from the self-emission images and the diode signal structure. Several copper and aluminum rods were electropolished without a noticeable difference in the diode array but noticeable difference in the self-emission images observed near the time of earliest observable emission for several shots. A greater difference might have been observed if higher resolution imaging was available during the MG VI experiment. The type of alloy has an effect on the expansion rate, time of surface

expansion, time of plasma formation, and surface temperature as will be discussed in the next three chapters, however, the load hardware appears to perform well with all load alloys and surface types, ohmically heating to the time of plasma formation. The only exception to this was with the new transmission line that showed clear signs of early plasma formation.

Chapter IV: Surface Temperature Estimates Using Visible Radiometry

The surface temperature of our pulsed rods was estimated using an array of photodiodes. A lower bound on the temperature is determined by approximating that the surface of the rod radiates as a blackbody. A blackbody is a perfect absorber and emitter, which by the laws of statistical mechanics must radiate a Planckian spectrum, when in thermodynamic equilibrium. The emissivity of a material is its relative ability to absorb and radiate as a blackbody. If an object has an emissivity of 1, then it is a perfect blackbody. If a material has an emissivity of 0, then it would not radiate. Aluminum in the solid state is highly reflective and has an emissivity that can vary from 0.05 to 0.4 based on the alloy, surface roughness and the oxidation state of the surface. The variations of the emissivity of aluminum, copper, nickel and titanium as they are heated through the melting stage are documented for only select regions of wavelength, most of those falling in the micron and longer wavelengths. The emissivity as the metals become vapor and form plasma is not known. With the emissivity of the metal surface unknown, it is chosen to be 1. This approximation is applied due to the continuum observed by visible spectroscopy on both aluminum and copper rods. The blackbody approximation provides a lower bound on the surface temperature. The light radiating from the metal rod is assumed to be emitted from a thin layer of surface plasma that is optically thick. Any error introduced with the blackbody approximation becomes more severe as the plasma becomes optically thinner and diverges further from the Planckian limit. The temperature estimate, and more importantly an abrupt change in temperature, will be utilized to determine time of plasma formation.

The emitted radiation is collected by optics and relayed to an array of photodiodes that are filtered to narrow the optical band to green light for optimal focusing of the image. With the blackbody assumption, the radiation intensity is a convolution of the filter transmission with the

Planck distribution curve. With a well-known geometry of the diagnostic, a lower bound temperature estimate can be determined.

This chapter will begin with a brief overview of the diagnostic and a discussion about some modifications made between experiments. The chapter will end with the analysis of the data and an estimate of the surface temperatures of aluminum, copper, titanium and nickel plasmas.

Section IV.A: Photon Statistics of a Blackbody

The photon statistics and equations discussed below are found in several thermal and statistics books[102]. When an electromagnetic radiation source is in thermal equilibrium, the spectrum can be represented by a Planckian distribution. Planck's law for the total power per unit area, per unit frequency emitted from a blackbody surface into 2π can be written as

$$I(\nu, T) = \frac{2\pi h\nu^3}{c^2}\frac{1}{\exp\left(\frac{h\nu}{kT}\right)-1} \quad \text{(IV.1)}$$

This equation can be used when a photodetector is fielded to deduce the surface temperature of an emitting blackbody. Equation IV.1 is the radiant energy per unit surface area, per unit time, per unit frequency. It is easier to use this equation by first changing the frequency dependence to a wavelength dependence. This cannot be done by simply replacing frequency with $\nu = c/\lambda$. The equation must be integrated over frequency to get the total emissive power

$$P(T) = \int_{\nu_1}^{\nu_2} \frac{2\pi h\nu^3}{c^2}\frac{1}{\exp\left(\frac{h\nu}{kT}\right)-1} d\nu \quad \text{(IV.2)}$$

A change of variables can now be applied with $\nu = c/\lambda$ and $d\nu = -\frac{c}{\lambda^2}d\lambda$. The limits of integration must also change to go from λ_1 to λ_2. Equation IV.2 can now be rewritten as

$$P(T) = \int_{\lambda_1}^{\lambda_2} \frac{-2\pi hc^2}{\lambda^5} \frac{1}{\exp\left(\frac{hc}{kT\lambda}\right)-1} d\lambda = \int_{\lambda_2}^{\lambda_1} \frac{2\pi hc^2}{\lambda^5} \frac{1}{\exp\left(\frac{hc}{kT\lambda}\right)-1} d\lambda \quad \text{(IV.3)}$$

The energy emitted per unit area, per unit time, per unit wavelength can now be written as

$$I(\lambda, T) = \frac{2\pi hc^2}{\lambda^5} \frac{1}{\exp\left(\frac{hc}{kT\lambda}\right)-1} \quad \text{(IV.4)}$$

This is the well-known Planck distribution. The total emissive power is determined from integrating over all frequencies. The result is the well-known Stefan-Boltzmann Law

$$P(T) = \int_0^{\infty} \frac{2\pi h\nu^3}{c^2} \frac{1}{\exp\left(\frac{h\nu}{kT}\right)-1} d\nu = \sigma T^4 \quad \text{(IV.5)}$$

This equation shows that the total emissive power of a radiating blackbody is proportional to T^4. This shows the tremendous sensitivity blackbodies have to temperature. A small increase in temperature can result in a substantial increase in radiant energy flux. The constant of proportionality is known as the Stefan-Boltzmann constant and is equal to 5.67×10^{-8} W/m^{2}K^4. The peak frequency for a particular temperature can be found by differentiating equation IV.1, setting it to zero, and solving for the frequency. This gives

$$\nu_{max} = \frac{T}{2.9\times10^{-3} K\cdot sec} \quad \text{(IV.6)}$$

Where the temperature is in Kelvin. This shows that the peak frequency is linearly proportional to the temperature. With diagnostics usually having a range of photon energy in which they can collect data, the Planck distribution can sometimes be simplified. If the photons that a detector are sampling have a much greater energy compared to the peak photon energy of a distribution peak for that material ($h\nu \gg kT$) then equation IV.1 can be simplified to the well-known Wien's approximation

$$I(\nu,T)=\frac{2\pi h\nu^3}{c^2}\exp\left(\frac{-h\nu}{kT}\right) \quad \text{(IV.7)}$$

This would be in the area of the distribution curve that is left of the peaks for a particular temperature. If the energy of the sampled photon is much less than the peak ($h\nu \ll kT$) then the exponential can be Taylor expanded with only the first two terms of the expansion kept to give

$$I(\nu,T)=\frac{2\pi h\nu^3}{c^2}\frac{1}{\exp\left(\frac{h\nu}{kT}\right)-1}\approx\frac{2\pi h\nu^3}{c^2}\frac{1}{1+\frac{h\nu}{kT}-1}=\frac{2\pi\nu^2kT}{c^2} \quad \text{(IV.8)}$$

Equation IV.8 shows that if the radiating blackbody is relatively cold then the detector will collect few photons. As the blackbody increases in temperature, the distribution will shift into the frequency range that allows for more detections and the intensity will begin to increase as $\exp\left(\frac{-h\nu}{kT}\right)$ with temperature. If the radiating blackbody is relatively hot then the detector will be collecting photons in the long wavelength tail of the distribution function and the intensity of radiation will be linearly dependent on the temperature.

In previous experiments the surface emission spectrum of the aluminum rod was observed to be a continuum in the visible spectrum. A Horiba Jobin Yvon CP140 spectrometer was coupled to a streak camera and showed no indication of line emission. From the onset of light detection, the emission appears to be a continuum. It was not possible to use the images collected by the streak camera to determine if the emission followed a blackbody distribution due to lack of calibration (the camera was on loan from Los Alamos National Laboratory). In MG-IV, a new diagnostic was fielded using an A5C38 linear photodiode array from OSI Optopelectronics[103] coupled to the same spectrometer that was previously coupled to the streak camera. The spectrometer was calibrated with the diode array such that the spectral distribution observed could be compared to the

blackbody distribution curve. The data showed the emitting radiation approach a blackbody distribution curve, however, there was a departure from this simple theory. There was also a dip in the radiation in the blue end of the spectra that was never understood. The assumption of a blackbody emitter could be better understood by calibrating the entire system by firing a carbon wire, however, this has yet to be done.

Section IV.B: Visible Light Radiometry Using Photodiode Array

With the blackbody approximation, a lower bound temperature is determined using a 38-element photodiode array. The temperature can be obtained from the voltage signal gathered on a scope by careful analysis of the geometric setup of the diagnostic as well as a well-known spectral response of the diode and filter. The rod is emitting light from the center of the vacuum chamber through 4π Steradians with only a small fraction being captured as it travels through the 3 inch port and is captured and relayed by an imaging lens. The rod image is magnified as it is captured and relayed to the diode array and collected by a 4.39 mm $\times$ 0.89 mm diode element. In previous experiments, only a green Wratten filter was used to narrow the bandwidth of the incoming light. In MG-VI an additional infrared filter was used to narrow the band even further and observe the results of filtering out the softer photons that could be arriving prior to plasma formation. The responsivity of the photoconductive elements as a function of wavelength is well characterized by the manufacturer and is given in Amps/Watts. This permits the conversion of light intensity into diode current that will then be dropped across 50 ohms to produce a voltage signal on the digitizing scope. The losses due to debris shields, optical window, lenses and filtering must be carefully taken into account. With information on these losses, the geometry, filter bandwidth,

and diode response, the total number of photons emitted from the rod and reaching the detector can be determined, and a lower bound rod surface temperature estimate can be reached.

Diagnostic

The diagnostic fielded in MG-V to MG-IX experiments was the same as that fielded in the MG-IV experiment. Aside from the addition of an IR rejection filter in MG-VI, the only modification made in the recent experiments was the lens and port window were built into a single machined aluminum holder that attached directly to the chamber. This was done as a simplification to allow the attachment of the lens to be done quicker and with greater ease. The lens has a 300 mm focal length and a diameter of 3 inches that relays the image just under two meters to the photodiode array. A schematic of the diagnostic is shown in Figure IV.1.

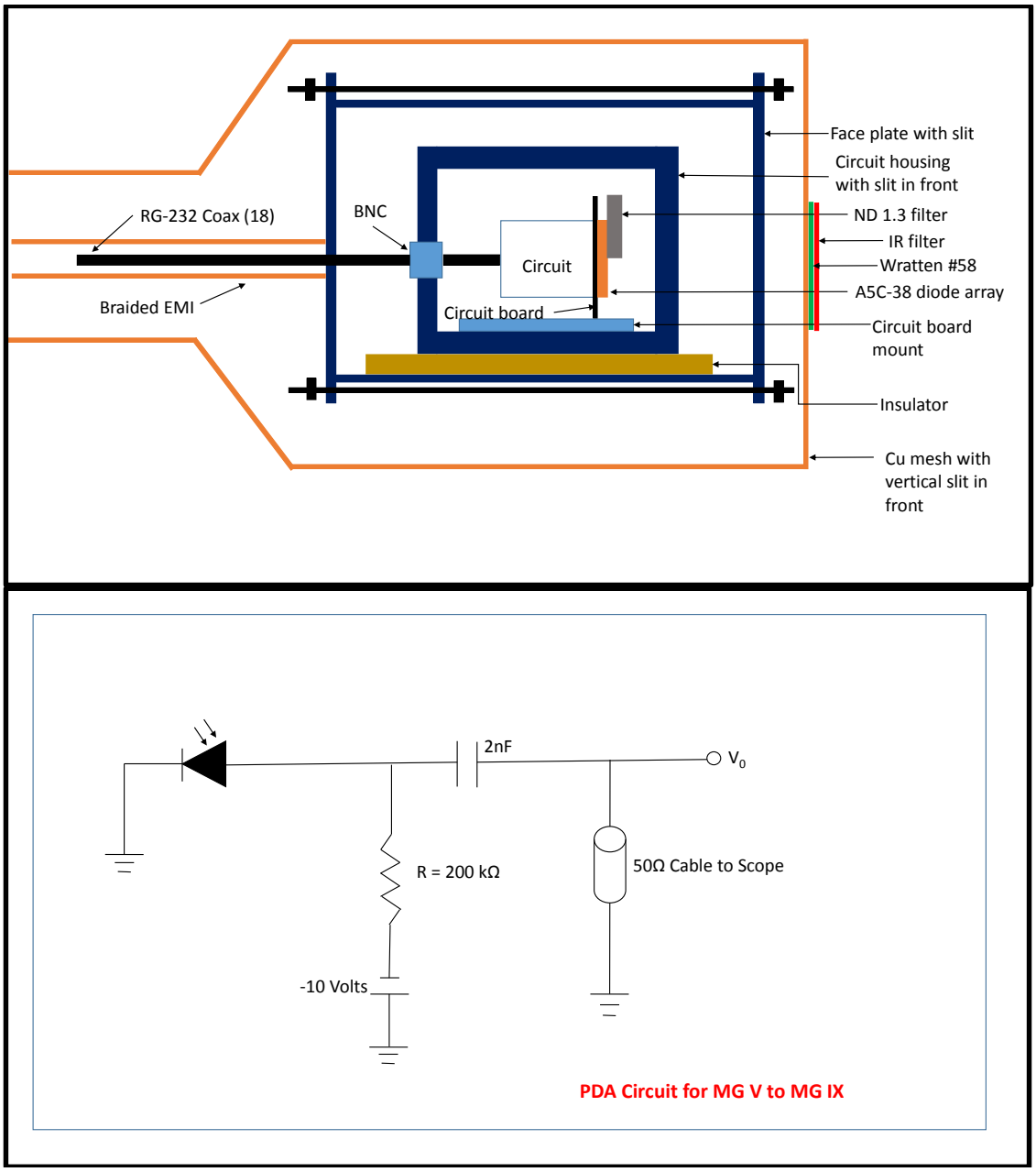

Figure IV.1 Schematic of photodiode array circuit and enclosure with filtering used during the MG VI to MG IX experiments.

The array is attached to a circuit board that allows for biasing of the elements used. Every other diode element is negatively biased to -10 volts, with the elements in between grounded to reduce cross-talk. The elements are connected with RG-232 coaxial cables that run the signal to a nearby sreenbox. The cables are shielded with copper mesh that covers the cables along the entire pathway back to the screen box, where the mesh is attached to the outer wall of the screenbox.

The cables enter the box through a small hole and are connected to a digitizing scope inside. Ferrite cores are placed around the cables to help reduce the noise in the system to levels below 15mV peak to peak. The biasing circuit is housed inside an EMI shielding box made from 1/16 inches thick aluminum sheet metal. The housing has many seems so the entire structure is wrapped with copper mesh.

The photodiode array has 38 elements, but only 15 elements are used, with one of them being ground. This allows for 14 elements to be used to collect signals. The rod image is relayed to the array with a magnification such that the initial diameter allows for the entire width of the array elements to be covered by the rod image. The multi-element array allows for spatial resolution of the load surface emission in time, providing the ability to observe the amount of non-uniform emission that can occur, especially early in time. The top half of the array is covered with a neutral density filter. Neutral density (ND) filters use a log 10 scale such that an ND 2 filter attenuates the light by a factor of 100. An ND 1.222 filter was used to attenuate the light by a factor of 16.67. The need for the ND filter is due to the saturation of the diodes as the signal approached several volts. The diodes that are covered by the ND filter do not saturate and can be used to interpret high temperatures in the late time of the current profile. The diodes without the ND filter allow for a more sensitive observation of the early onset of the temperature increase as the load surface begins to transition into plasma. The time response of the photodiode array is determined by the following equation:[104]

$$t_{response} = \frac{0.35}{f_{bw}} \quad \text{(IV.9)}$$

Where

$$f_{bw} = \frac{1}{2\pi R_{load} C_j} \quad \text{(IV.10)}$$

Where f_{bw} is the bandwidth, R_{load} is the load resistance (50Ω), C_j is the junction capacitance (12pF at -10V bias), and $t_{response}$ is the response time of the diode. The response time of the photodiode array is calculated to be 1.3ns.

The spectral filtering included a Wratten #58 green filter and a FGS900 Thorlabs infrared (IR) filter. The transmission curves for the filters along with the responsivity of the A5C-38 detector is shown in Figures IV.2 and IV.3.

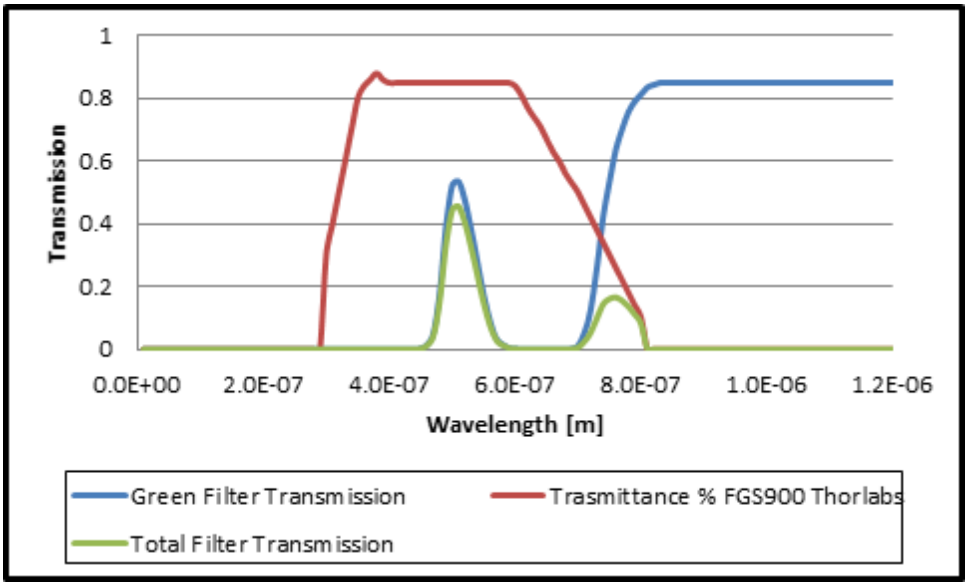

Figure IV.2 The transmission curves for the Wratten and IR rejection filters used in MG-VI to MG-IX. (Transmission curve for FGS900 courtesy of Thorlabs, Inc. https://www.thorlabs.com. Transmission curve for Wratten Green filter courtesy of Kodak Photographic Filters Handbook.[105])

In earlier experiments, the filter transmission for the Wratten #58 was given by the transmission curve that is found on the Thorlabs website. This transmission curve ends at 700 nm, leaving the observer to believe that there is no transmission outside of this spectral region. It was realized later by Dr. Fuelling that the transmission curve was not correct. Using the curves provided by Kodak, it is seen that there is another envelope of transmission in the infrared. This motivated the use of both the Wratten and IR rejection filters. It is clear from Figure IV.2 that the effect of

IR passing through the Wratten filter cannot be ignored as the response of the diodes is greatest in the NIR.

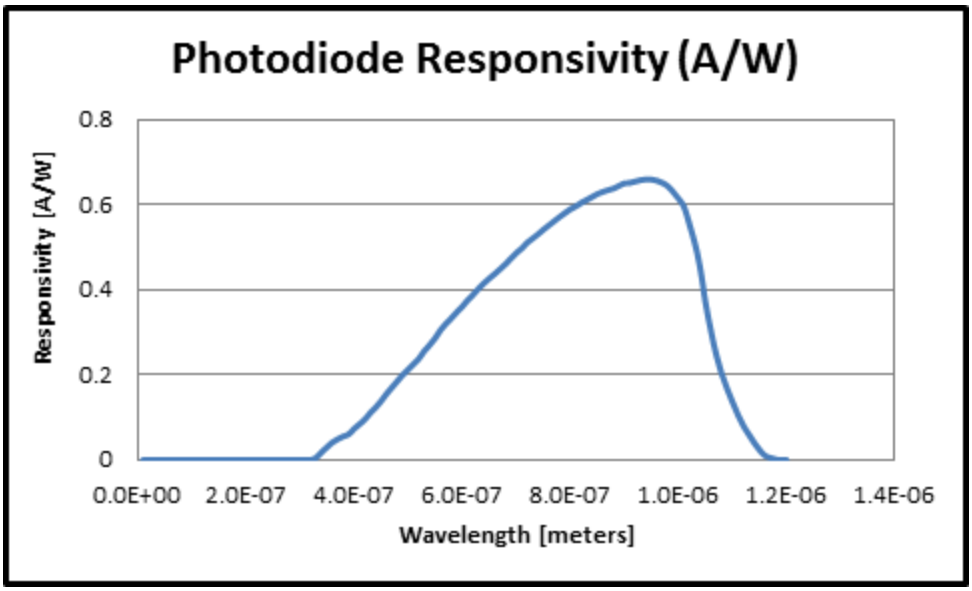

Figure IV.3 The responsivity of the diodes shows an increasing response toward the infrared, with a sudden drop at 950 nm. (Characterization data from OSI Optoelctronics http://www.osioptoelectronics.com/)

The geometry of the optics and diagnostics are important in determining an estimate of the surface temperature of the rod. The variation in optical geometry between experiments is shown in Table IV.1. Equations IV.11 allow for the calculations of the magnification of the image, the solid angle of the optical system, and the light emitting area. The last row is the light emitting area multiplied by the solid angle, which is limited by the debris shield aperture in the port window.

$$M = \frac{-S_i}{S_o}$$

$$Emitter\ area = \left(\frac{element\ length}{M} \times \frac{element\ height}{M}\right) = \frac{Detector\ Element\ Area}{M^2} \qquad \text{(IV.11)}$$

$$Solid\ Angle\ \Omega = \iint \frac{\hat{n}}{R^2} da = \frac{Aperture\ Open\ Area}{(Aperture\ to\ Source)^2}$$

	MG II	MG III	MG IV	MG V	MG VI-IX
Imaging System					
Lens focal length	250	300	300	300	300
Lens radius	22.5	76.2	76.2	76.2	76.2
Objective Distance (mm)	406	346	350	355	355
Image Distance (mm)	1200	1930	2053	1911	1911
Aperture Defining Solid Angle	Lens	Debris Shield	Debris Shield	Debris Shield	Debris Shield
Radius (mm)	22.5	25.4	25.4	25.4	25.4
Distance from Source (mm)	406	300	300	300	300
Detector Characteristics					
Length (single element) (mm)	1	4.39	4.39	4.39	4.39
Height (single element) (mm)	1	0.89	0.89	0.89	0.89
Active area (mm^2)	1.00	3.91	3.91	3.91	3.91
Number of active elements	3	15	14	14	14
Active element separation in image plane (mm)	7.5	1.98	1.98	1.98	1.98
Bias voltage	-20V	-10V	-10V	-10V	-10V
Calculated quantities					
Magnification	-2.96	-5.58	-5.86	-5.38	-5.38
Solid Angle (Steradians)	9.65E-03	2.25E-02	2.25E-02	2.25E-02	2.25E-02
Emitter Area (Square meters)	1.15E-07	1.26E-07	1.14E-07	1.35E-07	1.35E-07
Active Element Separation in Object Plane (mm)	2.54	0.35	0.34	0.37	0.37
Solid Angle*Emitter Area	1.10E-09	2.83E-09	2.56E-09	3.042E-09	3.042E-09

Table IV.1 The geometric layouts of the optical system changed from experiment to experiment. This effects the light collection capabilities and, therefore, effects the sensitivity of capturing early light.

With the blackbody equation, the transmission curves of the filters, the responsivity of the diode, and the geometric layout of the diode optical system, the voltage can be translated into a lower bound surface temperature. This calculation is performed using a Microsoft Excel spreadsheet. A temperature and wavelength can be chosen, 0.1 eV and 500nm for example, and substituted into equation IV.4. This will provide the power per unit radiating area per solid angle. Multiplying this by the radiating area and solid angle, equation IV.11, provides the power radiated by the surface. This power must be multiplied by the power loss due to attenuation in the debris shield, optical window, and lens. This power can now be multiplied by the responsivity of the diode, in Amps/Watt, to get the amperes produced by the diode. This is dropped across 50 ohms so is multiplied by 50 to determine the voltage on the scope. This voltage represents the voltage that is expected to be observed on the scope for a radiating body at 0.1 eV and at a wavelength of 500nm. This procedure is done for every wavelength in the wavelength range 10-1200nm in steps of 10nm, holding the temperature constant. The voltage for each wavelength is then summed across the wavelength range to get the total voltage for a radiating blackbody at 0.1 eV. The voltage is determined for temperatures up to 25eV and a voltage versus temperature dependence can be found and plotted. The temperature plot is broken into four regions: 0-1eV, 1-2eV, 2-4eV, and >4eV. The plot of temperature versus voltage for 0-1eV is shown in Figure IV.4 with a polynomial fit. The voltage signals from each shot are then put into the polynomial fits to determine a blackbody temperature. The voltage signals from the diode elements that do not have the ND filter in front of them are substituted into the polynomials that are fit for the temperature ranges of 0-1 and 1-2eV. The voltage signals from the diode elements that do have

the ND filter in front of them are substituted into the polynomials that are fit for the temperature ranges of 2-4 and >4eV. The polynomials for the four temperature ranges for the filter setup with the Wratten and the IR rejection filter are as follows:

$$-1231 \cdot x^4 + 752.11 \cdot x^3 - 155.52 \cdot x^2 + 14.224 \cdot x + 0.2114 \quad \text{for } 0\text{eV} < \text{T} < 1\text{eV}$$

$$-0.1825 \cdot x^2 + 1.4187 \cdot x + 0.6265 \quad \text{for } 1\text{eV} < \text{T} < 2\text{eV}$$

$$1.0028 \cdot x + 0.8821 \quad \text{for } 2\text{eV} < \text{T} < 4\text{eV} \qquad \text{(IV.12)}$$

$$0.9644 \cdot x + 0.9997 \quad \text{for } 4\text{eV} < \text{T}$$

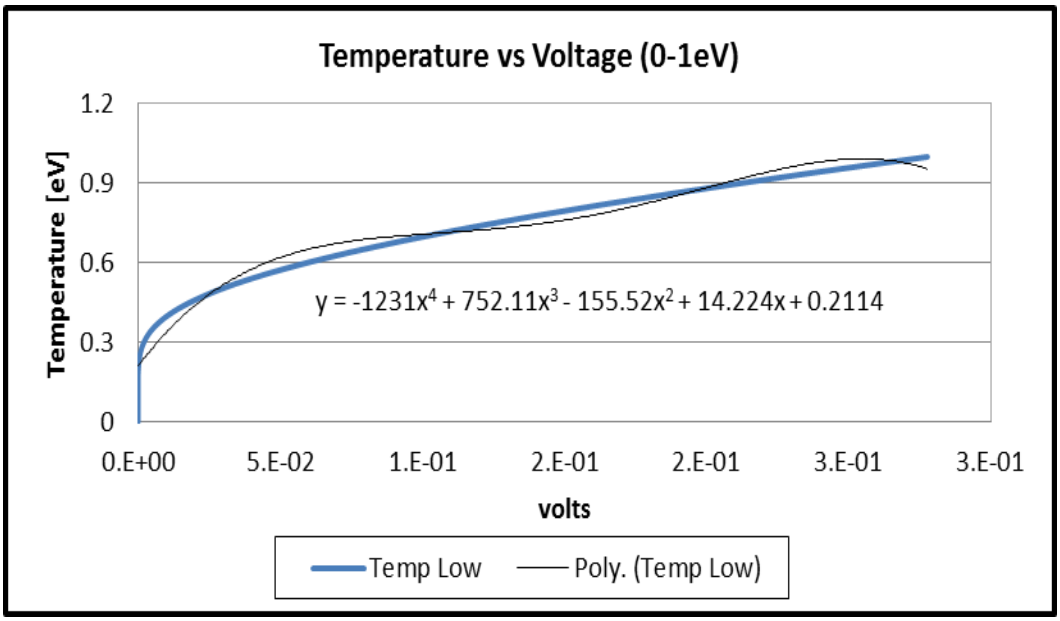

Figure IV.4 Plot of temperature versus voltage (from 0-1eV) for the optical setup of the MG experiments applying the blackbody approximation.

Experimental Results

The first goal of the MG-VI experiment was to determine the effect of the filtering. The first few shots implemented the same filtering system as used in previous experiments with only the Wratten #58 filter placed in front of the entrance slit. After a few shots the IR rejection filter was placed over the Wratten filter to narrow the bandwidth to an envelope limited to the visible region. The voltage signals are shown in Figure IV.5 for the 1.00-mm-diameter aluminum. There is a small DC shift in the PDA signals that has been removed from these as indicated in the legends of the plots.

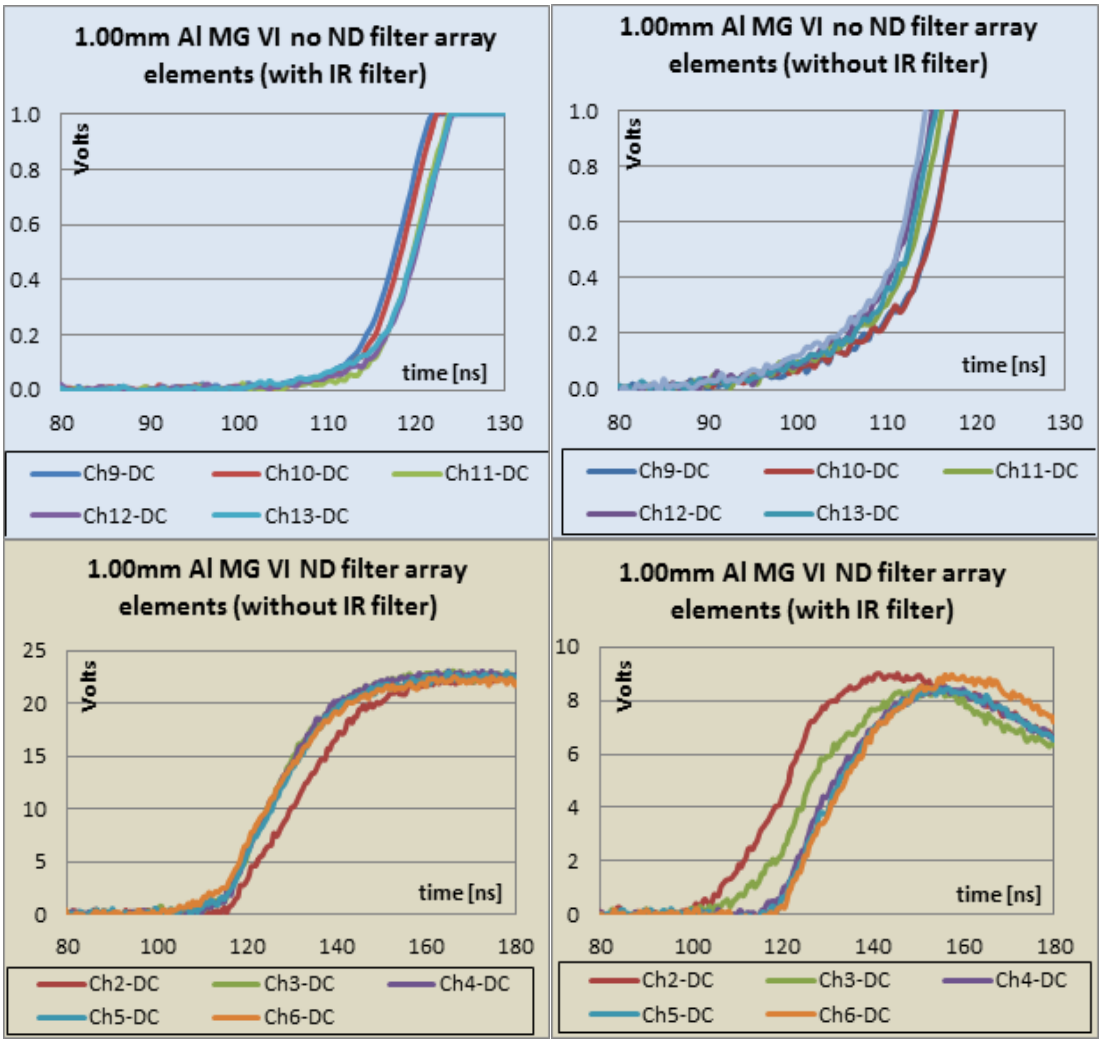

Figure IV.5 The aluminum 1.00-mm-diameter loads with no IR rejection filter show a long ramp in the PDA signals before the sharp increase in voltage. The sharp increase indicates plasma formation. The filters with the IR rejection filter show a reduction in the early ramp in both duration and amplitude.

The peak voltage is higher for the signals that include the Wratten filter and the ND filter, but no IR rejection filter. This was expected and indicates that the loads radiate in the infrared after surface plasma has developed. If the load did not radiate in the IR then the extra IR rejection filter would only attenuate by approximately 10% as seen from Figure IV.2. A more subtle difference is observed in the early time signals that do not have an ND filter. The signals that include only the Wratten and no ND or IR rejection filters have an early ramp up in signal intensity that reaches about 0.2 volts before the sharp increase in diode signal. The ramp for IR and green light is about 20 ns in length and was observed on many aluminum shots in previous experiments. The signals with both the Wratten and the IR rejection filter show a peak voltage of about 9 volts, compared to 23 volts for the Wratten only shots. The length of time for the green-light ramp is shortened to approximately 5 ns with the sharp increase in signal occurring when it reaches about 0.8 volts. The timing of the ramp coincides with the early spots and non-uniform filamentation observed in the ICCD images. Figure IV.6 plots several voltage curves from MG IV of the aluminum 1.0-mm-diameter shots without an IR rejection filter. Comparing these signals with the timing of the ICCD pictures for the 1.00-mm-diameter aluminum loads in Figure IV.7 the ramp is rising when the ICCD observes early surface spots with the sharp increase in signal occurring near the time of filamentation. This leads one to believe the ramp is caused by the evolution of the non-uniform to uniform surface emission. However, prior to the onset of surface plasma, the metal has melted and formed surface vapor, reaching temperatures of a fraction of an eV. The hot vapor is predicted to emit radiation in the infrared. This would explain the reduction in the signal with the addition of the IR rejection filter. Since there is still a ramp observed with the IR rejection filter in place, it is believed that the early ramp seen with only the Wratten filter in place, is a combination of the radiating aluminum vapor and liquid, and the early onset of visible plasma spots.

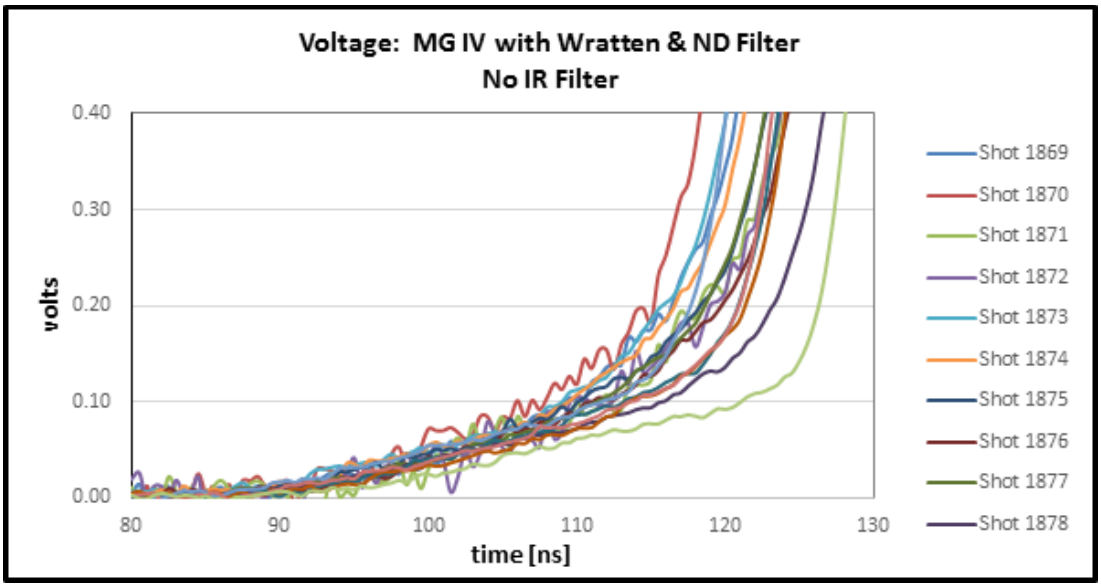

Figure IV.6 The 1.00-mm aluminum from MG-IV has a 20-30 ns ramp similar to what is observed in MG-VI. The ramp is thought to be a combination of infrared radiation and early non-uniform green-light plasma emission.

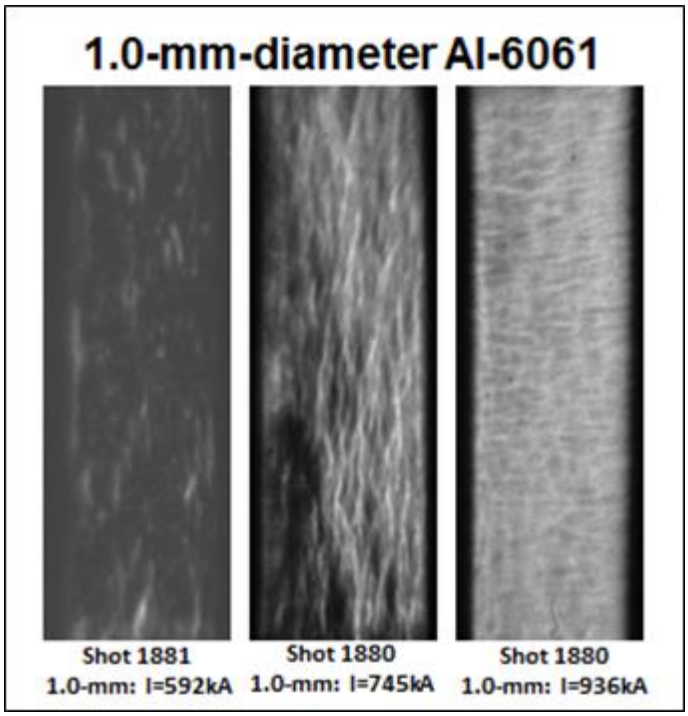

Figure IV.7 The evolution of 1.00-mm aluminum in MG-IV illustrates the timing of the non-uniform plasma emission in comparison to the photodiode array signal. The first image appears to occur in the ramp of the PDA signal, with the second occurring at the sharp rise in signal. (Images courtesy of T.J. Awe)

A similar effect was observed with copper 101. It was never intended to use the PDA without the IR rejection filter when shooting copper, however, there were a couple shots where the IR rejection filter was not placed back in front of the PDA after some aluminum shots for which we wanted to measure the IR radiation. It is interesting to see similar results for the copper as for aluminum. Figure IV.8 shows the results for copper 101 0.7-mm-diameter with the shot with the Wratten filter and no ND or IR rejection filters, showing a ramp lasting about 20ns while the shot with the Wratten and IR rejection filter with no ND filter having a ramp lasting about 5ns. The voltage signals including the ND filter with the different color filtering, with and without the IR rejection filter, also show that the surface is radiating in the IR thorough peak current as the voltage is twice as large for the shot without the IR rejection filter on the PDA. There is also a qualitative difference in the voltage waveforms that have the ND filter, with the voltage signals with the IR rejection filter having more structure than the signals without the IR rejection filter. There were not enough shots performed for a complete comparison to be made, leaving it difficult to come to any conclusion. This effect could be due to shot to shot variations, however, this is unlikely since this kind of difference has not been observed before with loads that have many shots performed.

The shift in the timing for the diode signals observed between the IR rejection filtered and non-IR rejection filter copper rods is not attributed to the filtering but a small variation in initial rod diameter for the two shots and shot to shot variations. The shot to shot variations is illustrated in Figure IV.6 with the diode traces for Al 6061 1.0-mm-diameter. A spread of about 10 ns was observed for the diode trace. This will be discussed again later in this chapter.

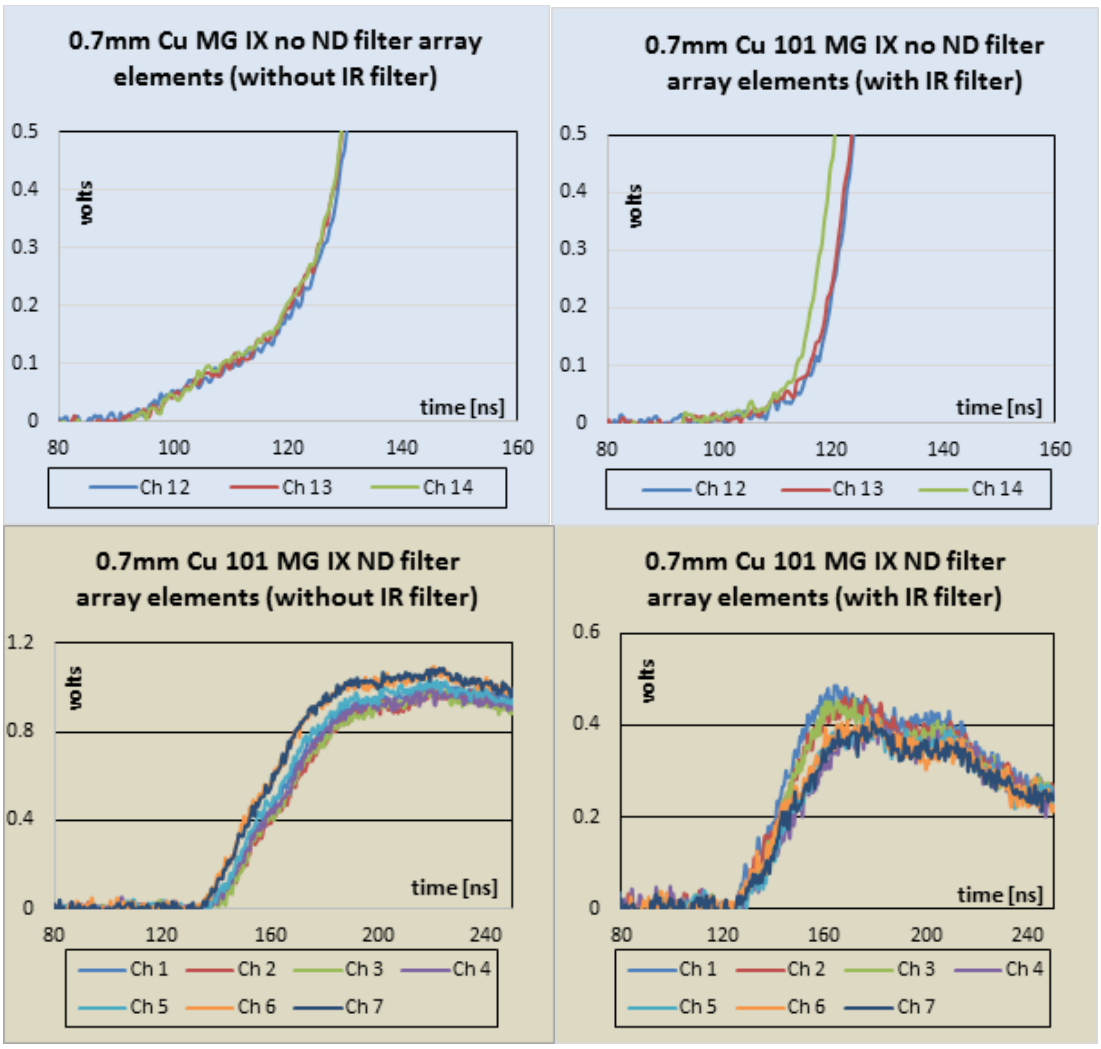

Figure IV.8 The copper 101 0.7-mm-diameter loads show a similar effect in the filtering as was observed with the aluminum loads. Shots without IR rejection filtering observe a long ramp that leads to the sharp increase in diode signal, with the shots with the IR rejection filter having this ramp significantly reduced.

When first analyzing the voltage signals for copper and aluminum it was noticed that the voltage signals for the elements with the ND filter would sometimes go slightly negative before going positive. The signals from these elements were expected to show a small delay relative to those without the ND filter due to the fact that the ND filter reduced the sensitivity of these elements. However, some of the signals showed a delay of nearly 8 ns before the filtered signal began to rise with a small decrease in signal occurring before the rise begins. The sharp decrease in signal occurs at about the same time that the unfiltered elements begin to rise in signal. Examples of

such results are illustrated in Figures IV.9 and IV.10. The red trace is an average of the elements that are not covered by the ND filter and therefore have a higher sensitivity. The blue trace is an average of the elements that are covered by the ND filter and show a sharp, negative signal at the time of the red trace rising. The 0.7-mm copper and the 0.8-mm copper loads show a distinct difference. The blue trace for the smaller copper load goes more negative than the same trace for the larger copper load. The rise rate for the 0.7-mm load is faster than is for the 0.8-mm load by nearly a factor of two. The elements are likely inductively coupled so that when the elements without the ND filter begin to show signals, the capacitors that are next to these elements show a rise in bias voltage (more negatively biased).

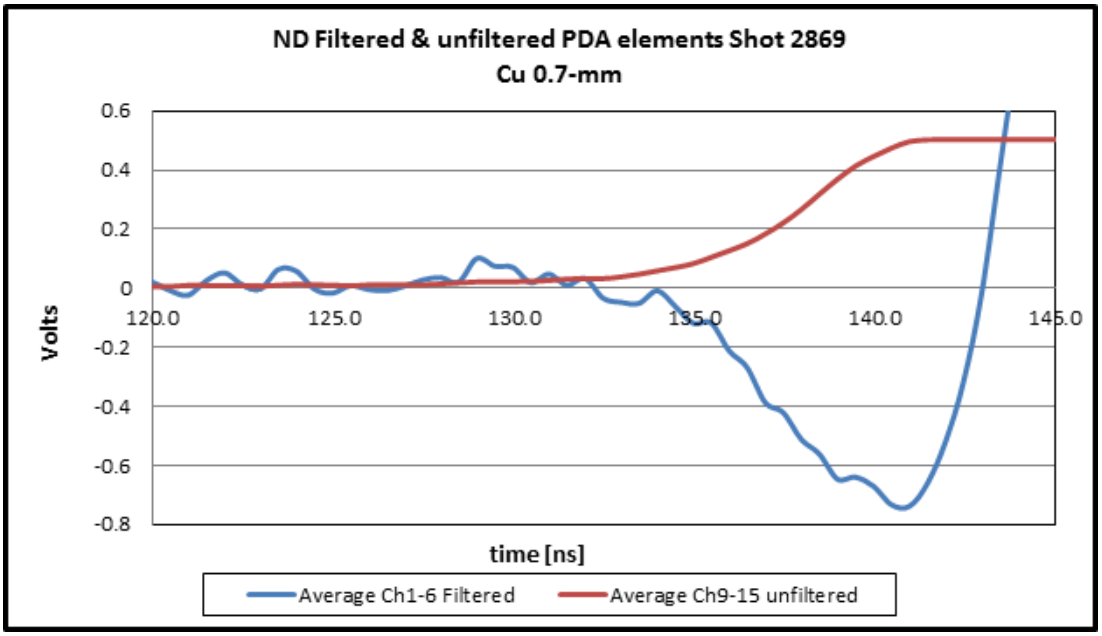

Figure IV.9 The Cu 0.7-mm loads show a strong "inductive-like" response when the unfiltered diodes begin to rise in signal.

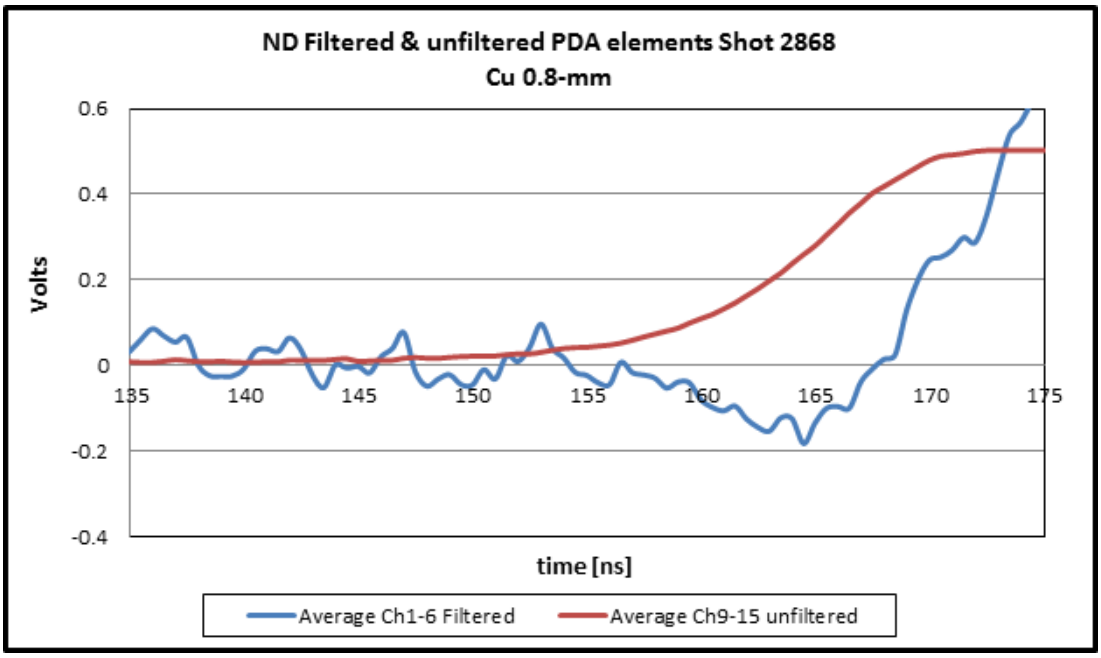

Figure IV.10 The Cu 0.8-mm loads show a similar trend as the 0.7-mm rods but with less of an "inductive" dip in the signal.

This would in turn appear as a negative voltage on the scope. To account for this, the negative going slope is brought to zero such that the beginning of the rising edge will now begin at a voltage of zero rather than a negative voltage. The negative peak is taken to be the new zero for the diodes that record these signals due to the thought that these diodes have a more negative bias due to the inductive coupling in the circuit. This effect had been observed on previous experiments with aluminum for 0.5-, 0.64-, and 0.8-mm-diameter loads but was not taken into account when determining temperatures. As the load diameters increase, the negative going signals become smaller and eventually disappear.

The first loads fired in the MG-VI experiment were the 1.00-mm-diameter aluminum. These loads are always the first to be shot because it is the diameter size that has been shot the most and turns to plasma near the middle of the current rise at ~700 kA. This allows us to immediately observe that the machine, diagnostics, and the loads are behaving properly and dialing in on any

timing discrepancies or filtering problems. As discussed in Chapter III, the first few shots had some problems behaving properly but eventually the loads started to behave as they had in previous experiments. Figure IV.11 shows the early temperature estimates of the aluminum with the sharp rise occurring at similar times as before. It is thought that the problems early on are due to using refurbished hardware allowing for poor contacts at the cathode end of the load configuration. The slip-fit that provides the contact might be a poor fit when the hole in the anode and cathode pieces are machined open. Perhaps the surface that is in the bore hole of a new hardware piece is smoother than that of a refurbished piece. There is no evidence of this and it has not been thoroughly studied. The addition of the IR rejection filter allowed for a proper temperature estimate to be approximately 11 eV compared to the 20 eV temperature estimate from the MG-IV analysis. The temperature analysis done in previous experiments used the Wratten filter only and a transmission curve, provided by Thorlabs, that did not take into account the IR light transmission. The incorrect Wratten transmission curve allowed for a temperature estimate that was too large. Figure IV.12 shows the temperature estimates using the correct transmission curves, with the peak aluminum temperature reaching between 9 and 12 eV.

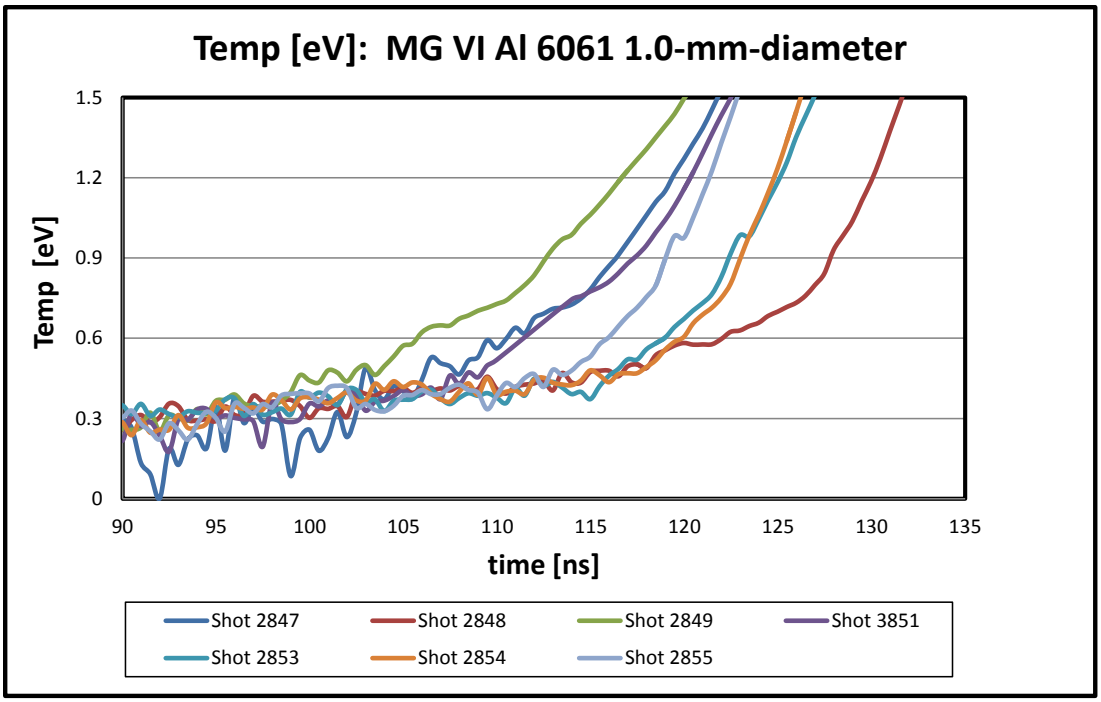

Figure IV.11 The aluminum 1.00-mm-diameter rods show a sharp increase in temperature as the blackbody temperature approaches 0.5 eV.

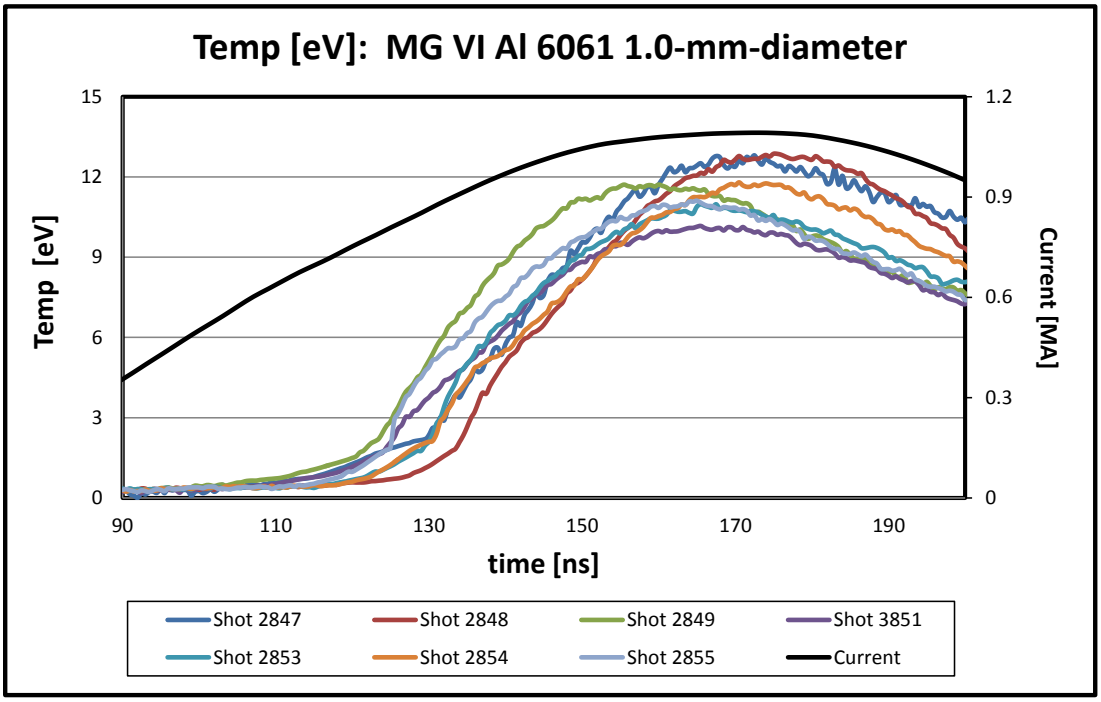

Figure IV.12 The aluminum 1.00-mm-diameter peak temperature was ~11 eV. This is almost half of the estimated temperature from previous campaigns that used the incorrect transmission curves.

The first copper loads to be fired were copper 101. This alloy was used because of the high purity of the metal, 99.99% pure. The smallest copper 101 loads fired were 0.7-mm-diameter as

discussed in Chapter III with the exception of one 0.5-mm-diameter load that was machined into a double barbell shape. The difficulty with machining ultra-high purity copper is that it is very soft, such that it is difficult to machine down to smaller diameters on a lathe. The temperature estimates for the MG VI loads are shown in Figures IV.13 through IV.16. Figure IV.17 plots all the copper 101 diameters ranging from 0.5-mm to 1.0-mm on one plot along with the current profile. The peak temperature estimates progressively decrease with increasing diameter until reaching 1.0-mm-diameter copper rods, which show no sign of increasing temperature, with the exception of shot 2862 that shows a small increase in temperature that quickly saturates at a fraction of an eV. This outlier shot is likely due to the 1.0-mm-diameter copper 101 rods being on the edge of forming plasma. This will be touched upon in the conclusion chapter.

The sudden increase in diode signal, and hence temperature, indicates plasma formation. As illustrated in Figures IV.17 and IV.18, the metal surface forms plasma later in time for progressively larger initial diameter, with the 1.0-mm-diameter rods not making surface plasma. The 0.5- and 0.7-mm-diamter loads have similar diode profiles, with the temperature increasing towards peak current, then a second increase in temperature and peak in temperature occurring after peak current by 10s of ns. The 0.8-mm-diameter rods do not have the same profile. The 0.8-mm rods approach peak temperature near peak current, and then appear to hit a flat top similar to a curve expected for diode saturation. It is not possible for this to be a saturating diode due to the varying “flat top” with varying initial load diameter. If it were saturation, the smaller diameter loads would also saturate near the same level. The 0.8-mm-diameter loads vary in initial load diameter from 0.8mm to 0.85mm, causing a small spread in the data. The 1.0-mm-diameter rods show no sudden increase in temperature as already mentioned, however, the signals do have

a small increase in signal that is likely due to a dimly glowing surface from the vapor surface as it begins to expand as well as some bright dots starting to form on the surface.

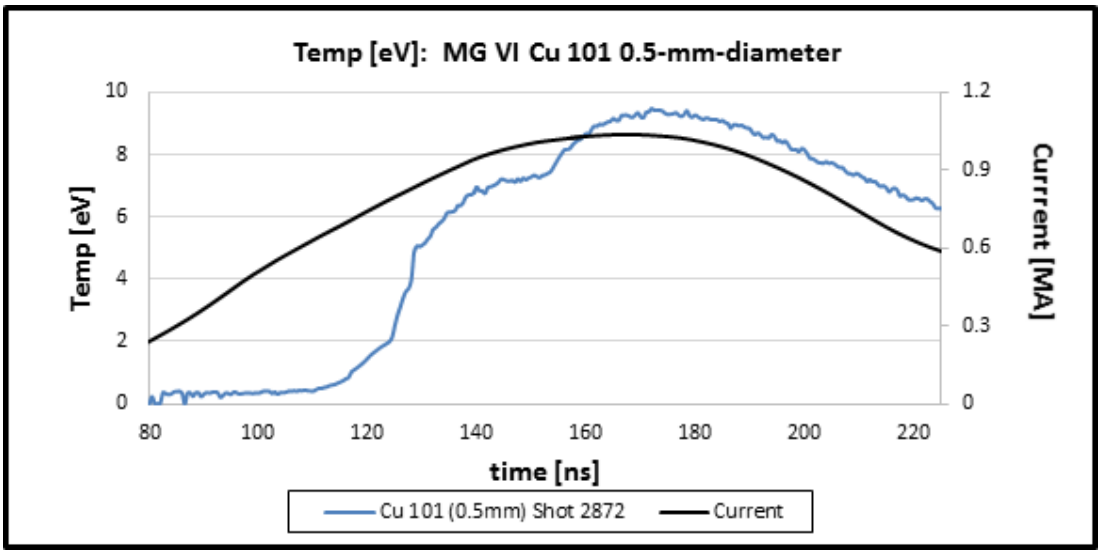

Figure IV.13 The copper 0.5-mm-diameter rods show a peak temperature of ~9 eV with the peak suspiciously arriving past peak current.

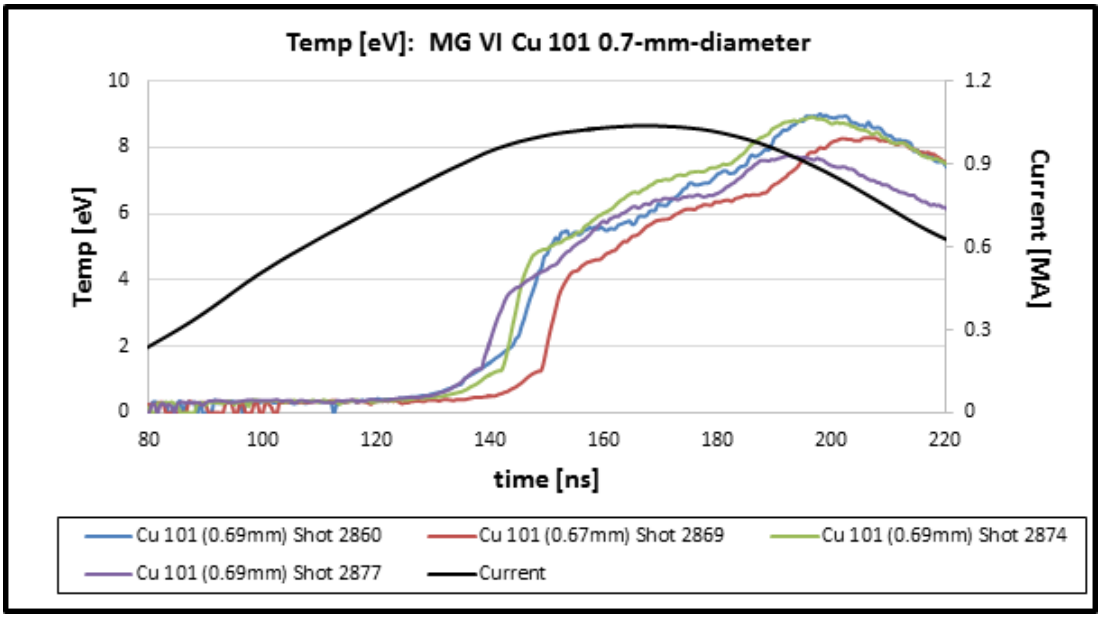

Figure IV.14 The copper 0.7-mm-diameter rods show a peak temperature of ~8 eV with the peak suspiciously arriving past peak current similar to that of copper 0.5-mm-diameter.

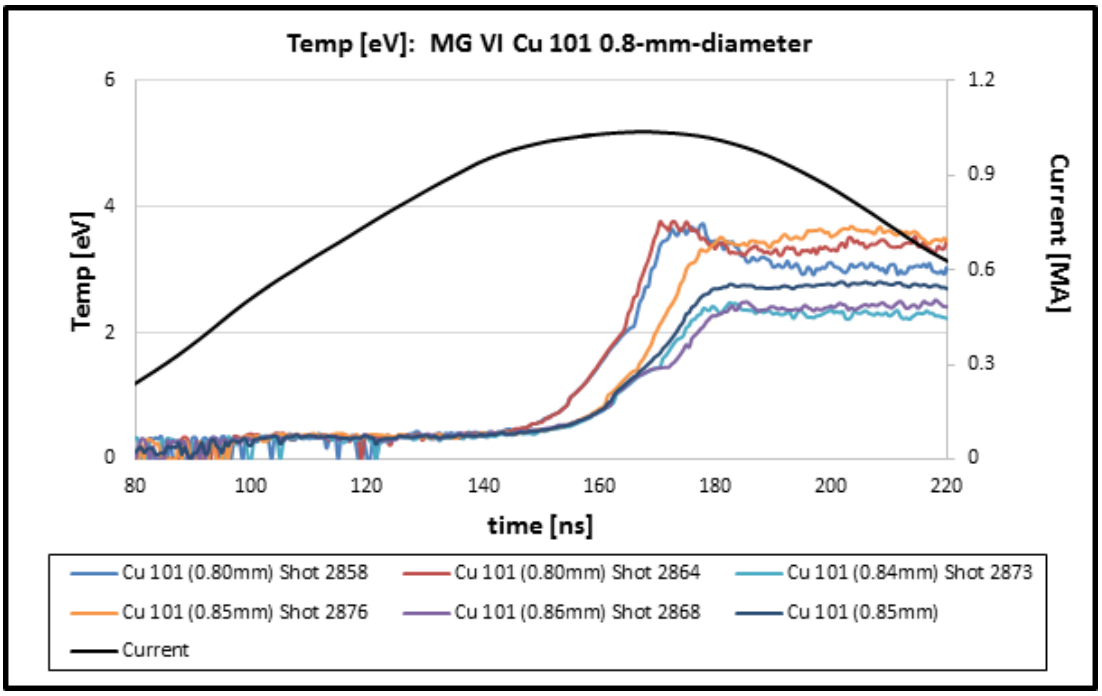

Figure IV.15 The copper 0.8-mm-diameter rods show a peak temperature of 2-3.5 eV. The spread is due to the variation in rod diameter as shown in the legend of the figure.

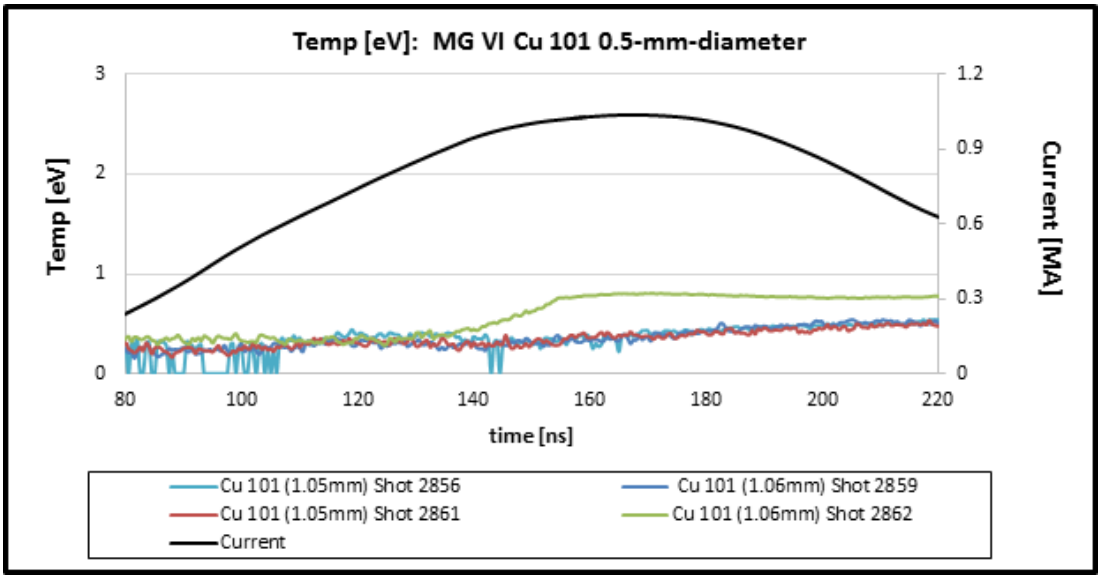

Figure IV.16 The copper 1.00-mm-diameter rods show no sharp increase in PDA signal. This is an indication that plasma did not form on the surface as was predicted by the ICCD images seen in Chapter III.

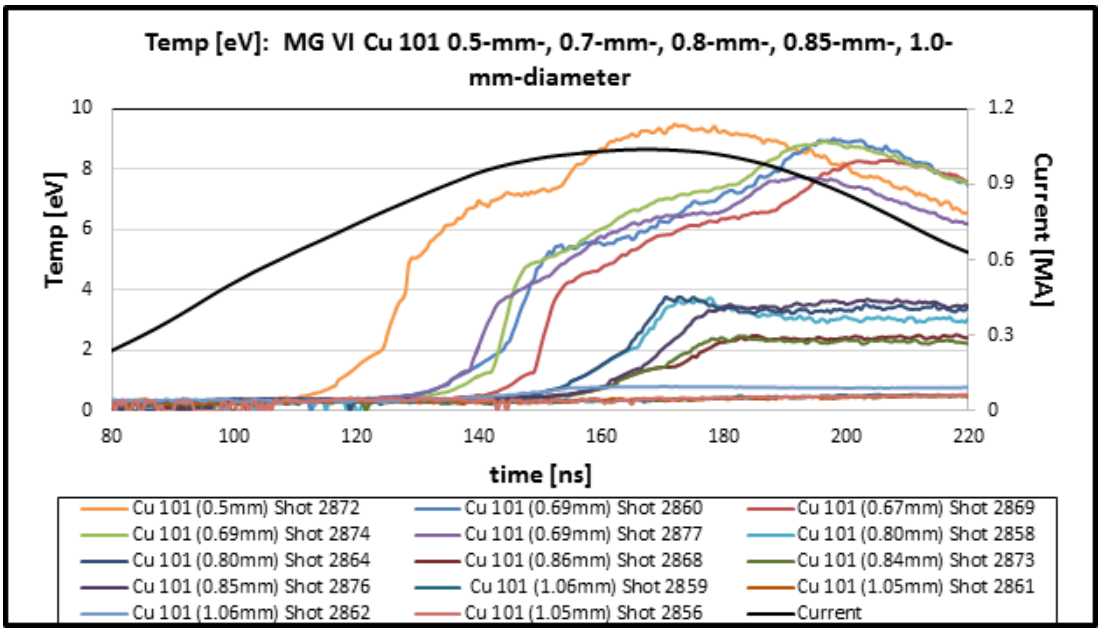

Figure IV.17 Temperature traces for all copper rods are plotted together and clearly show the dependence of the time of initial signal as well as peak temperature with the rod diameter.

Figure IV.18 is a zoomed in plot of the copper 101 shots of MG VI. A couple trends are noticed by zooming in on the diode signals. First, the signal is limited by noise in the system, with a minimum surface temperature of ~0.35 eV being observed. This is above the vaporization temperature for copper (0.24 eV), so that the surface temperature is not observed until after the metal has formed surface vapor or bi-phase and has begun to expand. Second, the high amplitude noise that limits the temperature that can be observed, becomes a flat signal prior to the sudden increase in the diode signal. This suggests that prior to the sudden increase in temperature (plasma formation), the surface is glowing in the visible.

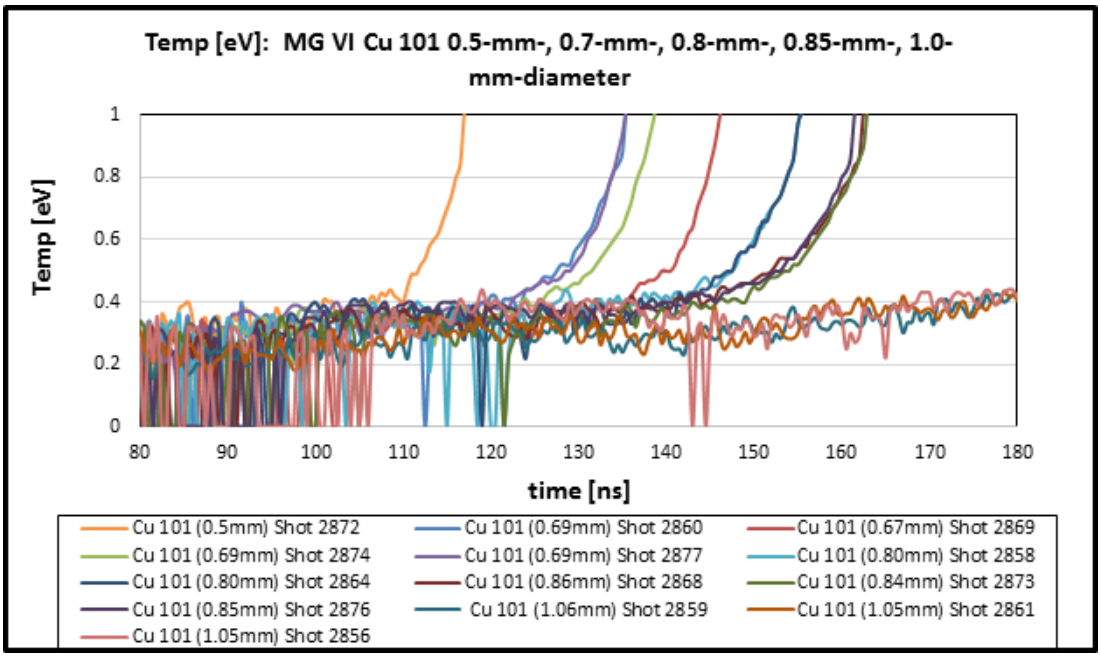

Figure IV.18 The sharp increase in early temperature is indicative of plasma formation and is shown to depend on rod diameter with small diameters forming plasma earlier than large diameter.

With the difficulty of machining pure copper 101, it was decided that we should switch to a copper alloy that would be easier to machine, and more importantly, able to machine down to 0.5-mm-diameter without using the double barbell style. Copper 145 was used because of the similarities in room temperature conductivity, thermal conductivity, and density. Copper 145 has ~0.7% tellurium added to it for added machinability. In MG VII, copper 145 was shot to complete a scan of diameters for copper that would include the range from 0.5- to 1.00-mm-diameter. The experiment began with shooting a 0.7-mm-diameter copper 145, shown in Figure IV.19, to ensure that the 145 alloy was acting similar to the 101 alloy shot in MG VI. We did not have the ability to analyze on the fly during the experiment, but it was assumed that the alloys would act the same due to the physical characteristics mentioned above. We then shot several copper 145 0.5-mm-diameter rods. It was noticed quickly that there appeared to be something wrong with the PDA system, with the voltage signals appearing to be smaller than expected for the copper as well as the aluminum that we were shooting. By shot 3397 it was clear that the diode array was not

functioning properly. The array was replaced during shot 3398 and was back online by shot 3399. It was never determined what went wrong with the diode array, however, it appears that it did not have an effect on the initial time of diode signal, but did have an effect on the peak voltage. This is illustrated in Figure IV.20 that plots the 0.5-mm-diameter copper 145 shots from MG VII. Shot 3393, 3394, and 3395 show a progressive drop in signal while shot 3403 was with the new diode array.

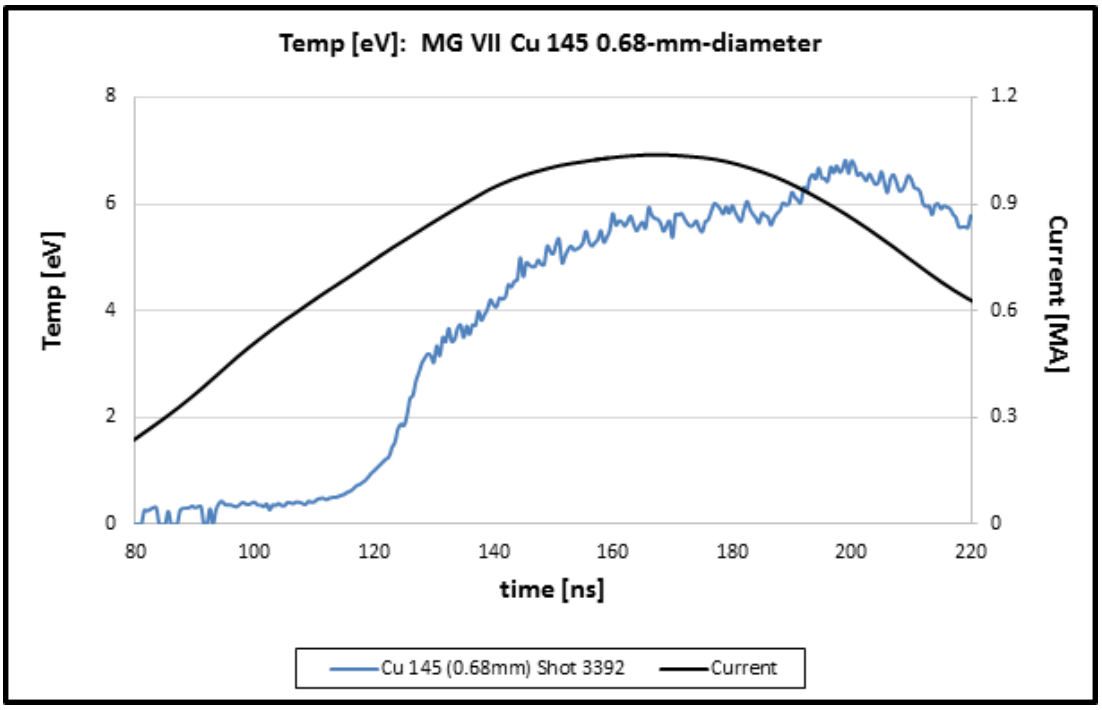

Figure IV.19 Copper 0.7-mm-diameter has a similar double hump in the diode signal. The 145 alloy showed signal at an earlier time than the copper 101 from MG VI.

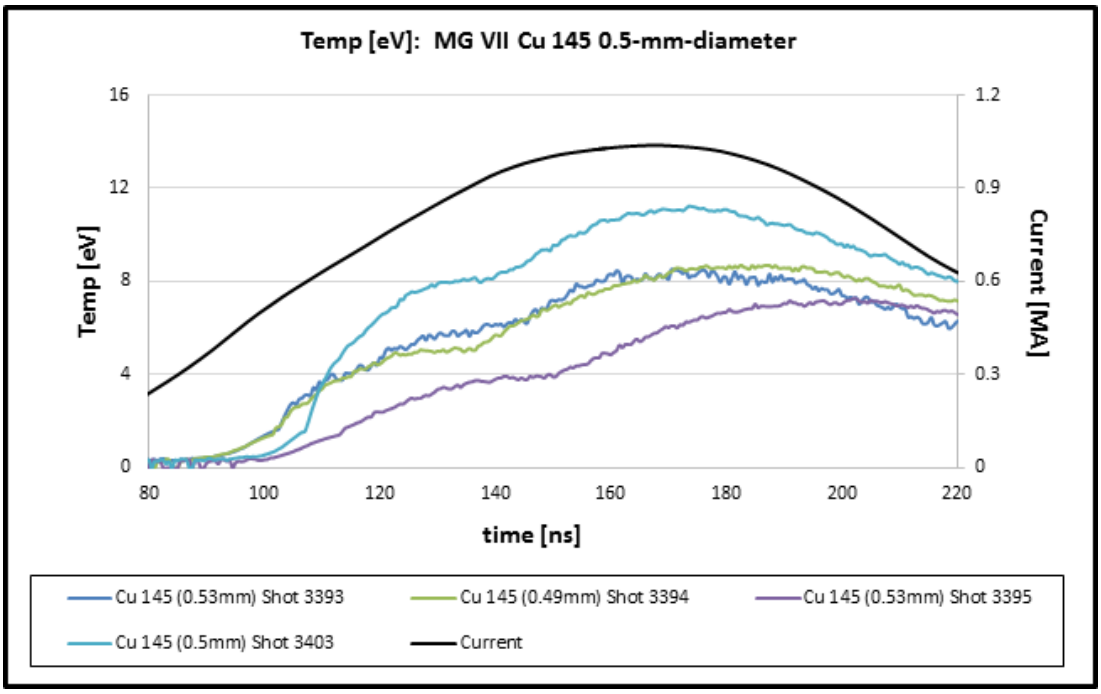

Figure IV.20 The copper 145 0.5-mm-diameter signals show a similar structure to that of the copper 101 0.5-mm-diameter. The initial rise in signal is earlier in time with a larger peak temperature. Only shot 3403 utilized a functioning diode array.

The time of surface plasma formation as determined by the sharp increase in signal on the diode turned out to be significantly different for the two alloys. For 0.7-mm-diameter copper, the 101 alloy showed a sharp increase between 130 and 140ns while the 145 alloy showed a sharp increase around 120ns. The dramatic difference between these two similar alloys made us believe there might be an error in the timing of one of our experiments despite the fact that the aluminum rods appeared to be forming plasma at approximately the same time for each experiment. The goal was to determine this in MG VIII by shooting 0.7-mm-diameter rods of both alloys on the same experiment to determine if they were truly different. Several rods of both alloys were shot, however, there were problems with these shots such that reliable data was not collected. The two copper 145 shots are plotted in Figure IV.21. These traces line up quite well with the one shot of the same alloy and diameter from MG VII. This gave us confidence that the copper 145 was likely correct, hovever, there was still doubt about the timing of the copper 101 from MG VI.

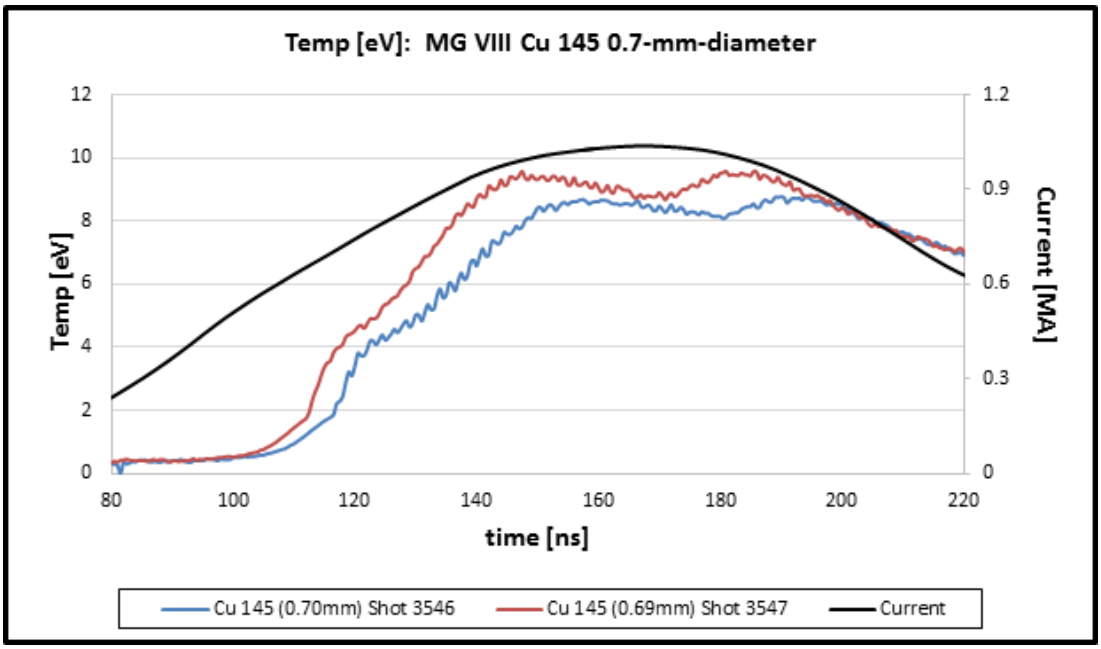

Figure IV.21 Copper 145 0.7-mm-diameter shots from MG VIII show similar times for plasma formation as was observed in MG VII.

The goal of MG IX was to add more diameters to the data set of copper 145 by shooting 0.7-, 0.8-, and 0.9-mm-diameter loads. A comparison with copper 101 was also desired on the same experiment as was attempted in MG VIII. The results of the copper 145 shots are shown in Figures IV.22 through IV.24. All shots before 3763 did not have the IR rejection filter on the PDA system and are marked in the legends of each of the plots. Two copper 145 rods were shot without the IR rejection filter and show a different structure in the diode signal. Figure IV.22 shows the temperature plots for two copper 145 shots with the IR rejection filter in place and two without the IR rejection filter in place. The peak temperatures vary from ~6-8.5 eV. There is a clear difference in the shape of the temperature signals past peak current. This difference in diode signal structure past peak current is not of great concern. The physical properties being studied are prior to, and near peak current.

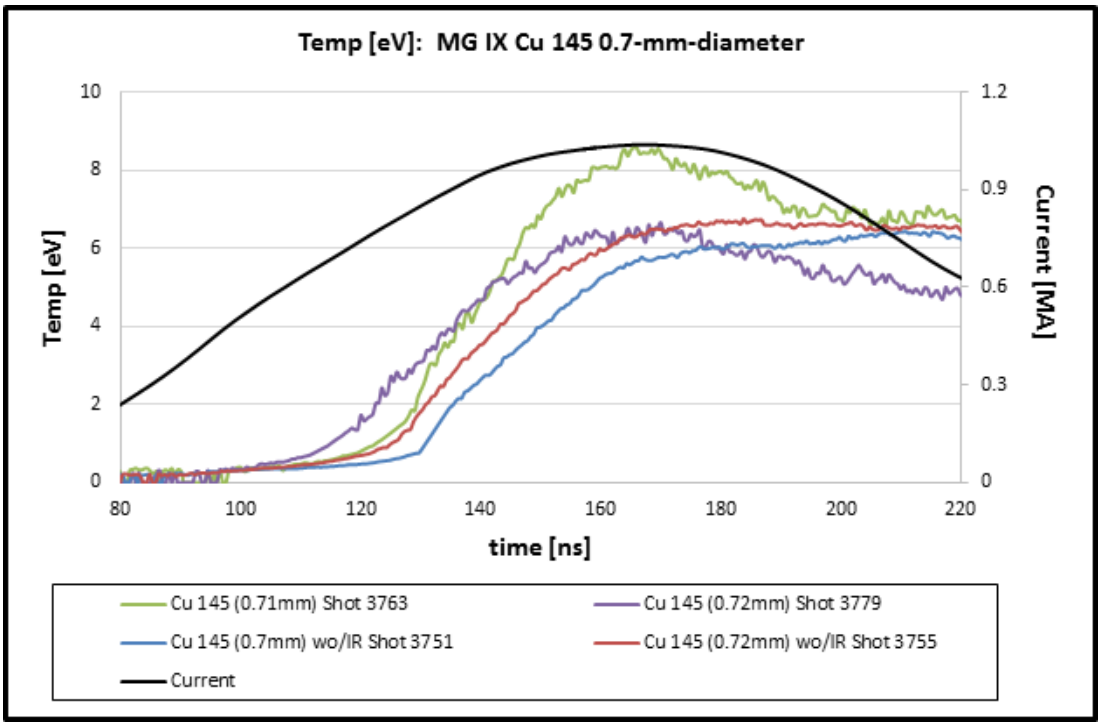

Figure IV.22 Copper 145 0.7-mm-diameter shots from MG IX with shots 3751 and 3755 not having the IR rejection filter in front of the diode array.

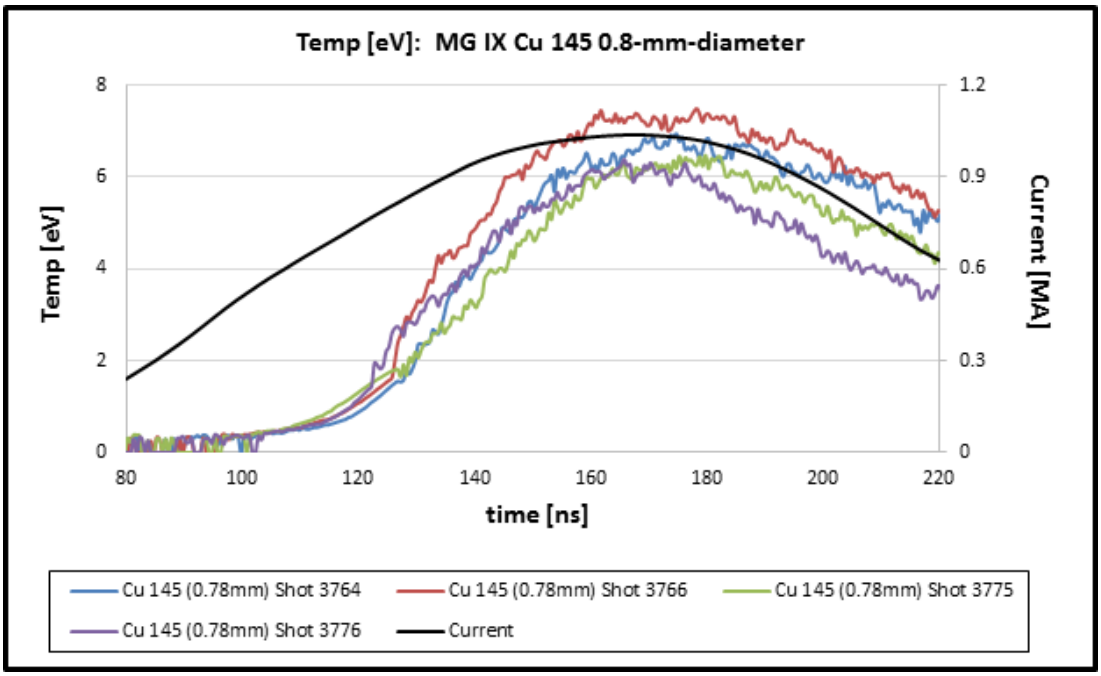

Figure IV.23 Copper 145 0.8-mm-diamter from MG IX show initial signals at similar times with peak temperature occurring at about 7eV.

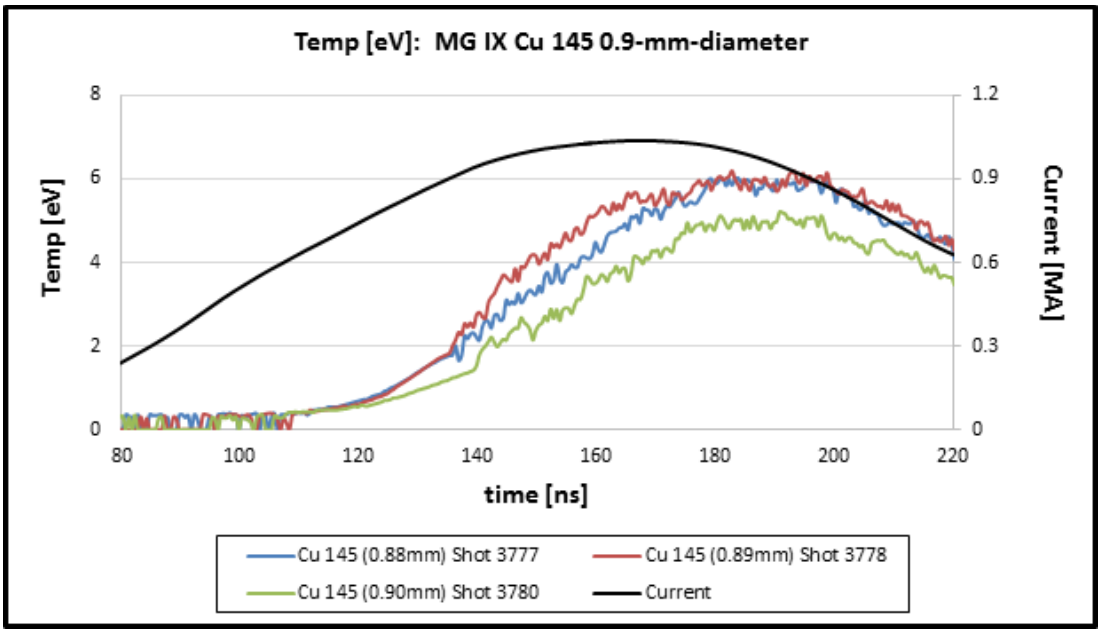

Figure IV.24 Copper 145 0.9-mm-diameter from MG IX show initial signals at similar times and peak temperature of about 6eV.

Several copper 101 0.7-mm-diameter rods were shot along with one 0.9-mm-diameter rod. The results of these shots are plotted in Figures IV.25 and IV.26. The copper 101 shots from MG IX had several difficulties with one shot flashing over as was observed by the ICCD cameras. The three successful shots are plotted in Figure IV.25. There is a spread in the time of initial signal of about 14ns. This spread is more than expected based on previous shots of copper.

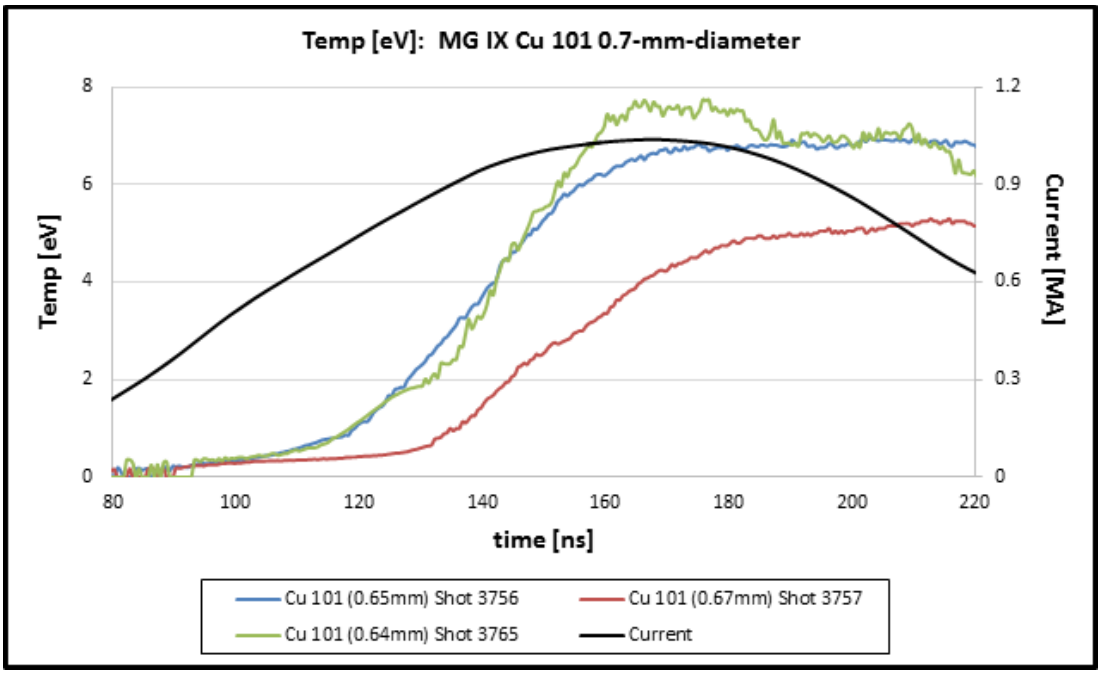

Figure IV.25 Copper 101 0.7-mm-diameter from MG IX show a spread in the time of initial signal as well as peak temperature.

The copper 101 0.9-mm-diameter temperature is shown in Figure IV.26. The temperature signal is similar to those observed in MG VI with 0.85-mm-diameter rods, with the rod forming plasma near peak current and peak temperature reaching only a few eV.

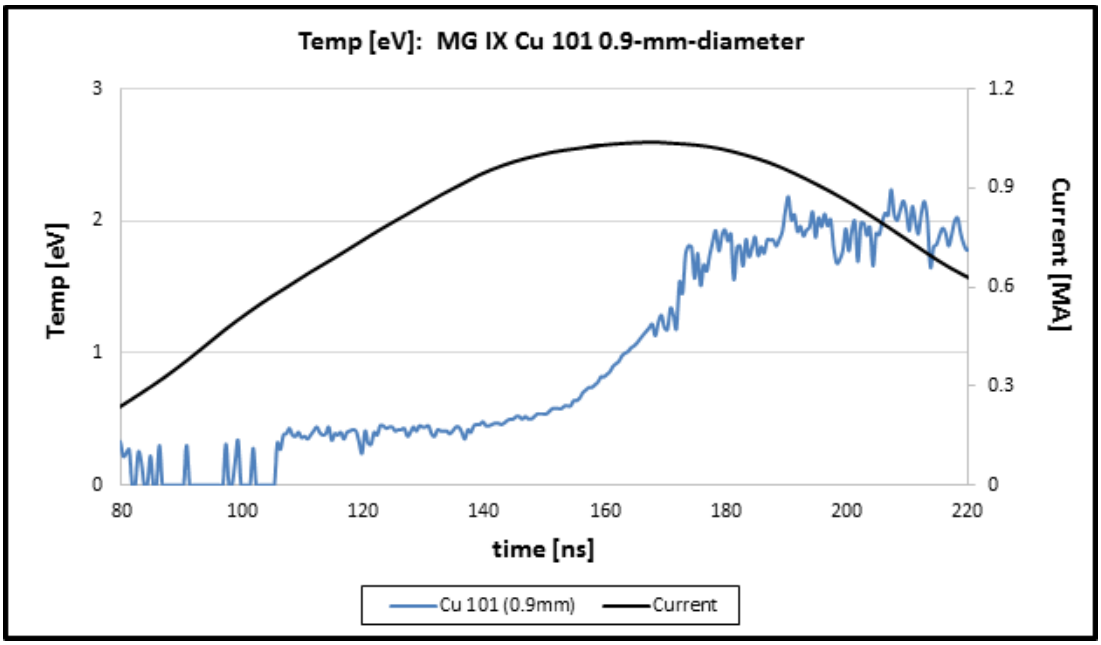

Figure IV.26 Copper 101 0.9-mm-diameter from MG IX formed surface plasma near peak current with a similar profile to that of similar diameter copper 101 rods shot in MG VI.

The results of all temperature curves for copper 145 and copper 101 rods are plotted in Figures IV.27 and IV.28 respectively. Each diameter is averaged, excluding the shots that did not have the IR rejection filter in front of the diode array. Both alloys show a trend of decreasing peak temperature with increasing initial diameter. The copper 145 rods were never machined to an initial diameter of 1.0-mm, so a direct comparison between copper 145 and 101 cannot be observed for this diameter.

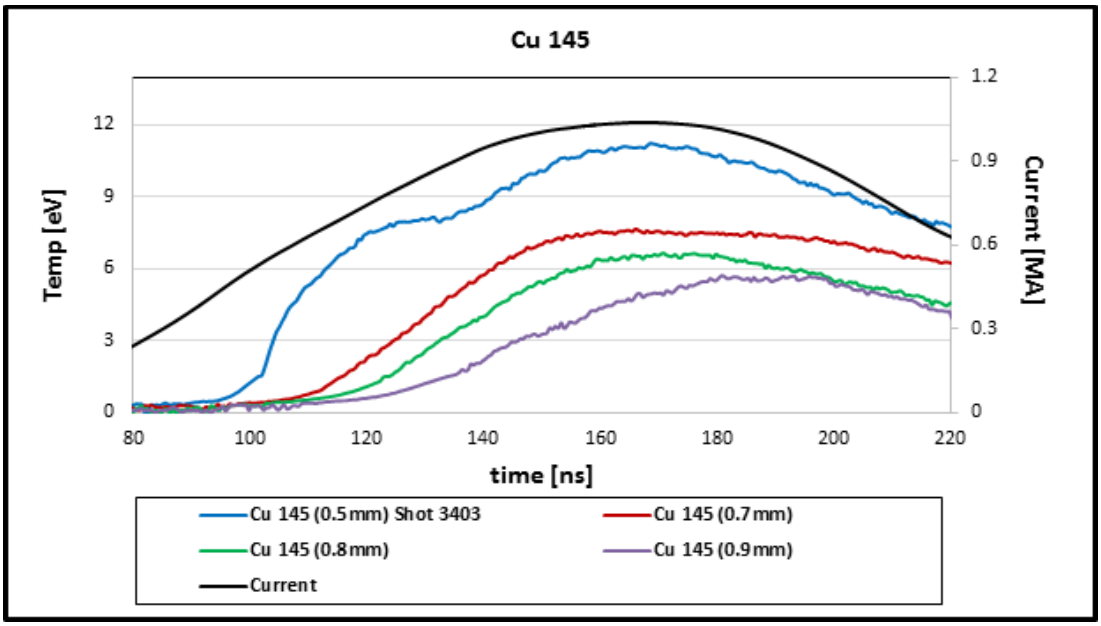

Figure IV.27 Copper 145 diode traces show a peak temperature that progressively gets smaller with increasing initial diameter. The time of initial signal also progressively begins later in the current profile with increasing initial diameter.

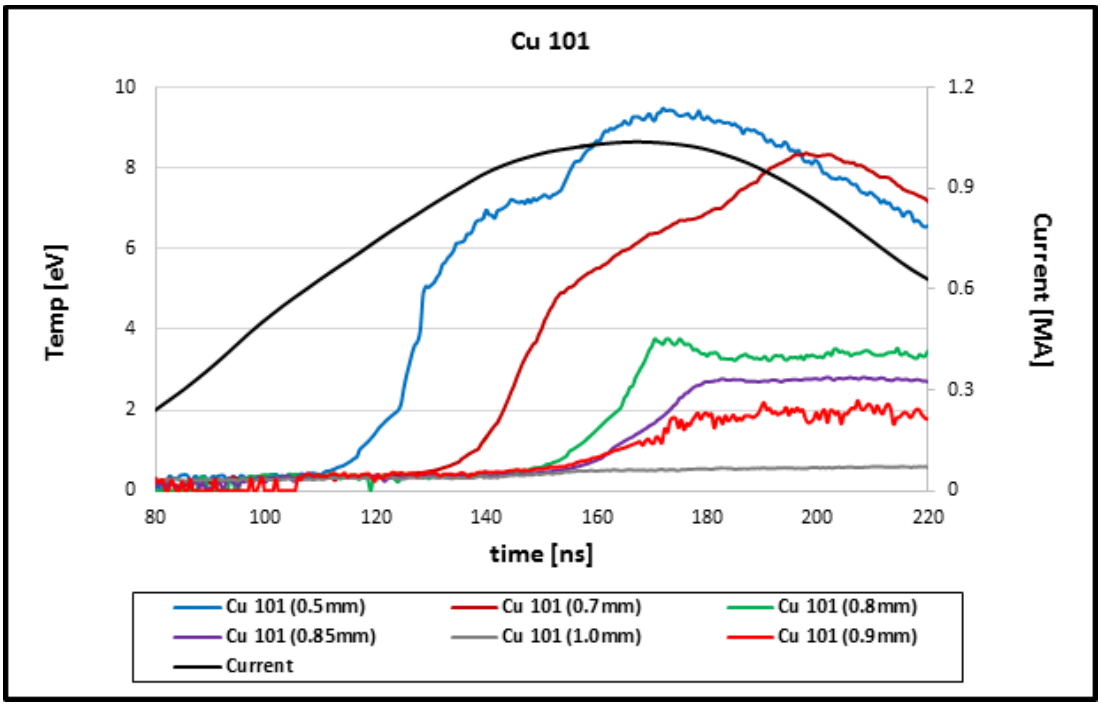

Figure IV.28 Copper 101 diode traces show a peak temperature that progressively gets smaller with increasing initial diameter. The time of initial signal also progressively begins later in the current profile with increasing initial diameter with the 1.0-mm-diameter show no substantial increase in signal.

Figure IV.29 plots the copper 145 and 101 alloys for initial diameters of 0.5- and 0.9-mm to illustrate the difference in temperatures for the two alloys. The difference is clear, with the copper 145 reaching greater peak termperature.

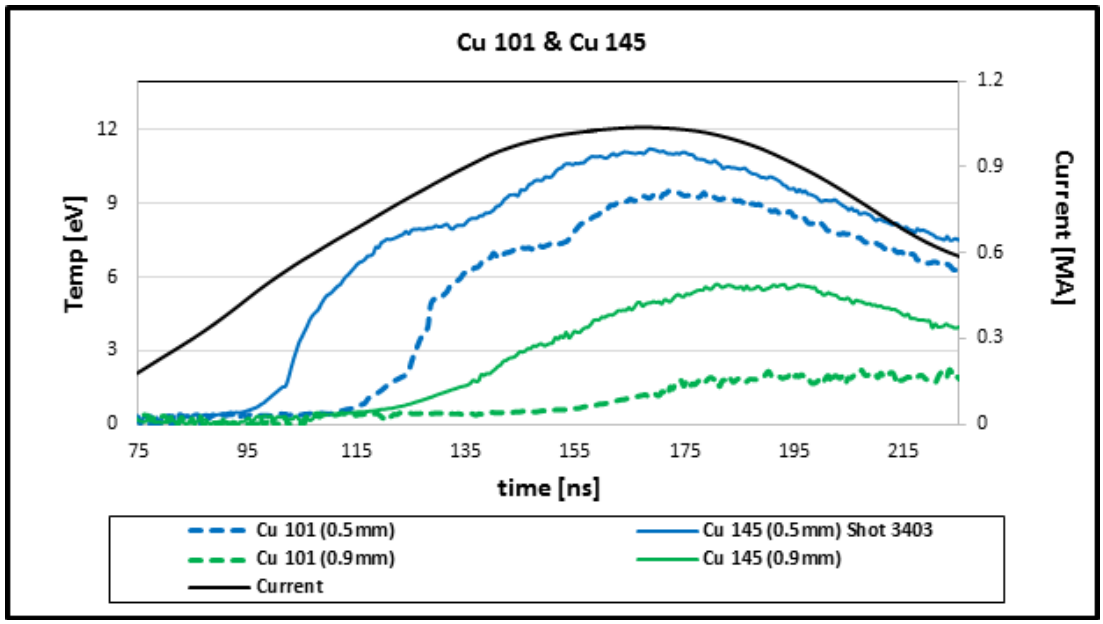

Figure IV.29 Comparing the peak temperature of several initial diameters of copper 101 and 145 shows a dramatic difference in temperature.

Figure IV.30 plots the initial voltage signals for the copper alloys for all the MG experiments. Once again, the signals have been averaged for each diameter and the few shots that did not employ the IR rejection filter are not included in this illustration. The copper 145 and 101 are represented by the blue and red traces respectively. A clear shift in the time of plasma formation is observed for each diameter as the alloy is changed, with the copper 145 forming plasma earlier than copper 101.

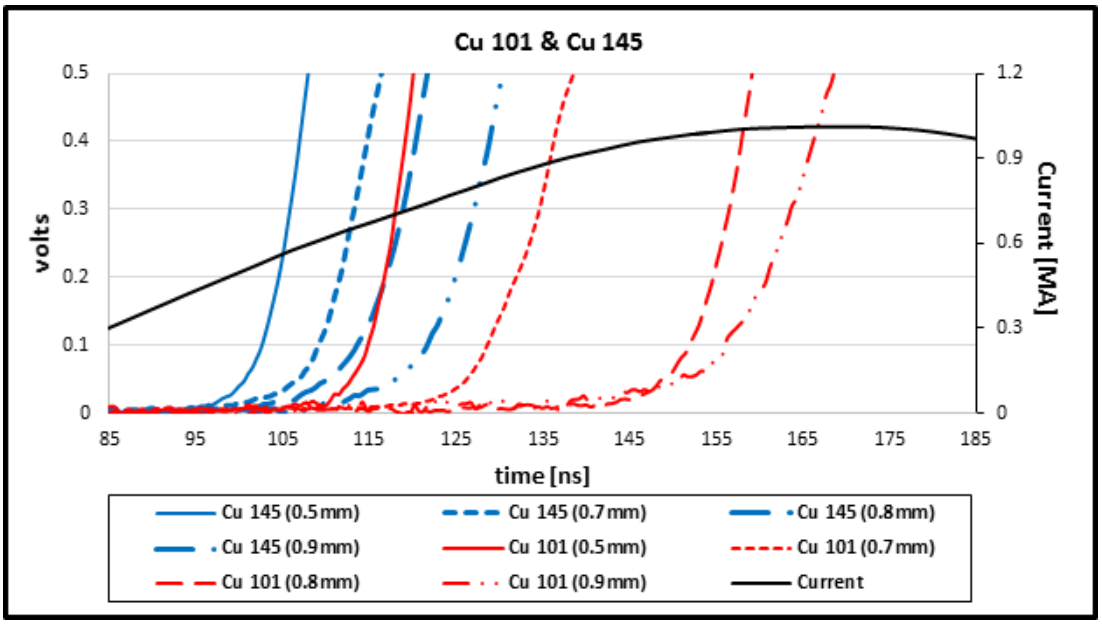

Figure IV.30 The time of plasma formation (abrupt increase in temperature) is dramatically different for the two copper alloys, with copper 145 (blue traces) forming plasma earlier in the current profile than the copper 101 (red traces).

To determine a quantitative time of plasma formation, a technique needed to be utilized that allowed for the filter type to have no systematic effect on the time of plasma formation. Using a specific voltage or temperature to determine time of plasma formation could lead to questionable results as the alloy is varied, with the equation of state not being certain for different alloys. Using the sharp increase in voltage and temperature is a consistent way of determining the time of plasma formation. However, the actual point at which the temperature begins to increase suddenly is spread over several ns for both filtering sets. For both filtering configurations, there was a ramp that lead to a sudden increase in termperature, with the lack of the IR rejection filtering providing a longer and larger amplitude ramp as discussed earlier in this chapter. The profile near time of plasma formation can be split into three parts: the ramp, the sharp increase in signal, and the linear rise in temperature shortly after plasma formation. A line can be fit to the first and last profile sections with the intersection of these two lines providing the time of plasma formation. An example of this mathematical procedure is illustrated in Figure IV.31 for a copper shot that did not have the IR rejection filter fielded in front of the diode array.

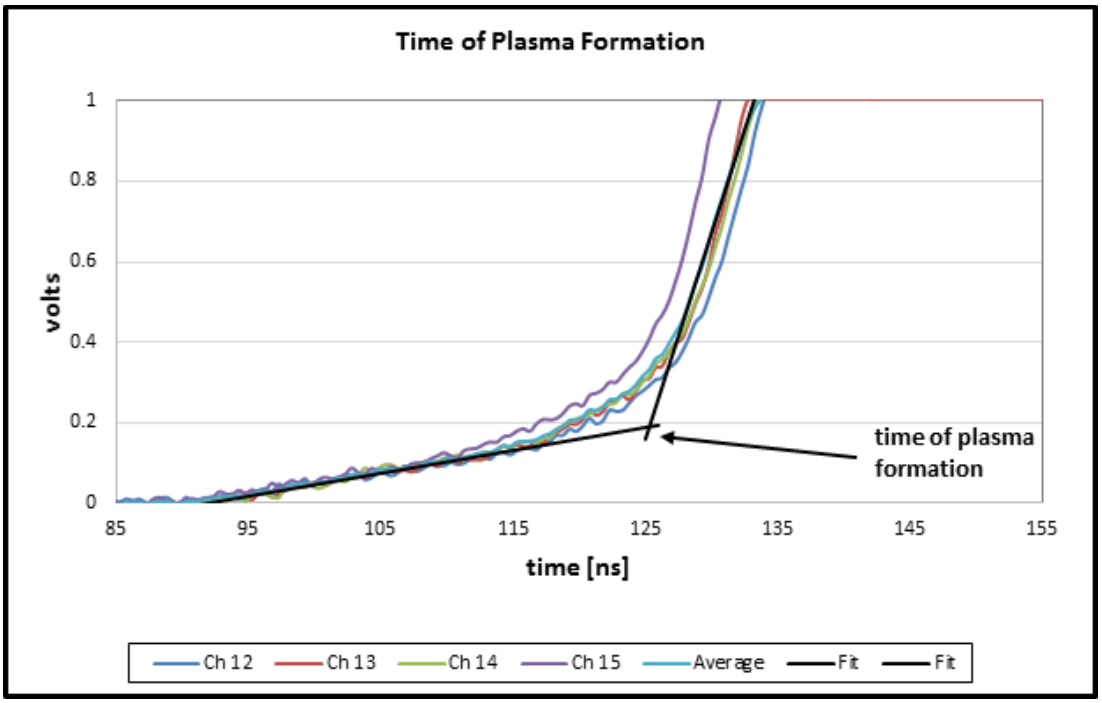

Figure IV.31 Time of plasma formation is determined by fitting lines to the two linear sections of the diode signal and determining the time at which these two lines intersect.

Time of plasma formation is determined by the intersection of the two lines. Qualitatively looking at the voltage traces, we can see that the intersection falls in a part of the voltage rise that would be near the middle of the second part of the profile. The uncertainty is determined by the length of the second part of the voltage profile, and is usually between 4 and 8 ns for the shots that did not have the IR rejection filter, and about 3 to 4 ns for those shots that did field the IR rejection filter. This provides an uncertainty in the range of ±2 to ±4ns for shots without the IR rejection filter and ±2ns for those shots with the IR rejection filter.

Without the IR rejection filter in place, a voltage signal is measured for 10s of ns before plasma formation as shown in Figure IV.32.

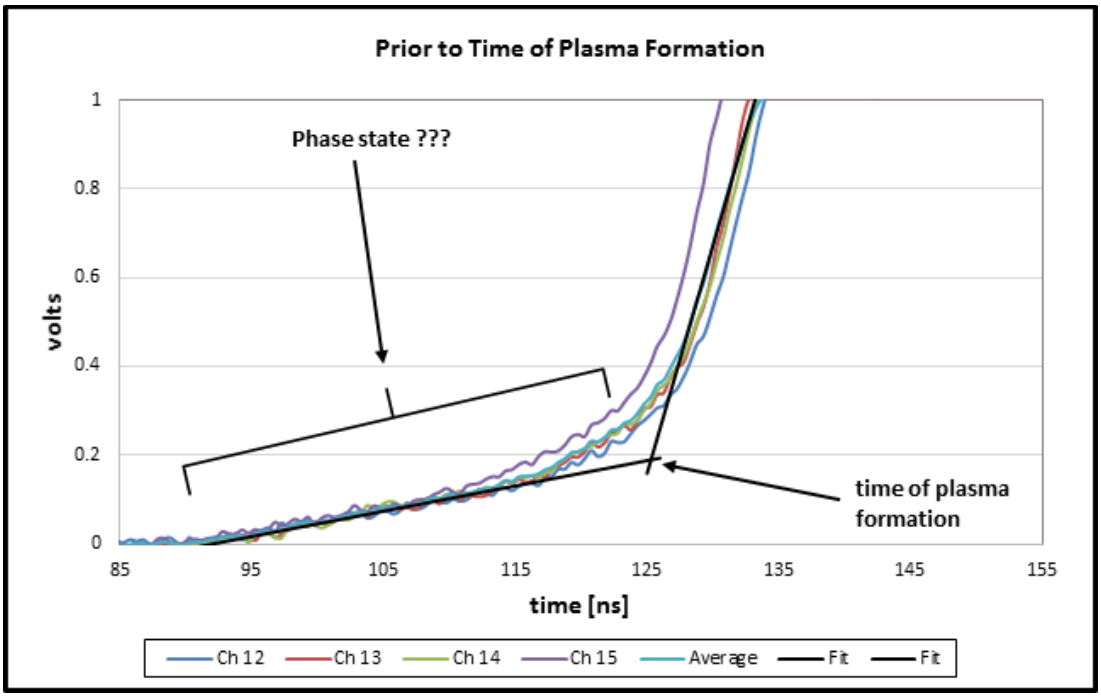

Figure IV.32 A voltage signal is observed several ns prior to plasma formation.

A zoomed-in image of the voltage is shown in Figure IV.33 and shows the initial signal to be observed at ~92 ns with the signal being too weak and/or buried in the electrical noise of 0.02 volts prior to this time.

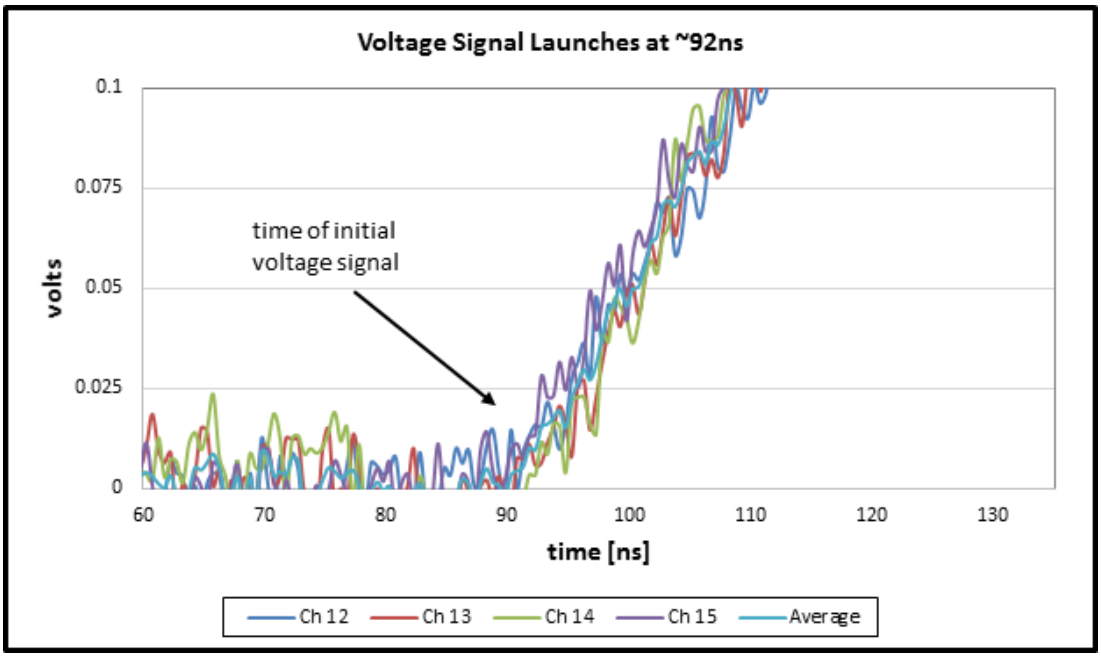

Figure IV.33 The voltage signals in the diode array are limited by a noise level of ~0.02 volts.

The earliest signal measured corresponds to a surface temperature of ~0.23 eV if the surface is assumed to be radiating as a blackbody. The early time temperature evolution is illustrated in Figure IV.34. The temperature estimate determined with the blackbody assumption provides a lower temperature bound that indicates the rod to be in a vapor or biphase state from that point until the time of plasma formation. This illustrates the desire to not use the IR rejection filter on future experiments, allowing for more sensitivity prior to plasma formation. A comparison between different alloys and filtering sets will be presented at the end of this chapter.

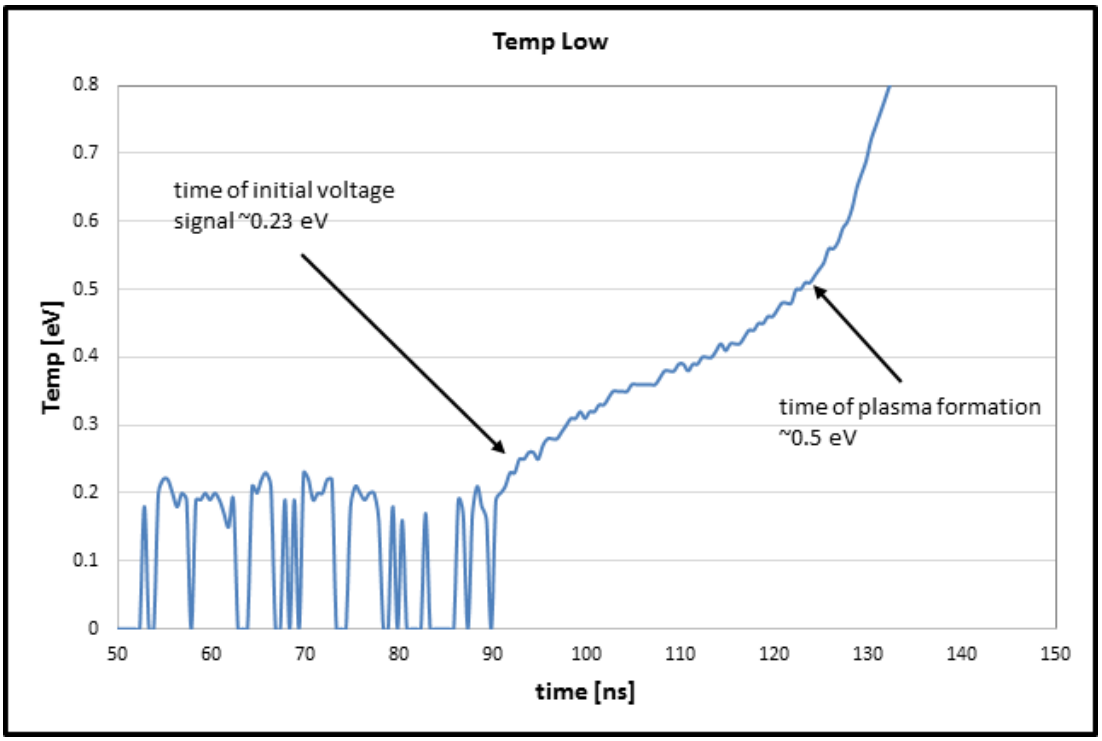

Figure IV.34 The initial time of voltage signal corresponds to a temperature of ~0.23 eV.

Titanium II rods were fired on MG VII and IX experiments. The initial goal was to have rods of initial diameters 0.75- and 1.0-mm-diameters. Due to the difficulty in the machining properties of titanium, one of the rods came out to be undersized at 0.67-mm-diameter. Figure IV.35

illustrates the temperatures for all titanium rods shot. Despite the difference in initial diameters, the peak temperatures of all titanium rods approaches a similar value, with the small diameter titanium rod (0.67-mm) reaching ~12.5 eV and the large diameter titanium rod (1.05-mm) reaching ~15 eV. In comparison to copper 101, the difference between 0.7- and 1.0-mm-diameter was 8 eV and a fraction of an eV (1.0-mm did not form plasma) respectively. There is one shot of titanium (shot 3761) that does not reach a temperature comparable to the other shots. This is likely due to a misalignment of the array such that the load was not completely covering the array elements during the shot.

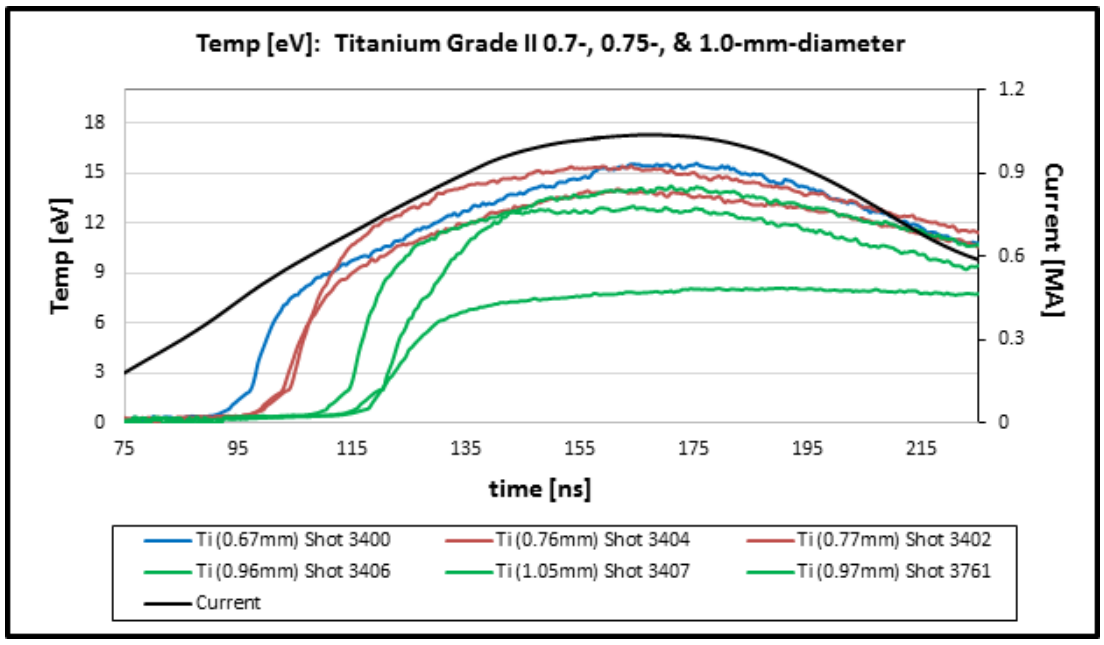

Figure IV.35 Titanium rods shot in MG VII and IX experiments show peak temperature ranging from 12.5 to 15 eV for initial diameters ranging from 0.67-mm to 1.05-mm.

The voltage signals for all titanium shot are shown in Figure IV.36. The same trend is observed with titanium as was observed for copper alloys with the time of plasma formation occurring earlier in time with decreasing initial diameter. Shot 3761 did not have the IR rejection filter attached and shows a long ramp in Figure IV.36 as was observed with other metals.

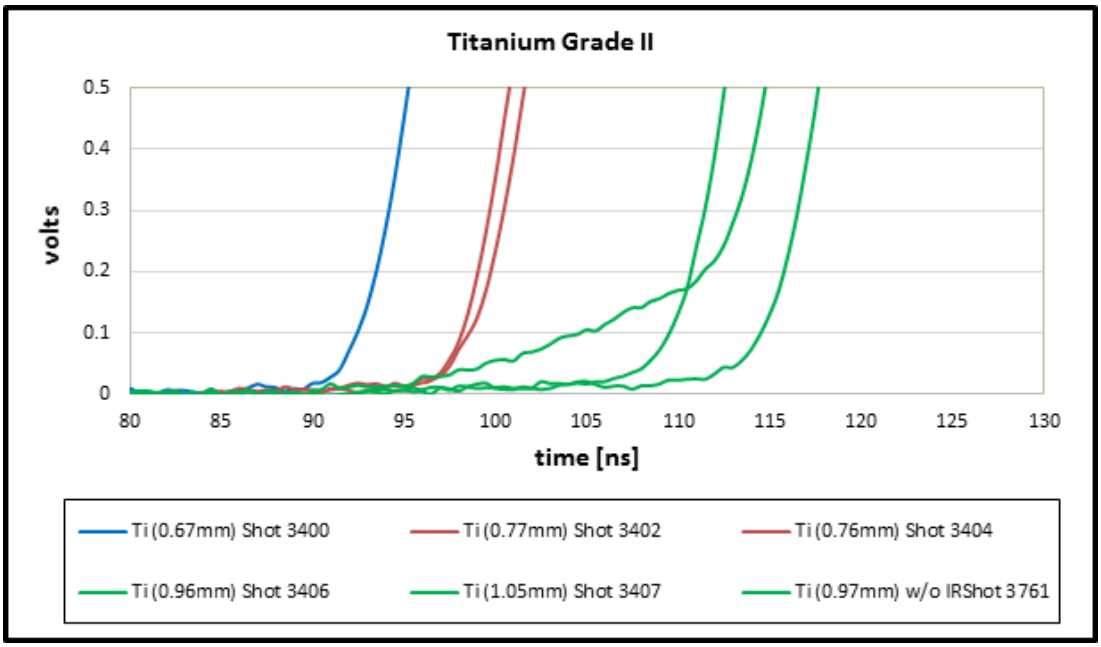

Figure IV.36 The voltage signals of titanium illustrate the time of plasma formation for different initial diameters with time of formation occurring earlier for decreasing initial diameter.

Nickel 200 rods were shot on MG VII and IX with one rod being shot on each experimental campaign. The results for 0.75-mm-diameter rods are illustrated in Figure IV.37 with the temperature reaching ~11 eV for shot 3401 and ~7 eV for shot 3761. The apparent low signal observed for shot 3760 is thought to be a misalignment of the array as was observed with the titanium shot 3761. Figure IV.38 illustrates the time of plasma formation for the nickel 200 shots with the voltage signal showing a large ramp for the shot that did not have the IR rejection filter in front of the diode array.

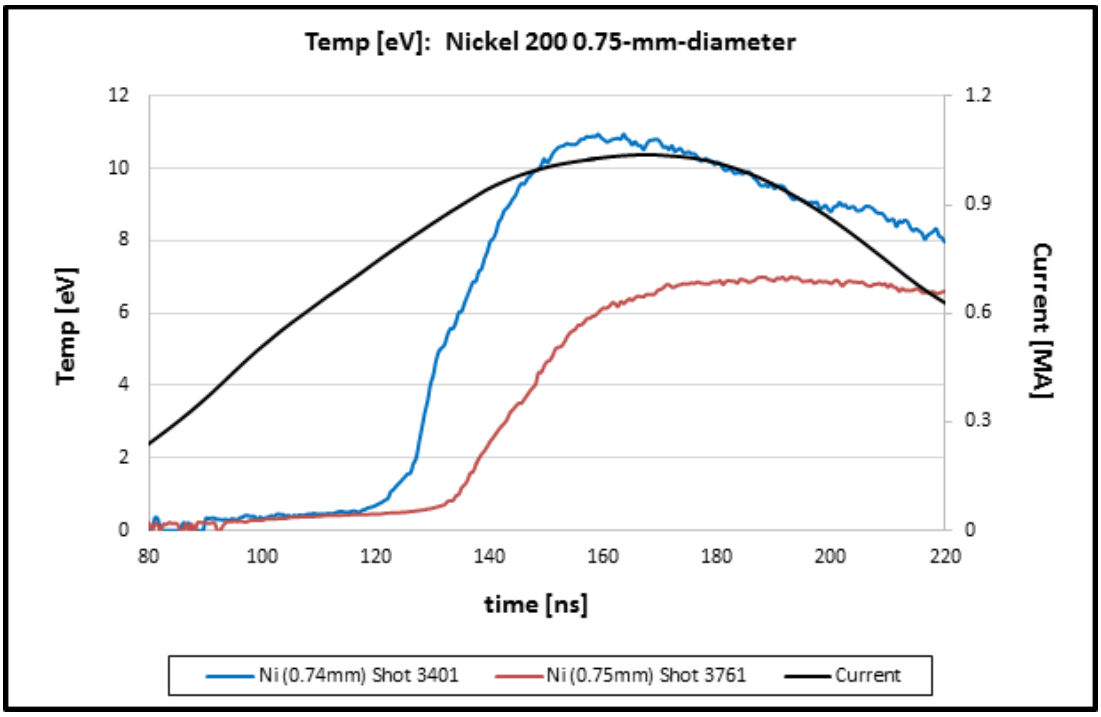

Figure IV.37 Nickel 200 0.75-mm-diameter rods have peak temperatures of 11 eV and 7 eV, indicating a likely misalignment of the array on shot 3760.

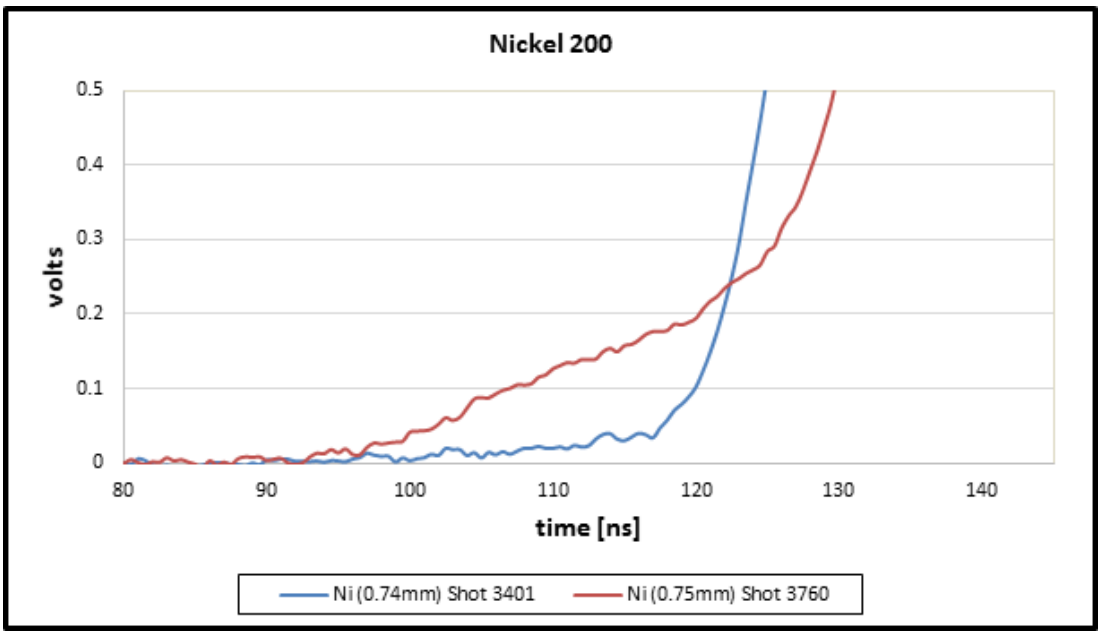

Figure IV.38 The Nickel 200 rods form plasma near 120-125ns with a long ramp observed for the shot (3760) with no IR rejection filter in front of the array.

A comparison between the voltage signals early in time and the temperature profiles is illustrated in Figures IV.39 and IV.40. The titanium alloys shows the greatest difference with the time of

plasma formation occuring 10s of ns prior to all other alloys and reaching a peak temperature of several eV greater than all other alloys.

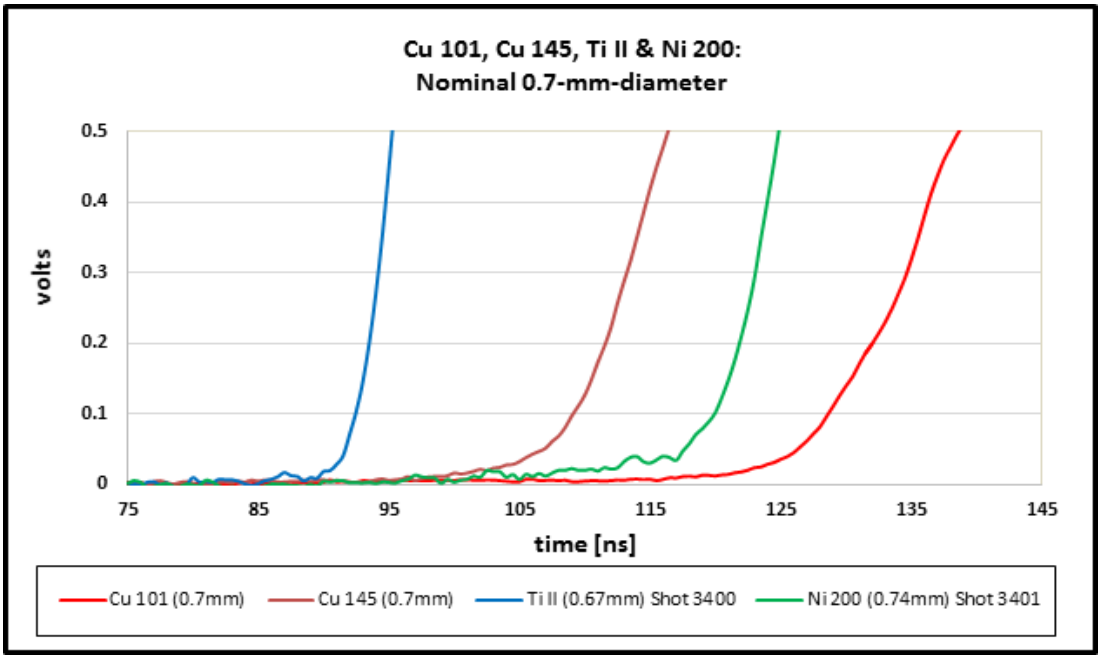

Figure IV.39 The diode signals for the four alloys show a dramatic difference in time of plasma formation with the titanium rods forming plasma 10s of ns before the other alloys.

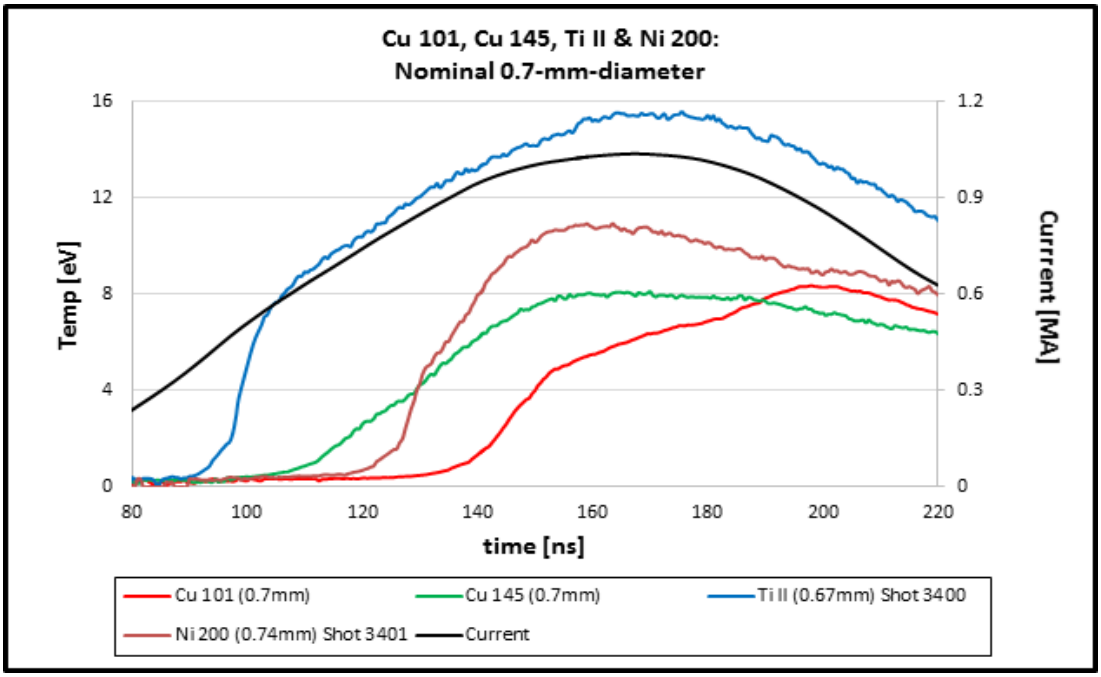

Figure IV.40 The temperature profiles of titanium II, nickel 200, copper 101, and copper 145. The titanium shows a dramatic difference in peak temperature from the other alloys.

Earlier in this chapter, the process utilized to determine the time of plasma formation was discussed. The time was determined by finding the intersection of two lines fit to the early linear ramp region of the signal and the sharp linear rise region of the signal. This process gives a temperature range at the time of plasma formation, as follows. The temperature is first calculated by assuming a blackbody (emissivity=1) and then calculated by assuming the emissivity is the same as the metal when it is in the solid state. Figure IV.41 is a plot of temperature at time of plasma formation as a function of initial diameter for Cu 101, Cu 145, Ni 200, and Ti II. The circles are for all data that was collected with the IR rejection filter in place and the triangles are for data that was collected without the IR rejection filter in place. The data that was collected without the IR rejection filter in place demonstrate a clear trend towards lower temperature estimates at time of plasma for all alloys.

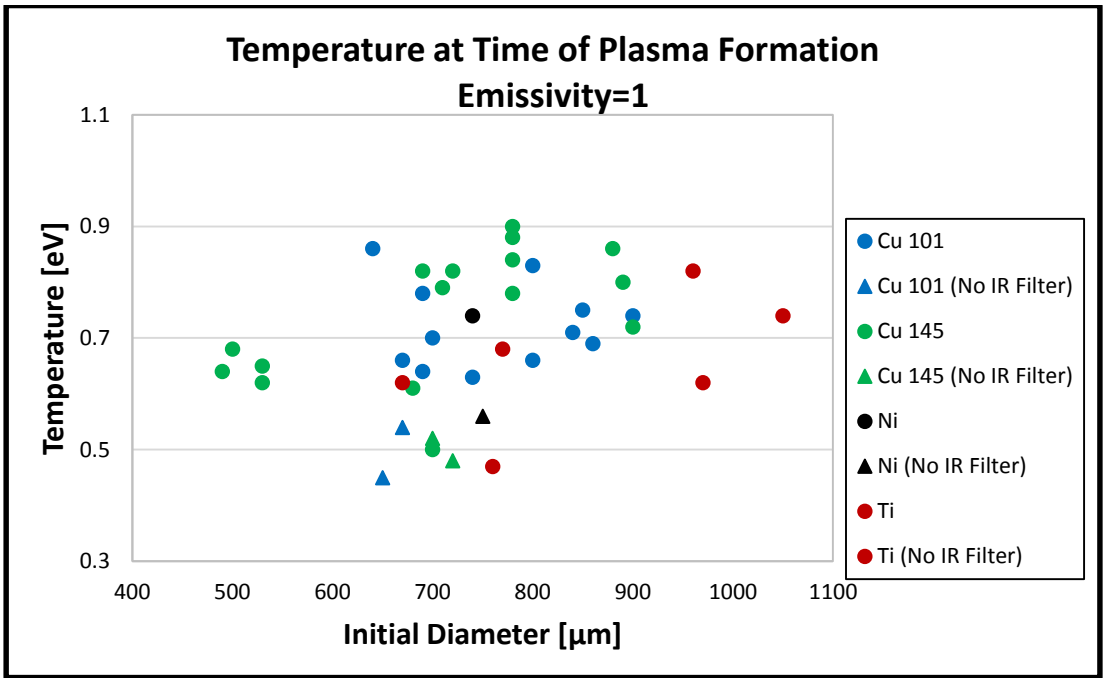

Figure IV.41 The temperature at time of plasma for all alloys determined by the diode and assuming emissivity of 1.

Figure IV.42 plots the same data but uses the solid state emissivity for Cu 101 (0.1), Cu 145 (0.1), Ni 200 (0.3), and Ti II (0.3). A separation is observed between the copper and the nickel and titanium alloys as would be expected for the different emissivities that were used in the calculation.

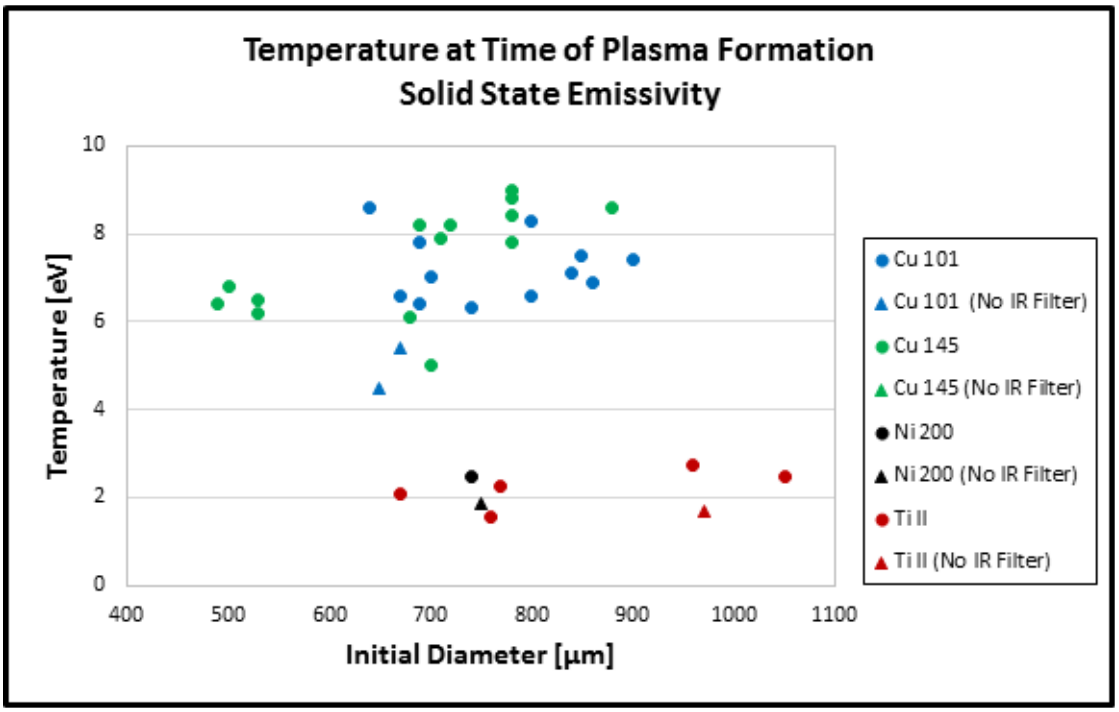

Figure IV.42 The temperature at time of plasma for all alloys determined by the diode and assuming emissivity is the same as solid state emissivity for each alloy.

Table IV.2 lists the data that is plotted in the above figures with the average temperatures taken for each alloy for a particular filter set as well as the assumed emissivity. The average temperatures for all alloys with and without the IR rejection filter in place are the same within one standard deviation when the emissivity is assumed to be one. When the emissivity is taken to be the same as when in the solid state, the difference in average temperatures between the copper alloys and the nickel and titanium alloys is a factor of 2 to 3. For all alloys, the temperature at which plasma forms (according to the process utilized) is between 0.5 and 7.5 eV. The ICCD images shown in Chapter III show good correlation between the images and the diode signals.

The sharp rise in the diode signal (time of plasma formation) corresponds well with the time of filaments. The dots and glowing rod observed early in time corresponds to the time of the early ramp when there is no IR rejection filter. To understand the phase of the region near this sharp increase in signal, knowing the stability and expansion of the surface would be valuable. This will be done next with laser shadowgraphy.

	Average Temp (ε=1) w/IR Rejection Filter [eV]	Standard Deviation [eV]	Average Temp (ε≠1) w/IR Rejection Filter [eV]	Standard Deviation [eV]	Average Temp (ε=1) w/out IR Rejection Filter [eV]	Average Temp (ε≠1) w/out IR Rejection Filter [eV]
Cu 101	0.72	0.07	7.2	0.7	0.49	4.9
Cu 145	0.74	0.11	7.4	1.1	0.50	5.0
Ni 200	0.74	N/A	2.5	N/A	0.56	1.9
Ti II	0.67	0.12	2.2	0.4	0.50	1.7

Table IV.2 The average temperature for each alloy at the time of plasma for emissivities equal to one and the solid state emissivity.

Chapter V: Surface Expansion, Development and Evolution of Instabilities

Surface expansion velocity and surface magnetic field were determined by timed resolved measurement of the load radius as a function of time. The measurements of the load radius, R(t), were made using laser shadowgraphy in both the 266 nm wavelength as well as the 532 nm wavelength. Our original goal was to use only the 532 nm Ekspla laser for shadowgraphy, but with failure of the laser to work on multiple occasions, Dr. Ivanov adapted the 266 nm Ekspla laser to be used for shadowgraphy as well as interferometry. Work will be presented showing the expansion speeds of copper 101, copper 145, titanium grade II, and nickel 200. Data showing z-pinch instabilities will be presented using both laser shadowgraphy as well as visible light emission observed using the 12-frame Hadland and a 16-frame SIMX intensified CCD cameras. These two cameras are also used to determine expansion rates, but as will be seen, the shadowgraphs are much more reliable.

This chapter will first describe the diagnostics used in our experiment to study expansion rates. A detailed explanation of the method of analyzing the data for each diagnostic as well as the sources of error for each will be discussed. An interpretation of this analysis will be used to describe the surface plasma as it is pinched against the load surface and then radially accelerated outward as it passes peak current. Analysis of the development and evolution of the z-pinch instabilities shall be presented with possible seeding mechanisms discussed.

Section V.A: Diagnostic Overview

Laser Shadowgraphy: 532nm

The radius of a rod during a shot was determined by backlighting the load with a short pulse laser, a method commonly known as shadowgraphy. The pulses were captured by relay lenses outside of the vacuum chamber and relayed to CCD cameras in a protected screen box. The source is an Ekspla manufactured Class IV Nd:YAG laser. The laser is a 532 nm wavelength, 100 mJ pulse with a pulse length of 150 ps. The laser pulse is split in multiple places and travels along different paths of different lengths, allowing for images to be captured at different times on a single shot of Zebra. We captured two images using the 532 nm Ekspla laser with pulses separated by 15ns or 25 ns, depending on the experiment. The two paths were created by having the laser pass through a half wave-plate and then a split polarization cube. By continuing to pass the light through beam splitting cubes, multiple paths with different path lengths are created. A glan prism is placed in the laser path to avoid mixing of different polarizations and hence laser light from different paths. The design of the optics is such that the delay between the two laser pulses can be varied between a few ns up to approximately 25 ns. The larger spacing between the pulses was picked for two reasons:

1) The larger the separation between the two pulses, the smaller the error bars will be for the expansion speed.
2) The large separation is desired for the purpose of covering a large section of our current rise time. If the current rise time was significantly smaller, a smaller delay would likely be necessary.

The 15ns spacing used on three of the experiments was done so to allow for more data points at different times of the current profile to be attained within the region of the linear rise by changing the delay cables from shot to shot. The CCD cameras used for capturing the shadowgraphy images were Finger Lakes Instruments cameras with 2054×2054 pixels. Given our small magnification the images had approximately 3.8 to 10 microns per pixel, depending on the experiment. The magnification was determined by imaging a 4-40 bolt as well as a resolution reticle.

Laser Shadowgraphy: 266nm

The experiment utilized a 532nm laser for two-frame laser shadowgraphy and a 266nm laser for laser shadowgraphy and interferometry. The 532nm laser had pulse separation of 15ns while the 266nm laser had a pulse separation of 33ns. This work was done primarily by Dr. Ivanov with the help of his students Austin Anderson, Sara Altemara and Daniel Papp.

SIMX, and Hadland ICCD cameras

To capture the visible surface emission of the loads, a 12-frame Hadland intensified CCD, and a 16-frame SIMX intensified CCD were fielded. The Hadland and SIMX were time gated for 5 and 4 ns respectively. The Hadland camera had a green Wratten filter as well as an IR rejection filter placed in front, to allow for greater spatial resolution during the MG VI campaign. Only a green notch filter to filter out Ekspla was used in front of the SIMX camera. An intensified CCD camera allows us to capture images that would otherwise be too dim to observe through its high-gain intensifier. The load is imaged to the photocathode where the photons are converted to photoelectrons. These electrons are accelerated by an applied electric field into a Microchannel Plate (MCP). The MCP is a disk honeycombed with channels that the photoelectrons with cascade down, causing secondary emissions via the large potential difference set across the channels. The

electrons will then be accelerated by another electric field to a phosphor plate where they are converted into photons. A fiber optic output couples the phosphor to the CCD for image recording. The multi-frame images allow for several images to be taken on a single shot of the same rod, reducing any error that may be introduced by shot to shot variation.

Section V.B: Results of Laser Shadowgraphy

Expansion speed using Ekspla laser shadowgraphy

To determine the expansion rate of the loads, the data from two shadowgraph images separated in time was analyzed. The images were processed using the image processing program ImageJ. This program allowed the images to be processed into an Excel spreadsheet and analyzed. The first step is to open the image in ImageJ. With the cursor, a square area around the shadowgraph of the load can be outlined as shown in Figure V.1. This area is then summed up by the program and can be exported into Excel. The radius is determined by first removing any DC shift in the image. This is done by averaging the values along the length of the shadow, where the values should be zero, and subtracting this value from the entire lineout. Once this is done, the right and left edge of the load can be found. Figure V.2 illustrates how this is done. The values of the top of the left edge, A, and the top of the right edge, B, are found and then divide by two to determine the full width half max. With the resolution in micron/pixel known, the radius can be determined.

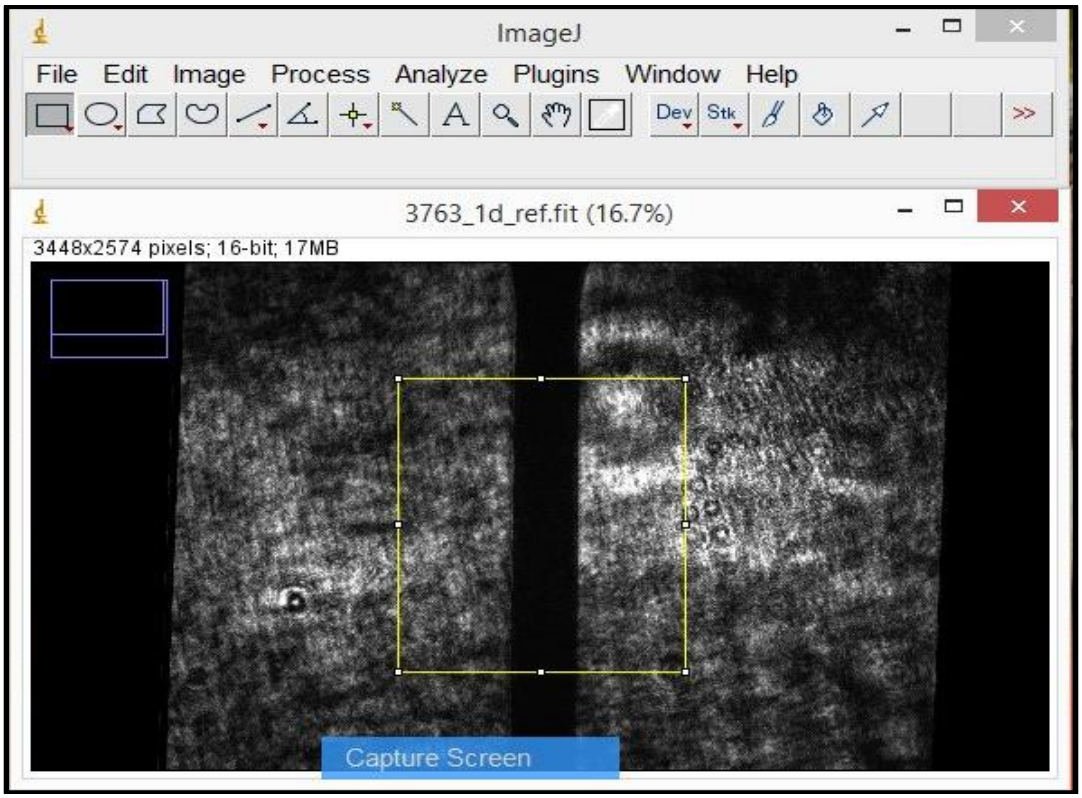

Figure V.1 The shadowgraph image can be imported into ImageJ and a lineout can be taken by drawing a square around the load with the cursor. Selecting the Analyze tab followed by Plot Profile produces a line out that can then be exported into Excel.

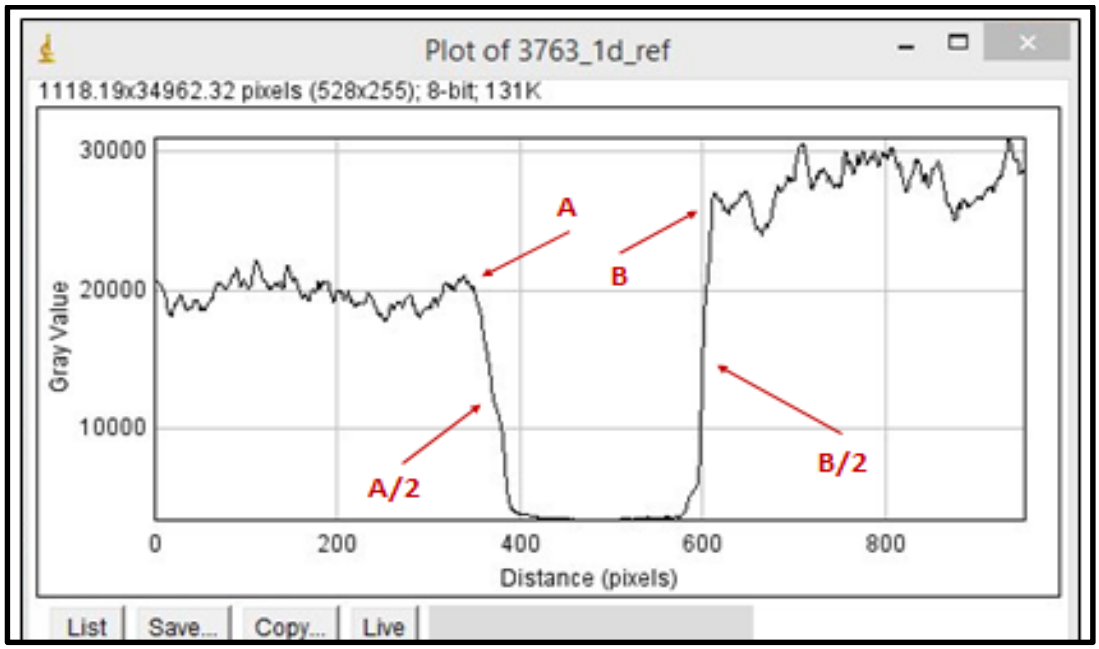

Figure V.2 The rod radius can be determined in Excel by finding the full width half maximum of the rod profile.

Plots of experimental results are shown below. The initial rod diameters were determined with microscope images. Each rod was imaged with backlighting and frontlighting. The lineouts were taken of the backlit images and exported into an Excel spreadsheet. The magnification of the microscope image was determined with a lineout of an Air Force Resolution Target image. The resolution was determined to be 3.2 to 3.4 μm/pixel for all campaigns. The error was determined to be less than a pixel because the edge of each image was only 2 pixels wide. The initial diameter is also determined with lineouts of preshot shadowgraphs for comparison to the microscope images and to verify the magnification is not changing from shot to shot in the shadowgraph optical path. The change in diameter is then determined with the lineouts of the shadowgraphs captured during a shot. The change in radius is then determined by taking the difference between preshot and shot shadowgraph diameters and dividing by 2. In Figures V.3-V.6 the copper 101 1.0-mm-diameter rod expansions have been illustrated with the change in radius versus time plotted along with the current profile. Figure V.3 plots the 532 nm laser shadowgraph radius of copper 101 1.0-mm-diameter for each shot with a line fitted to each shadowgraph pair for an individual shot. The expansion of the rod does not change past peak current due to the lack of plasma formation as determined by the diode array as discussed in chapter IV. For rods that form plasma, the expansion rate of the rod surface should accelerate due to the *dB/dt* changing sign. A trend toward faster expansion is observed near peak current between 150 and 170 ns. This time in the current trace is associated with the time of dB/dt becoming negative. This provides a decrease in magnetic pressure as the current in the rod (and thus the surface magnetic field strength) decreases. The negative dB/dt leads to an increase in area enclosing the magnetic field lines as discussed in Chapter I.C and equation I.44. With the electrons tied to the magnetic field lines (not ideally tied to the field lines since this is not Ideal

MHD as shown by equation I.49), the charged surface particles accelerate radially outward with the expanding magnetic flux.

Figure V.4 shows a plot of the 1.0-mm-diameter data with a line fitted to the data points. This process gives an expansion of ~3.3 μm/ns with an $R^2=0.9354$. According to Excel help menu, "the r-squared value can be interpreted as the proportion of the variance in y attributable to the variance in x[106]." It is found mathematically with the following equation:

$$R = \frac{\sum_i^n (\bar{x}-x_n)(\bar{y}-y_n)}{\sqrt{\sum_i^n (\bar{x}-x_n)^2 \sum_i^n (\bar{y}-y_n)^2}} \quad \text{(V.1)}$$

The closer the R^2 is to 1, the more accurate the fitted line is to the data points.

Figure V.5 plots the data points for copper 101 1.0-mm-diameter expansion using the 266 nm laser with a line fitted to the data. These shots only had one data point per shot with the 266 nm laser because it was currently only being fielded in parallel with the 266 nm interferometry and had not had the delay system set up yet for a second beam path. Figure V.6 plots data from the 532 and 266 nm laser. The data lines up quite nicely, however, the fitted lines suggest a different expansion for the two lasers; 4.1 μm/ns for the 266 nm laser and 3.3 μm/ns for the 532 nm laser. The difference between the two is due to the data points in the 532 nm plot that have nearly no expansion bringing the expansion speed down. This will be modified later in this chapter.

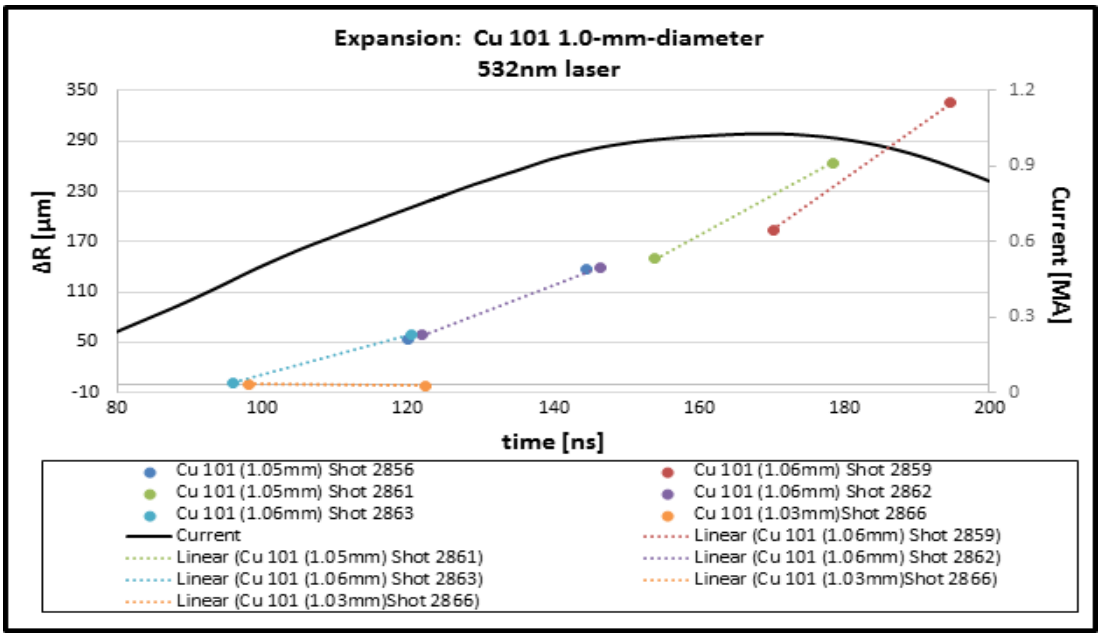

Figure V.3 Change in radius for copper 101 1.0-mm-diameter shots using 532nm laser shadowgraphy.

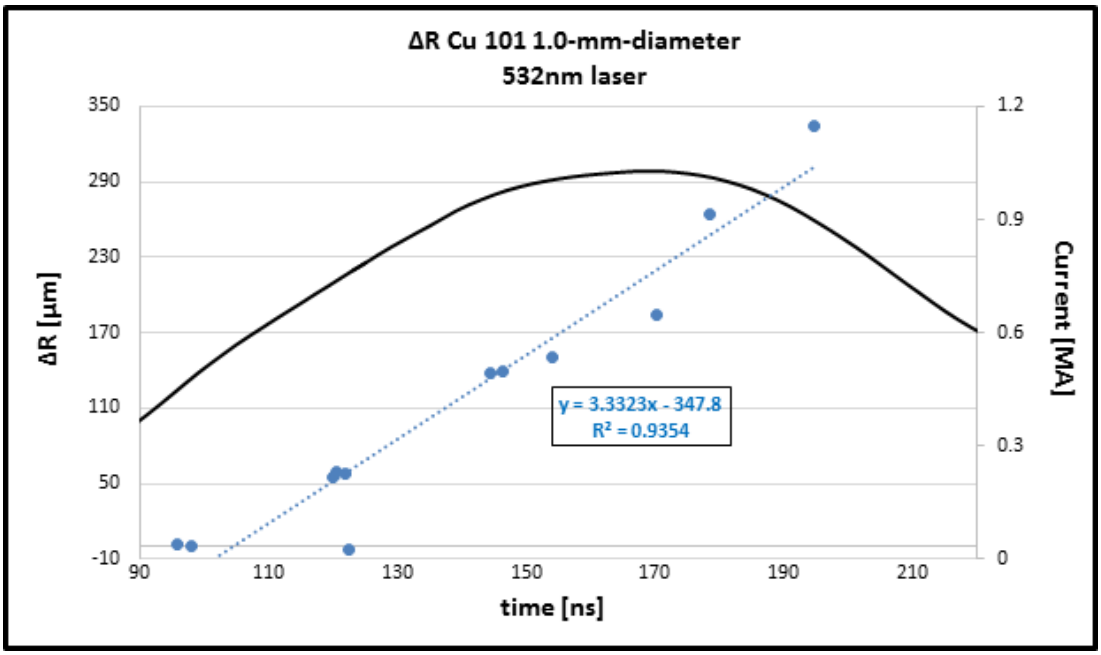

Figure V.4 Linear fit for all copper 101 1.0-mm-diameter 532nm laser shadowgraphy.

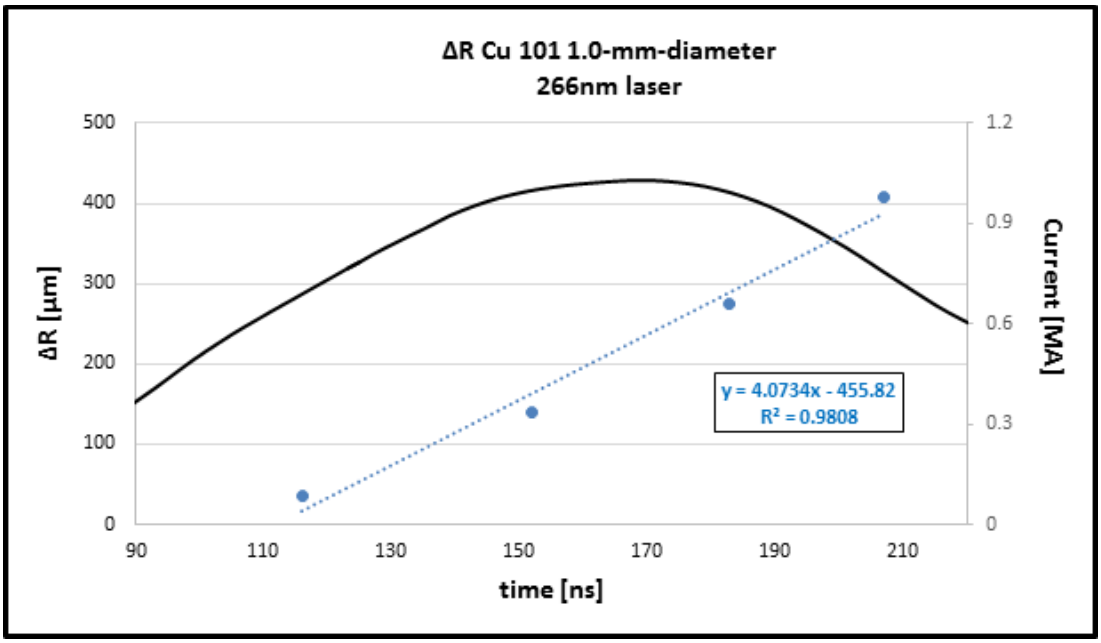

Figure V.5 Linear fit for all copper 101 1.0-mm-diameter 266nm laser shadowgraphy.

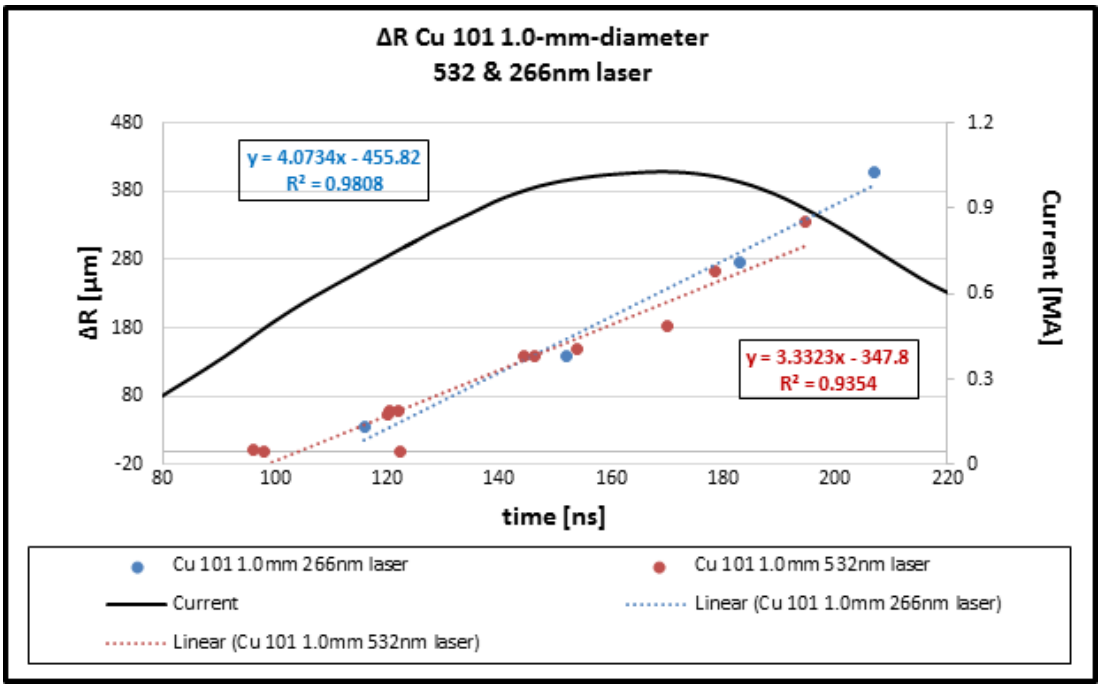

Figure V.6 Comparison between expansion of copper 101 1.0-mm-diameter rods using 532nm and 266nm laser shadowgraphy. The difference in radial expansion is due to the 532nm shadowgraphy including several images with negligible expansion.

Figure V.7 plots the 532 nm laser shadowgraph radius for copper 101 0.8-mm-diameter for each shot with a line fitted to each shadowgraph pair for an individual shot. Since the 0.8-mm-diameter rods form plasma, the assumption of constant expansion through peak current can no longer be

applied. The point in time that the expansion becomes non-linear is taken at the time that the current becomes non-linear, which has been estimated to be about 145 ns. Figure V.8 plots the expansion data for the copper 101 0.8-mm-diameter with the 532 nm laser with lines fit for the two different expansion regions. The expansion prior to peak current is 3.3 µm/ns with an accelerated expansion past peak current of 5.4 µm/ns. Figures V.9 and V.10 plot the results for the 0.8-mm-diameter expansion with the 266 nm laser. All of the data points with this laser and diameter rod were near and past peak current and shows an expansion of 5.0 µm/ns. Figure V.11 plots data for the copper 0.8-mm-diameter rods using both 532 and 266 nm laser and illustrates good agreement between the two wavelengths.

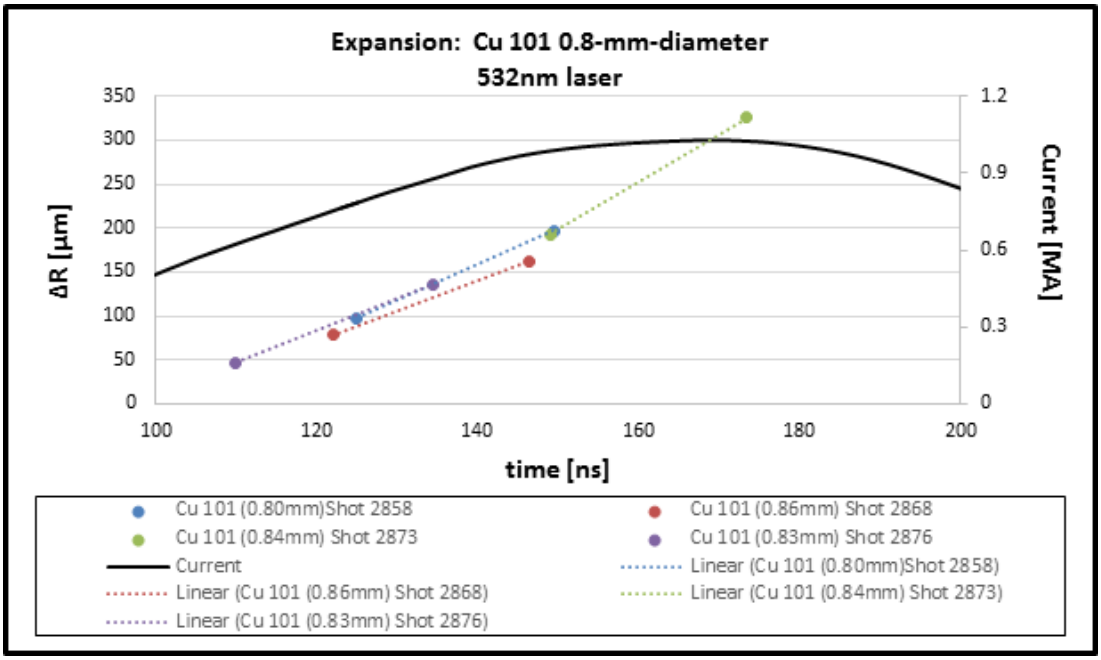

Figure V.7 Change in radius for copper 101 0.8-mm-diameter shots using 532nm laser shadowgraphy.

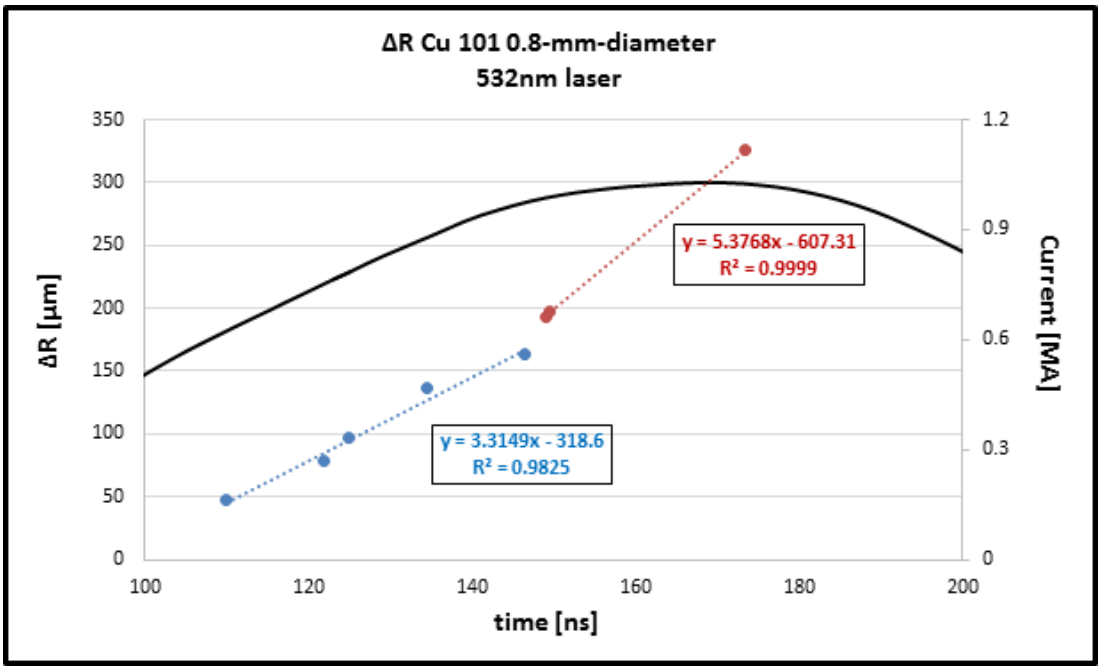

Figure V.8 Linear fit for copper 101 0.8-mm-diameter rods using 532nm laser shadowgraphy with accelerated expansion near peak current indicating a reversal in the pinch effect due to decreasing and reversing sign of dB/dt.

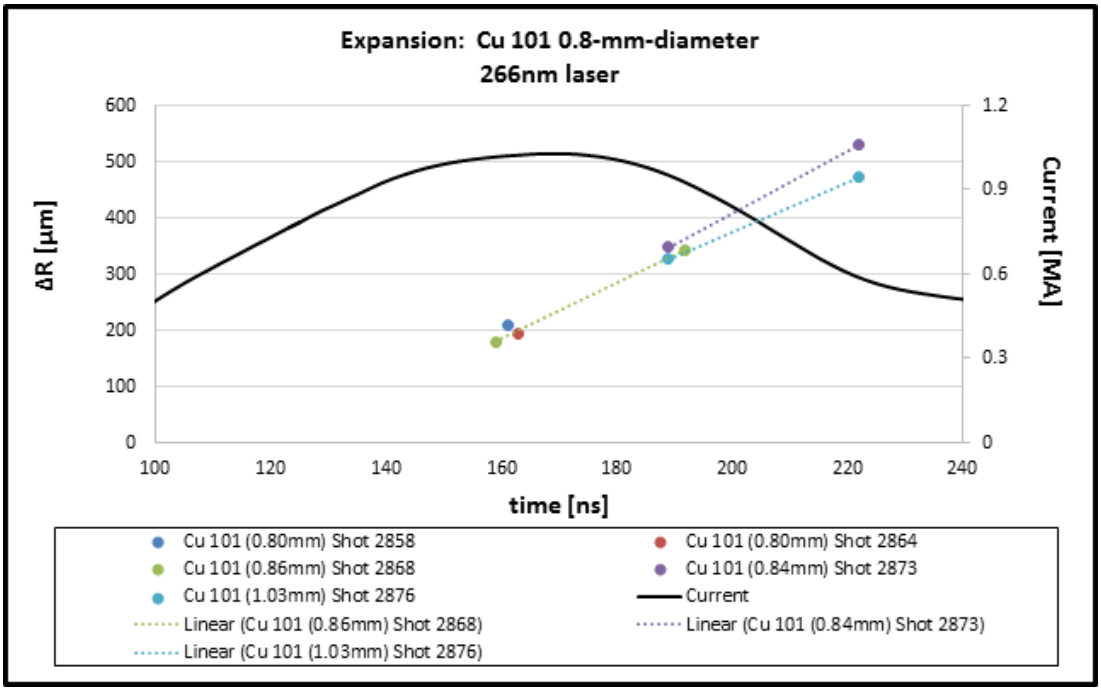

Figure V.9 Change in radius for copper 101 0.8-mm-diameter shots using 266nm laser shadowgraphy.

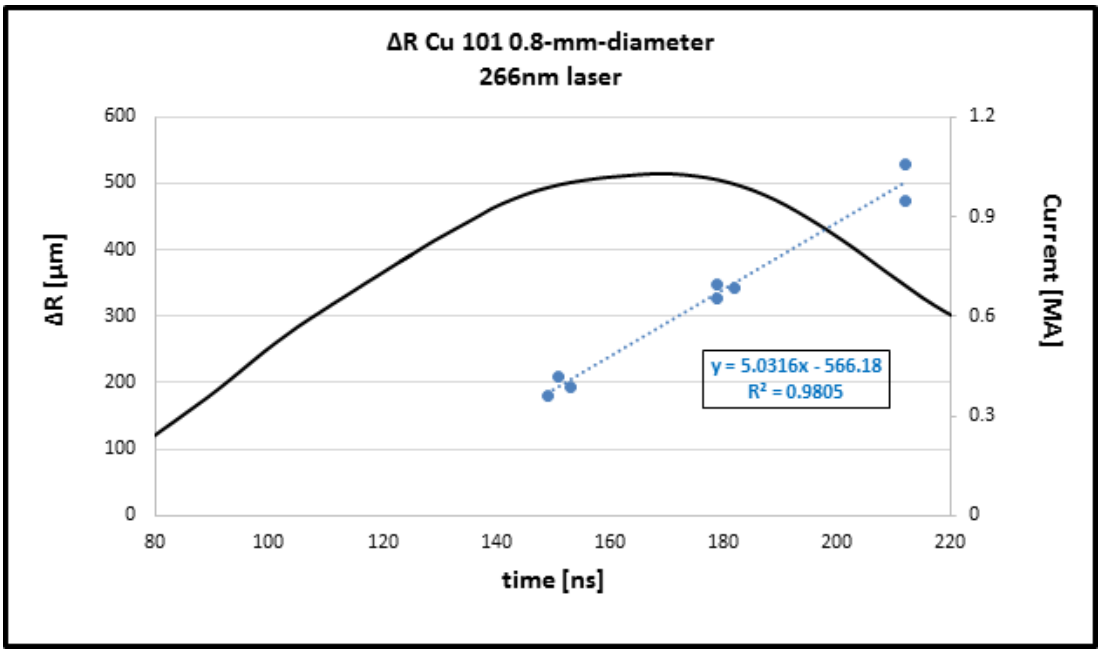

Figure V.10 Linear fit for copper 101 0.8-mm-diameter rods using 532nm laser shadowgraphy.

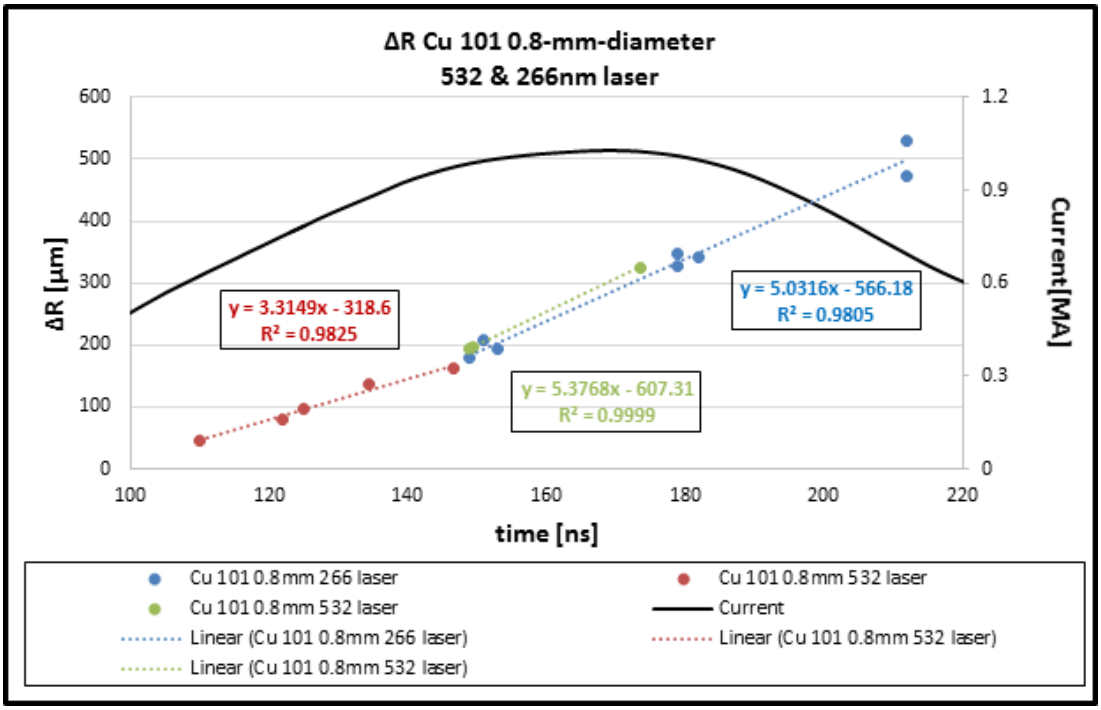

Figure V.11 Comparison of expansion for 532nm and 266nm laser shadowgraphy of copper 101 0.8-mm-diameter rods.

Plots of the expansion rate for copper 101 0.7-mm-diameter rods are plotted for the 532 nm laser in Figures V.12 and V.13 and for the 266 nm laser in Figures V.14 and V.15. The results for the copper 101 0.7-mm-diameter rods for both laser wavelengths is plotted in Figure V.16.

The results show an expansion rate of 4.8 µm/ns prior to peak current and 7.6 µm/ns past peak current with the 532 nm laser and and expansion rate of 3.3 µm/ns prior to peak current and 4.7 µm/ns past peak current with the 266 nm laser. This indicates a possible difference between the two laser wavelengths in determining expansion based on penetration depth of the two laser frequencies, however, there are few data points to make this claim.

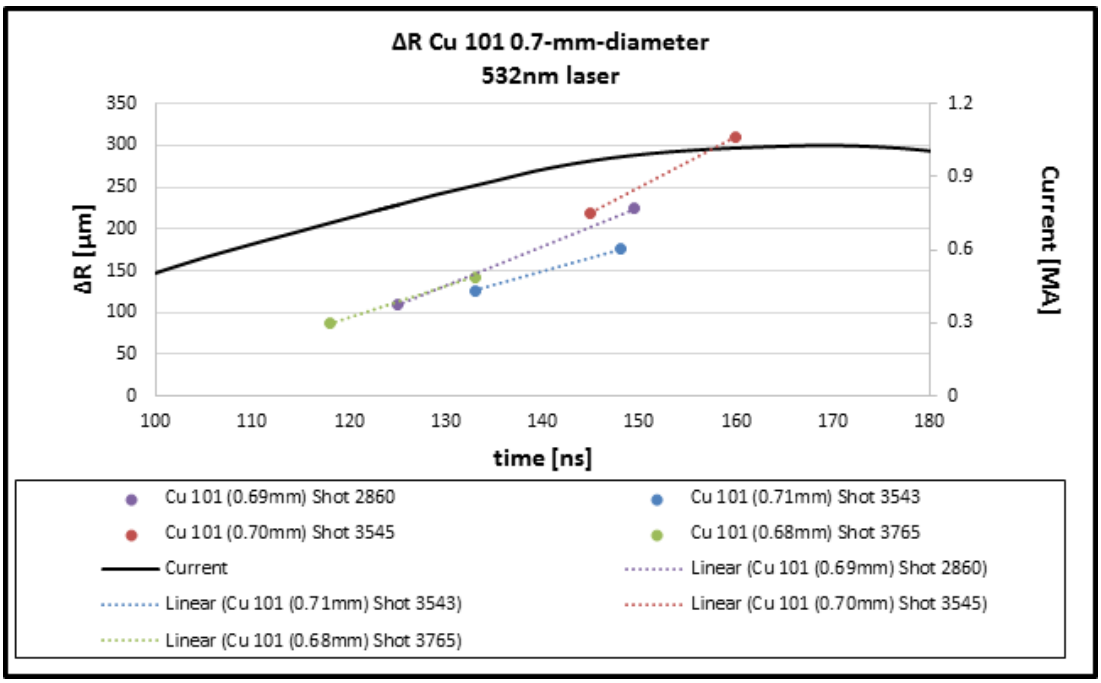

Figure V.12 Change in radius for copper 101 0.7-mm-diameter shots using 532nm laser shadowgraphy.

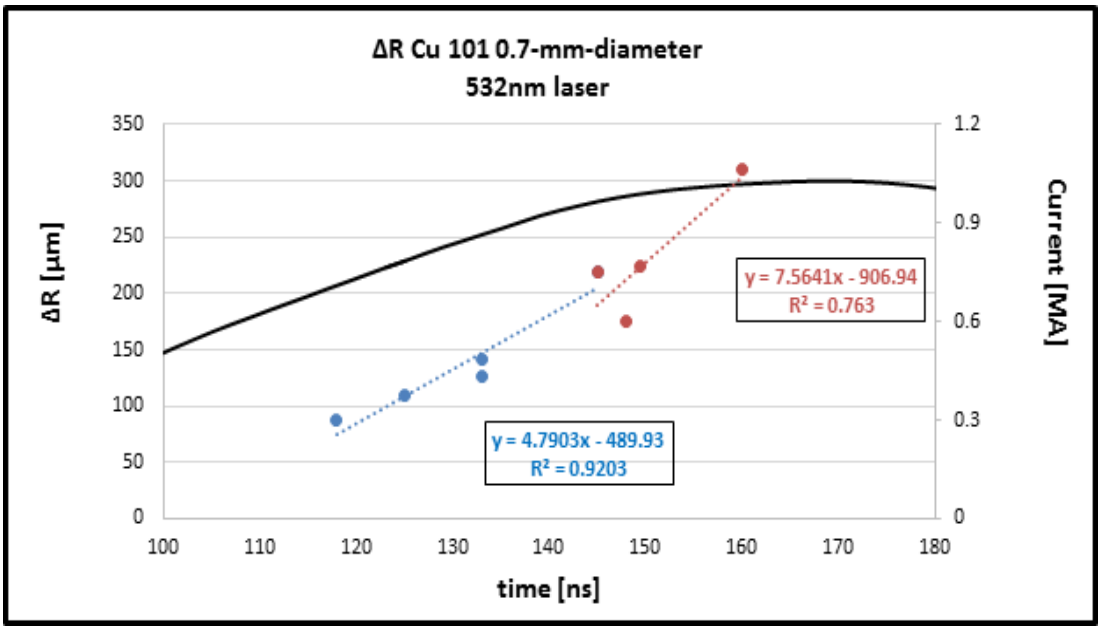

Figure V.13 Linear fit for expansion of copper 101 0.7-mm-diameter shots using 532nm laser shadowgraphy.

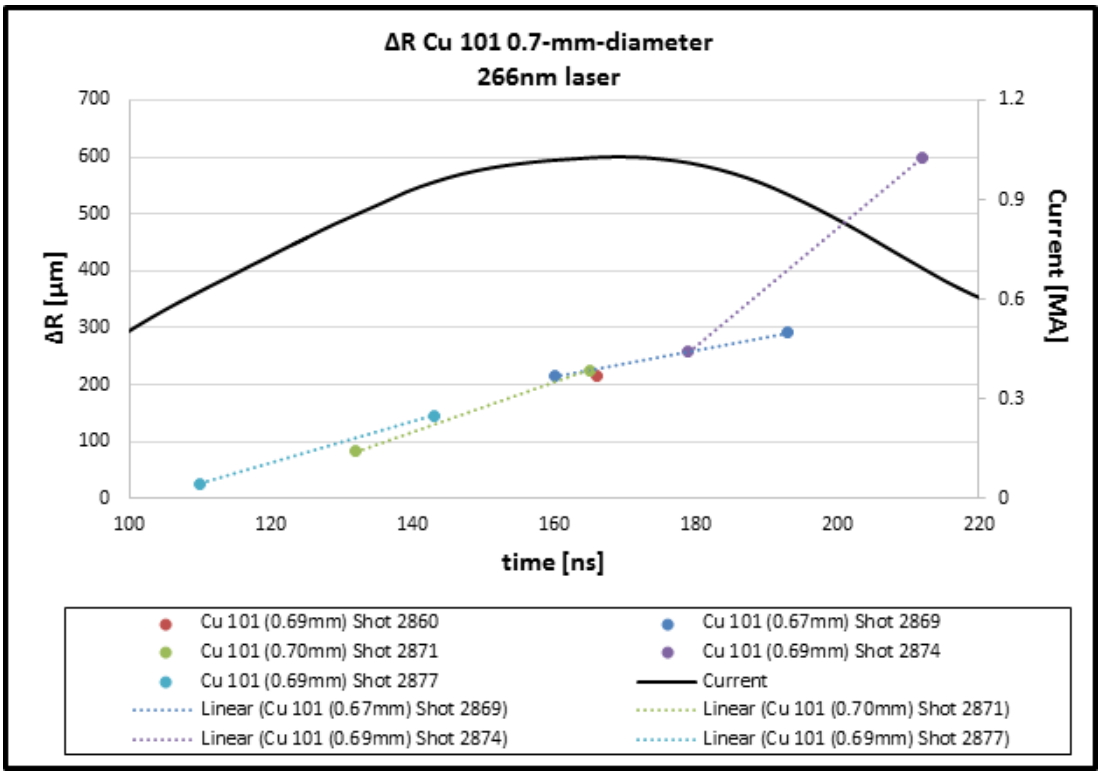

Figure V.14 Change in radius for copper 101 0.7-mm-diameter shots using 266nm laser shadowgraphy.

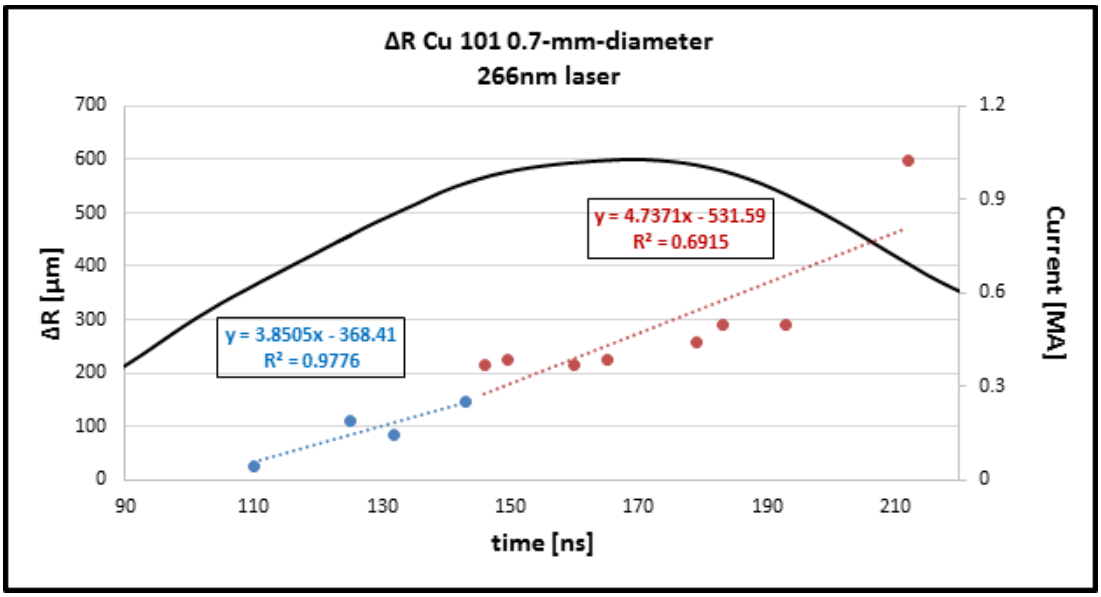

Figure V.15 Linear fit for copper 101 0.7-mm-diameter rods using 266nm laser shadowgraphy with accelerated expansion near peak current indicating a reversal in the pinch effect due to decreasing and reversing sign of dB/dt.

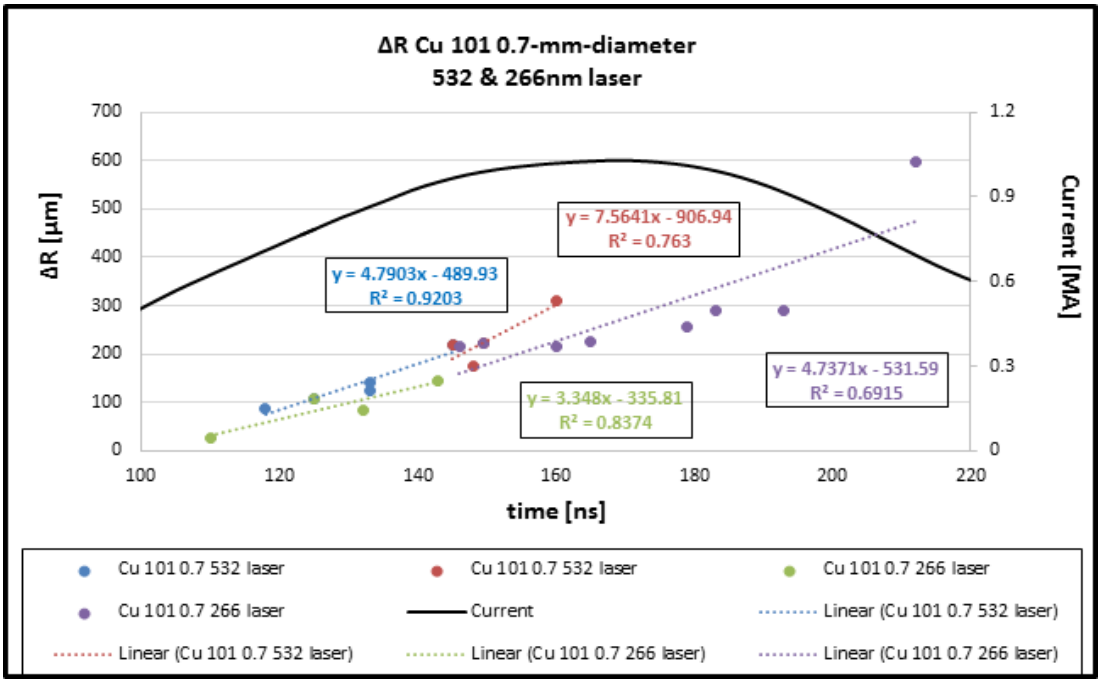

Figure V.16 Comparison of expansion of copper 101 0.7-mm-diameter rods using 532nm and 266nm laser shadowgraphy.

The copper 145 rods were imaged with the 532 nm wavelength laser only. The expansion rate results for the 0.5-, 0.7-, 0.8-, and 0.9-mm-diameter rods are plotted in Figures V.17-V.24. All rod

diameter showed results in the 3-4 µm/ns range with the exception of the 0.8-mm-diameter rods. With so few shots, this descrepancy is not understood.

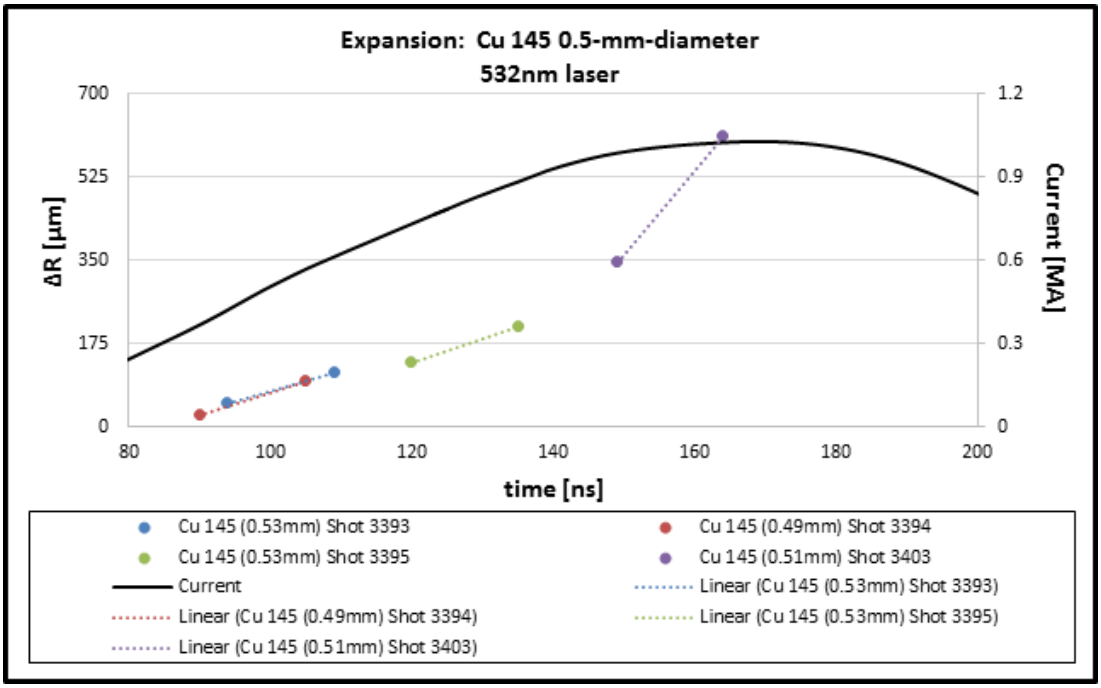

Figure V.17 Change in radius for copper 145 0.5-mm-diameter shots using 532nm laser shadowgraphy.

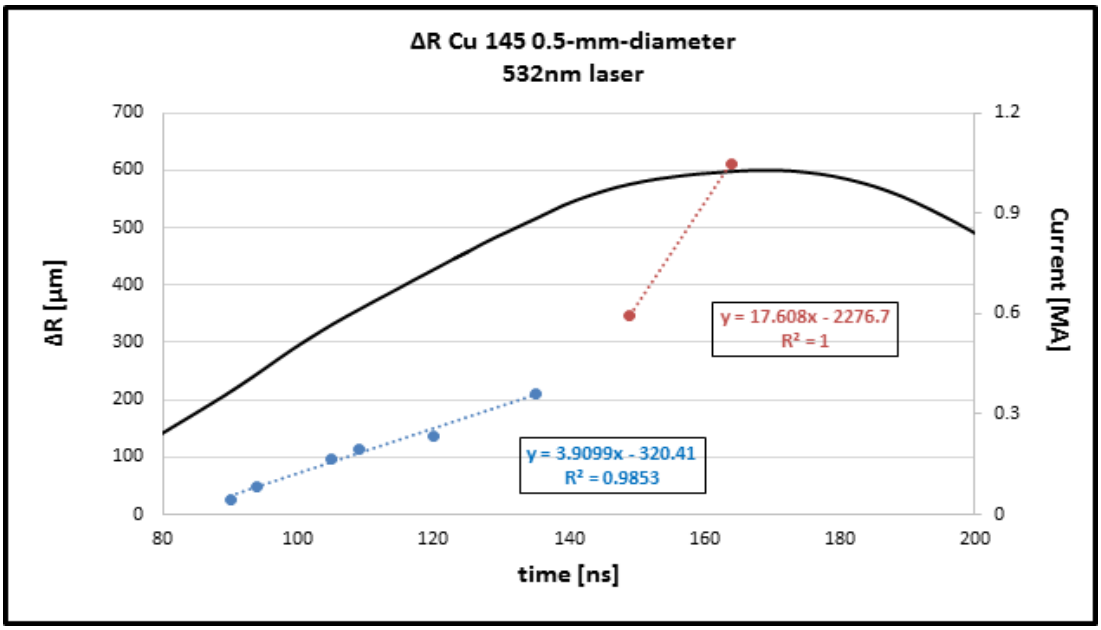

Figure V.18 Linear fit for copper 145 0.5-mm-diameter rods using 532nm laser shadowgraphy with accelerated expansion near peak current indicating a reversal in the pinch effect due to decreasing and reversing sign of dB/dt.

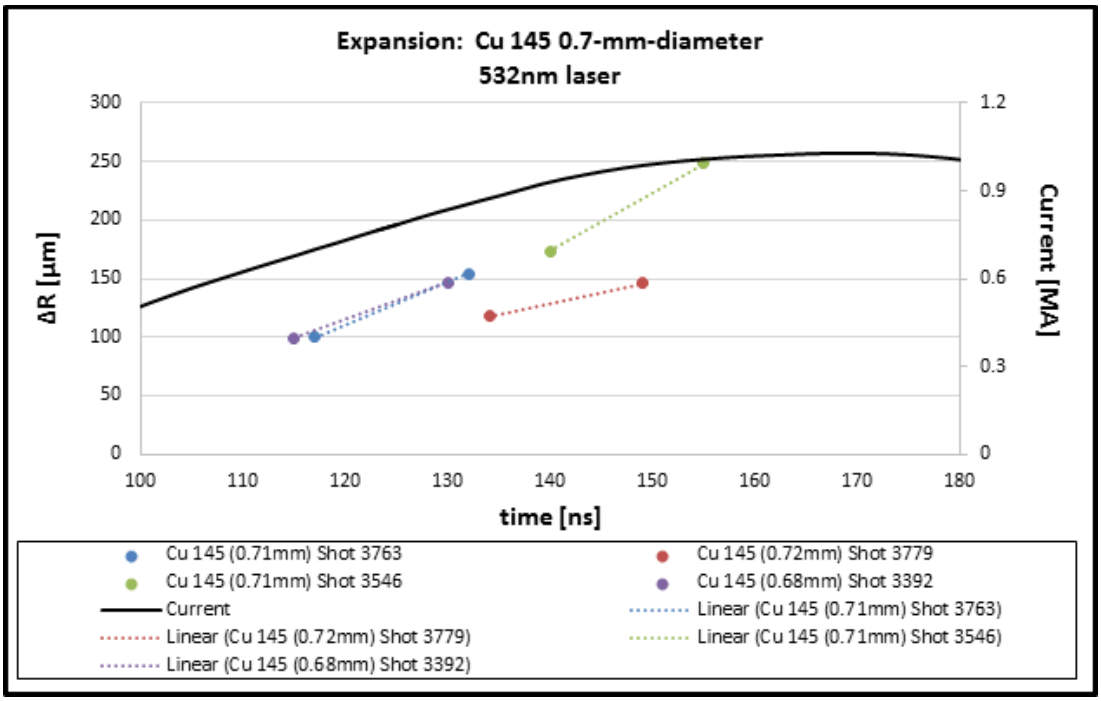

Figure V.19 Change in radius for copper 145 0.7-mm-diameter shots using 532nm laser shadowgraphy.

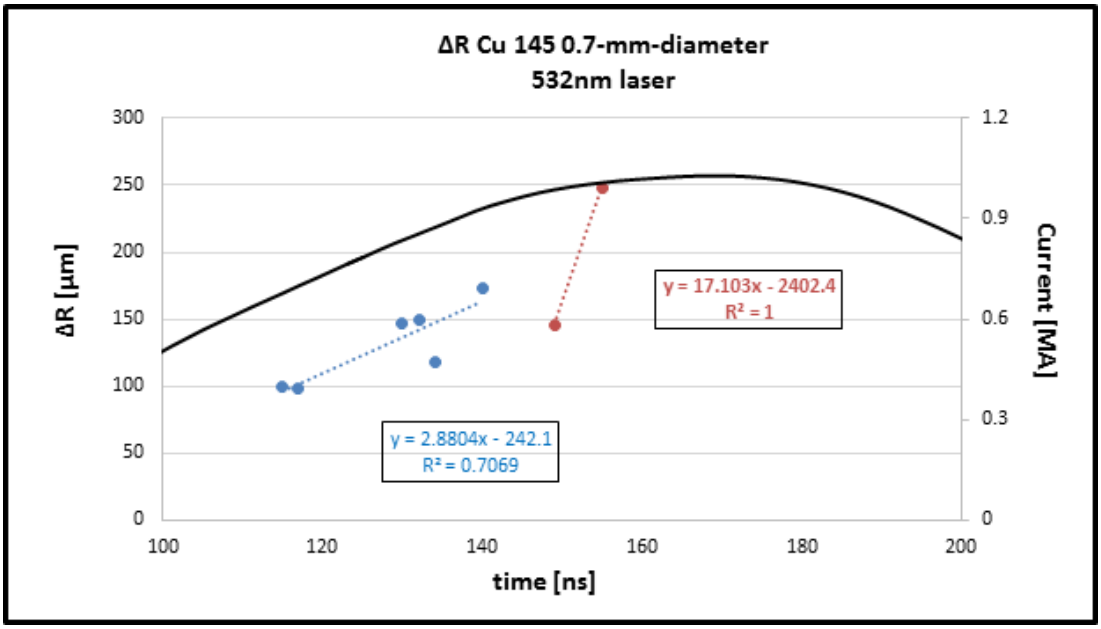

Figure V.20 Linear fit for copper 145 0.7-mm-diameter rods using 532nm laser shadowgraphy with accelerated expansion near peak current indicating a reversal in the pinch effect due to decreasing and reversing sign of dB/dt.

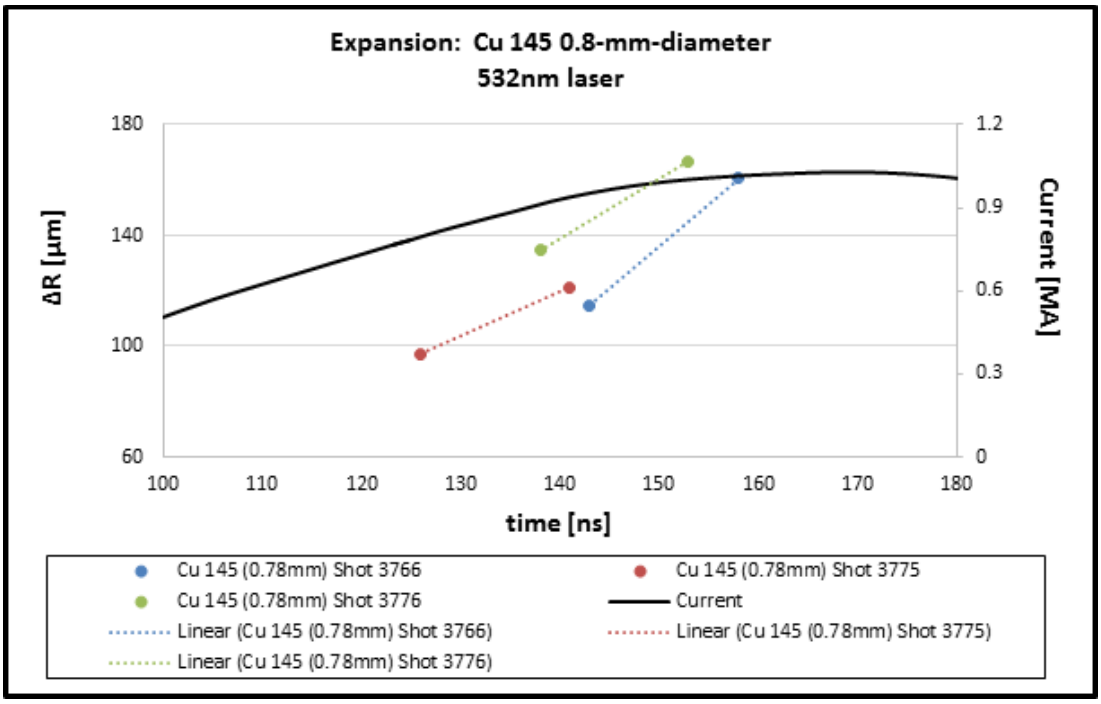

Figure V.21 Change in radius for copper 145 0.8-mm-diameter shots using 532nm laser shadowgraphy.

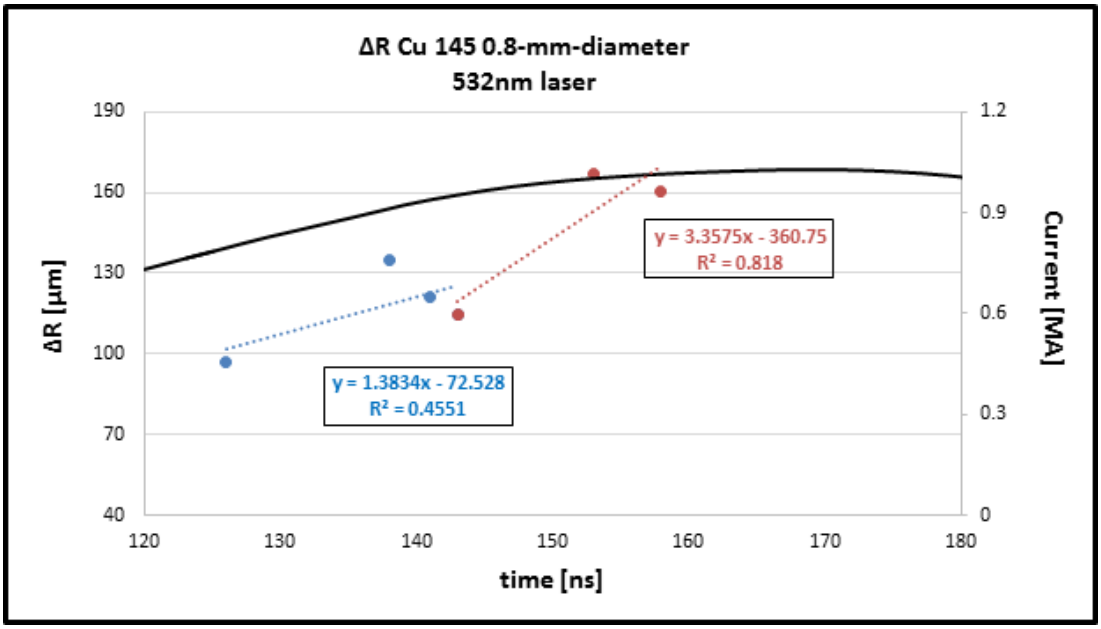

Figure V.22 Linear fit for copper 145 0.8-mm-diameter rods using 532nm laser shadowgraphy with accelerated expansion near peak current indicating a reversal in the pinch effect due to decreasing and reversing sign of dB/dt.

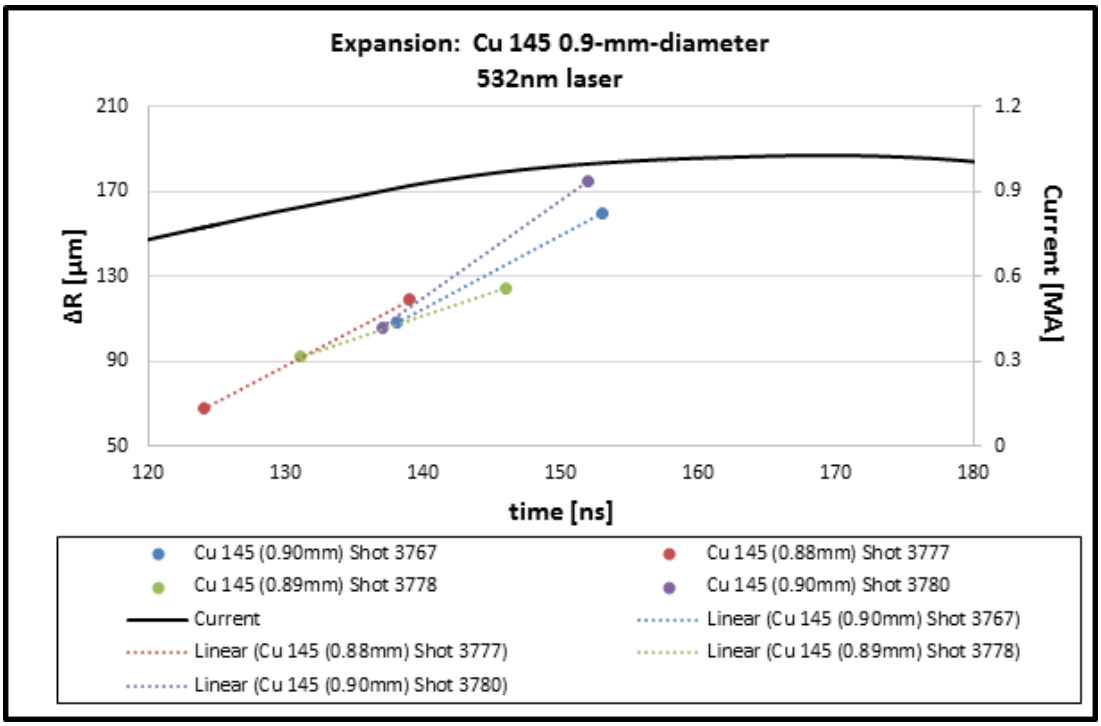

Figure V.23 Change in radius for copper 145 0.9-mm-diameter shots using 532nm laser shadowgraphy.

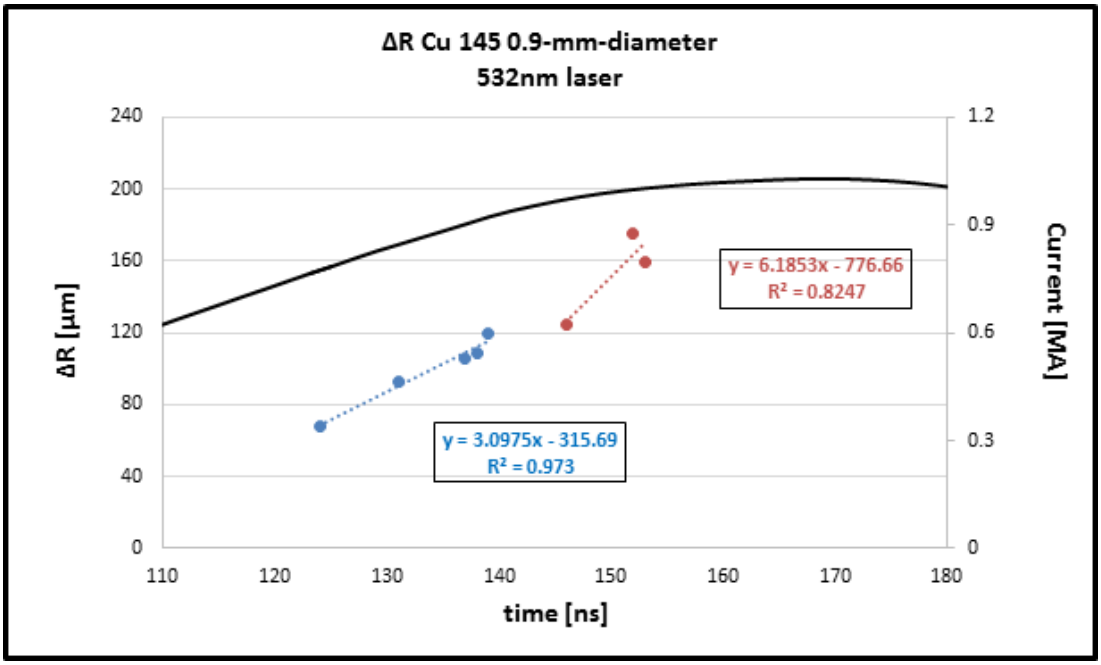

Figure V.24 Linear fit for copper 145 0.9-mm-diameter rods using 532nm laser shadowgraphy with accelerated expansion near peak current indicating a reversal in the pinch effect due to decreasing and reversing sign of dB/dt.

Several shots of titanium and one shot of nickel were imaged with the 532 nm laser shadowgraphy. Figures V.25-V.28 plot the shots for titanium and Figure V.29 plots the one shot

of nickel. The nickel appears to be expanding quite slow, at a rate of 1.25 µm/ns, however, one shot does not provide enough evidence for this. The titanium appears to be expanding at a faster rate than the copper alloys, with the smaller diameters expanding at a rate of 7.2 µm/ns and the 1.0-mm-diameter rods expanding at 5.0 µm/ns.

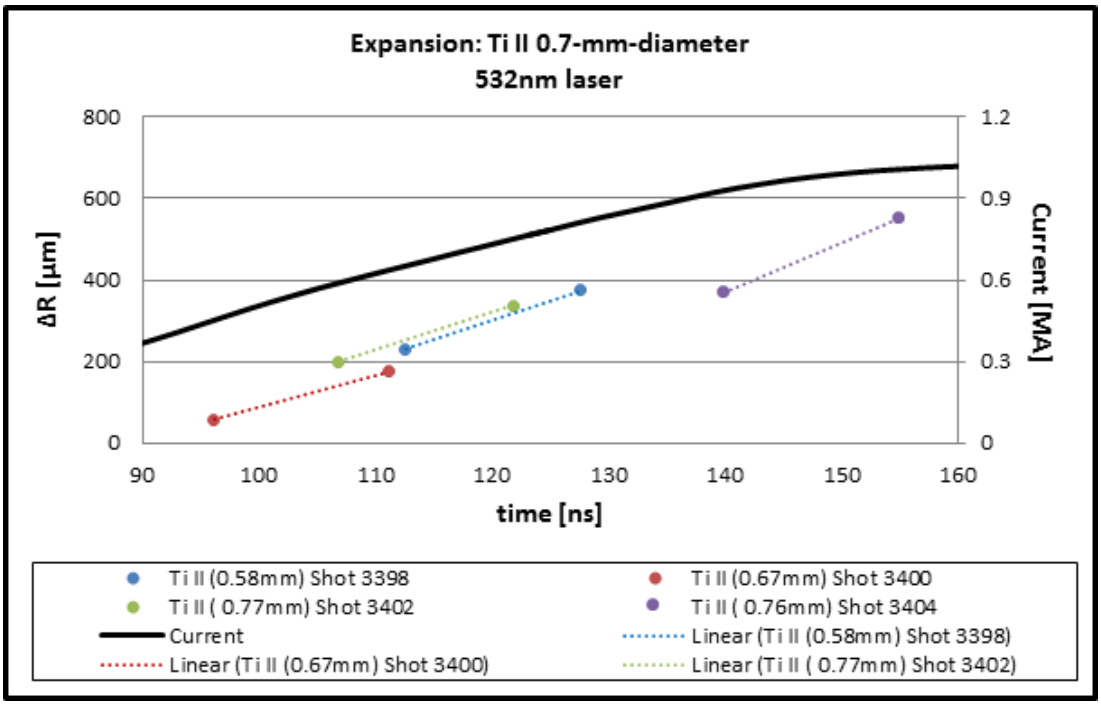

Figure V.25 Change in radius for titanium II 0.7-mm-diameter shots using 532nm laser shadowgraphy.

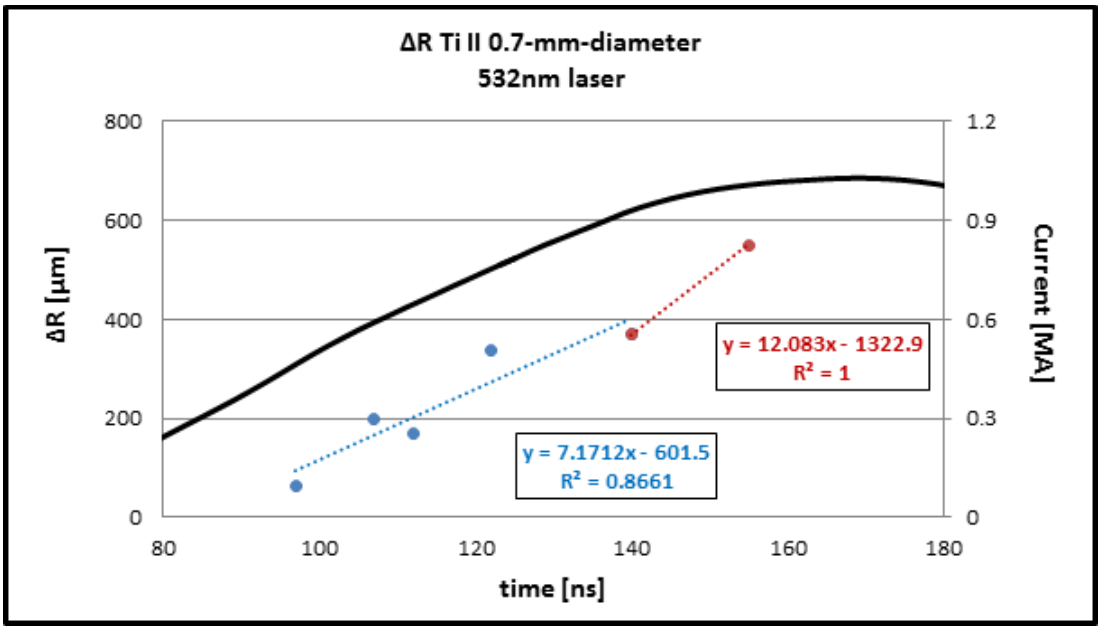

Figure V.26 Linear fit for titanium II 0.7-mm-diameter rods using 532nm laser shadowgraphy with accelerated expansion near peak current indicating a reversal in the pinch effect due to decreasing and reversing sign of dB/dt.

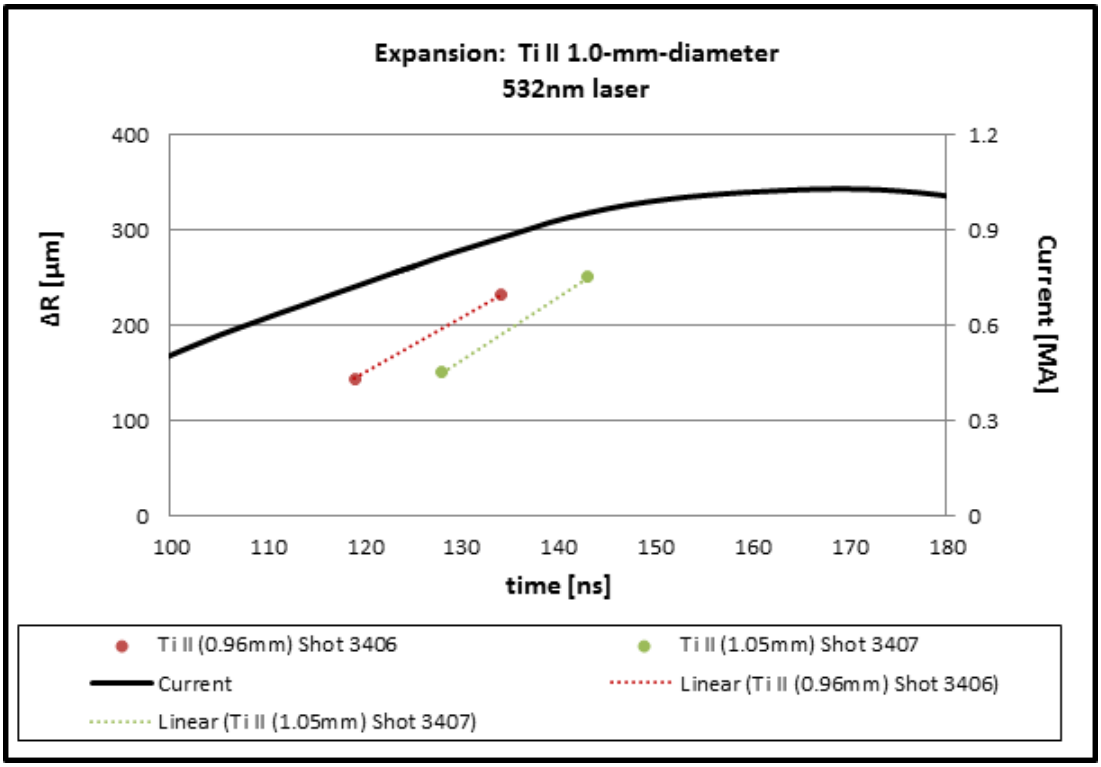

Figure V.27 Change in radius for titanium 1.0-mm-diameter shots using 532nm laser shadowgraphy.

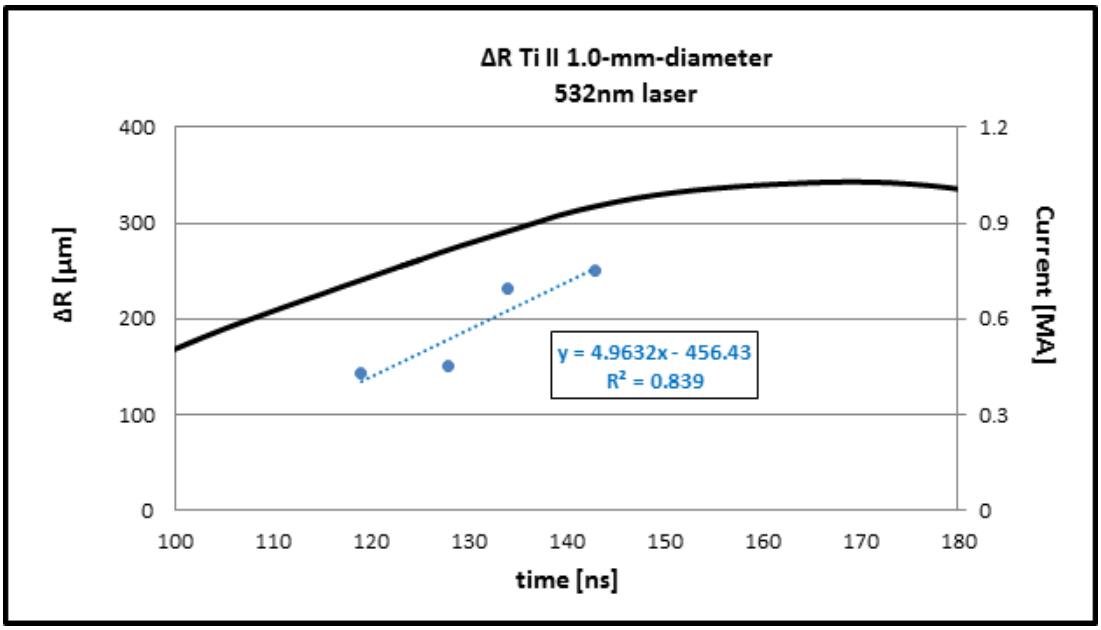

Figure V.28 Linear fit for titanium II 1.0-mm-diameter rods using 532nm laser shadowgraphy with accelerated expansion near peak current indicating a reversal in the pinch effect due to decreasing and reversing sign of dB/dt.

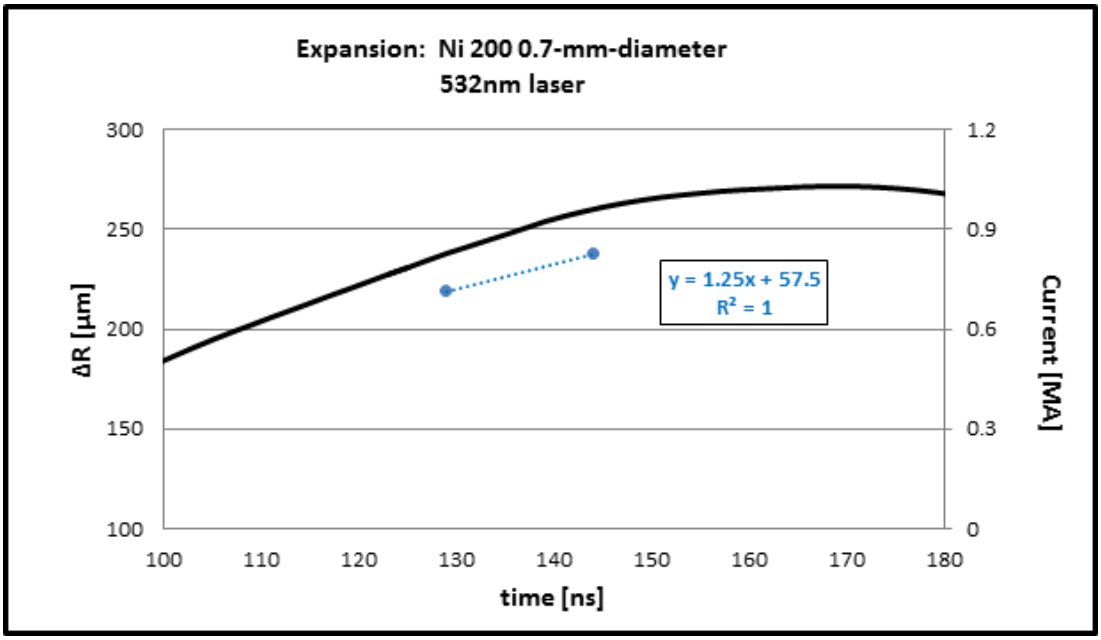

Figure V.29 Change in radius for nickel 200 0.7-mm-diameter shots using 532nm laser shadowgraphy.

The method of finding a linear fit to the shadowgraph plots to determine expansion rates has several problems. The first is the fact that for a particular rod diameter, there are not very many data points that lie within the linear regime of the rising current pulse. The second problem

is the fact that for any particular nominal diameter, say 0.8-mm-diameter, there is a spread in the initial rod diameter. A difference in diameter of 50μm changes the surface magnetic field when rising at 50MG/μs by about 0.25MG. This changes the timing by about 5ns. To remove the systematic error introduced by the different rod diameters, data from all rod diameters was plotted with the change in radius plotted versus time as well as initial diameter. This 2D linear plot uses the following equation:

$$y = m_1 x_1 + m_2 x_2 + b \qquad \text{(V.2)}$$

Where *y* is the change in radius in μm, m_1 is a unitless scaling factor, x_1 is the rod initial diameter in μm, m_2 is the expansion rate in μm/ns, x_2 is time in ns, and b is the *y*-intercept of the linear equation. Using the LINEST Function[107] in Microsoft Excel, the data is plotted utilizing equation V.2. The initial diameter, change in radius, and time of image exposure is inputted into the LINEST Function. When the function is run, it outputs m_1, m_2, b, and the standard deviation in each. The expansion rate given by this operation can be used to get the time of each shadowgraph exposure since initial expansion. By setting *y* (the change in radius) to zero, and solving for x_2**,** the time of initial expansion for each data point can now be calculated. Subtracting the time of initial expansion from the time of the image exposure gives the time since surface explosion for that particular shadowgraph image. That is, the new time is now the amount of time since the surface began to expand a.k.a., the time of surface explosion.

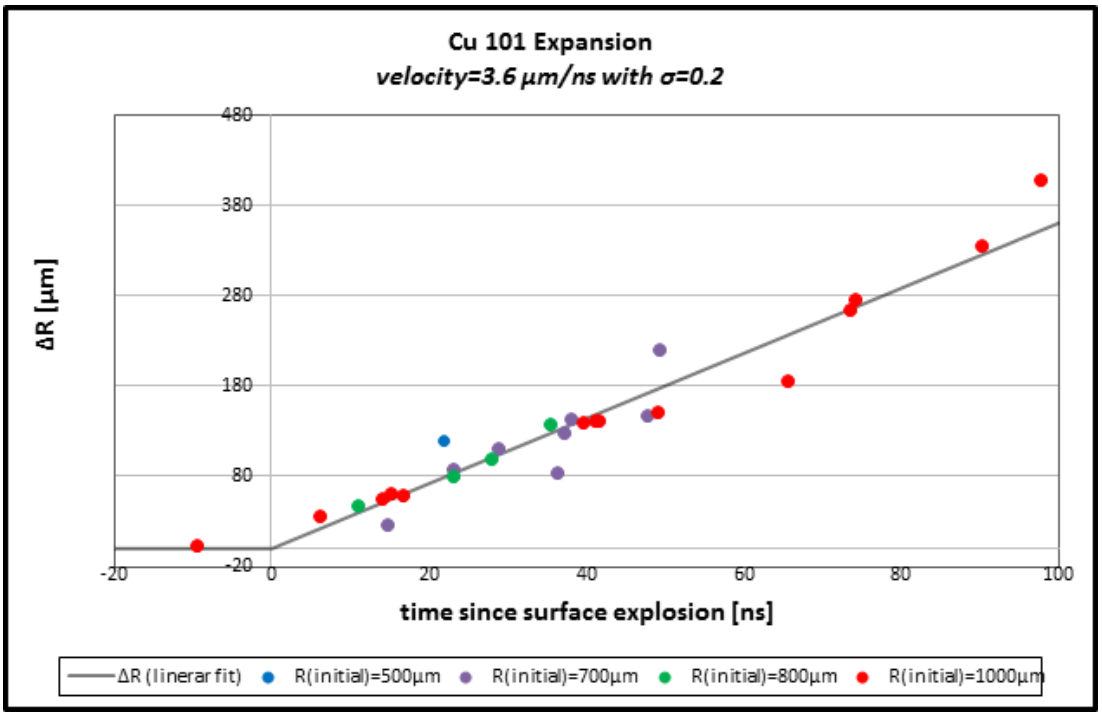

Figure V.30 Linear expansion for all copper 101 diameters fitted to a line using Microsoft Excel Linest function for a 2D fit.

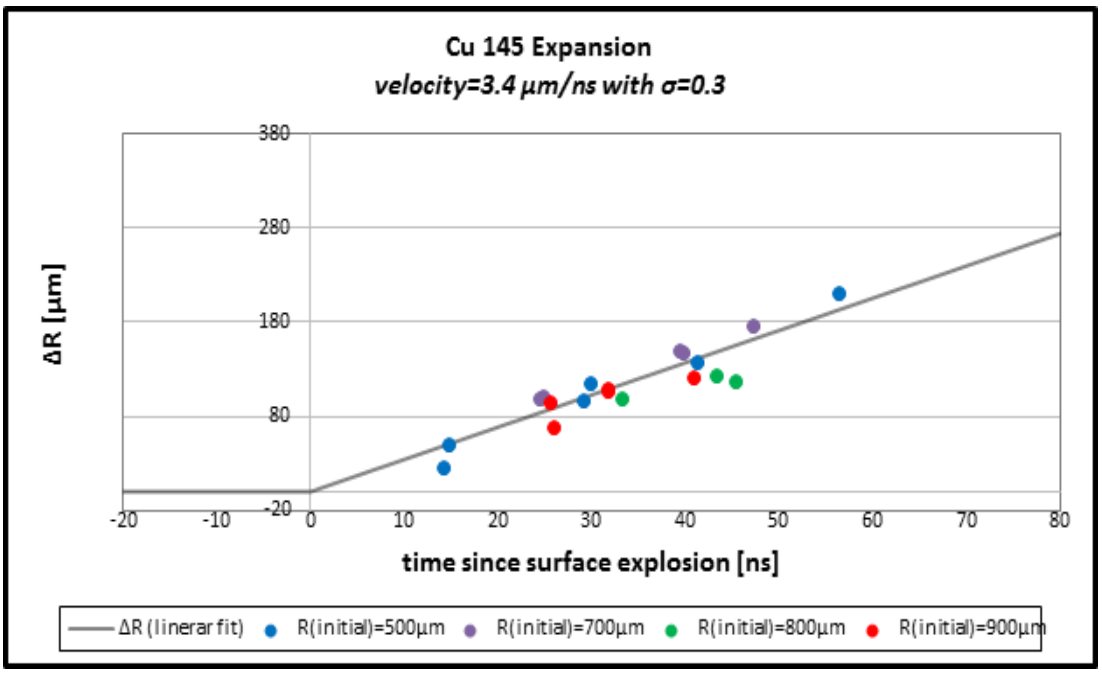

Figure V.31 Linear expansion for all copper 145 diameters fitted to a line using Microsoft Excel Linest function for a 2D fit.

Doing this for every shot and plotting the change in radius as a function of "time since surface explosion" provides a linear data set for all diameters of a particular alloy. Figures V.30

and V.31 plot the expansion rates for copper 101 and copper 145. The copper 101 has an expansion rate of 3.6μm/ns with a standard deviation of 0.2 and copper 145 has an expansion rate of 3.4μm/ns with a standard deviation of 0.3. The two copper alloys expand at rate that is indistinguishable.

Figures V.32 plots the results for the titanium rods with an expansion rate of 5.8μm/ns with a standard deviation of 1.0. This is a large standard deviation, so a sensitivity test was done removing one data pair, (one pair of images for each rod diameter shot) to observe how it varied the outcome. The diameter that provided the most change was the 580μm diameter rod. When the 580μm rod is removed from the data set, the LINEST function is run again. This provides a new linear equation which is used to determine a new time of surface expansion for each shot. Since the LINEST function shows a clear change in expansion speed by removing this smaller diameter load, it is not surprising that the time since explosion shifted for the remaining shots that were run through the LINEST function. Figure V.33 shows the result of removing this data pair, with the expansion rate becoming 7.2μm/ns with a standard deviation of 0.5. This is a much better result, however, there must be justification for removing this data pair. Since these images were taken earlier in the current profile, the instabilities were not larger than the larger diameter rods at the time of their exposure. The effect this shot has on the resulting expansion rate is not understood. More data would help determine the expansion rate of titanium and if it is indeed constant for varying initial diameter.

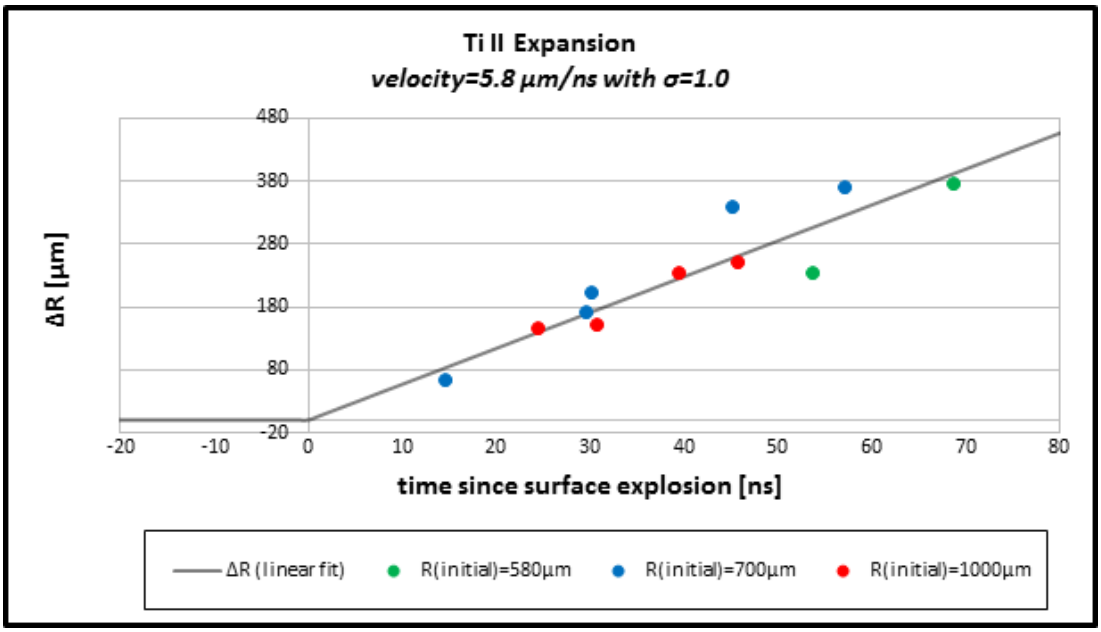

Figure V.32 Linear expansion for all titanium II diameters fitted to a line using Microsoft Excel Linest function for a 2D fit.

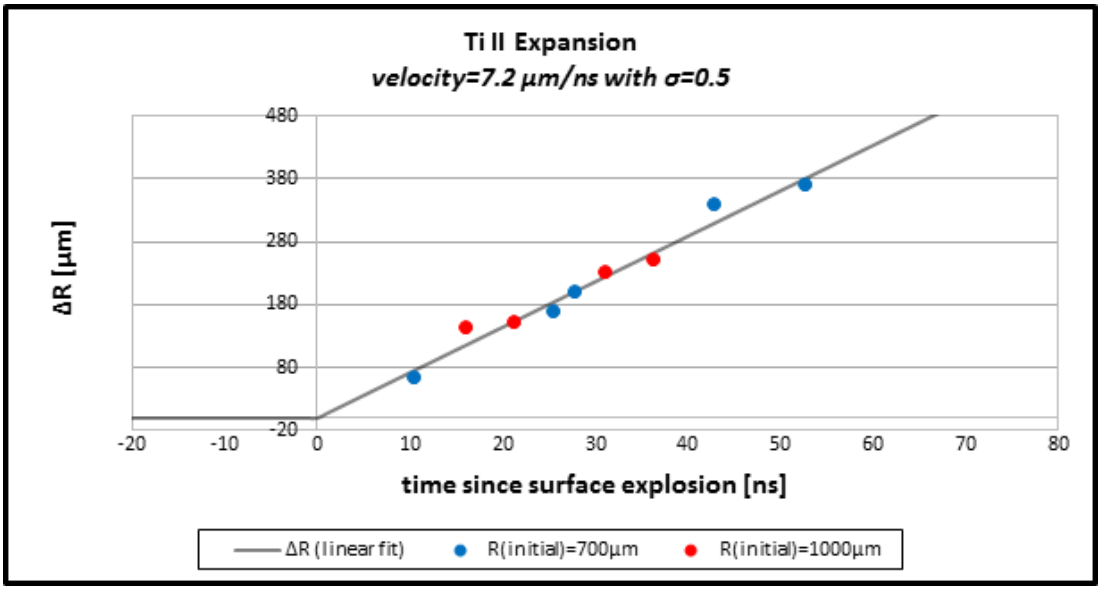

Figure V.33 Linear expansion for all titanium II diameters with the 580µm diameter shot removed. The linear fit has a smaller standard deviation and a larger velocity with the smaller rod diameter removed from the data set.

The same LINEST function was applied to aluminum data from the MG IV experiment, resulting in an aluminum expansion rate of 3.2µm/ns with a standard deviation of 0.2. Listed below are the metals shot with the corresponding atomic weight, boiling point, expansion rate, and sound speed for each corresponding metal.

Element	Atomic Weight	Boiling Point [eV]	Expansion Rate [μm/ns]	Sound Speed[108] [μm/ns]
Aluminum	26.9	0.24	3.2	6.3
Titanium	47.9	0.31	5.8	6.1
Nickel	63.5	0.26	1.5	5.6
Copper	58.7	0.24	3.6	4.6

Table V.1

If the expansion is driven by the thermal expansion of a surface vapor (one that we will call an ideal gas), then the rate of expansion is expected to be proportional to $\sqrt{T/M}$, where *T* is the temperature, and *M* is the mass of the expanding material. Since the expansion is driven by the gas (with a dense plasma likely pinned up against it due to $J \times B$), the temperature should be in the range of the boiling point. There is not enough data for nickel to justify a comparison here, however, the aluminum, copper, and titanium should be comparable. The copper and titanium show about a 28% deviation in relative expansion rates from what would be expected for an expanding ideal gas. Qualitatively, the results are acceptable since the titanium surface is expected to expand at a faster rate. The comparison of relative expansions of copper and aluminum shows a deviation of 40% from expected. And the results are contrary to what is expected, with aluminum expanding at a slower rate than copper despite having nearly the same temperature but a much less massive atom. A similar deviation is observed by comparing the experimental results with the sound speed of each metal. The copper and titanium follow similar trends with the aluminum expanding much slower than expected with respect to the other metals.

The similar expansion rate observed for the copper 101 and 145 alloys is not a surprise, however, as shown in Chapter IV, bulk plasma forms on the surface of copper 145 earlier in the current profile than it does for copper 101. Figure V.34 is a plot of the change in radius for several shots of copper 101 and 145 at the time of plasma formation as determined by the diode signals. Only shots that provided shadowgraph images in the linear rise of the current profile, and hence were plotted in Figures V.30 and V.31, were plotted in Figure V.34. A separation is observed between the two alloys with copper 101 observing a larger expansion at the time of plasma formation. Both alloys show a surface expansion of approximately 50-250μm at time of plasma formation. The divergence of the expansion for copper 101 at larger initial diameters may be due to the rods reaching the non-linear part of the current profile by the time of plasma formation. The copper 145 looks consistant across all initial diameters. This is interesting if it is assumed there is a magnetic threshold for surface explosion. If all diameters expand at the same rate, and they start expanding at the same threshold, then with the smaller diameters observing a larger dB/dt, it is expected that they would expand less by the time of plasma formation. This will be discussed again in Chapter VII.

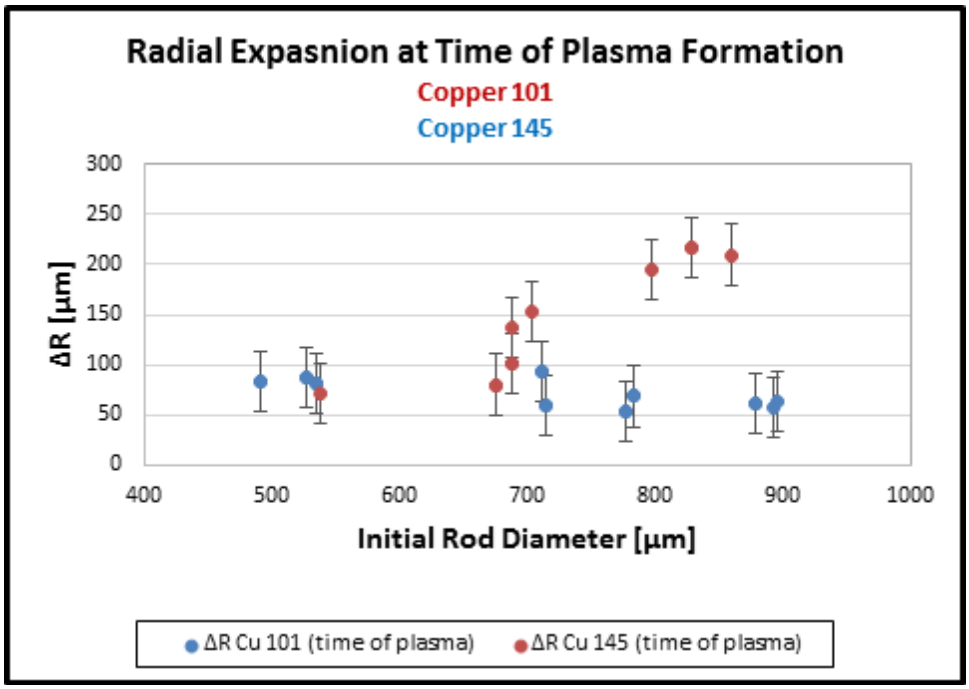

Figure V.34 The change in radius at the time of plasma formation for copper 101 and 145. A divergence is observed at the larger initial diameters for copper 101 with copper 145 appearing constant across all initial diameters.

Surface instability formation and evolution using Ekspla laser shadowgraphy

Laser shadowgraphs provide information as to the development and evolution of surface instabilities. Figure V.35 shows several shadowgraph images of copper 145 0.8-mm-diameter rods progressively increasing in surface magnetic field. The red lines indicate the initial rod diameter and are a good indicator of the expansion of the surface and the evolution of the instabilities.

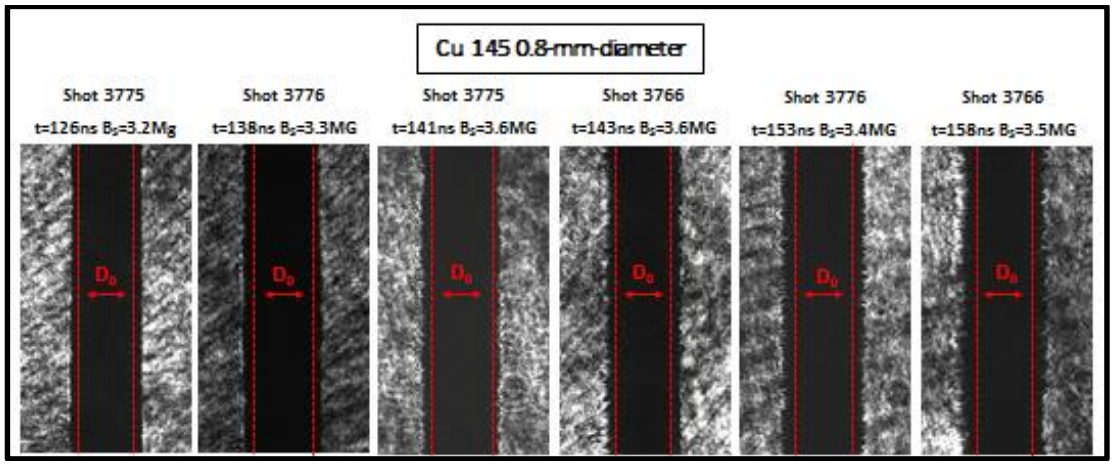

Figure V.35 Laser shadowgraphy images of copper 145 0.8-mm-diameter rods. The expansion of the surface and the development and evolution of surface instabilities is observed.

With the copper 145 rods forming plasma earlier than the copper 101, it is expected that the 145 alloy form surface instabilities prior to the 101 alloy. Figure V.36 shows shadowgraphs for copper 101 and 145 rods with similar initial diameters at similar times in the current profile. Despite the similar surface magnetic field, the copper 145 rods have formed surface instabilities that can be clearly observed in the shadowgraph images, while the copper 101 rod surface appears to be smooth and stable.

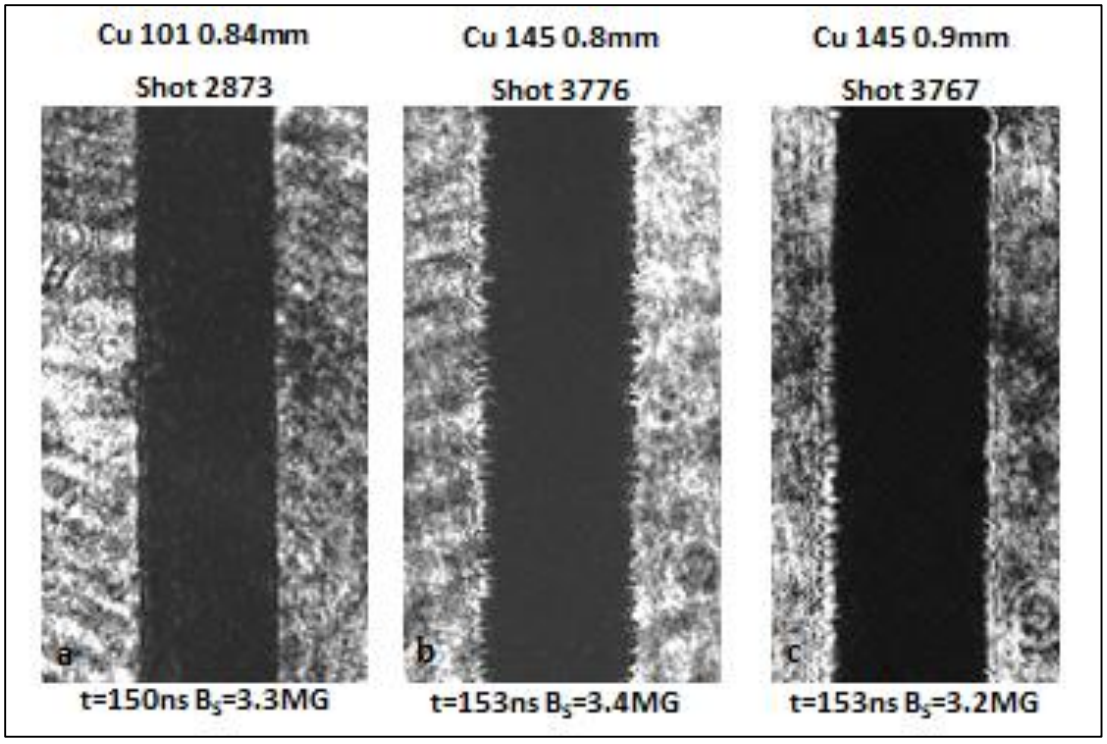

Figure V.36 A comparison between copper 101 and copper 145 rods near the same time in the current profile and surface magnetic field show clear differences in the surface structure. The copper 145 observes surface instabilities near surface magnetic field of 3.2MG while the copper 101 still shows a smooth surface at a field of 3.3MG.

A dramatic difference in the surface instabilities is observed by changing the initial diameter of the rods. Titanium forms plasma at much earlier times than other alloys shot in the MG experiments and therefore, forms surface instabilities earlier in the current profile. Figure V.37 shows the formation and evolution of surface instabilities on titanium II 0.7-mm-diameter rods. The instabilities are observed by 600 kA with dramatic instabilities forming near peak current.

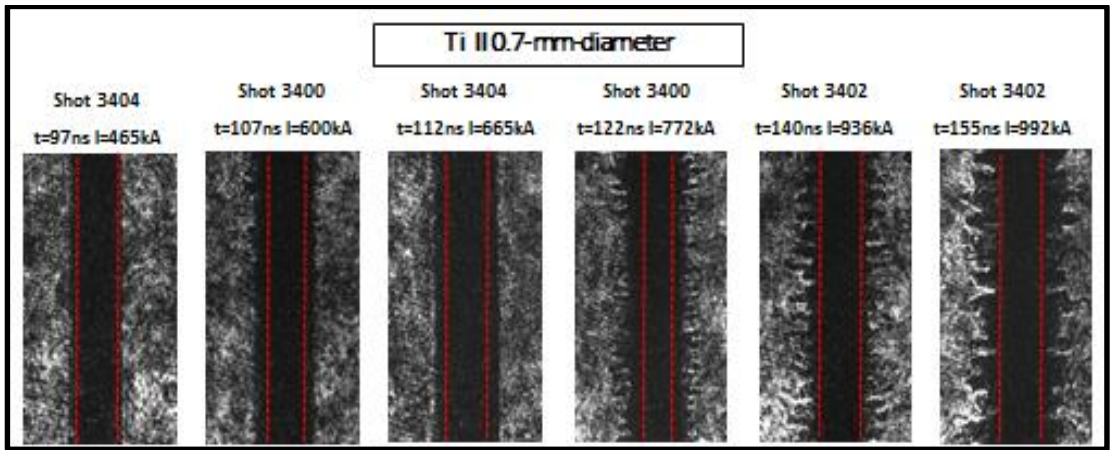

Figure V.37 Laser shadowgraphy of titanium 0.7-mm-diameter rods show large instability growth.

By increasing the initial diameter, the time of plasma formation is shifted to later times in the current profile, and the time of development of surface instabilities shifts later in time as well. This leads to much smaller amplitudes in instabilities as can be seen by comparing figure V.37 to figure V.38. Figure V.38 shows the evolution of the surface of titanium II 1.0-mm-diameter rods, with the surface forming much smaller amplitude surface instabilities than the 0.7-mm-diameter titanium rods.

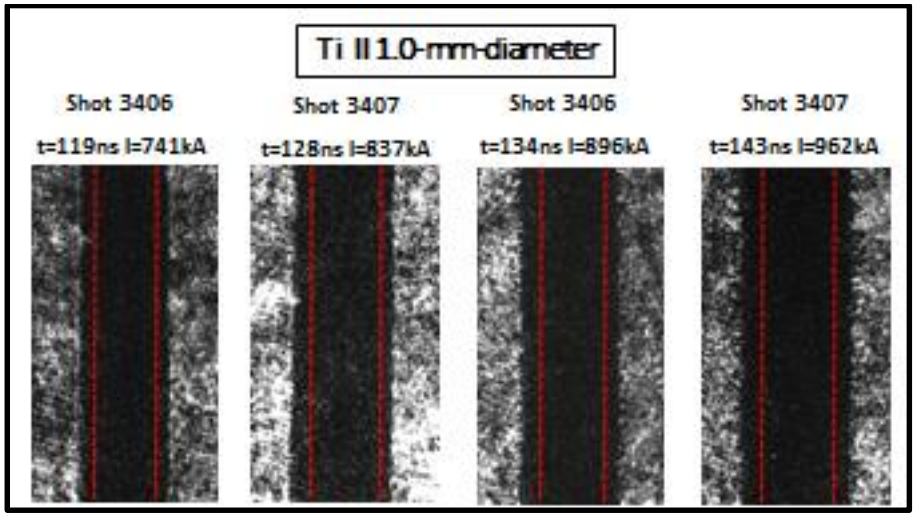

Figure V.38 Laser shadowgraphy of titanium II 1.0-mm-diameter shows much less surface instability growth in comparison to the titanium II 0.7-mm-diameter rods.

A comparison of all four alloys is shown in figure V.39 with copper 101, copper 145, nickel 200, and titanium II. All rods have an initial diameter of ~0.7-mm-diameter. The titanium shows large

amplitude instabilities while the copper 145 and nickel 200 have small amplitude instabilities. The copper 101 has a smooth surface, showing no sign of large surface instabilities.

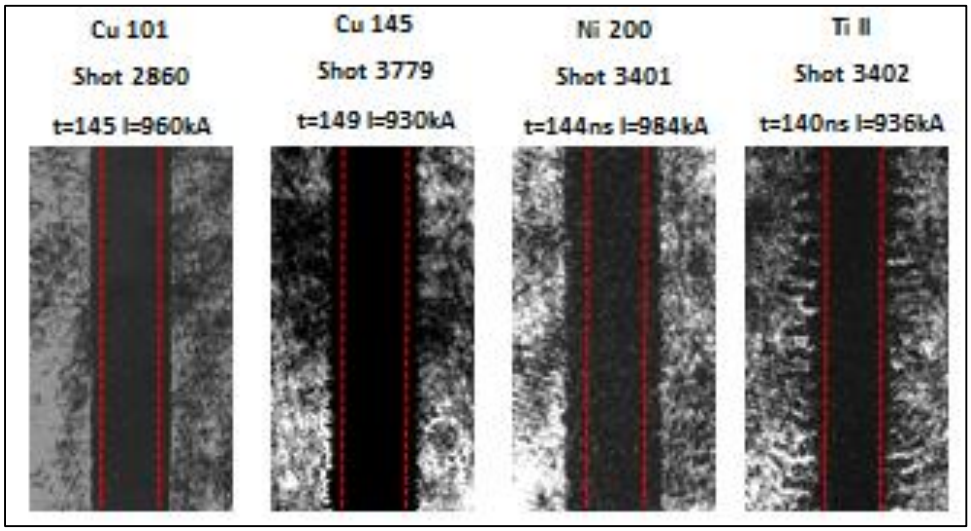

Figure V.39 Laser shadowgraph images of copper 101, copper 145, nickel 200 and titanium II at nearly the same time in the current profile and with nearly the same initial diameter.

Section V.C: Results of Multi-Frame ICCD Self-Emission Images

Expansion rate and surface instability using 12-frame and 16-frame ICCD cameras

Multi-frame ICCD cameras were fielded on MG VI and MG IX experiments to observe the evolution of surface emissions, the development of surface instabilities, and determine the expansion rate. The 12-frame Hadland ICCD camera was fielded in MG VI as described in chapter III. The camera appeared to be working on the first couple shots, as the timing was dialed in. Figure V.40 is an image of aluminum 6061 and shows good light collection, however, the spatial resolution is quite poor. Images "a-c" show non-uniform surface emission with a sharp line appearing (see red arrows) that evolves into early instability formation by image "f". This is believed to be formed by machining artifacts as discussed in chapter III.

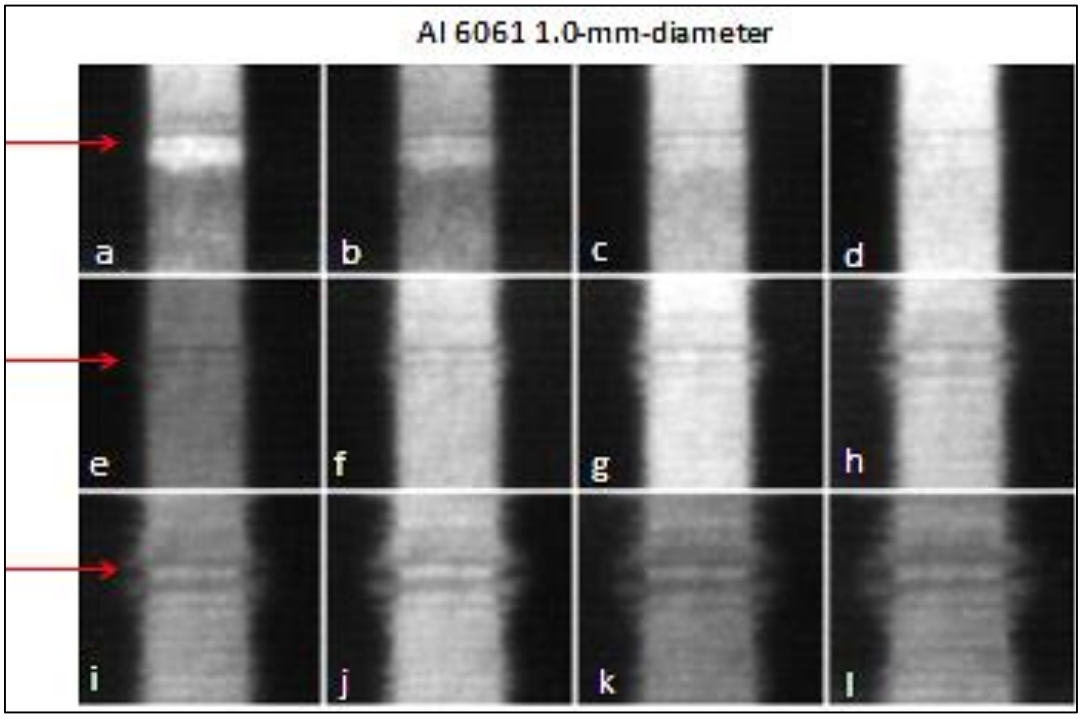

Figure V.40 12-frame imaging with the Hadland ICCD show the evolution of instabilities seeded my machining artifacts on the surface of an aluminum 6061 rod.

The instabilities can be seen become dim compared to the surrounding stable regions. This is due to the expansive cooling of the plasma as the instabilities expand out across the magnetic field lines. The following shot of aluminum 6061 is shown in figure V.41 and illustrates the camera condition getting worse with the light collection dropping and the spatial resolution getting worse. Non-uniform surface emission can still be observed in images a-d, with clear instabilities forming by image "i". Every shot following had little to no light collection with no ability to make out any surface structure. The cause of this malfunction was never determined.

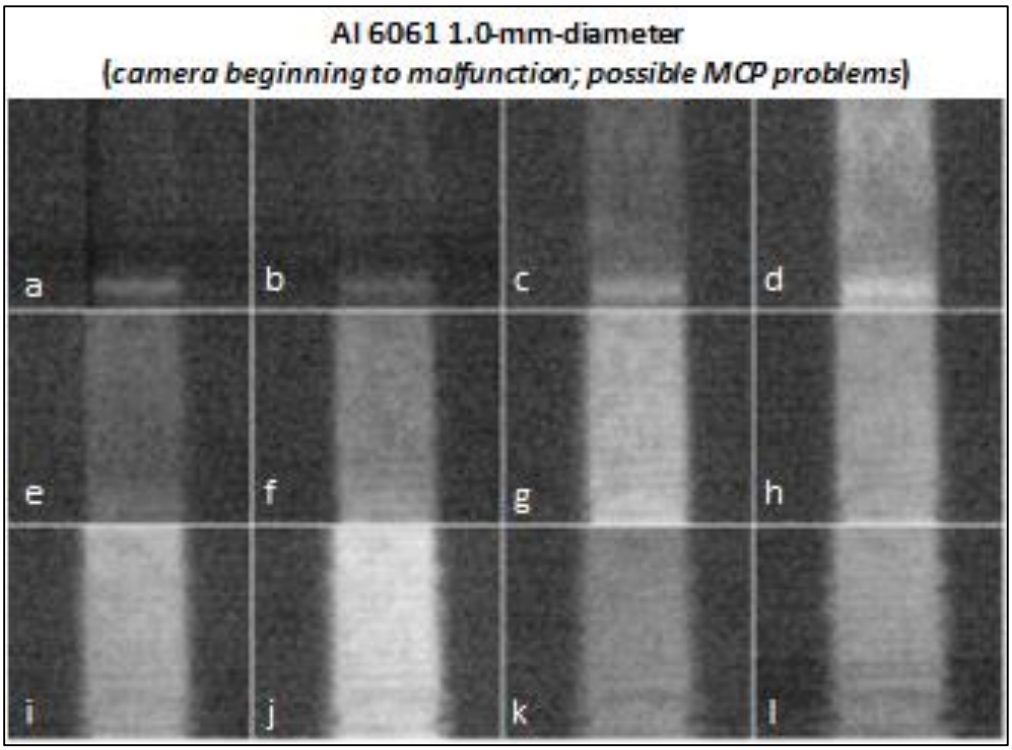

Figure V.41 Machining artifacts are observed to emit light early and evolve into large late time surface instabilities. Some surface structure is observable with strata clearly observed in frames "f-l", however, the light collection and resolution is poor.

The SIMX 16-frame ICCD camera was more successful in collecting light as well as achieving higher spatial resolution as discussed in chapter III. There was a problem triggering the camera, with the camera appearing to trigger at different times from shot to shot. It also appears that the time gate for each image as well as the individual image gate was not triggered properly, with several images appearing to overlap and others seeming to have 10s of ns of time gap between them. It is possible that this a problem of poor EMI shielding.

Figure V.42 shows the results of copper 101 0.7-mm-diameter with 4 ns gates with 0 ns between the end of one frame and the start of the next. There are not 16 images due to several of the early images having no observable structure but still observing enough of an edge for a lineout, and therefore, have not been included in Figure V.42. Figure V.43 is a plot of the radius of the load in time with the shadowgraph data plotted for a comparison. Image frame "a" is the fourth data point in the expansion data in Figure V.40. Several aspects of the SIMX plots stick out immediately. First, there is a clear discontinuity between frames 8 and 9, with frames 9 and 10 appearing flat. Second, there is a shift in time between the visible emission data and the Ekspla shadowgraph data. Third, the time of plasma formation for shot 3756 was shown to occur at 106 ns, which would fall somewhere between frames "b" and "d". The SIMX data can be shifted such that frame "c" falls at 106 ns. Figure V.44 is a plot of the time shifted SIMX data with the Ekspla shadowgraph data plotted as well. The data lines up much better with Ekspla shadowraphs, and also places the images on the current profile at times that match well with the diode array in terms of plasma formation and instability formation. Because of the timing concerns with the multi-frame ICCD, a difference in observed radii between self-emission and shadowgraphy can not be determined. Awe showed in his dissertation[109] that there was a possibility of the

shadowgraphs observing a larger diameter than the streaked self-emission, however, the difference fell within the error of the analysis.

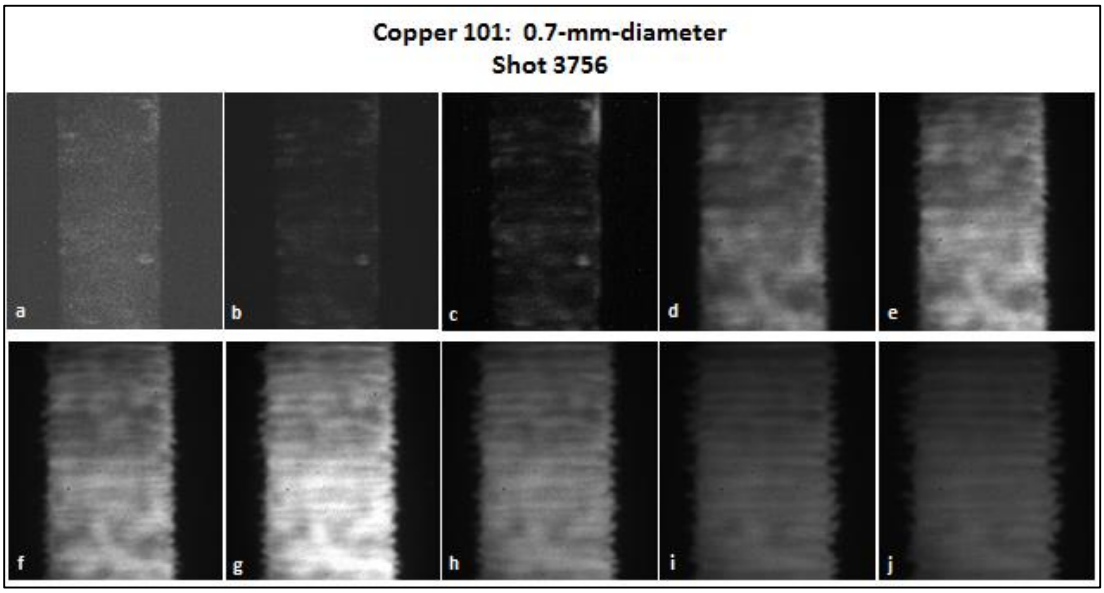

Figure V.42 The 16-frame image SIMX ICCD camera shows early structure on the surface of the copper 101 rods. Frames that did not have images due to lack of light emission are not included in the images shown in this chapter.

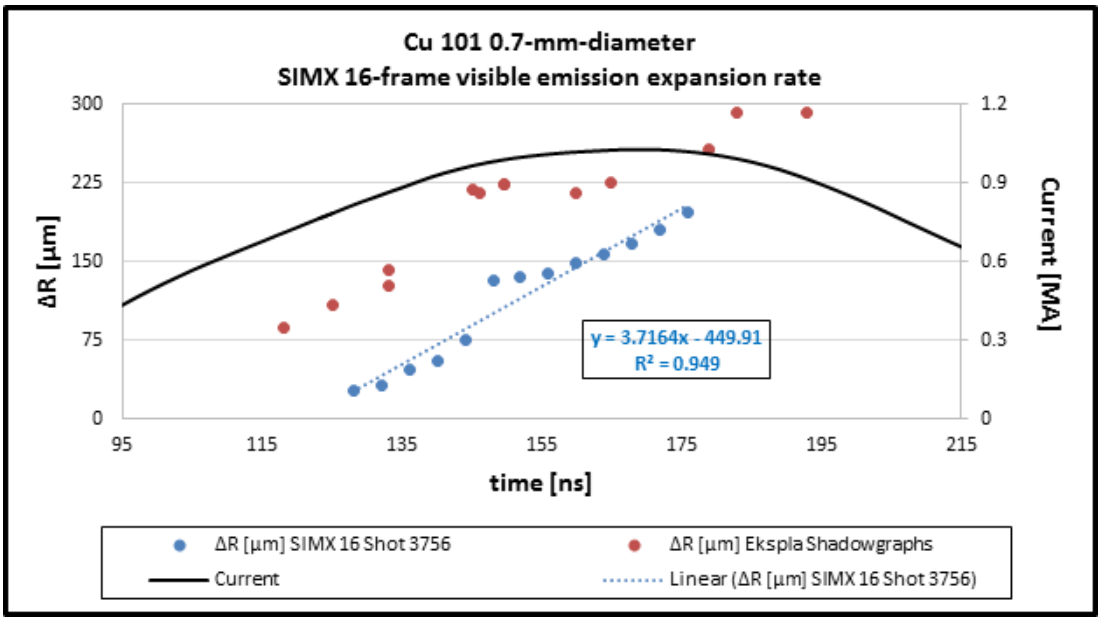

Figure V.43 Radial lineouts taken of the SIMX ICCD images provide a linear expansion estimate. A comparison with the shadowgraph results shows a clear discrepancy caused by incorrect time-base signals from the SIMX camera, discovered after the experiment.

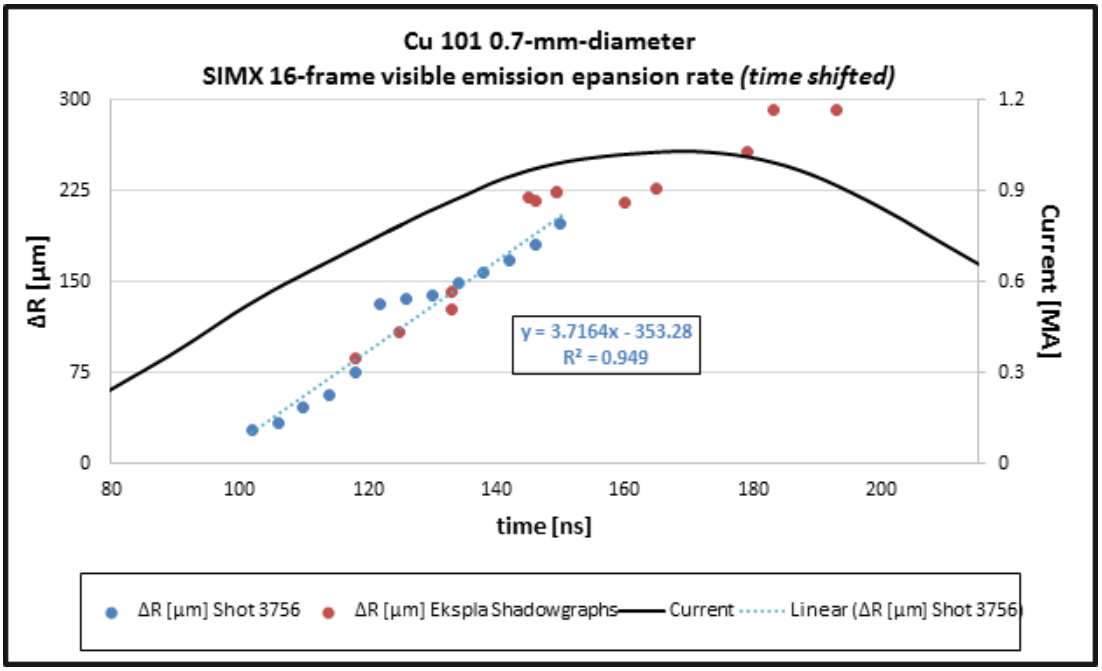

Figure V.44 Timing of the SIMX images were shifted based on matching the timing of images with images observed with the single frame ICCDs.

Figures V.45 and V.46 show the results for copper 145, with all 16 frames providing quality images. All image frames except the last two in figure V.43, frames "g" and "h", were used to determine the expansion rate. The last two images were clipping on the edge and were not considered useful for determining expansion. The expansion results are plotted in figure V.47 along with the results of the Ekspla shadowgraphy for comparison. Similar to what was observed for the copper 101 images, there is a discontinuity between frames 8 and 9 of the camera, with frames 7 and 8 becoming flat.

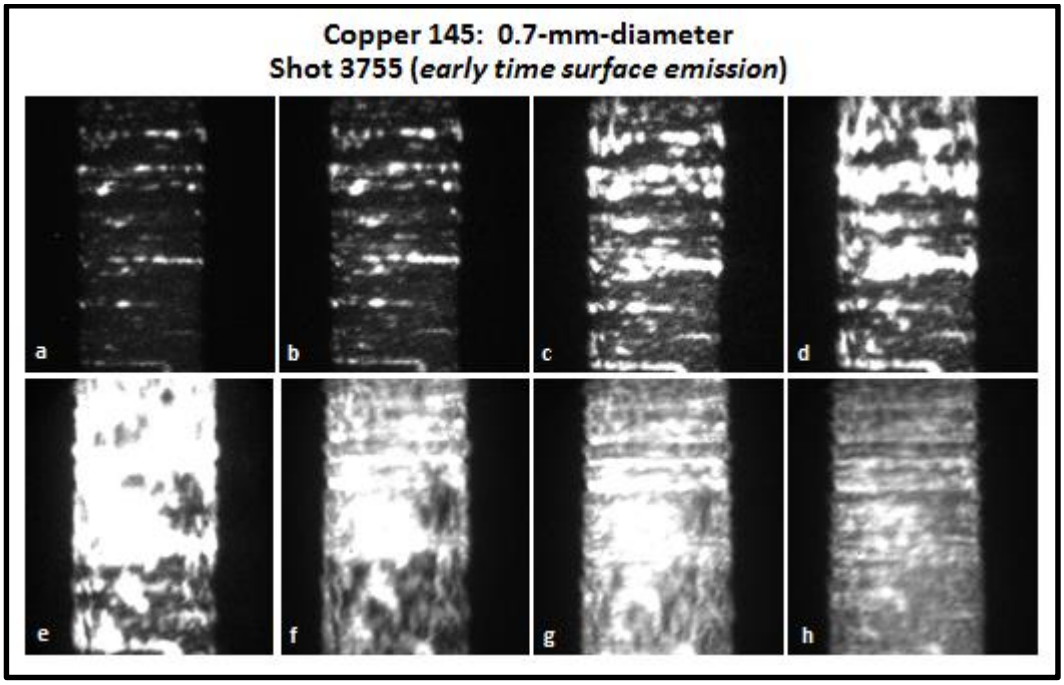

Figure V.45 Copper 145 images captured by the SIMX ICCD show early non-uniform structure with strata that appears to match machining artifact left by the lathe.

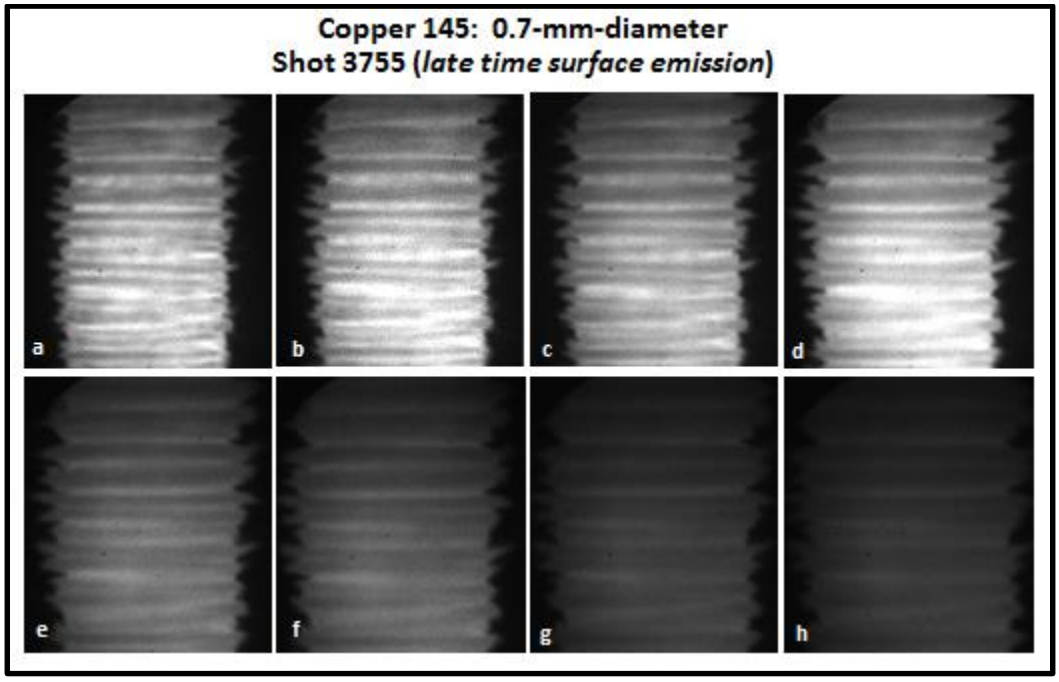

Figure V.46 Copper 145 images captured by the SIMX ICCD show late time instability growth with the expanded part of the instability emitting less light. This cooling effect is expected for an expanding plasma instability.

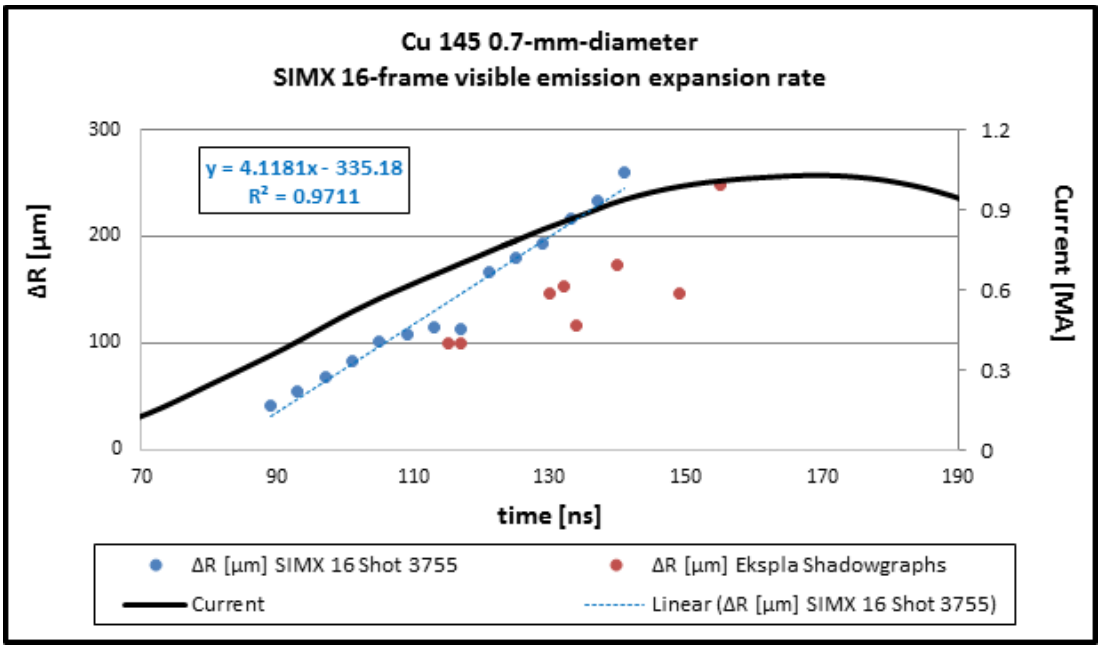

Figure V.47 The expansion rate determined by the lineouts of the copper 145 SIMX images compared to the shadowgraph results.

The nickel 200 had 13 images that could be used to determine the expansion rate, with the first five frames, shown in figure V.48, having very little light emission or observable surface structure. The following 8 frames have much more light, shown in figure V.49, but appear to be out of focus compared to some of the other shots captured with the SIMX camera. Figure V.50 plots the expansion for the SIMX images along with the one Ekspla shadowgraph pair for a comparison. There is once again a discontinuity between camera frames 8 and 9 (image frame "e" from figure V.48 and image frame "a" from figure V.49). It is difficult to theorize the expansion rate of nickel 200 with only one Ekspla shot and the SIMX camera not operating correctly. It is interesting to note that the expansion rate for the Ekspla shot and the two regions of the SIMX expansion rate for nickel suggest an expansion rate of 1.3 μm/ns, 1.2 μm/ns, and 1.7 μm/ns respectively.

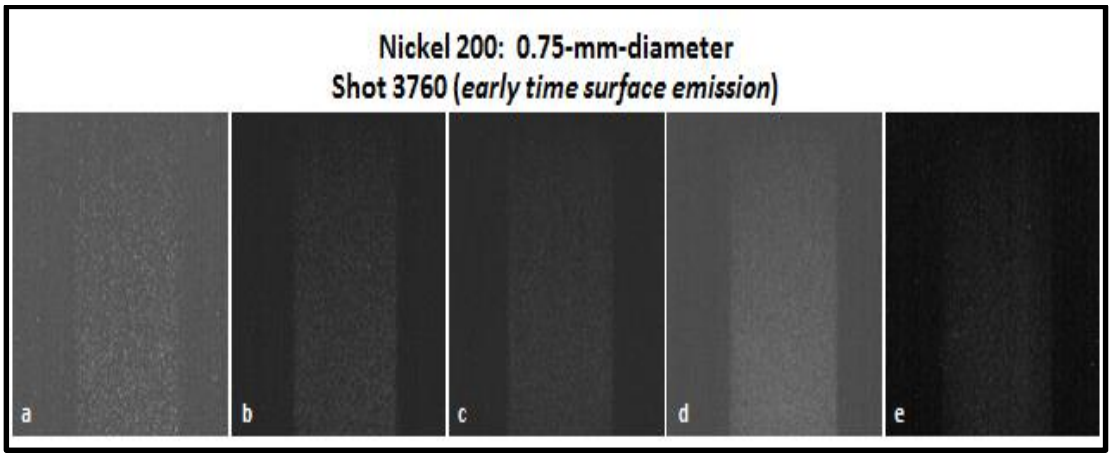

Figure V.48 Nickel 200 images with the SIMX show early uniform emission. Any possible structure was lost due to poor resolution due to a bumped optic.

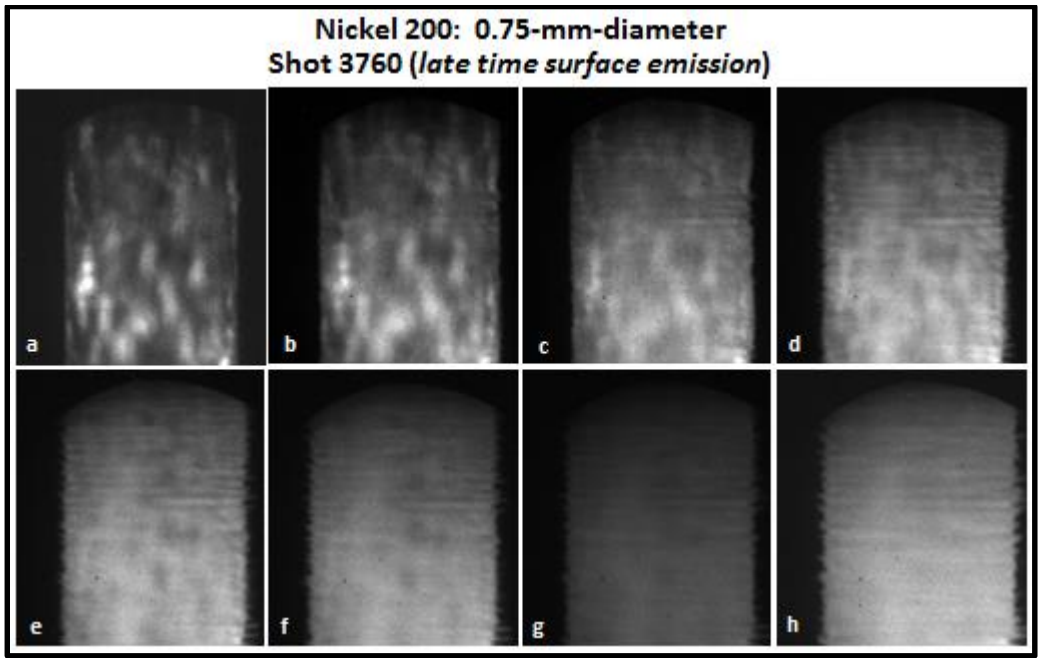

Figure V.49 Nickel 200 images with the SIMX show non-uniform surface structure form strata that evolve into late time MRT instabilities.

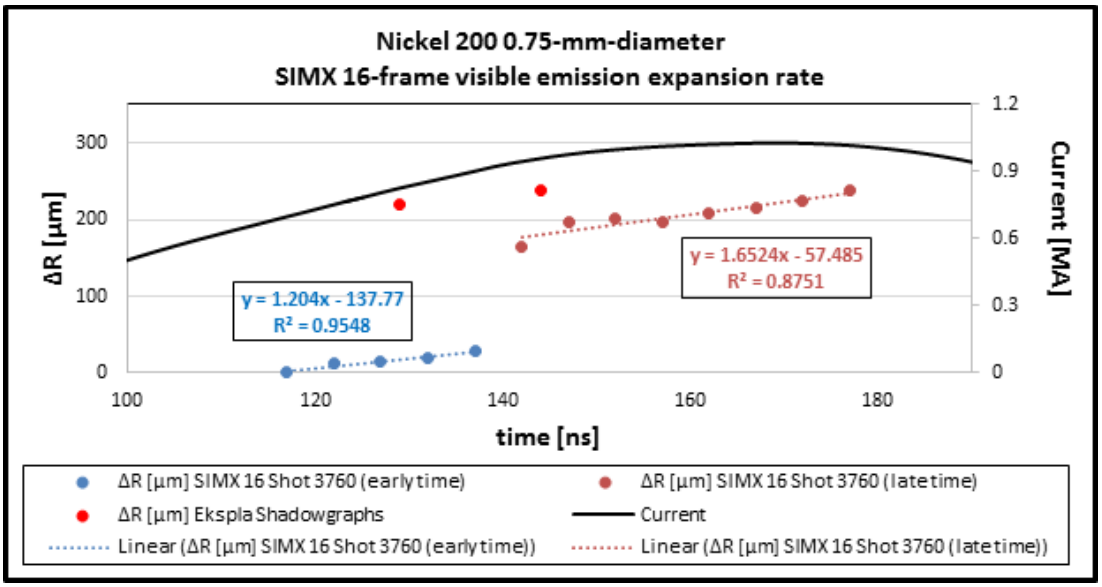

Figure V.50 Linear expansion of nickel 200 using lineouts of the SIMX images compared to laser shadowgraphy. An abrupt jump in the radius indicates a jump in the timing of the camera trigger.

The titanium II images are shown in figure V.51 with only 9 frames having quality images. All images were utilized to determine the expansion rate with the exception of the last frame, image "i", due to the image running out of the field of view. Similar to nickel 200, there is a large discontinuity that occurs between the camera frames 8 and 9. The expansion data is shown in figure V.52 with the early images and the late images being fit to separate line as was done with nickel 200. The titanium II images appear to have poor spatial resolution, with only one image showing non-uniform surface emission. Very little structure is observed in this image, frame "a", compared to some of the copper 101 and 145 images presented in this chapter and chapter III. As was discussed in chapter III, this is thought to be due to one of the relay lenses being knocked out of position such that the resolution was degraded.

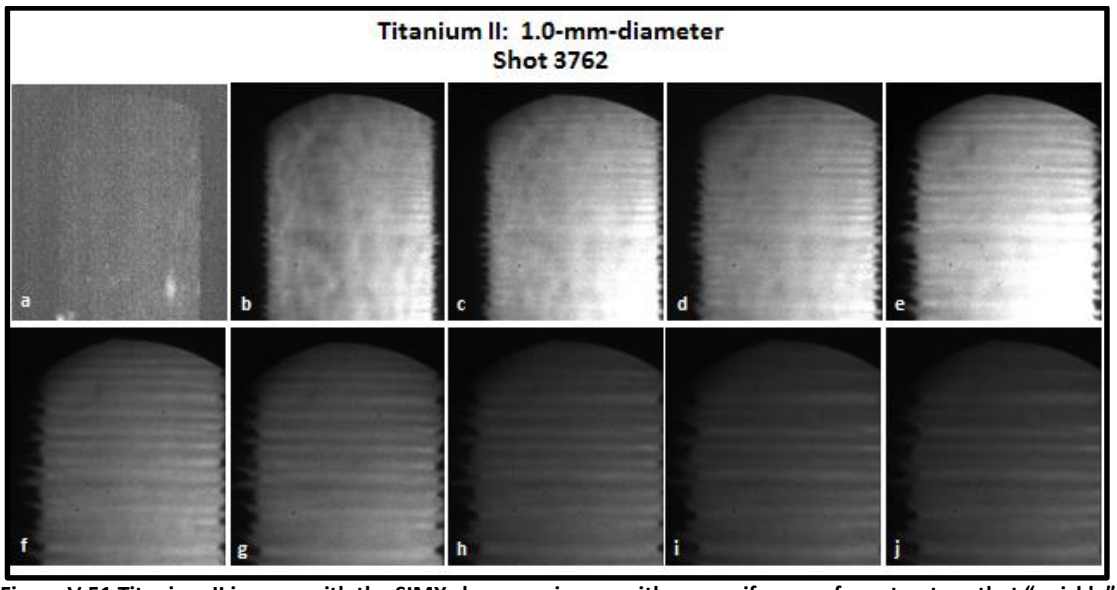

Figure V.51 Titanium II images with the SIMX show one image with non-uniform surface structure that "quickly" form strata that evolve into late time MRT instabilities.

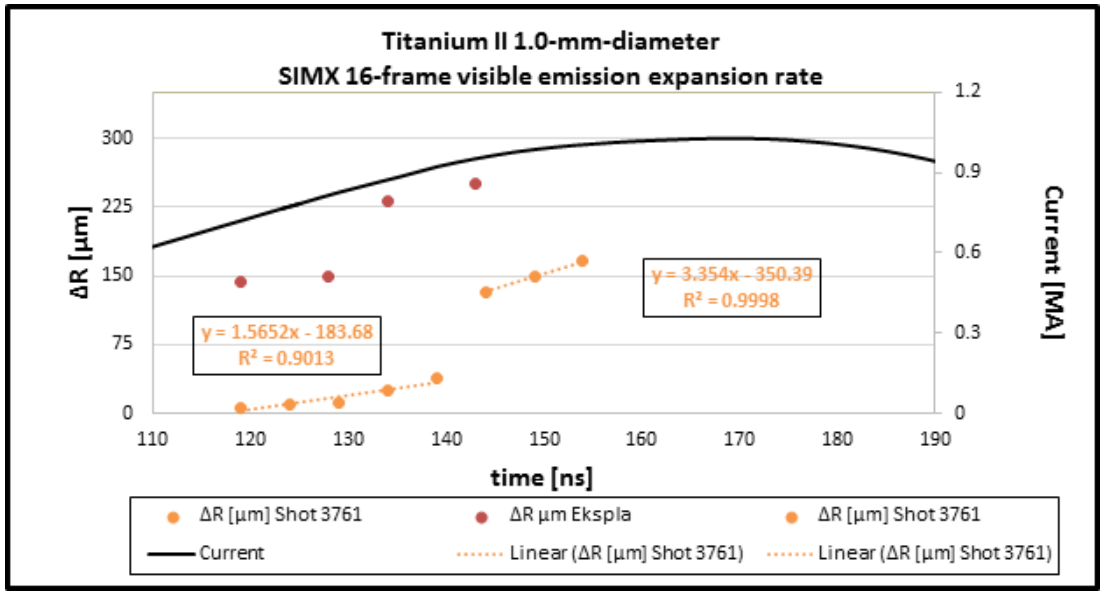

Figure V.52 Linear expansion of titanium II using lineouts of the SIMX images compared to laser shadowgraphy. An abrupt jump in the radius indicates a jump in the timing of the camera trigger as was observed with the nickel shot.

The late time instabilities observed on the copper, titanium, and nickel can be analyzed to determine which modes are developing and how they progress in time. The first step is to go through all the images from a single shot and see if there is a region of the image that appears to

stay in focus or not have pixel saturation that can blur out the modes. The preference was to take the lineout of the entire rod in each image. This was done on some but not all due to saturation of the pixels. Each region was kept the same for each frame on a single shot. But shot to shot variation in how much of the load was in the lineout does exist. A lineout is taken and imported into Microsoft Excel. An example of a lineout is shown in Figure V.53 for titanium shot 3761. The lineout included the radial section of the rod out to the edge and the vertical section was taken to include the rod up to where the image is clipped in the right and left corners.

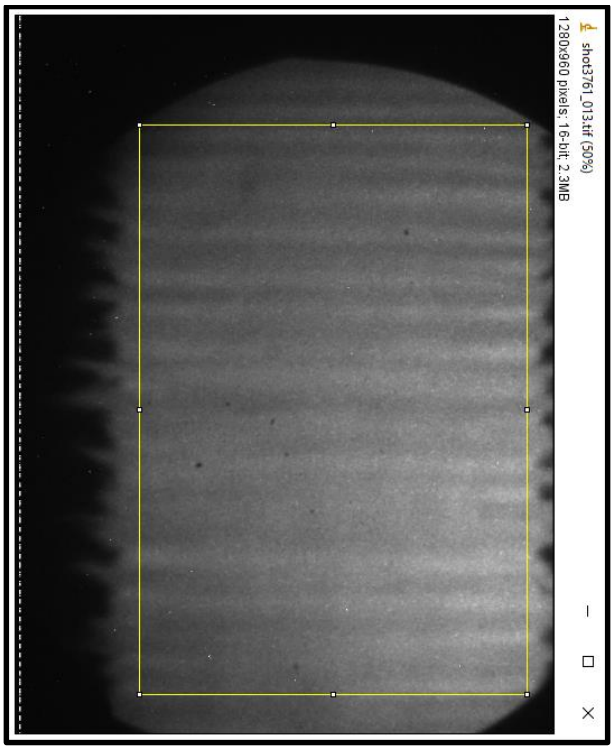

Figure V.53 A region of an image from the SIMX ICCD camera was captured using ImageJ. The region was exported as a lineout into Microsoft Excel where a Discrete Fourier Transform was taken to determine the wavelength modes of instability.

A one-dimensional Discrete Fourier Transform (DFT) is conducted in the z direction (the direction of current flow) using a Python code written by graduate student Trevor Hutchinson. For a single lineout a mean was calculated with a standard deviation of photon counts. For each wavelength mode determined by the DFT, the variance from the mean was found. The output provided the

wavelength modes and the corresponding variation from the mean. These columns were plotted for each frame. The results for copper 145 shot 3751 are shown in figure V.53 and V.54. The plots have discrete wavelength modes with a polynomial fit for each frame. The fit was added to help visually observe any trends in the modal behavior from frame to frame. Figure V.53 plots the wavelength modes that are in the range from 0-620μm. The top, middle and bottom plots have frames 5-7, 5-10, and 5-16 respectively. This makes it easier to see the evolution of the modes. Figure V.53 shows modes growing near 200, 250, and 500μm, and quickly die off by frame 15.

Figure V.54 shows the same images but the DFT results in the 300-1200μm wavelength range. Growth of instability modes near 600 and 900μm is observed with the 900μm modes starting with a small energy density per pixel, then quickly increasing and possibly saturating.

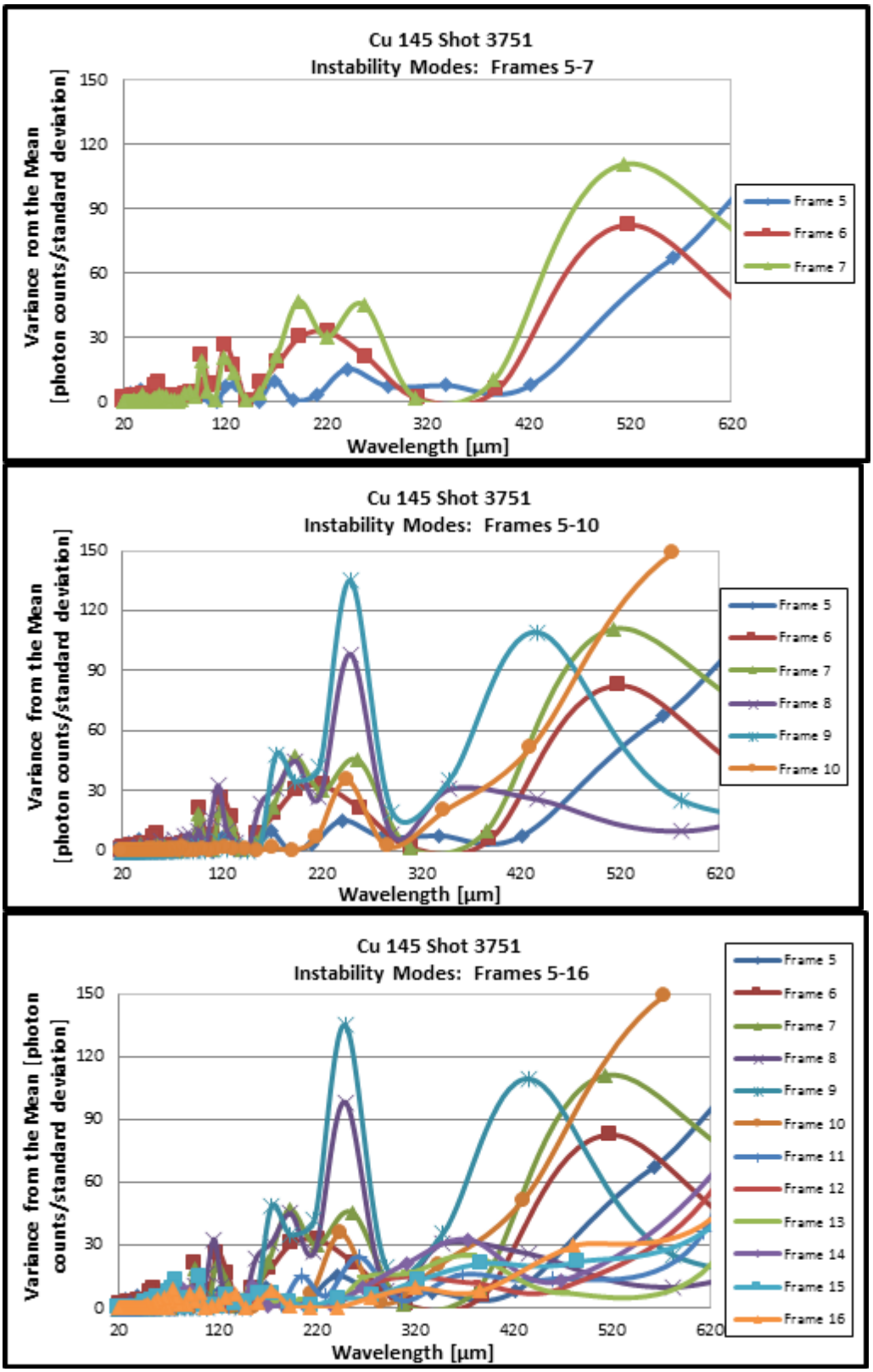

Figure V.54 The evolution of instability modes observed in the SIMX 16-frame ICCD camera. Each frame shows the observed modes of instability determined with a Fast Fourier Transform.

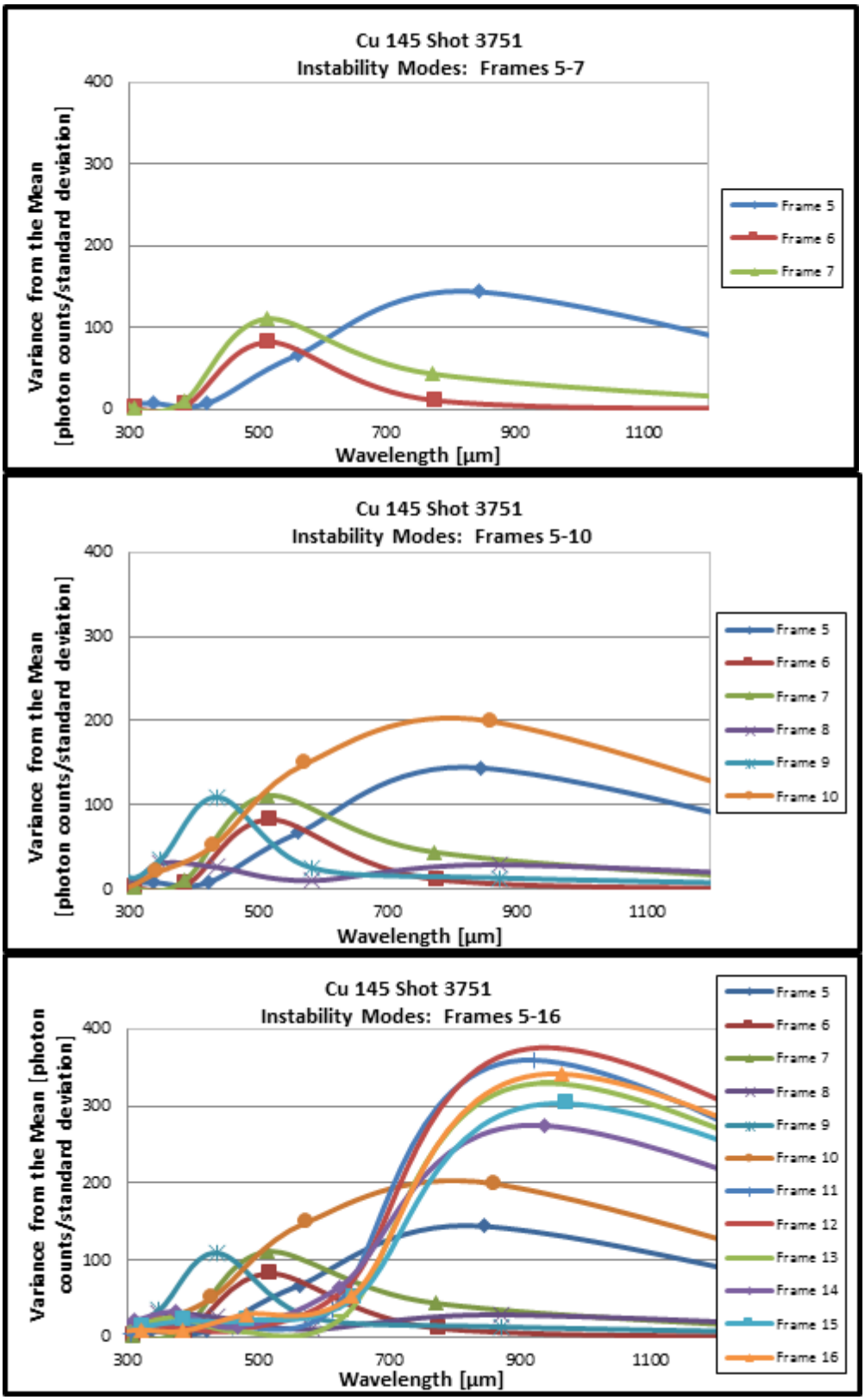

Figure V.55 The evolution of instability modes observed in the SIMX 16-frame ICCD camera. Each frame shows the observed modes of instability determined with a Fast Fourier Transform.

For the dominant wavelengths, the variance from the mean was plotted as a function of camera frame, with increasing camera frame equivalent to increasing current time. The results for copper 101 are shown in figure V.55. Growth in the wavelengths <1000µm show growth early in time, with all of them becoming small late in time. The 1020µm wavelength is the dominant mode in all frames.

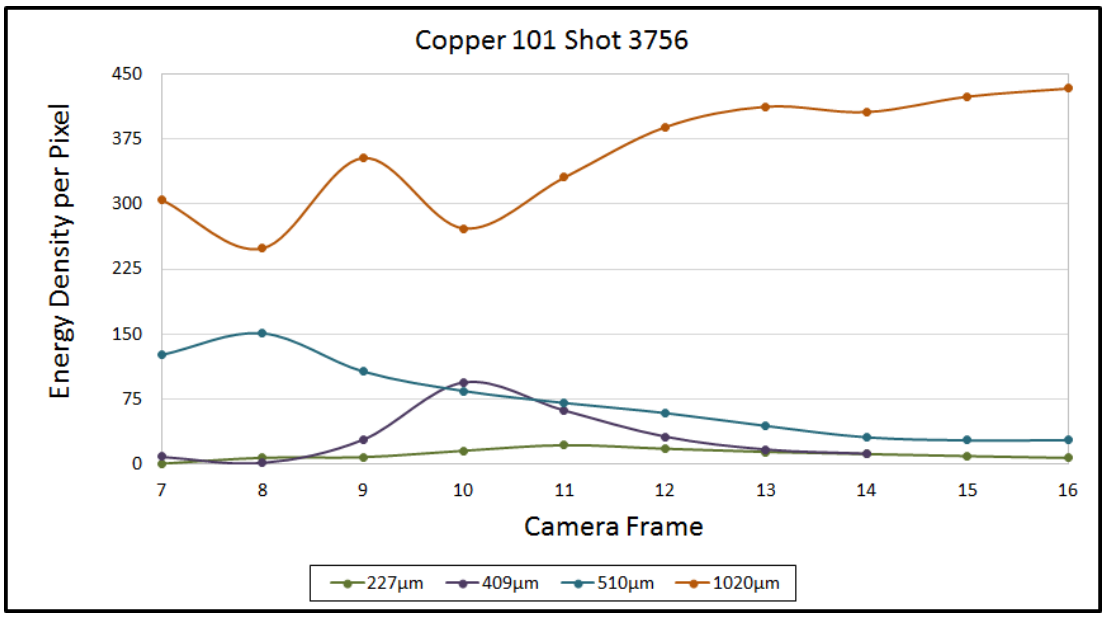

Figure V.56 Evolution of dominant wavelength modes of instability in time for Cu 101. The longest wavelength modes survives late in time.

The results for two copper 145 shots are shown in figures V.56 and V.57. Figure V.56 shows several modes between 200 and 600µm growing early in time and then quickly die off later in time. The mode near 900µm is not the dominant mode early in time, however, near the time that the other modes appear to be diminishing, the long wavelength mode grows sharply.

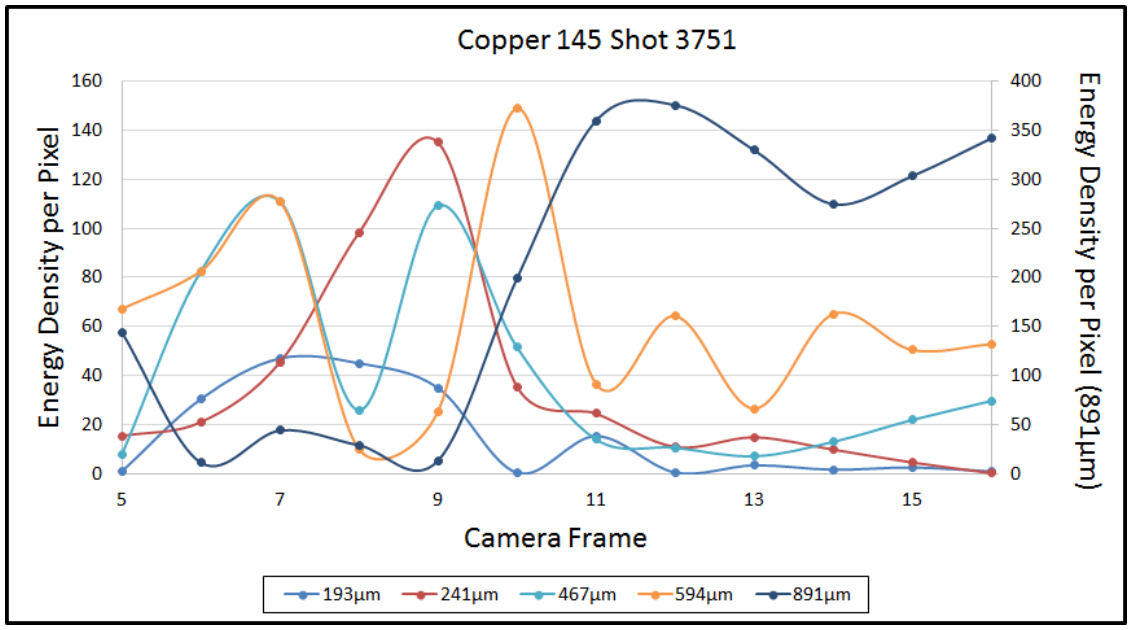

Figure V.57 Evolution of dominant wavelength modes of instability in time for Cu 145. Modes between 190 and 600µm grow early in time, with the longest wavelength modes dominating late in time.

Figure V.57 shows a similar result with lower wavelength modes dominating early in time, but diminishing late in time with the longest wavelength mode increasing. The oscillation in frames 4-8 in the top of the figure is due to frames 5 and 6 having poor image quality due to saturation of the pixels. It is likely that those modes are gradually diminishing across several camera frames.

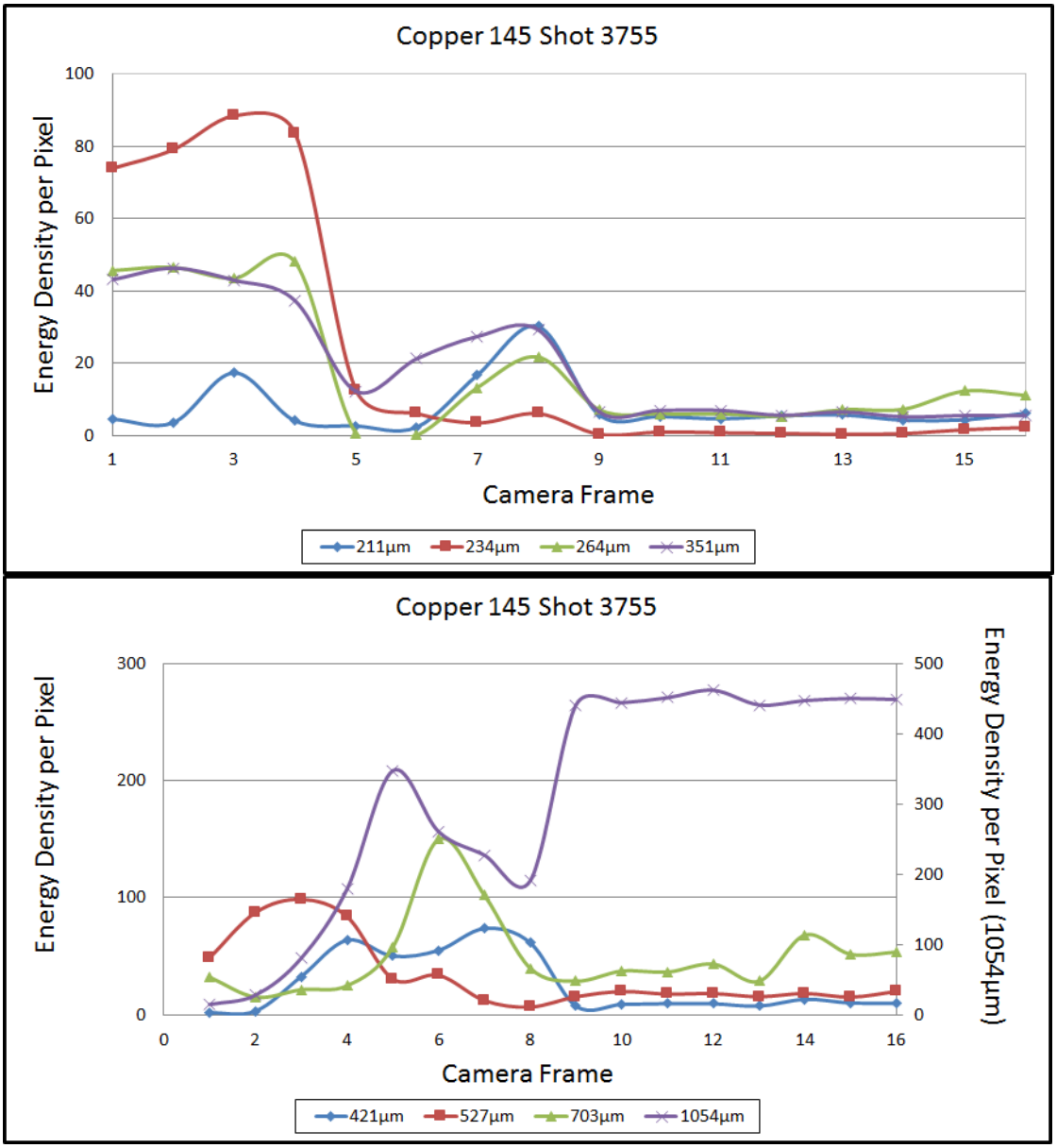

Figure V.58 Evolution of dominant wavelength modes of instability in time for Cu 145. Modes between 200 and 703µm grow early in time, with the longest wavelength modes dominating late in time.

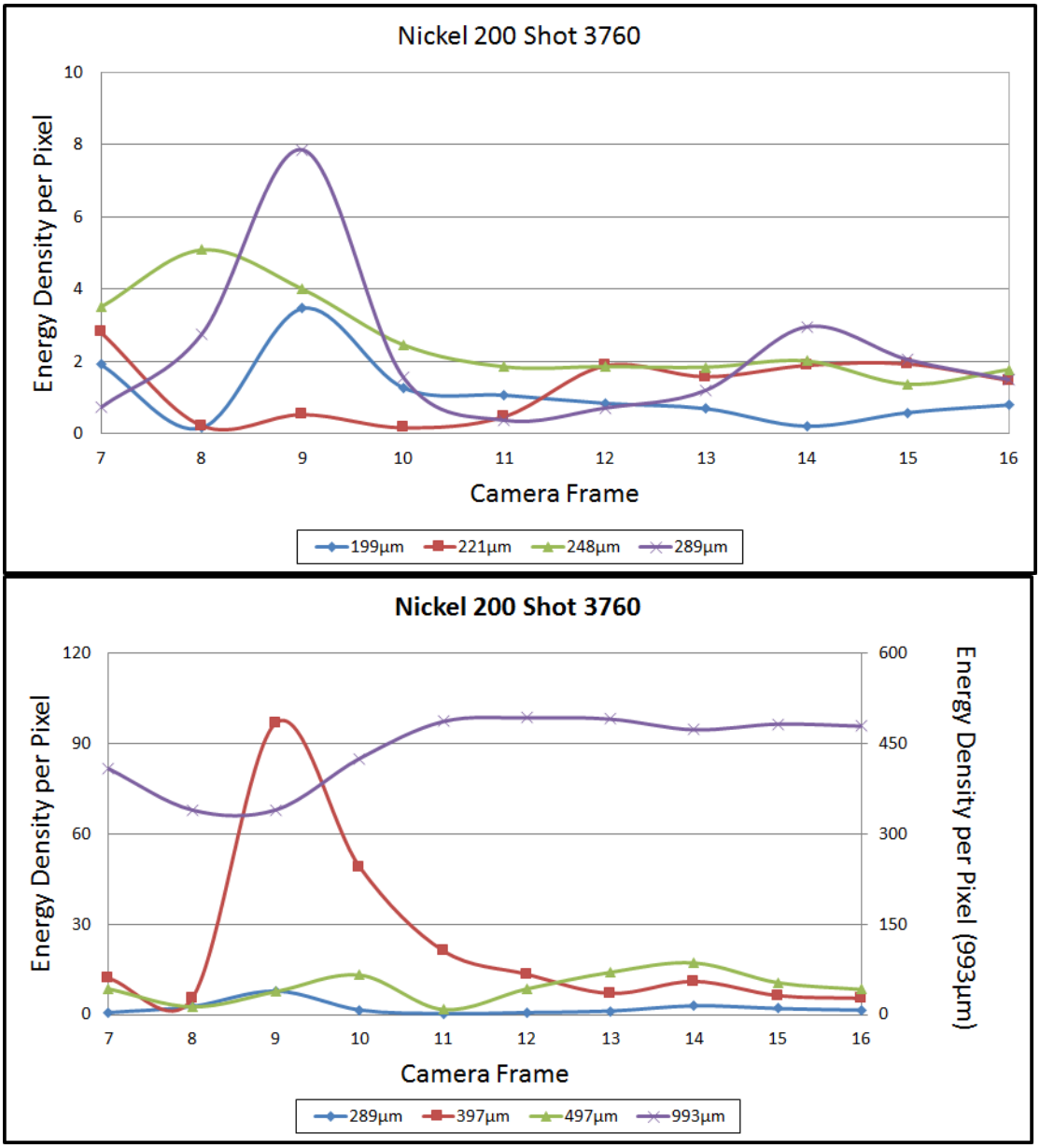

Figure V.59 Evolution of dominant wavelength modes of instability in time for Ni 200. Modes between 199 and 500µm grow early in time, with the longest wavelength modes dominating late in time.

The nickel and titanium show similar results as shown in figures V.58 and V.59.

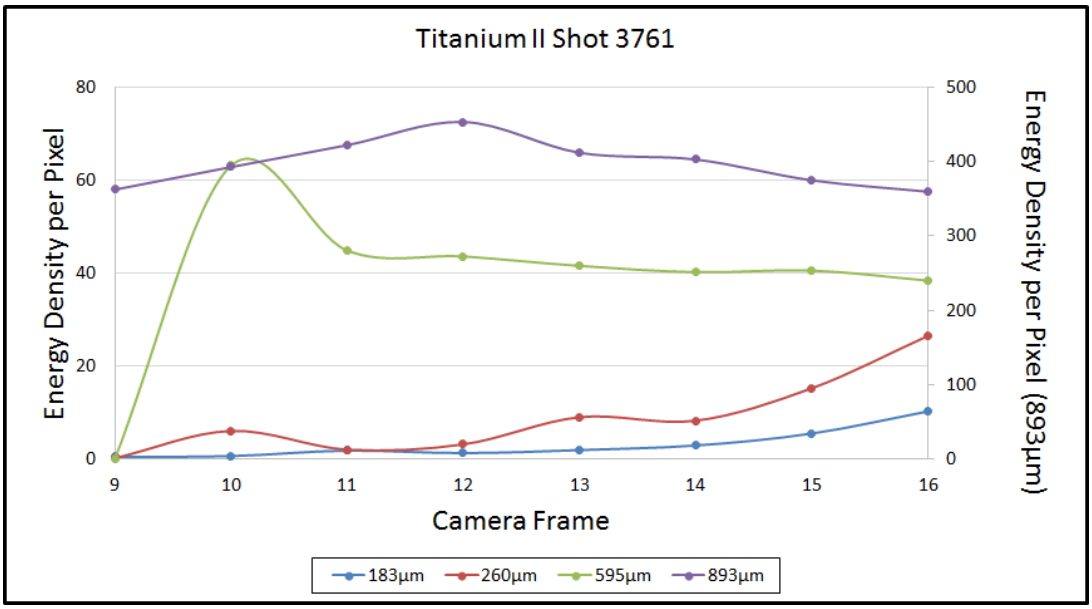

Figure V.60 Evolution of dominant wavelength modes of instability in time for Ti II. Modes between 260 and 600μm grow early in time, with the longest wavelength modes dominating late in time.

How the late time instabilities form is not well understood. As discussed in chapter I, electrothermal instabilities that form in the melting phase could seed late time MRT instabilities. However, the lack of spatial and temporal resolution in the above images prohibits our ability to determine if instabilities early in time match well with the wavelengths predicted by theory. The long wavelength mode dominates, as is expected and has been observed in other experiments[110].

Chapter VI: Extreme Ultraviolet Emission

Extreme Ultraviolet (EUV) diagnostics were fielded to determine the ionization state of aluminum and copper surface plasma. A McPherson Model 310/g grazing incident spectrometer was fielded with a multistrip microchannel plate (MCP) detector. The spectrometer had sensitivity in the range of 8 to 70 nm (155 to 17 eV). The resolving capability of the spectrometer was $\lambda/\Delta\lambda\sim400$ at $\lambda=30.4$ nm and $\lambda/\Delta\lambda\sim300$ at $\lambda=11.0$ nm with the entrance slit of 30 μm. Broadband EUV photodiodes were fielded with coatings that consisted of 200 nm of aluminum or 100 nm of Si and 200 nm Zr with a sensitivity range of 16 to 73 eV and 60 to 100 eV respectively. The EUV photodiodes and spectrometer were primarily designed, fielded and analyzed by Dr. Stephan Fuelling of the UNR Physics Department. This chapter will use the results of Dr. Fuelling's work to allow for a better understanding of the experiment as a whole. The chapter will begin with a brief description of the photodiode diagnostics. The data collected by the two EUV diodes confirm the formation of plasma and a comparison between aluminum and copper diode signals will be presented. A brief overview of the EUV spectrometer will be presented with limited details of the design of the diagnostic. The results of aluminum and copper shall be presented with a comparison to modeling predictions. The aluminum loads shot in the MG VI experiment were entirely 1.00-mm-diameter with the timing of the spectrometer kept constant. The spectral region observed was varied by moving the instrument across the Rowland circle and allowed the regions spanning from 8.2 nm to 47.8 nm to be observed. The purpose for this was to flatfield the spectrometer as well as to determine the wavelength at which the line emission becomes continuous. The copper loads were also scanned from 8.2 nm to 74.3 nm with no line emission observed for any load diameter. The lines for aluminum and copper are determined using the web-based atomic database provided by NIST[111] for Al IV-VI and Cu I-V.

Section VI.A: EUV Photodiodes

Two AXUV silicon photodiodes were fielded in the MG experiments. The diodes had a thin film directly deposited to filter out low energy photons. One diode was filtered with 200 nm of Al while the other was filtered with 100 nm of Si and 200 nm of Zr. The detectable energy ranges for these filters were 16 to 73 eV and 60 to 100 eV, respectively. The filter transmission curves are shown in figure VI.1. Directly deposited filters are preferred over foil filters because of the ease of handling (foil filters are fragile and difficult to mount) and allow for a light tight system meaning that all photons that reach the detector must pass through the filters. The photodiodes were purchased from International Radiation Detectors (IRD) and have an active area of 1.0 mm $\times$ 1.0 mm. The diodes were mounted in an ISO 63 flange and placed approximately 2.6 meters from the load. Due to the proximity, the use of a fast shutter valve was necessary to protect the diodes from load debris. The shutter has dimensions of 2.00" $\times$ 1.5" with the shutter motion being in the vertical (1.5") direction. The diodes had to be placed such that they would have a clear line of sight through this opening. The flange was mounted to the chamber by a long stainless steel tube with the fast shutter directly in front of it. The EUV spectrometer was mounted to the same tube approximately 0.75 meter behind the diode flange. With the spectrometer, photodiode, and the fast shutter valve all in line, careful design was needed to ensure that there was a clear line of sight for both the spectrometer and the diodes through the rectangular aperture of the fast shutter valve to the load. The diodes were mounted in the flange with a rectangular tube in the center such that the slit of the EUV spectrometer received light emission from the load with the photodiodes in a position to still collect light.

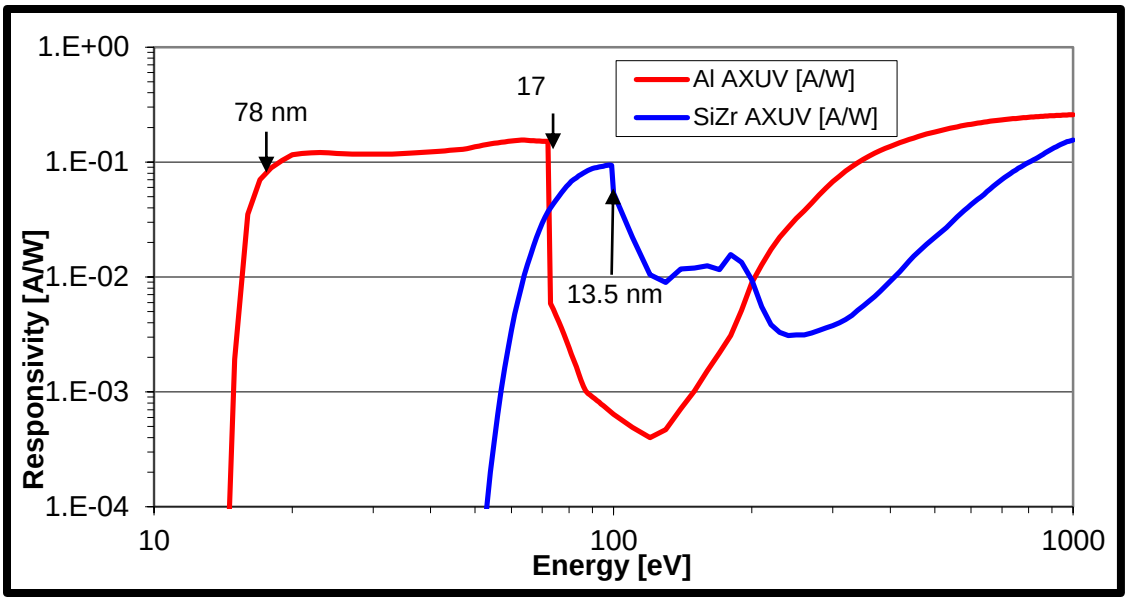

Figure VI.1 The responsivity of the AXUV photodiodes with the corresponding directly deposited filters.(Figure courtesy of S. Fuelling, UNR)

The photodiodes reached several volts for the aluminum and copper loads. The onset of EUV emission should occur after the onset of visible emission from the surface of the loads. In MG III and MG IV the emission of EUV photons was observable nearly 15 ns after the observed emission of visible light. If it is assumed that the plasma is a blackbody in both the visible and EUV wavelengths, then the difference in time for the onset of radiation emission is understood from the shift in blackbody intensity as described by Wein's displacement law. The observation of EUV emission is one of the many indicators of plasma formation.

Section VI.B: EUV Spectroscopy

The EUV spectrometer fielded for measuring spectral emission was a McPherson Model 310/g grazing incidence spectrometer. The spectrometer has 6 MCP strips (Model 40.6-MCPH, from X-ray Specialty Instruments) that are DC biased up to 400 volts. During a shot, an electronic gate increases the voltage to 900 volts for 5 ns. The MCP strips are activated at different times using cables to delay the gating between each strip by 10 ns. Only the middle two strips were

used to collect data. The grating has a 600grooves/mm with iridium coating and a blaze angle of 2°. The photocathode consists of gold strips coated with CsI to improve the sensitivity in the EUV range. The MCP and camera assembly is shown in figure VI.2.

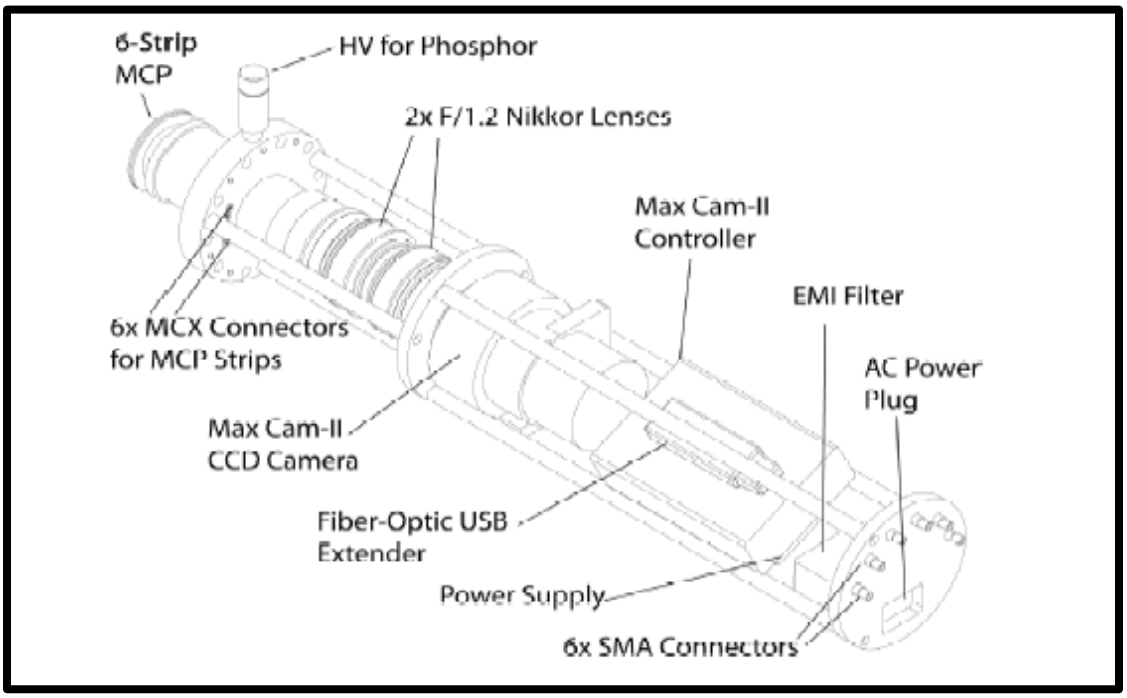

Figure VI.2 The MCP/Camera assembly Nikkor lenses, controller and EMI filter. SMA connectors at the back of the assembly electrically connected to the MCP strip. An EMI filter was used to protect the system from EMI power spikes. A fiber-optic USB extender was used to control the camera. A plastic optical fiber was used to trigger the camera.(Figure courtesy of S. Fuelling, UNR)

The MCP is coupled to a fiber optic reducer which is then coupled to two F/1.2 Nikkor camera lenses to a Peltier-cooled 1024×1024 pixel camera (Finger Lake Instruments, Max Cam II). This assembly is connected to a larger assembly that includes a bellow, the spectrometer grating, and an entrance slit. The entire assembly is shown in figure VI.3.

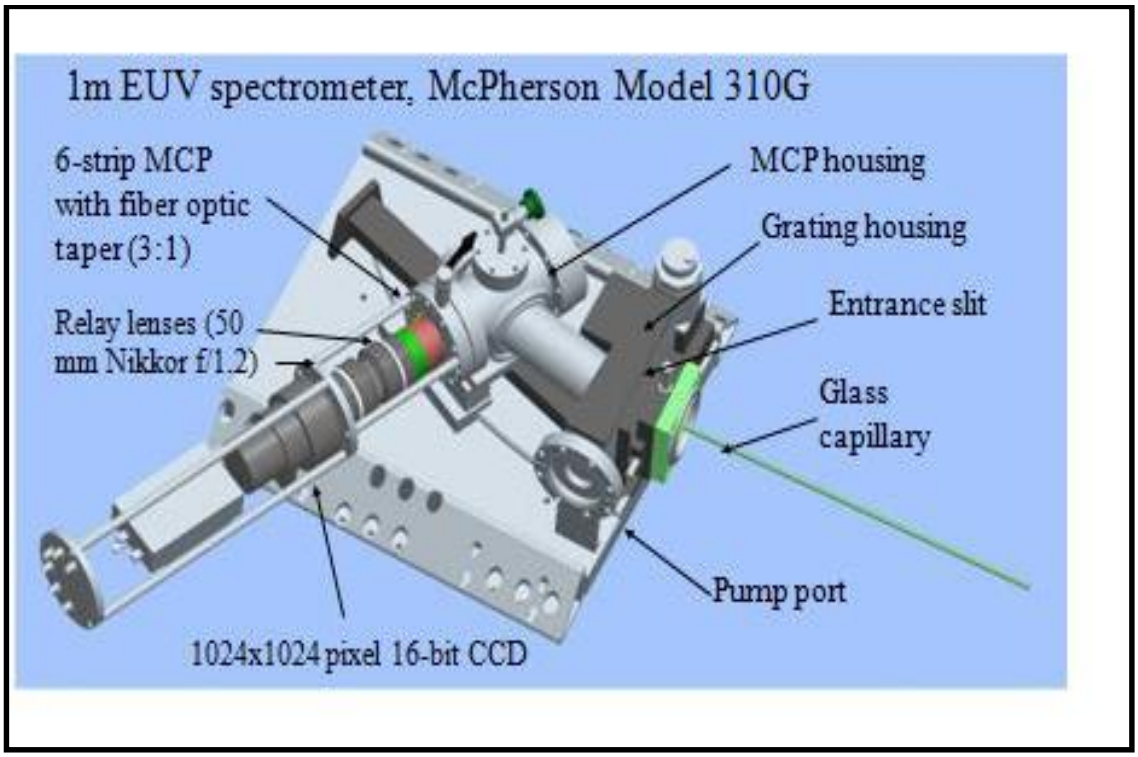

Figure VI.3 The McPherson spectrometer with the grating housing and pump port with a glass capillary guiding light to the entrance slit. The glass capillary was not used in the experiment.(Figure courtesy of S. Fuelling, UNR)

The glass capillary shown in the figure was used in the calibration of the spectrometer with a microwave plasma source, but was not used during experiments. The assembly is connected to the chamber by a long steel tube with a bellows at the connection to the Zebra chamber to decouple the spectrometer from shocks and stresses in the system during a shot. A pneumatic fast shutter valve was placed near the assembly and was triggered before the Zebra current pulse due to its long internal delay so it would stay open during the Zebra pulse but close before debris would reach the valve and the spectrometer. Figure VI.4 shows a rough image of the entire set-up, including the EUV diodes that were placed between the shutter valve and the spectrometer.

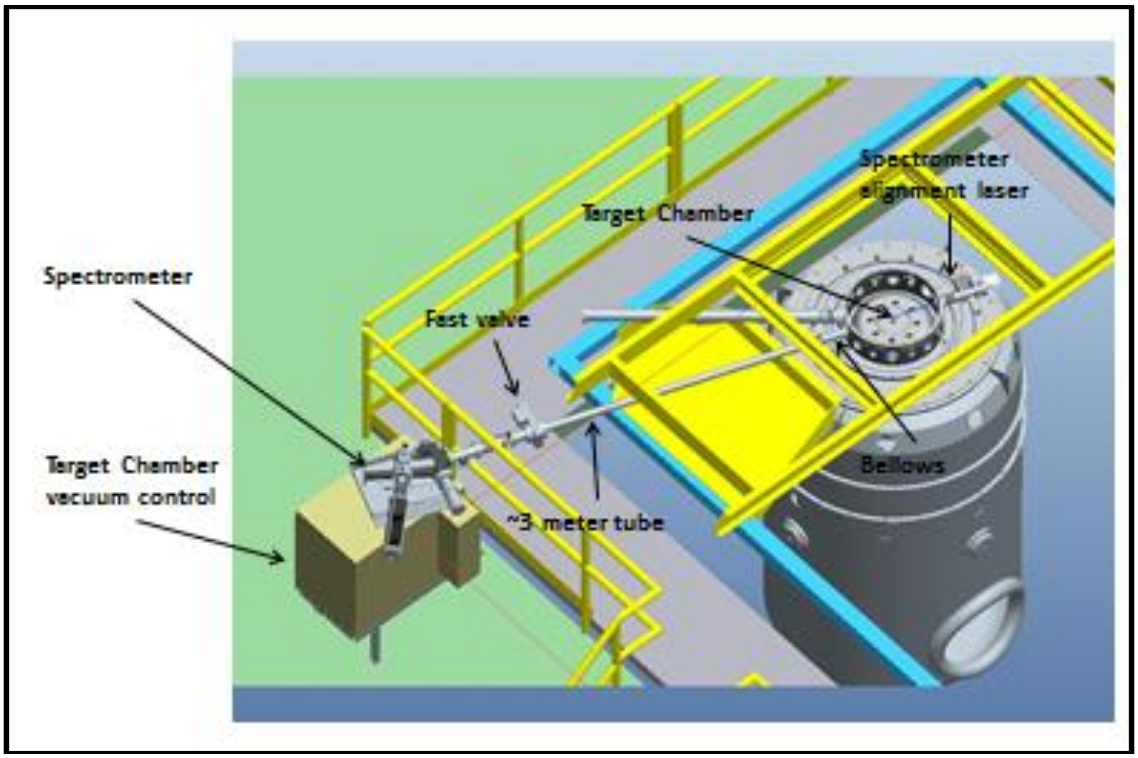

Figure VI.4 The EUV spectrometer was placed on a scaffolding that was on top of the target chamber vacuum control box. A 3 meter tube connects the spectrometer to the target chamber with a bellow to isolate the spectrometer from shock during a Zebra shot. A faster shutter valve was placed in the line of the 3 meter tube to protect the spectrometer from debris during a shot. (Figure courtesy of S. Fuelling, UNR)

The spectrometer was fielded to measure spectral emission in aluminum and copper plasmas in the wavelength ranges from 8.2 to 74.3 nm. For the aluminum rods in previous experiments in the range was 8 to 18 nm only. This spectral range contains Al IV-VI with the ratios providing a temperature estimate. The ion charge state and line intensity depends strongly on the temperature of the plasma. This allows a temperature estimate to be determined from the ratios of line intensity between different charge states of a single element. Figure VI.5 is a plot of the ionization fraction for three charge states of an aluminum plasma using the PrismSPECT software. The plasma parameters used in this simulation include a plasma density of 5×10^{-3} g/cm^3 in a 1 μm layer of aluminum. The results from MG-IV indicated a surface plasma reaching a

temperature of ~15 eV for all load diameters and sustaining a constant temperature. This is in disagreement with the visible photodiode array that shows a varying temperature in time.

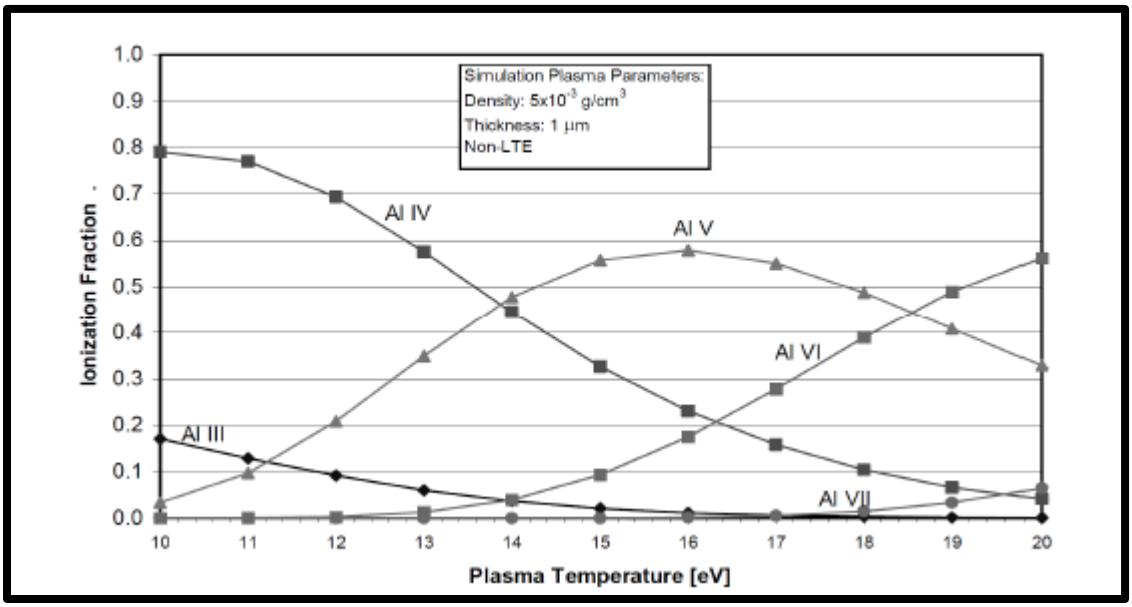

Figure VI.5 The ionization fraction of aluminum plasma for varying plasma temperatures.(Figure courtesy of S. Fuelling, UNR)

It was also observed that the emission lines transitioned into absorption lines late in time indicating a cool outer sheath backlit by a hot core plasma as described in Chapter I.

Section VI.C: Spectroscopy Results

One of the first goals of the MG VI experiment was to extend the wavelength region of the spectrometer data out to the maximum 85 nm. The interest in doing this was to observe when the surface radiation transitioned from line radiation to a continuum. Line radiation in the 8-18 nm range and continuum radiation in the visible range was observed in MG IV. By rolling the

spectrometer to longer wavelengths, it is possible to observe how the line radiation approaches the continuum. The spectral regions were overlapped to determine the response of the spectrometer. The results of overlapping spectral regions from 8 to 56 nm are illustrated in figure VI.6. The top image is figure VI.6 is the spectra from several shots that were recorded on the third MCP channel. The right end of each spectral region (longer wavelength) shows a non-uniform response with a reocurring ramp at the far right edge. The bottom image of the figure shows the correction to the spectrum after "flattening" the MCP response.

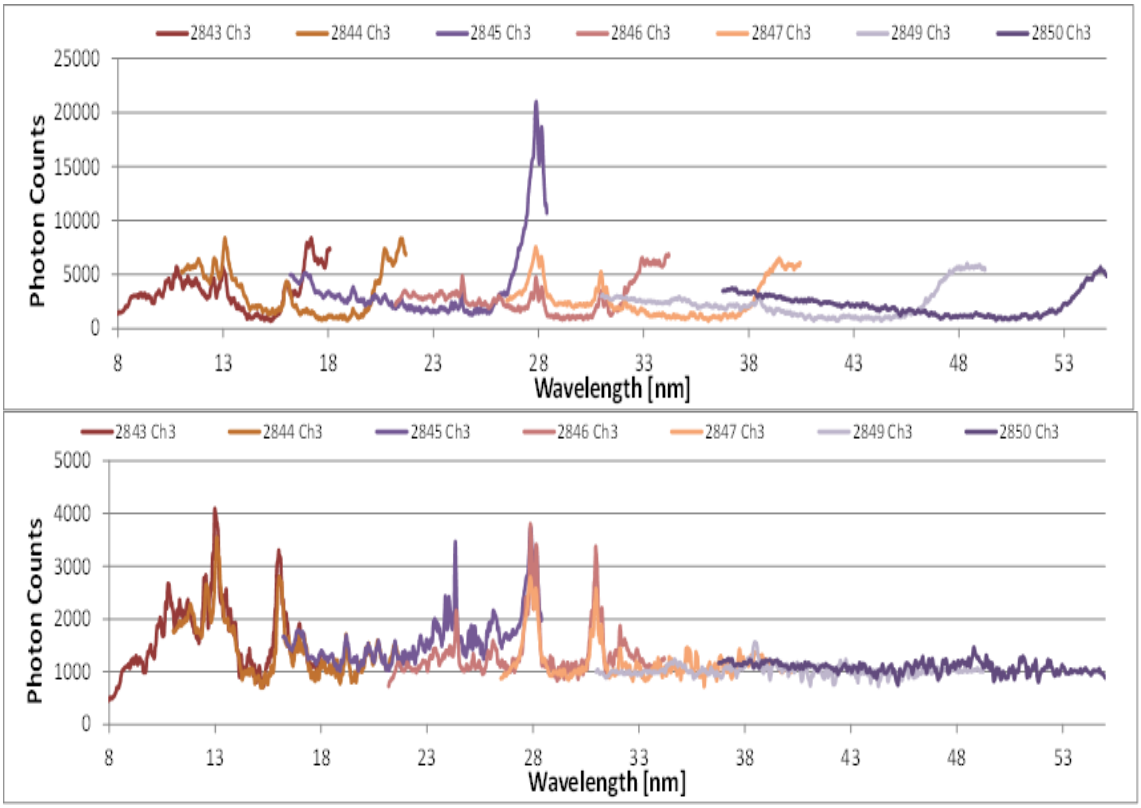

Figure VI.6 The spectra regions show the non-uniform response of the MCP (top image). The flattening of the response (bottom image) provides the corrected spectral response.(Figure courtesy of S. Fuelling, UNR)

As was discussed in chapter I the emission lines will broaden and approach the Planckian limit as the plasma density increases. This suggests that the emission of the visible spectrum is originating from a more dense region of the plasma. A first order line of sight approximation was achieved by using modeled atomic emission spectra from PrismSPECT with density and temperature data

taken from MHRDR simulation results. The geometry of the aluminum load was simplified by assuming the aluminum rod to be flat plasma layers.

Figure VI.7 is an illustration of several PrismSPECT simulations that utilized the work done by Irv Lindemuth for 120 density and temperature pairs. Lindemuth used a 1-D code named MHDR to determine the density profile of the aluminum load. The layers listed on the plot represent different layers of the surface, and hence, different densities and temperatures of the plasma from which the radiation is originating. PrismSPECT simulations were run for 120 different line pairs with “10 layers” representing the 10 innermost layers and “120 layers” representing the outermost 120 layers. Each layer was 0.5 microns in thickness. The figure shows some traits that would be expected. As the density of the radiating plasma increases, the radiation approaches the blackbody limit. The plots also indicate that as the spectra moves toward longer wavelength (lower energy photons) the emission transitions into a continuum that converges with the Plankian limit. Figure VI.8 is the same plot but zoomed in on the spectral region of the EUV spectrometer fielded in the MG experiments.

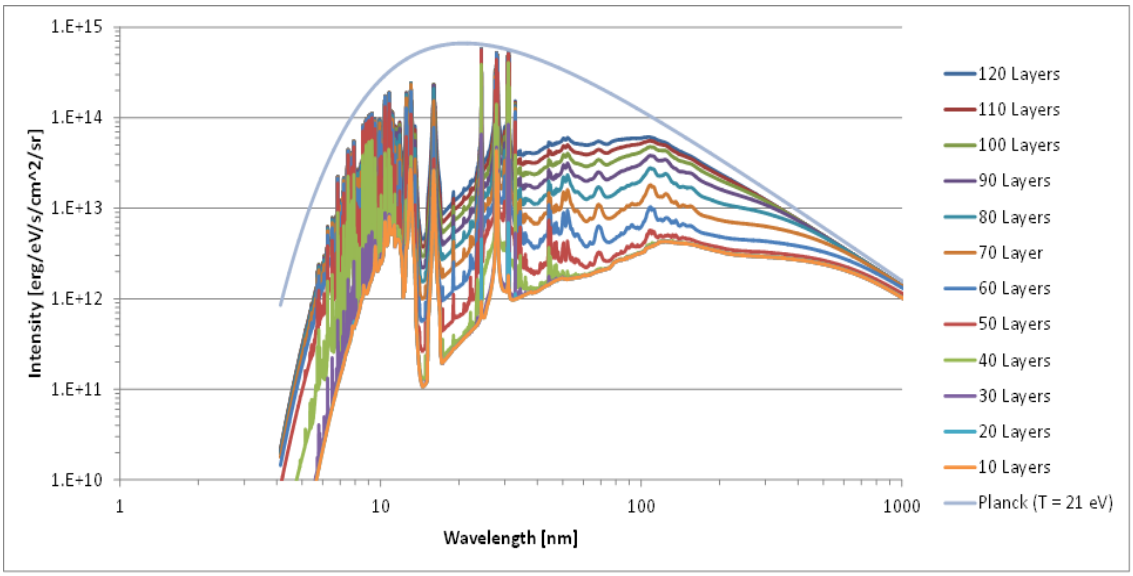

Figure VI.7 Plotted are 120 different line pairs with "10 layers" representing the 10 innermost layers and "120 layers" representing the outermost 120 layers. Each layer was 0.5 microns in thickness. At longer wavelengths the emission converges toward the blackbody limit.(Figure courtesy of S. Fuelling, UNR)

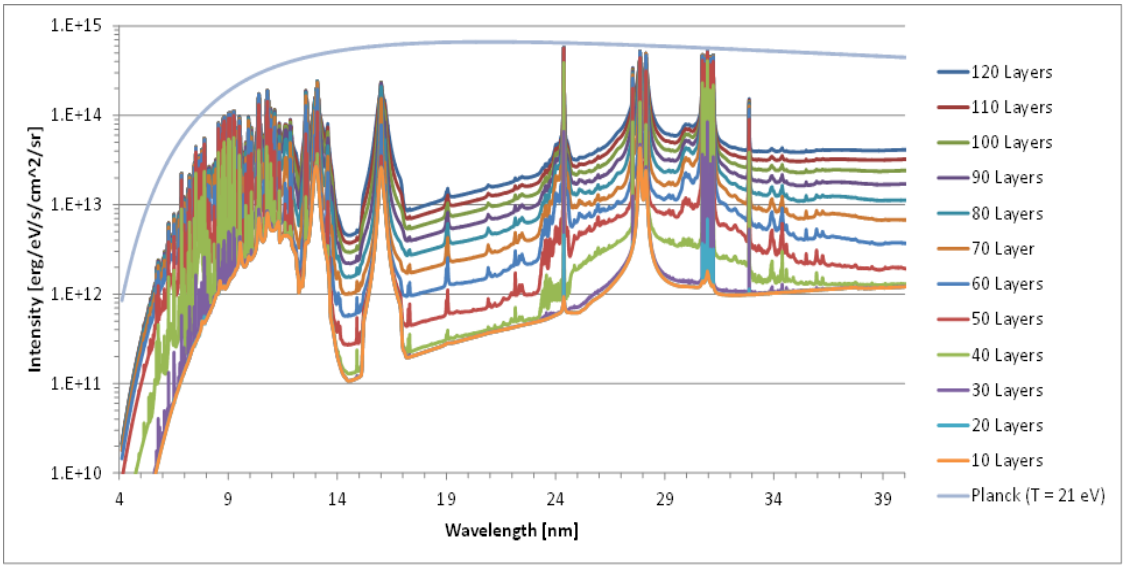

Figure VI.8 Line of sight radiation integration in 10 steps of 10 layers in the region of the EUV spectrometer fielded in the MG experiments.(Figure courtesy of S. Fuelling, UNR)

Figure VI.9 shows the results from rolling the spectrometer out to a wavelength of approximately 56 nm. The results from several shots are plotted along with results from NIST for Al IV-VI. Also plotted are the results of the spectra from line-of-sight integration of 120 plasma layers of temperature and density pairs from MHD modeling using the MHRDR code.

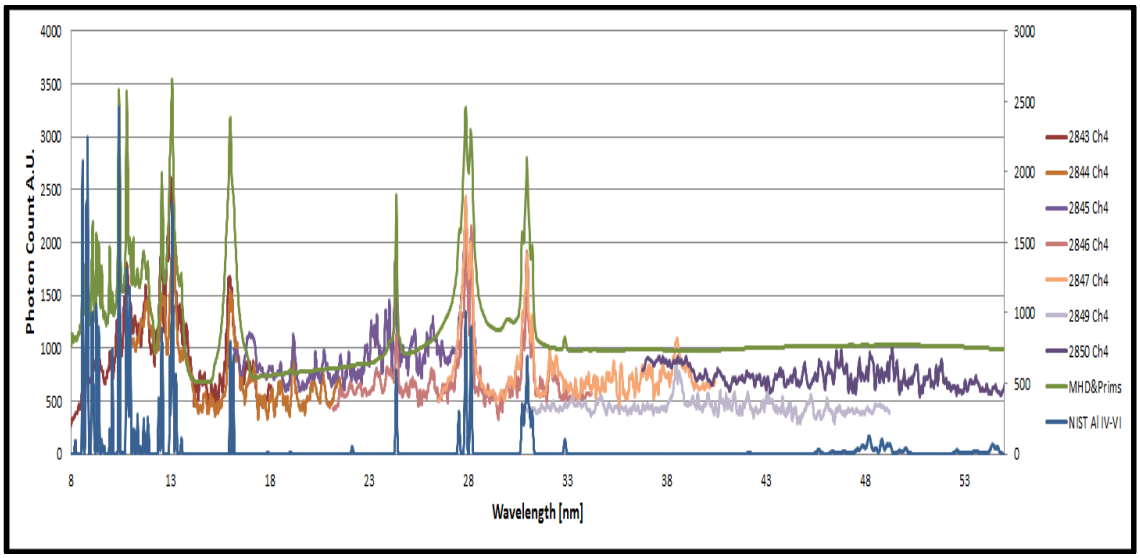

Figure VI.9 Spectra for aluminum 6061 with the colors representing different shots. Each shot rotated the across the Roland circle to provide a different spectral region. (Figure courtesy of S. Fuelling, UNR)

Figure VI.10 zooms in on three regions of interest to allow the emission structure to be seen more clearly. The longer wavelength data agree well with the Prism/MHD spectra, however, the agreement becomes worse at wavelengths below 14 nm. Due to the blaze wavelength of the grating at 14 nm, it is expected that the grating has a rapid decline of efficiency towards shorter wavelengths and is likely the cause of the discrepancy in this spectral region.

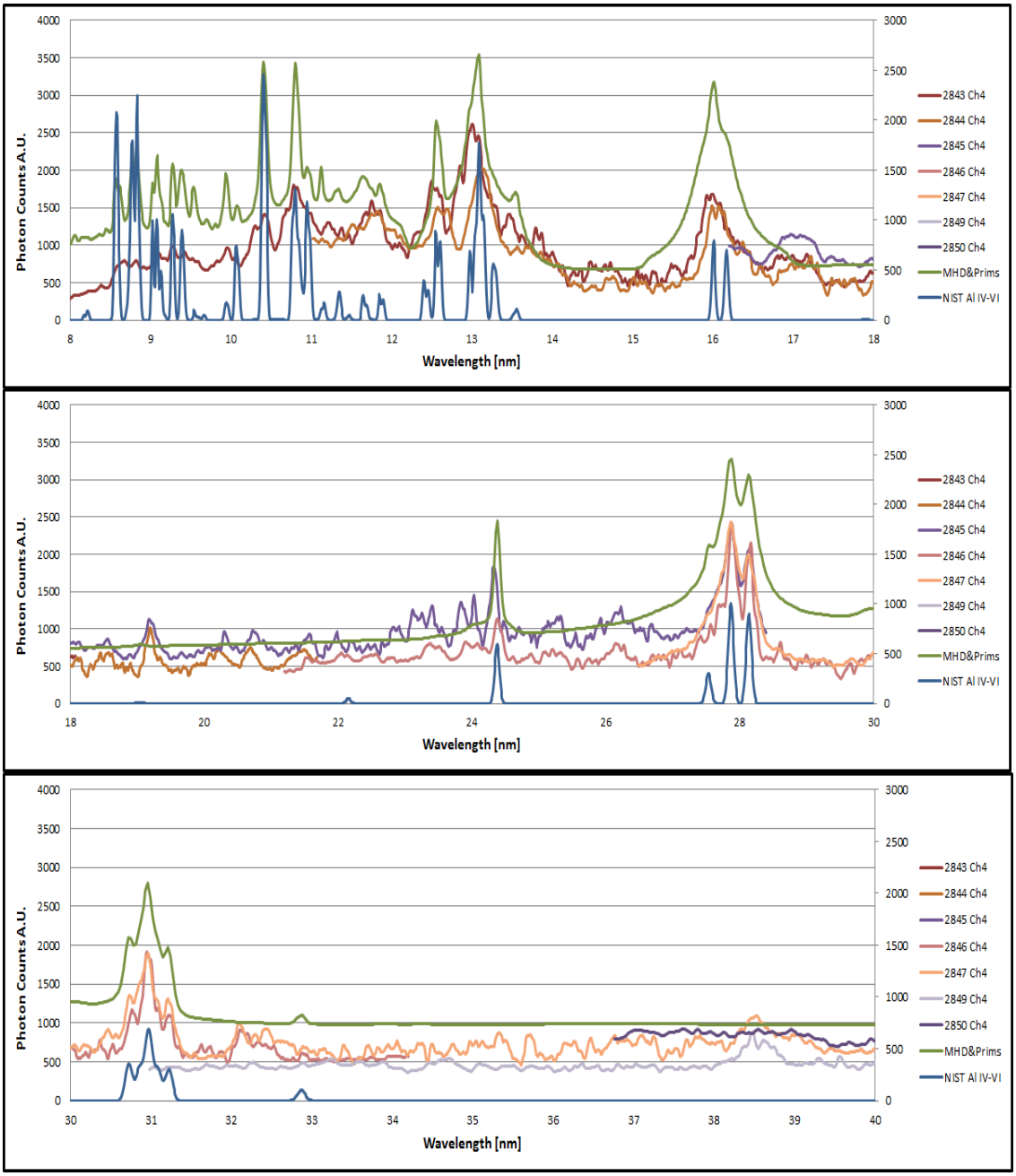

Figure VI.10 The three spectral regions show good agreement with simulations with the exception of wavelengths below the blaze ange, 14nm. This is likely due to the poor efficiency of the spectrometer at these wavelengths. (Figure courtesy of S. Fuelling, UNR)

Figure VI.11 shows the results of the experimental spectra, the modeled spectra using PrismSPECT and the MHRDR results, and a plot of a Planckian curve for a blackbody plasma radiating at a temperature of 21 eV. The data show the experimental spectra converging toward

the blackbody curve, however, the spectra and the blackbody curve do not quite meet. If the data had been collected out to 70 nm, the curves likely would have converged.

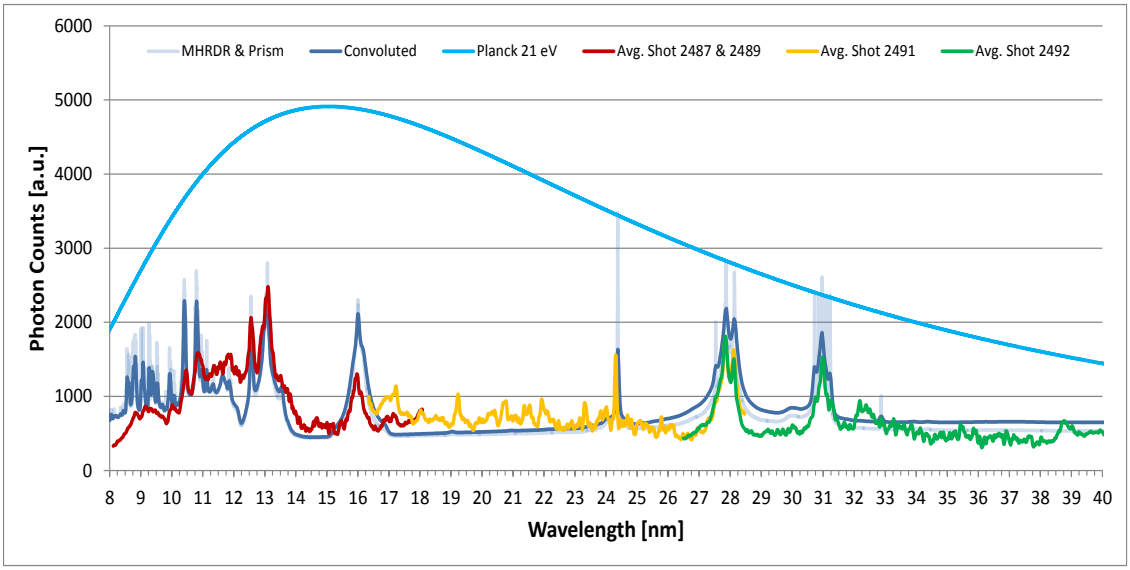

Figure VI.11 The spectra is observed to approach the blackbody limit at longer wavelengths. (Figure courtesy of S. Fuelling, UNR)

The copper 101 rods were the only other alloy that the spectrometer was fielded with in an attempt to determine a temperature. The results from several shots of copper on MG VI are shown in Figure VI.12 along with data from the NIST data tables. The lines expected by the NIST data tables are not shown in any of the results. This result is likely due to the surface temperature of the copper rods not reaching a sufficient temperature to emit line radiation. As discussed in chapter I, the low ionic charge in an element would require a lower electron density to be in an LTE regime. The difference in intensities for the continuous emission seen in the copper spectra correlates with the initial diameter of the copper rod, with smaller diameters emitting larger signals.

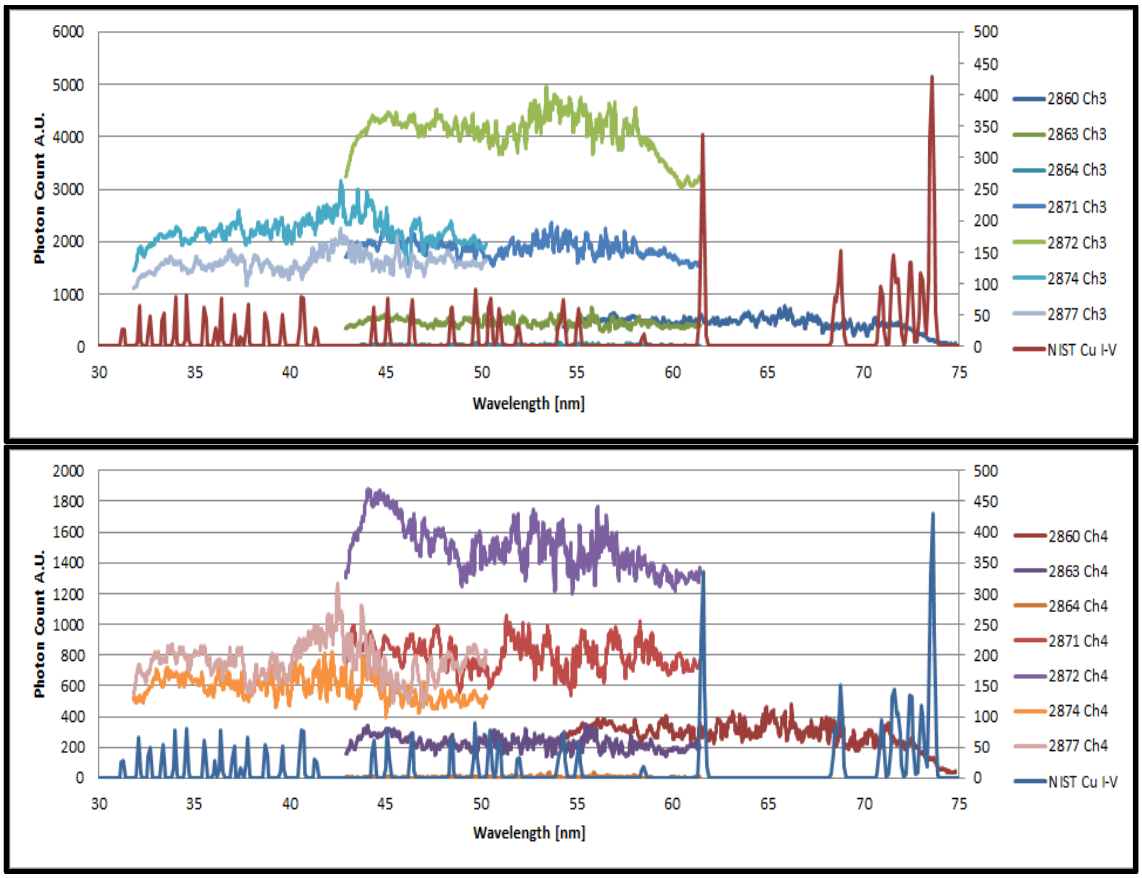

Figure VI.12 The copper rods did not observe line emission. Smaller initial rod diameters are likely to provide the plasma temperatures necessary to form line emission spectra. (Figure courtesy of S. Fuelling, UNR)

Section V.D: EUV Diode Results

The EUV diodes served several purposes in the MG experiments. First, they provided data as to timing of EUV photon generation. This allowed for the timing of the spectrometer to be best determined. The spectrometer was usually timed to be gated near peak current, so to maximize the photon flux and provide the best signal to noise ratio. If the spectrometer shows no signal, but the EUV diodes provide a strong signal, then we know there is a problem with our spectrometer system or perhaps looking in the wrong wavelength range. This could be a result of the fast shutter closing before the experiment (this is not likely), the timing of the spectrometer

could be incorrect, i.e. it could be gated too early, or there is a problem with the spectrometer with regards to the MCP. The diodes also serve as another indicator of plasma formation as well as to the timing of plasma formation with respect to different rod diameters and alloys. The EUV diodes do not show signal until the visible diodes show a surface temperature of 2-3 eV. Figure VI.13 shows results for EUV diode signals plotted along with the visible diodes discussed in chapter IV. The EUV diodes show initial signals approximately 20-30 ns after the initial signals for the visible diodes for both copper alloys. The timing of the EUV diodes is tied to the timing of the visible diodes and is observed with a time shift in the EUV diodes corresponding to a time shift in the visible diodes. The aluminum coated diodes did not provide reliable signals for the copper 101 rods due to damage done to the coating after the fast shutter valve failed to close, allowing debris to reach the diodes during a Zebra shot. It is interesting to note that the copper 145 shots show a progression in heating of the surface for all three different types of diode response regions. The visible diodes show signal first, the aluminum coated AXUV diodes second, and the SiZr AXUV diodes third. This illustrates nicely the heating timescale for the surface plasma.

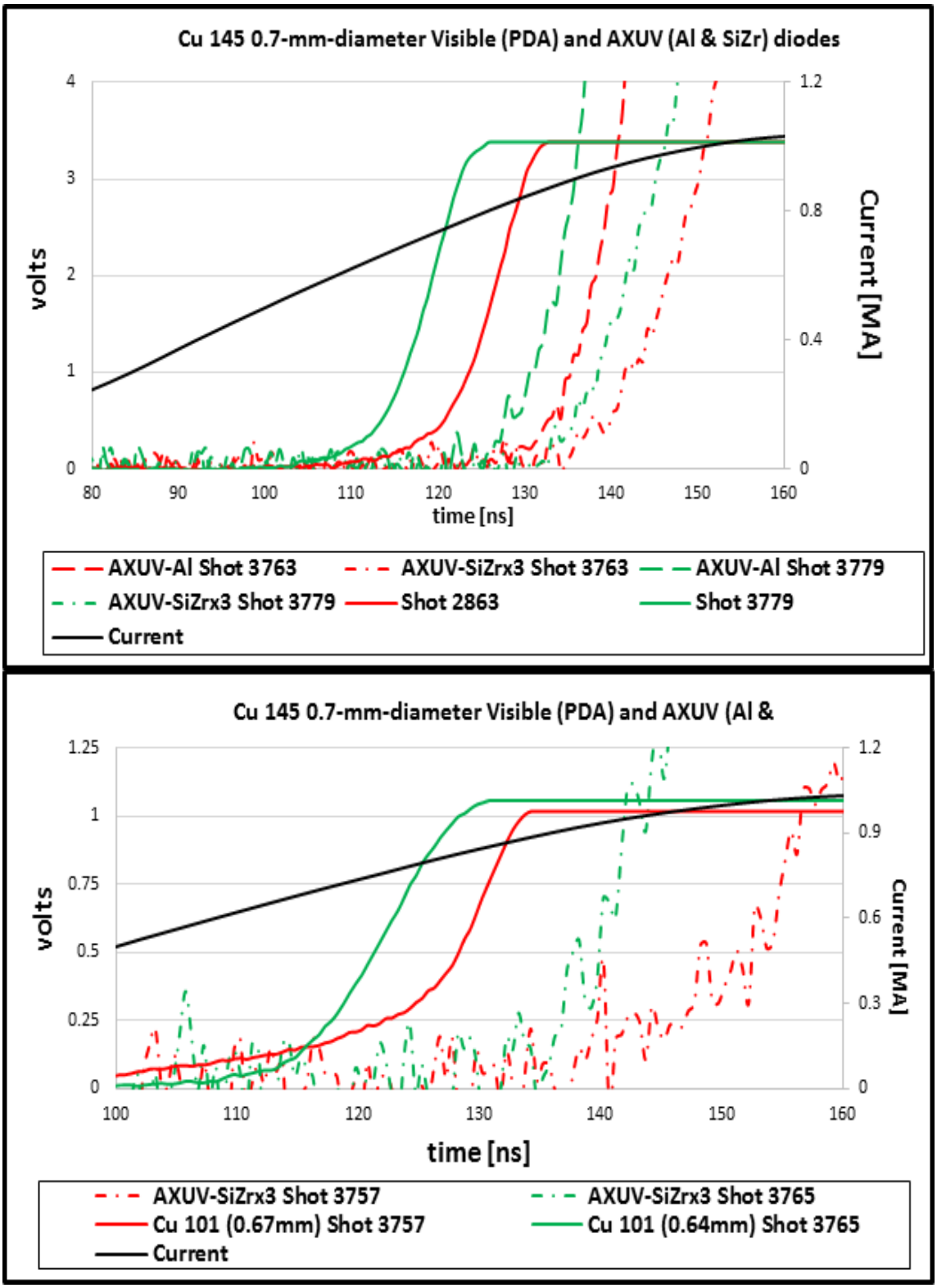

Figure VI.13 The EUV diode signals for copper 101 and copper 145 show a delayed onset with respect the visible diodes.

Chapter VII: Results: Thresholds for Explosion and Plasma Formation

Plasma formation on the surface of mega-ampere pulsed conductors has been observed for copper 145, copper 101, titanium II and nickel 200 alloys. Initial diameters were varied for all alloys except nickel. The most extensive study was performed on the copper alloys with copper 101 initial diameters varying from 500μm to 1500μm and the copper 145 initial diameters varying from 500μm to 900μm. The titanium alloys varied in initial diameter from 600μm to 1000μm and the two nickel shots were both 750μm in initial diameter. All load diameters formed plasma, with the exception of copper 101 rods which did not form plasma for any diameter >900μm. Plasma formation is observed with several diagnostics, but the initiation time of bulk surface plasma formation is determined by the abrupt increase in visible photodiode signals. Figure VII.1 illustrates the results observed in the diagnostics for the cases when plasma does and does not form. The photodiode signal observes a sharp increase in signal, which can be interpreted as an abrupt increase in conductivity when plasma forms as has been observed experimentally as well as in Quantum Molecular Dynamic simulations[112,113,114,115]. The increase in conductivity will cause an abrupt increase in current density in the plasma layer, but is also likely to cause an abrupt increase in emissivity. The emissivity is not known in this temperature and phase region for any spectral region, however, trends that have been observed in the solid to liquid states may be similar in terms of sign for the vapor to plasma transition. The laser shadowgaphy images provide observations of expansion as well as the development and evolution of surface instabilities. The sudden expansion of the surface of a heated conductor is not sufficient to claim plasma formation. The development of surface instabilities does indicate surface plasma formation. The self-emission images provide a third indicator of plasma formation. The images first show non-uniform dots begin to glow. These dots grow in number and eventually (2-10 ns) filament in the

direction of current flow. The filaments increase in number, as well as physical size, leading to a uniform surface emission. The early dots are believed to be plasma; however, the filamentation occurs near the time of the abrupt increase in the visible diode signal. The filaments are an indicator of bulk plasma formation and are likely caused by positive feedback of electrothermal instabilities as dη/dT becomes negative. An electrothermal process will also cause a positive feedback that leads to bulk plasma formation. There are several shots with copper 101 1.0-mm-diameter and aluminum 6061 2.0-mm-diameter rods that form dots without subsequent bulk plasma indicators: filaments are not observed, the surface expands 100s of microns, surface instabilities do not form, and the diode signals remain flat.

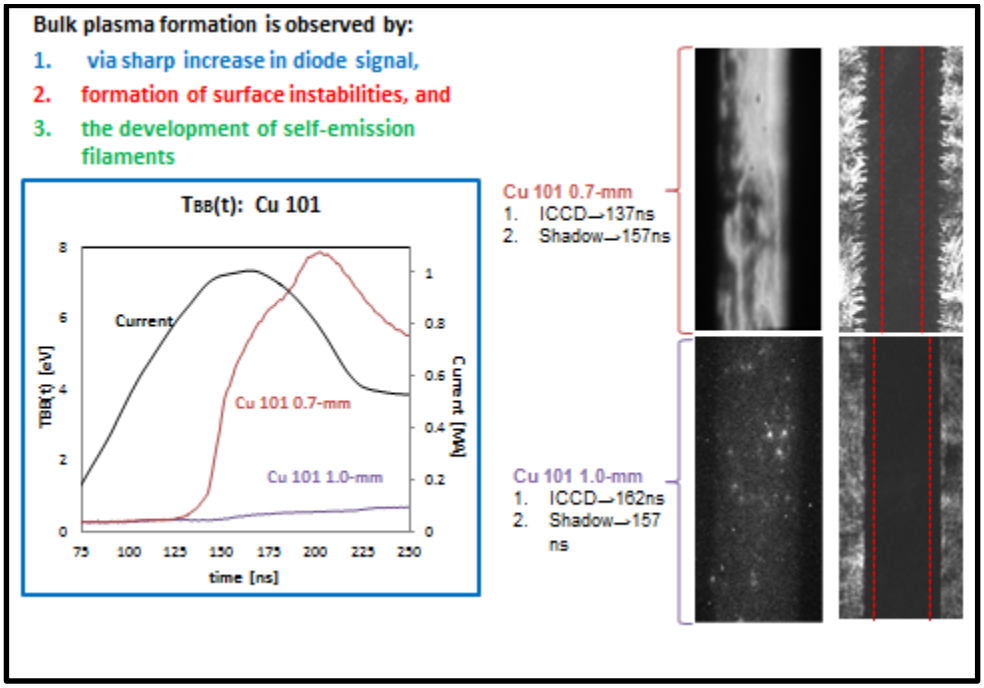

Figure VII.1 Plasma formation is observed by the abrupt increase in diode signal, the development of surface instabilities, and the filamentation of self-emission.

This provides two data sets to distinguish between. The observation of plasma formation indicated by an abrupt increase in diode signal, the development of surface instabilities, and the formation of surface filamentation observed by self-emission. The other data set observes a small

increase in the diode signal in the form of a long ramp, the expansion of the surface of the conductor, but no instability formation, and the surface of the rod glowing and forming bright dots, but never filamenting in the direction of current flow. The latter of these two data sets is thought to essentially show expanding bi-phase material. The diode signal shows that the signal level of the ramp is at least a fraction of an eV suggesting that the ramp must be observing the surface of the load in a state that has formed vapor (boiling point of copper and aluminum is ~0.24 eV) as was discussed in chapter IV. The expanding surface was determined to be expanding at a rate of 3.6, 3.4, 5.8, and, 3.2μm/ns for copper 101, copper 145, titanium II, and aluminum 6061 respectively. There is not enough data for nickel to determine the expansi rate. The expansion rates allow for the determination of the time of initial expansion, assuming the expansion is linear back to the time of initial expansion. This is justified by the observation of the copper 101 rods that have not expanded on several shots in the MG VI experiment. This data appears to suggest a nearly linear expansion. The time of initial expansion was determined for both copper 101 and 145.

With the time, current profile, and initial radius known, the surface magnetic field at time of surface expansion (surface explosion, B_{ex}) is determined using the following equation:

$$B_{ex} = \frac{\mu_0 I(T_{ex})}{2\pi R_i} \qquad \text{(VII.1)}$$

Where the radius, R_i is the initial radius of the rod. The current is taken to be flowing at the surface of the initial rod diameter. The results for both copper alloys is plotted as a function of initial diameter in Figure VII.2. The error bars on these are quite large due to the error in the expansion rates. It appears that the two alloys have similar thresholds for surface explosion. It is not clear why there is a deviation near 580μm initial diameter. More data with higher resolution

optics would be need to reduce the error bars on this plot, however, it clearly indicates that you must have a surface magnetic field greater than 1MG to form surface vapor.

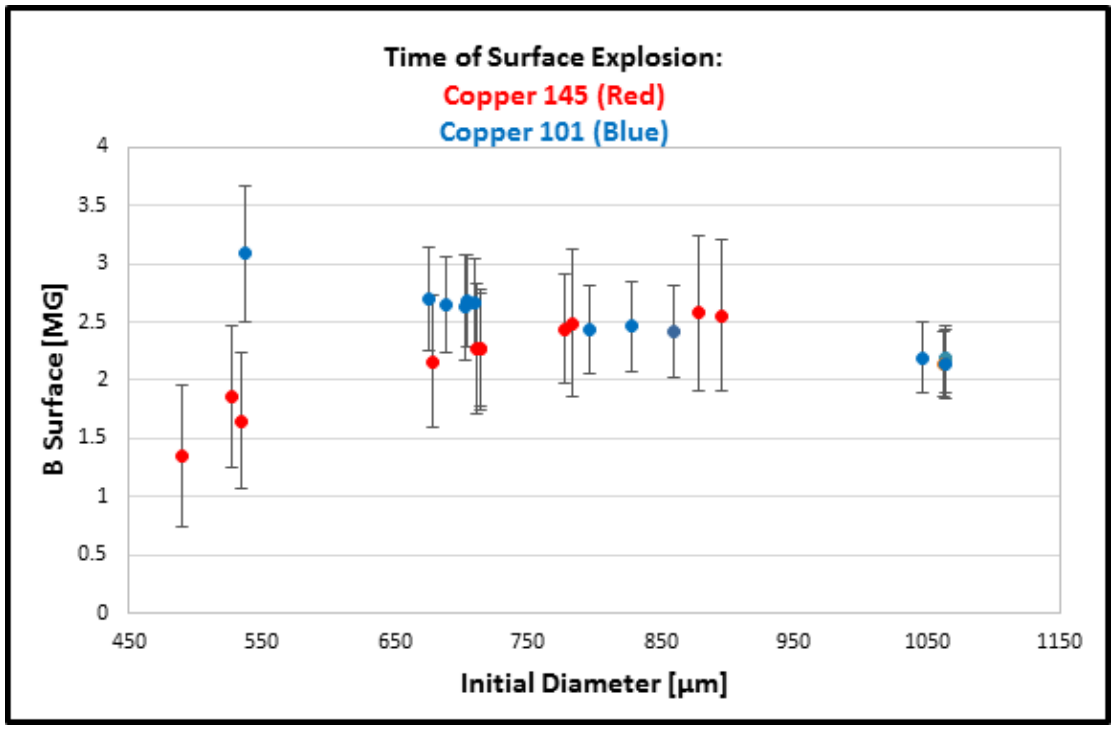

Figure VII.2 The time of expansion (explosion) is determined finding a linear fit to the laser shadowgraph expansion data. With the current profile determined by differential B-dots, the surface magnetic field threshold for surface explosion is found. The threshold for surface explosion is plotted as a function of initial diameter for copper 101 and copper 145.

The results for aluminum 6061 are shown in Figure VII.3. The aluminum forms surface vapor at lower surface magnetic field. Once again, the error bars are quite large, however, the surface explosion occurs prior to the surface reaching 1.5MG.

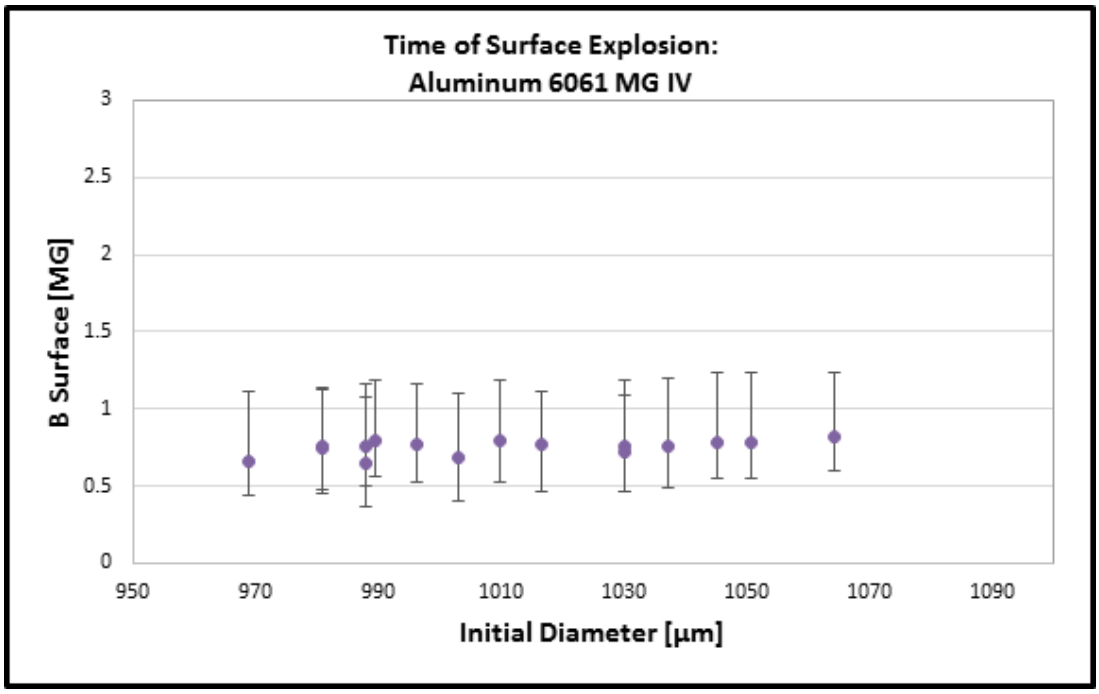

Figure VII.3 The time of explosion is determined finding a linear fit to the laser shadowgraph expansion data. With the current profile determined by differential bdots, the surface magnetic field threshold for surface explosion is found. The threshold for surface explosion is plotted as a function of initial diameter for aluminum 6061.

The metal vapor is able to expand out across the magnetic field lines due to its high resistivity. A small amount of current is believed to still be deposited into the vapor, with a heating rate that is greater than the expansive cooling. At a surface magnetic threshold, the vapor ionizes, causing more current to be deposited into this layer, causing an abrupt increase in temperature. The time of this is recorded by the diode and can be used along with the known current profile and rod radius to determine the threshold for plasma formation. The threshold for plasma formation is determined using the following equation:

$$B_s = \frac{\mu_0 I(T_p)}{2\pi R(T_p)} \qquad \text{(VII.2)}$$

Where $R(T_p)$ is the radius at the time of plasma formation, T_p, as determined by the laser shadowgraphy. As discussed in Chapter V, the radii observed by the shadowgraphy is not expected to be significantly different from the self-emission radius compared to the errors in the

analysis. The current is taken to be flowing at the diameter observed by the laser shadowgraphy. Tables VII.1 and VII.2 list the results for copper 101 and copper 145 respectively, with the initial diameter, time of plasma formation, current at time of plasma formation, and the surface magnetic fields all listed. The copper 101 and 145 rods form plasma at magnetic field thresholds of 3.5MG and 3.0MG with standard deviations of 0.18MG and 0.15MG respectively.

Cu 101 has a magnetic threshold of 3.5MG with a standard deviation of 0.18MG				
Diameter [µm]	**Shot**	**Time of Plasma (Tp)**	**Current at Tp [kA]**	**B threshold [MG]**
555	2872	111	649000	**3.7**
690	2860	133	866000	**3.5**
672	2869	142	993000	**3.8**
688	2877	131	855000	**3.5**
703	2871	138	955000	**3.7**
688	2874	126	781000	**3.4**
669	3757	125	786000	**3.5**
637	3765	117	705000	**3.4**
650	3756	106	573000	**3.0**
797	2858	152	1009000	**3.5**
797	2864	154	1032000	**3.5**
859	2868	158	1113000	**3.5**
844	2873	159	1070000	**3.4**
828	2876	159	1080000	**3.4**
900	3785	157	1013266	**3.1**

Table VII.1 Surface magnetic field threshold for plasma formation for copper 101 is 3.5 MG.

The results for both copper alloys are plotted in Figure VIII.4. Included in this plot are the two copper 101 alloys that were electropolished in MG VI. These rods show no clear difference in the time of plasma formation from the other rods. The 900μm copper 101 rod (found at the bottom of table VII.1) has a threshold of 3.1MG, much lower than the other shots and similar to the thresholds found for copper 145. This is understood to be an effect with rods that are close to reaching the threshold near peak current. Analysis of this shot shows that the surface magnetic field reaches a maximum of 3.2MG on that particular shot at 146ns. The surface magnetic field remains at ~3.2MG for 2ns before it begins to decline to 3.1 MG at 157ns.

Cu 145 has a magnetic threshold of 3.0MG with a standard deviation of 0.15MG				
Diameter [µm]	**Shot**	**Time of Plasma (Tp)**	**Current at Tp [kA]**	**B threshold [MG]**
510	**3393**	103	546000	**3.2**
530	**3394**	100	494000	**2.9**
490	**3395**	104	560000	**3.3**
530	**3403**	105	554000	**3.1**
680	**3392**	117	698000	**3.2**
721	**3547**	109	614000	**3.0**
704	**3562**	104	550000	**2.8**
714	**3546**	110	620000	**3.0**
714	**3755**	112	646000	**3.1**
710	**3763**	120	734000	**3.3**
717	**3779**	113	639000	**3.0**
777	**3764**	119	724000	**3.1**
780	**3766**	118	694000	**3.0**
777	**3775**	113	647000	**2.9**
783	**3776**	117	686000	**3.0**
880	**3777**	123	764000	**3.0**
890	**3778**	123	746000	**2.9**
900	**3780**	125	764000	**2.9**

Table VII.2 Surface magnetic field threshold for plasma formation for copper 145 is 3.0 MG.

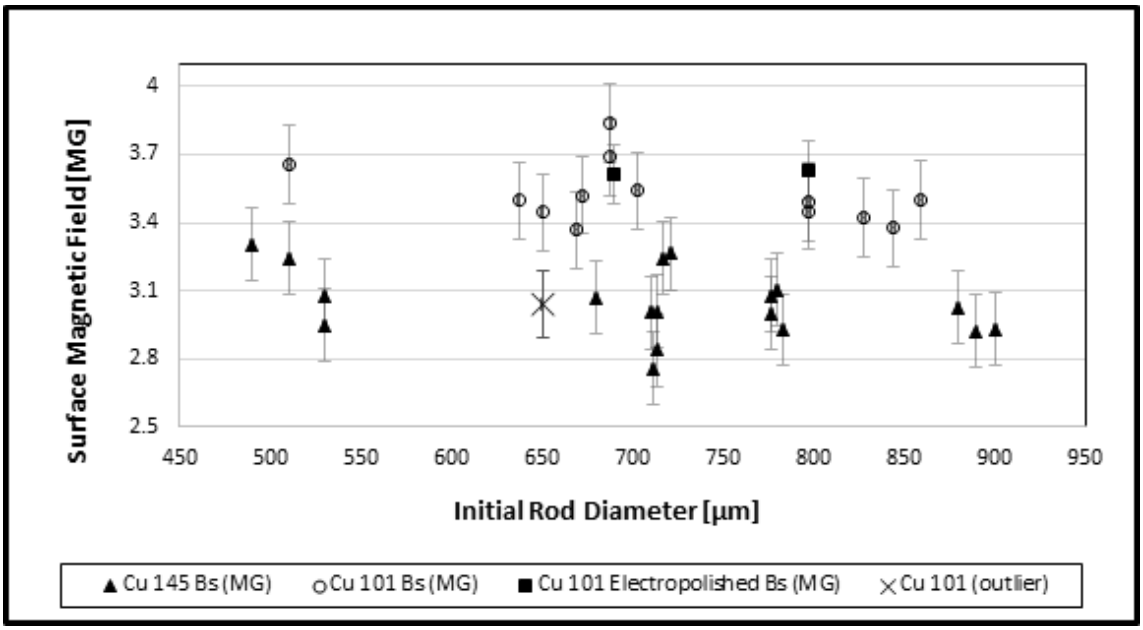

Figure VII.4 The threshold for plasma formation for copper 101 and copper 145 plotted as a function of initial rod diameter.

The results for all titanium and nickel shots are listed in table VII.3. Titanium II forms plasma at a surface magnetic field of 2.2MG with a standard deviation of 0.16MG. Nickel 200 forms plasma at a surface magnetic field of 2.6MG.

Ti II has a magnetic threshold of 2.2MG with a standard deviation of 0.16MG				
Diameter [µm]	**Shot**	**Time of Plasma (Tp)**	**Current at Tp [kA]**	**B threshold [MG]**
666	3400	90	369	**2.0**
767	3402	96	460	**2.0**
757	3404	96	464	**2.1**
960	3406	107	607	**2.2**
1051	3406	110	644	**2.3**
970	3761	113	654	**2.4**
Ni 200 has a magnetic threshold of 2.6MG				
740	3401	120	735	**2.5**
750	3460	127	810	**2.7**

Table VII.3 Surface magnetic field thresholds for plasma formation for titanium II and nickel 200.

Figure VII.5 plots the surface magnetic field thresholds for copper 101, copper 145, titanium II and nickel 200 as a function of initial diameter. This plot takes into consideration the outer radius that has expanded from the time of surface explosion.

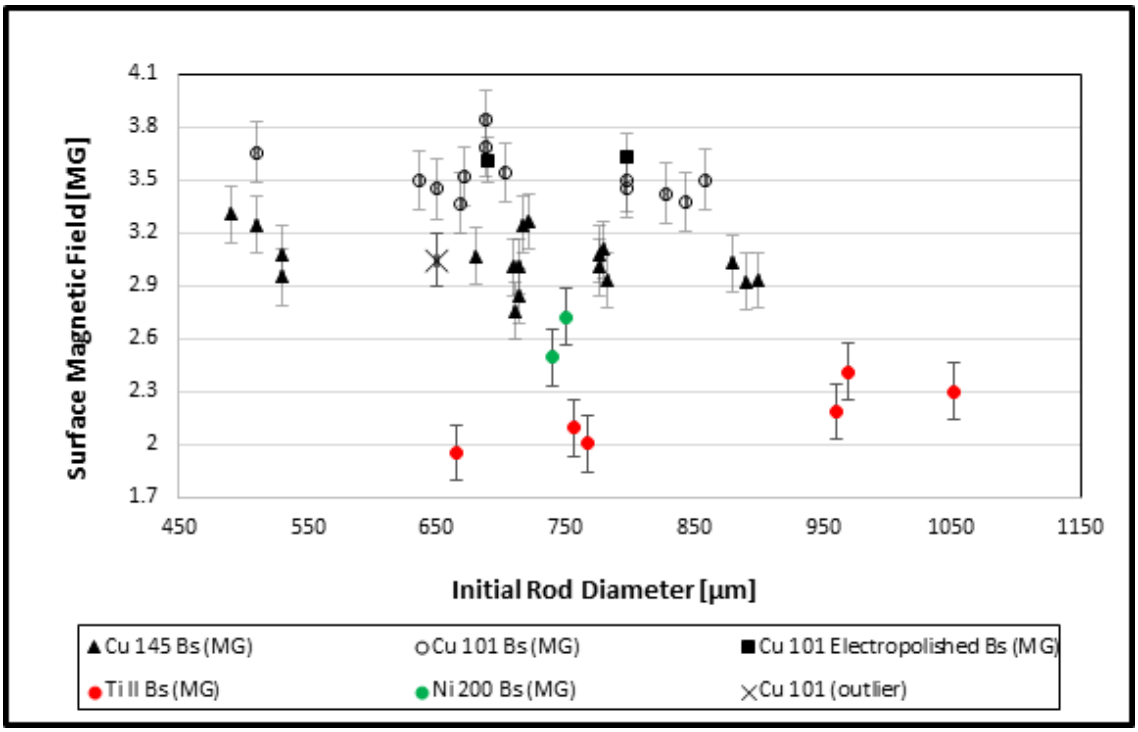

Figure VII.5 Plasma forms on the surface of a metal conductor at different thresholds. The surface magnetic field thresholds for plasma formation for copper 101, copper 145, titanium II, and nickel 200 are plotted versus their initial diameter.

As discussed in the Introduction, the distinction between surface explosion and bulk surface plasma formation is not accounted for by other research. If the data here is analyzed using the initial diameter of the rods to determine the surface magnetic threshold, the results would be shifted dramatically. Figure VII.6 show the result of this analysis, with the thresholds for copper 101 and 145 approaching 5.0 and 3.5 MG respectively.

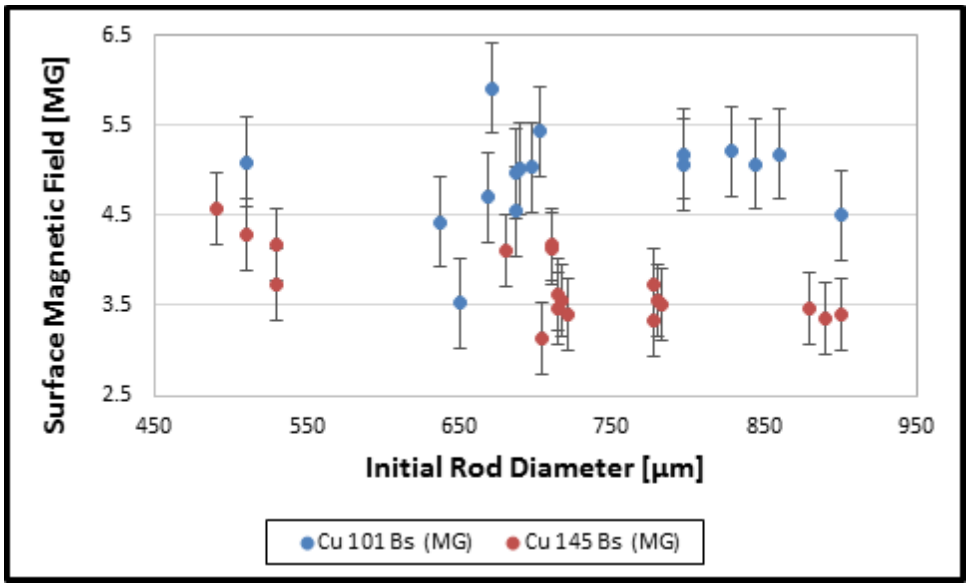

Figure VII.6 The surface magnet field thresholds for copper 101 and 145 without surface expansion included.

The results for the expansion speed, time of surface explosion, time bulk surface plasma formation, and peak temperature estimates all show a spread that need to be interpreted. There are error bars involved with all measurements that lead to a little spread which include a ±2ns error in the PDA timing of plasma formation and a ±10-30 µm error in the laser shadowgraphy (depends on optical system and laser speckle of each experiment). The initial diameters of the rods has an insignificant error (a few microns) and the current profile in time is time resolved to half of a ns. The error bars in the diagnostics may not sufficiently describe the scatter in the data. Some differences in rods of the same alloy may be different in ways that have not been characterized. To start, the rods in MG VI were put into a sonic bath, then cleaned with alcohol and acetone. There was no observable difference in the aluminum 6061 on this experimental campaign, however, the effects of the sonic bath on copper 101 versus aluminum 6061 has not been characterized. The copper 101 on MG VI and MG IX were not from the same batch since they were bought several years apart. There may be a difference in hardness or grain structure

that may affect the EOS. The copper 145 rods in each experiment were bought at different times from the same purveyor with the specifications claiming a tellurium percentage of 0.0-0.7%. This number may be significantly different from purchase to purchase and has never been characterized. To try to minimize the spread in the data, the rod specifications need to be controlled and individually characterized through SEM/EDS tests along with hardness tests.

Chapter VIII: Summary of Results, Unanswered Questions, Future Work

Section VIII.A: Summary of Results

The MG experiments conducted at the Nevada Terawatt Facility are designed to study the effects of ohmically heating thick metal conductors with a mega-ampere current pulse such that the current flows non-uniformly in a skin layer. Diagnostics are fielded to observe the surface as it is heated to the point of plasma formation.

The diagnostics fielded permit the observations of temperature, surface emission, surface expansion, surface evolution, and instability growth, from the time near the boiling point up to and through plasma formation. It was shown by Awe that aluminum forms plasma when the surface magnetic field reaches 2.2MG regardless of initial rod diameter. Presented here are the results of pulsing copper 101, copper 145, titanium II, and nickel 200.

As the metal rod is pulsed by an intense current, the surface ohmically heats in a skin layer. The surface will form vapor when the surface reaches a temperature of a fraction of an eV. At the time of vapor formation, the surface begins to expand as the resistive vapor diffuses across the magnetic field lines. The expansion rate of the alloys tested here were 3.6, 3.4, 5.8, and 1.5μm/ns for copper 101, copper 145, titanium II, and nickel 200 respectively. The surface magnetic field threshold for vapor formation, or surface explosion, was calculated to be 2.3MG with a standard deviation of 0.2 and 2.2MG with a standard deviation of 0.4 for copper 101 and copper 145 respectively. The times for surface explosion for titanium and nickel were not determined due to a lack of sufficient data, with only one shot for nickel, and the few shots for titanium having enough spread in the data that the error bars spread from 0 to 3MG.

As the heated metal surface expands, the vapor continues to heat as a small fraction of the current flows through the expanding region. When the surface reaches a magnetic threshold, plasma forms. These thresholds were calculated to be 3.5, 3.0, 2.2, and 2.6 MG for copper 101,

copper 145, titanium II, and nickel 200 respectively. The difference in the threshold for plasma formation observed for copper 101 and copper 145 is not understood. The copper alloys Cu-101 and Cu-145 have slightly different material properties. At room temperature, Cu-145 has 8% lower electrical conductivity and 10% lower thermal conductivity than Cu-101. Cu-145 has a 1% higher coefficient of thermal expansion than Cu-101. The two alloys have equal specific heat, mass density, and modulus of elasticity. Cu-145 has higher yield strength and ultimate tensile strength, making it mechanically "harder," which facilitates precision cutting with standard machine tools. The clear difference between the two alloys is the addition of 0.7% tellurium to the copper 145 alloy. With the room temperature properties being so similar, it is unlikely that the metals act different before forming vapor. While in the vapor state, the copper is still several orders of magnitude more conductive than room temperature tellurium. With a highly resistive tellurium mixed in with the copper vapor, the current will "bend" around the tellurium forming regions of higher current density. This effect may lead to a local heating of the copper that will accelerate it through the vapor state and ionize at a lower threshold.

Section VIII.B: Remaining Questions and Future Work

Question 1: What is the emissivity of the metal surface in time as it is heated and evolves through several phase states? The temperature estimates made with the photodiode array data assumed a blackbody emitting surface. This is justified by the continuum observed in the visible spectra

for both copper and aluminum. This allows for a lower bound estimate of the surface temperature because a blackbody assumes a perfect radiator.

Future work: To determine the emissivity as a function of time the aluminum loads could have a thin layer of carbon deposited on the surface. This would need to be done over half of the load, e.g. coat the top half with carbon and leave the bottom half uncoated. By imaging the light to a mirror that spits the light along the midsection where the crossover from aluminum to coating is located, light from these two sections could be collected by photodiodes and compared. The complication with this problem is to ensure the coating is thick enough such that there is no mixing of carbon with the underlying plasma as the surface begins to melt, vaporize, and ionize, yet not so thick that the surface magnetic field varies enough to allow the top and bottom sections of the load to be heated at different rates and with different concluding effects.

Question 2: How can optics and other materials be placed into the chamber such that they are not in the AK gap? This problem was first studied with the aluminum transmission line that was tested on MG V experiment and failed due to early plasma formation, likely at the corner of the cathode piece.

Future work: The original thought was to use stainless steel instead of aluminum to hold back any early plasma formation in the transmission line. It was quickly realized that this would not be an efficient solution in the long term of a campaign. The reason for this is that after several shots, the steel transmission line would be coated with aluminum from the exploding aluminum wire loads resting on top. A more complete remedy would be to open up the gap between the cathode

piece and the anode return current profile. If this is done, there are several other pieces that would need to be modified such as the cathode knife-edge. This could be done and is a first step in developing a vacuum chamber that allows for optical and other components to be placed in the chamber while still maintaining an experiment that allows for the study of ohmically heating metal conductors.

Question 3: How is the physics of phase transformation from the solid to liquid to gas to plasma and any combination of these affected by the metal properties? Is there a threshold for plasma formation for all metals and what metal characteristics vary the threshold?

Future work: This question has already begun to be answered over the past several experiments. The aluminum and copper showed similarities in terms of surface emission structure. Both metals were observed to begin with spots that evolved into filaments and eventually into uniform emission. It was observed that Al 1100 and 6061 show no observable difference in our experiments, however, Cu 101 and 145 show significant differences in time of plasma formation as well as peak temperature. Titanium was also shot with varying diameters and appears to have a threshold for plasma formation. To determine what characteristics are driving these trends more metals would need to be added to the shot list with variations in physical properties such as the following:

1. Electrical conductivity
2. Thermal conductivity
3. Boiling point

4. Ionization energy

A brief list of possible metals includes titanium, nickel, tungsten, and lithium.

Question 4: How does the surface finish affect plasma formation, instability growth, surface emission structure, and peak temperature?

Future work: Some work has already been done on this subject, but more work is necessary. A more thorough and larger amount of data needs to be collected on the effect of electropolishing. Other variations in surface features could include using single crystal metals and ultra-pure metals. The single crystal metal would reduce grain structure and possibly affect the onset of plasma dots and late time MRT. Using ultra-pure metals could possibly have a similar effect by reducing the amount of impure atoms such as silicon, magnesium and copper from the aluminum metal rods.

Question 5: Why does the expansion speed of titanium change with initial diameter? Why does the peak temperature of titanium appear to be nearly saturating? Why is the spread in time of plasma formation so small compared to aluminum and copper?

Future work: To get a better understanding of these effects, it is necessary to first collect more data using titanium loads. The titanium loads that had a diameter of 1.0-mm created plasma early enough in the current profile that loads with larger diameters that still form plasma would certainly be possible. Shooting loads with diameters ranging from 0.75-mm to 1.75-mm would provide a large data set from which the trends in all these effects could be better observed and understood.

Question 6: What is the density of the outer material of the load and in what phase state is the expanding material?

Future work: Interferometry has been utilized to try to determine the density of the surface plasma as well as the expanding gas using both 532-nm and 266-nm laser light. No fringe shifts have been observed for plasma or gas prior to peak current. Fringe shifts were observed past peak current when the plasma is being pulled out by the expanding magnetic flux, leading to a less dense surface plasma. The lack of fringe shifts due to plasma formation prior to peak current can be simply explained by the conjecture that the plasma is pinched against the cold metal rod with a high density such that it is greater than the critical density for the laser. However, this does not explain the lack of fringe shifts when there is thought to be an expanding gas. Perhaps the expanding metal material is not a gas, but a bi-phase material of gas and liquid, and perhaps even a foam. X-ray radiography would help determine what the surface states and densities are. By using the Leopard laser system in the short-pulse mode, the laser pulse can be focused down to a few micron spot, reaching an intensity of 10^{18} watts/cm^2.

Question 7: Is there a variation in the magnetic threshold for plasma if the rise rate of the surface magnetic field changes?

Future work: There has been no clear evidence that the magnetic threshold for plasma varies as the rise rate of the magnetic field varies. This has been done for rise rates in the range 30-80 MG/μs. It could be that this range is not wide enough to see the variations with the error bars of our diagnostics. A solution would be to vary the rise rate by going to a long pulse, ~200ns, that would reduce the rise rate by nearly a factor of 2. Care must be taken to ensure that the skin depth does not approach the radius of the metal conductor. Another possibility is to design a load that could utilize the load current multiplier to reach 1.7 MA in ~100ns. This would allow the rise rate to reach ~160 MG/μs. With the ability to expand the range to 10-160 MG/μs, variations in magnetic field threshold may be observed if it is to exist.

Question 8: Is there a difference in observed rod radius for different laser wavelengths?

Future work: It is difficult to measure a difference between rod radii between two shots with different laser wavelengths. This is due to the variation in the initial diameter as well as the error involved with taking shadowgraphs i.e. the laser speckle and optical resolution. One way to test this to do this at the NTF would be to field Dr. Ivanov's 4-wavelength (1064, 532, 266, 211 nm) laser shadowgraphy to get all wavelengths on one shot at one time. This would allow for a comprehensive study of the surface radius of the rod for different wavelengths. By conducting a scan in time from prior to the time of surface explosion to past peak current, limits on the electron density through the phase changes could be determined.

Appendix: Frequently used symbols

J	Current density
I	Current
E	Electric field
η	Electrical resistivity
B	Magnetic field
V	Electric potential
ρ	Mass density
ϵ_0	Permittivity of free space
μ_0	Permeability of free space
T	Temperature
C_v	Specific heat capacity
Q	Heat energy density
σ	Electrical conductivity
$\vec{u}$	Fluid velocity
P	Pressure
Υ	Instability growth rate
q	Electric charge
e	Electron charge
h	Plancks constant
κ	Thermal conductivity
τ	Characteristic time on Zebra
R_0	Initial rod radius
D_0	Initial rod diameter
v_D	Drift velocity
v_{th}	Thermal velocity
L	Inductance

[1] Clérouin, Jean, et al. "Electrical conductivity and equation-of-state study of warm dense copper: Measurements and quantum molecular dynamics calculations." *Physical Review B* 71.6 (2005): 064203.
[2] DeSilva, A. W., and J. D. Katsouros. "Electrical conductivity of dense copper and aluminum plasmas." *Physical Review E* 57.5 (1998): 5945.
[3] DeSilva, A. W., and J. D. Katsouros. "Erratum: Electrical conductivity of dense copper and aluminum plasmas [Phys. Rev. E 57, 5945 (1998)]." *Physical Review E* 59.3 (1999): 3774.
[4] DeSilva, A. W., and J. D. Katsouros. "Measurement of the electrical conductivity of metals in the vicinity of the critical point." *International journal of thermophysics* 20.4 (1999): 1267-1277.
[5] Oreshkin, V. I. "Overheat instabilities in the electric explosion of wires."*Technical Physics Letters* 35.1 (2009): 36-39.
[6] Shishlov, Alexander V., et al. "Gas-puff-on-wire-array Z-pinch experiments on the GIT-12 generator at microsecond implosion times." *Plasma Science, IEEE Transactions on* 35.3 (2007): 592-600.
[7] Rousskikh, A. G., et al. "Study of the strata formation during the explosion of a wire in vacuum." *Physics of Plasmas (1994-present)* 15.10 (2008): 102706.
[8] Oreshkin, V. I., et al. "Wire explosion in vacuum: Simulation of a striation appearance." *Physics of Plasmas (1994-present)* 11.10 (2004): 4771-4776.
[9] Oreshkin, V. I. "Thermal instability during an electrical wire explosion." *Physics of Plasmas (1994-present)* 15.9 (2008): 092103.
[10] Peterson, Kyle J., et al. "Electrothermal instability growth in magnetically driven pulsed power liners." *Physics of Plasmas (1994-present)* 19.9 (2012): 092701.
[11] Fowler, C. M., W. B. Garn, and R. S. Caird. "Production of very high magnetic fields by implosion." *Journal of Applied Physics* 31.3 (1960): 588-594.
[12] Lindemuth, I. R., et al. "Target plasma formation for magnetic compression/magnetized target fusion." *Physical review letters* 75.10 (1995): 1953.
[13] Slutz, Stephen A., and Roger A. Vesey. "High-gain magnetized inertial fusion."*Physical review letters* 108.2 (2012): 025003.
[14] Lemke, Raymond W., et al. "On the scaling of the magnetically accelerated flyer plate technique to currents greater than 20 MA." *Journal of Physics: Conference Series*. Vol. 500. No. 15. IOP Publishing, 2014.
[15] Stygar, William A., et al. "Energy loss to conductors operated at lineal current densities≤ 10 MA/cm: Semianalytic model, magnetohydrodynamic simulations, and experiment." *Physical Review Special Topics-Accelerators and Beams*11.12 (2008): 120401.
[16] Bykov, A. I., et al. "VNIIEF achievements on ultra-high magnetic fields generation." *Physica B: Condensed Matter* 294 (2001): 574-578.
[17] Awe, T. J., et al. "Threshold for thermal ionization of an aluminum surface by pulsed megagauss magnetic field." *Physical review letters* 104.3 (2010): 035001.
[18] Peterson, Kyle J., et al. "Electrothermal instability growth in magnetically driven pulsed power liners." *Physics of Plasmas (1994-present)* 19.9 (2012): 092701.
[19] Chaikovsky, S. A., et al. "Electrical explosion of metals in fast-rising megagauss magnetic fields." *Physics of Plasmas* 16.4 (2009): 42701.

[20] Chaikovsky, S. A., et al. "Skin explosion of double-layer conductors in fast-rising high magnetic fields." *Physics of Plasmas (1994-present)* 21.4 (2014): 042706.
[21] Labetskaya, N. A., et al. "Experimental research of electrical conductor explosion in the current skinning mode." *Discharges and Electrical Insulation in Vacuum (ISDEIV), 2012 25th International Symposium on*. IEEE, 2012.
[22] Oreshkin, V. I., and S. A. Chaikovsky. "Stability of a nonlinear magnetic field diffusion wave." *Physics of Plasmas (1994-present)* 19.2 (2012): 022706.
[23] Clérouin, Jean, et al. "Electrical conductivity and equation-of-state study of warm dense copper: Measurements and quantum molecular dynamics calculations." *Physical Review B* 71.6 (2005): 064203.
[24] DeSilva, A. W., and J. D. Katsouros. "Electrical conductivity of dense copper and aluminum plasmas." *Physical Review E* 57.5 (1998): 5945.
[25] DeSilva, A. W., and J. D. Katsouros. "Erratum: Electrical conductivity of dense copper and aluminum plasmas [Phys. Rev. E 57, 5945 (1998)]." *Physical Review E* 59.3 (1999): 3774.
[26] DeSilva, A. W., and J. D. Katsouros. "Measurement of the electrical conductivity of metals in the vicinity of the critical point." *International journal of thermophysics* 20.4 (1999): 1267-1277.
[27] Gathers, G. R. "Thermophysical properties of liquid copper and aluminum."*International Journal of Thermophysics* 4.3 (1983): 209-226.
[28] H. Knoepfel, Pulsed High Magnetic Fields (North-Holland, Amsterdam, 1970).
[29] Garanin, S. F. "Diffusion of a strong magnetic field in a dense plasma." *Journal of Applied Mechanics and Technical Physics* 26.3 (1985): 308-313.
[30] Garanin, S. F., and V. I. Mamyshev. "Cooling of a magnetized plasma at a boundary with an exploding metal wall." *Journal of Applied Mechanics and Technical Physics* 31.1 (1990): 28-34.
[31] Lindemuth, Irvin R., et al. "Computational interpretation of megagauss-magnetic-field-induced metallic surface plasma initiation and evolution."*Physical review letters* 105.19 (2010): 195004.
[32] Angelova, Milena, et al. "Sensitivity of M= 0 Growth to EOS and Other Material Properties." *Megagauss magnetic field generation and related topics, 2006 ieee international conference on*. IEEE, 2006.
[33] Garanin, S. F. "Diffusion of a strong magnetic field in a dense plasma." *Journal of Applied Mechanics and Technical Physics* 26.3 (1985): 308-313.
[34] Garanin, S. F., and V. I. Mamyshev. "Cooling of a magnetized plasma at a boundary with an exploding metal wall." *Journal of Applied Mechanics and Technical Physics* 31.1 (1990): 28-34.
[35] Peterson, Kyle J., et al. "Electrothermal instability growth in magnetically driven pulsed power liners." *Physics of Plasmas (1994-present)* 19.9 (2012): 092701.
[36] Chaikovsky, S. A., et al. "Electrical explosion of metals in fast-rising megagauss magnetic fields." *Physics of Plasmas* 16.4 (2009): 42701.
[37] Chaikovsky, S. A., et al. "Skin explosion of double-layer conductors in fast-rising high magnetic fields." *Physics of Plasmas (1994-present)* 21.4 (2014): 042706.
[38] Labetskaya, N. A., et al. "Experimental research of electrical conductor explosion in the current skinning mode." *Discharges and Electrical Insulation in Vacuum (ISDEIV), 2012 25th International Symposium on*. IEEE, 2012.
[39] Oreshkin, V. I., and S. A. Chaikovsky. "Stability of a nonlinear magnetic field diffusion wave." *Physics of Plasmas (1994-present)* 19.2 (2012): 022706.
[40] Awe, T. J., et al. "Threshold for thermal ionization of an aluminum surface by pulsed megagauss magnetic field." *Physical review letters* 104.3 (2010): 035001.

[41] Clérouin, Jean, et al. "Electrical conductivity and equation-of-state study of warm dense copper: Measurements and quantum molecular dynamics calculations." *Physical Review B* 71.6 (2005): 064203.
[42] DeSilva, A. W., and J. D. Katsouros. "Electrical conductivity of dense copper and aluminum plasmas." *Physical Review E* 57.5 (1998): 5945.
[43] DeSilva, A. W., and J. D. Katsouros. "Erratum: Electrical conductivity of dense copper and aluminum plasmas [Phys. Rev. E 57, 5945 (1998)]." *Physical Review E* 59.3 (1999): 3774.
[44] DeSilva, A. W., and J. D. Katsouros. "Measurement of the electrical conductivity of metals in the vicinity of the critical point." *International journal of thermophysics* 20.4 (1999): 1267-1277.
[45] Labetskaya, N. A., et al. "Experimental research of electrical conductor explosion in the current skinning mode." *Discharges and Electrical Insulation in Vacuum (ISDEIV), 2012 25th International Symposium on*. IEEE, 2012.
[46] Lindemuth, Irvin R., et al. "Computational interpretation of megagauss-magnetic-field-induced metallic surface plasma initiation and evolution."*Physical review letters* 105.19 (2010): 195004.
[47] Garanin, Sergey F., et al. "Numerical simulations of thick-aluminum-wire behavior under megaampere-current drive." *Plasma Science, IEEE Transactions on* 38.8 (2010): 1815-1821.
[48] Chace, William George, and Howard K. Moore, eds. *Exploding wires*. Vol. 4. Plenum Press, 1959.
[49] Haines, M. G., et al. "The past, present, and future of Z pinches." *Physics of Plasmas* 7.5 (2000): 1672-1680.
[50]Garanin, S. F. "Diffusion of a strong magnetic field in a dense plasma." *Journal of Applied Mechanics and Technical Physics* 26.3 (1985): 308-313.
[51] Awe, T. J., et al. "Threshold for thermal ionization of an aluminum surface by pulsed megagauss magnetic field." *Physical review letters* 104.3 (2010): 035001
[52] Knoepfel, Heinz. "PULSED HIGH MAGNETIC FIELDS. Physical Effects and Generation Methods Concerning Pulsed Fields Up To the Megaoersted Level." (1970).
[53] Knoepfel, Heinz. "PULSED HIGH MAGNETIC FIELDS. Physical Effects and Generation Methods Concerning Pulsed Fields Up To the Megaoersted Level." (1970).
[54] Awe. T. J. "Experimental Investigation of the Properties and Phase State of Thick Aluminum Surfaces Pulsed to Megagauss Level Magnetic Field in a Z-Pinch Geometry," PhD Dissertation
[55] Lea, Susan. *Mathematics for physicists*. Brooks/Cole-Thomson Learning, 2004.
[56] Oreshkin, V. I., and S. A. Chaikovsky. "Stability of a nonlinear magnetic field diffusion wave." *Physics of Plasmas* 19.2 (2012): 022706.
[57] H. Knoepfel, Pulsed High Magnetic Fields (North-Holland, Amsterdam, 1970).
[58] Goldston, Robert J., and Paul Harding Rutherford. *Introduction to plasma physics*. CRC Press, 1995.
[59] Chen, Francis F., and Schweickhard E. Von Goeler. *Introduction to Plasma Physics and Controlled Fusion Volume 1: Plasma Physics*. Springer, 2008.
[60] Goldston, Robert J., and Paul Harding Rutherford. *Introduction to plasma physics*. CRC Press, 1995.
[61] C. A. Croxton, *Introduction to Liquid State Physics* (J. Wiley & Sons, London, 1975).
[62] DeSilva, Alan W., and H-J. Kunze. "Experimental study of the electrical conductivity of strongly coupled copper plasmas." *Physical Review E* 49.5 (1994): 4448.
[63] DeSilva, A. W., and J. D. Katsouros. "Electrical conductivity of dense copper and aluminum plasmas." *Physical Review E* 57.5 (1998): 5945.

[64] Reinholz, Heidi, Ronald Redmer, and Stefan Nagel. "Thermodynamic and transport properties of dense hydrogen plasmas." *Physical Review E* 52.5 (1995): 5368.
[65] Likalter, Alexander. "Electric conductivity of expanded transition metals."*Physica Scripta* 55.1 (1997): 114.
[66] Redmer, Ronald. "Electrical conductivity of dense metal plasmas." *Physical Review E* 59.1 (1999): 1073.
[67] Tahir, N. A., et al. "Equation-of-state properties of high-energy-density matter using intense heavy ion beams with an annular focal spot." *Physical Review E*62.1 (2000): 1224.
[68] Recoules, Vanina, et al. "Electrical conductivity of hot expanded aluminum: Experimental measurements and ab initio calculations." *Physical Review E*66.5 (2002): 056412.
[69] Collins, L. A., et al. "Dynamical and optical properties of warm dense hydrogen." *Physical Review B* 63.18 (2001): 184110.
[70] Fois, E., A. Selloni, and M. Parrinello. "Approach to metallic behavior in metal–molten-salt solutions." *Physical Review B* 39.7 (1989): 4812.
[71] Clérouin, Jean, et al. "Electrical conductivity and equation-of-state study of warm dense copper: Measurements and quantum molecular dynamics calculations." *Physical Review B* 71.6 (2005): 064203.
[72] Lindemuth, Irvin R., et al. "Computational interpretation of megagauss-magnetic-field-induced metallic surface plasma initiation and evolution."*Physical review letters* 105.19 (2010): 195004.
[73] Hänström, A., and P. Lazor. "High pressure melting and equation of state of aluminium." *Journal of alloys and compounds* 305.1 (2000): 209-215.
[74] Wen, Chang-Da, and Issam Mudawar. "Emissivity characteristics of polished aluminum alloy surfaces and assessment of multispectral radiation thermometry (MRT) emissivity models." *International journal of heat and mass transfer* 48.7 (2005): 1316-1329.
[75] Wen, Chang-Da, and Issam Mudawar. "Emissivity characteristics of roughened aluminum alloy surfaces and assessment of multispectral radiation thermometry (MRT) emissivity models." *International Journal of Heat and Mass Transfer* 47.17 (2004): 3591-3605.
[76] Wen, Chang-Da, and Issam Mudawar. "Emissivity characteristics of polished aluminum alloy surfaces and assessment of multispectral radiation thermometry (MRT) emissivity models." *International journal of heat and mass transfer* 48.7 (2005): 1316-1329.
[77] Wen, Chang-Da, and Issam Mudawar. "Modeling the effects of surface roughness on the emissivity of aluminum alloys." *International journal of heat and mass transfer* 49.23 (2006): 4279-4289.
[78] Wen, Chang-Da, and Tzung-Yuan Chai. "Experimental investigation of emissivity of aluminum alloys and application of multispectral radiation thermometry." *Applied Thermal Engineering* 31.14 (2011): 2414-2421.
[79] Watanabe, H., M. Susa, and K. Nagata. "Discontinuity in normal spectral emissivity of solid and liquid copper at the melting point." *Metallurgical and Materials Transactions A* 28.12 (1997): 2507-2513.
[80] Watanabe, Hiromichi, et al. "Phase dependence (liquid/solid) of normal spectral emissivities of noble metals at melting points." *International journal of thermophysics* 24.1 (2003): 223-237.
[81] Burgess, George K., and Paul D. Foote. "Characteristics of radiation pyrometers." *Journal of the Franklin Institute* 179.4 (1915): 493-495.
[82] Kobatake, Hidekazu, Hossein Khosroabadi, and Hiroyuki Fukuyama. "Normal spectral emissivity measurement of liquid iron and nickel using electromagnetic levitation in direct current magnetic field." *Metallurgical and Materials Transactions A* 43.7 (2012): 2466-2472.

[83] Watanabe, Hiromichi, et al. "Phase (liquid/solid) dependence of the normal spectral emissivity for iron, cobalt, and nickel at melting points." *International journal of thermophysics* 24.2 (2003): 473-488.
[84] Krishnan, S., et al. "Optical properties and spectral emissivities at 632.8 nm in the titanium-aluminum system." *Metallurgical Transactions A* 24.1 (1993): 67-72.
[85] Oreshkin, V. I. "Overheat instabilities in the electric explosion of wires."*Technical Physics Letters* 35.1 (2009): 36-39.
[86] Oreshkin, V. I. "Overheat instabilities in the electric explosion of wires."*Technical Physics Letters* 35.1 (2009): 36-39.
[87] Shishlov, Alexander V., et al. "Gas-puff-on-wire-array Z-pinch experiments on the GIT-12 generator at microsecond implosion times." *Plasma Science, IEEE Transactions on* 35.3 (2007): 592-600.
[88] Rousskikh, A. G., et al. "Study of the strata formation during the explosion of a wire in vacuum." *Physics of Plasmas (1994-present)* 15.10 (2008): 102706.
[89] Oreshkin, V. I., et al. "Wire explosion in vacuum: Simulation of a striation appearance." *Physics of Plasmas (1994-present)* 11.10 (2004): 4771-4776.
[90] Oreshkin, V. I. "Thermal instability during an electrical wire explosion." *Physics of Plasmas (1994-present)* 15.9 (2008): 092103.
[91] Abramova, K. B., N. A. Zlatin, and B. P. Peregud. "Magnetohydrodynamic instability of liquid and solid conductors. Destruction of conductors by an electric current." *Zh. Eksp. Teor. Fiz* 69.6 (1975): 2007-2022.
[92] Sinars, D. B., et al. "Exploding aluminum wire expansion rate with 1–4.5 kA per wire." *Physics of Plasmas* 7.5 (2000): 1555-1563.
[93] Peterson, Kyle J., et al. "Electrothermal instability growth in magnetically driven pulsed power liners." *Physics of Plasmas* 19.9 (2012): 092701.
[94] Marinak, M. M., et al. "Three-dimensional HYDRA simulations of National Ignition Facility targets." *Physics of Plasmas* 8.5 (2001): 2275-2280.
[95] MICRO-IMPIOSIONS, T. H. E. R. M. O. N. U. C. L. E. A. R. "Lawrence Livermore Laboratory." (1976).
[96] Oreshkin, V. I., and S. A. Chaikovsky. "Stability of a nonlinear magnetic field diffusion wave." *Physics of Plasmas (1994-present)* 19.2 (2012): 022706.
[97] Garanin, S. F., and V. I. Mamyshev. "Cooling of a magnetized plasma at a boundary with an exploding metal wall." *Journal of Applied Mechanics and Technical Physics* 31.1 (1990): 28-34.
[98] Bujko, A. M., et al. "Investigation of the dynamics of a cylindrical exploding liner accelerated by a magnetic field in the megagauss range." *Megagauss fields and pulsed power systems*. 1990.
[99] Lindemuth, Irvin R., et al. "Computational interpretation of megagauss-magnetic-field-induced metallic surface plasma initiation and evolution."*Physical review letters* 105.19 (2010): 195004.
[100] Email communication with Dr. R. Presura
[101] Sinars, D. B., et al. "The effect of insulating coatings on exploding wire plasma formation." *Physics of Plasmas* 7.2 (2000): 429-432.
[102] Kittel, C., Kroemer, H. "Thermal Physics." (W. H. Freeman and Company 2000)
[103] *Multi-element Photodiode Array*. OSI Optoelectronics. Web. 04 December 2015. <http://www.osioptoelectronics.com/standard-products/silicon-photodiodes/photodiode-arrays/multi-element-photodiode-array.aspx>
[104] *Photodiode Tutorial.* Thorlabs Inc. Web. 04 December 2015. <http://www.thorlabs.us/tutorials.cfm?tabID=31760>

[105] *Kodak Photographic Filters Handbook*. Eastman Kodak company; Revised edition (1992)
[106] *Office Support-RSQ Function*. Microsoft Office. Web. 04 December 2015. <https://support.office.com/en-us/article/RSQ-function-d7161715-250d-4a01-b80d-a8364f2be08f>
[107] *Office Support-LINEST Function*. Microsoft Office. Web. 04 December 2015. <https://support.office.com/en-us/article/LINEST-function-84d7d0d9-6e50-4101-977a-fa7abf772b6d>
[108] *Material Sound Velocities.* Olympus. Web. 04 December 2015. <www.Olympus-ims.com/en/ndt-tutorials/thickness-gage/appendices-velocities/>
[109] Awe, T.J. "Experimental Investigation of the Properties and Phase State of Thick Aluminum Surfaces Pulsed to Megagauss Level Magnetic Field in a Z-Pinch Geometry." Doctoral Disseratation. University of Nevada, Reno (2009)
[110] Valenzuela, Julio C., et al. "Observations of plasma instability and precursor plasma in thin liners driven with a compact linear transformer driver." *Bulletin of the American Physical Society* 58 (2013).
[111] *NIST Atomic Spectra Database Lines Form*. National Institute of Standards. Web. 04 December 2015. <http://www.nist.gov/>
[112] Clérouin, Jean, et al. "Electrical conductivity and equation-of-state study of warm dense copper: Measurements and quantum molecular dynamics calculations." *Physical Review B* 71.6 (2005): 064203.
[113] DeSilva, A. W., and J. D. Katsouros. "Electrical conductivity of dense copper and aluminum plasmas." *Physical Review E* 57.5 (1998): 5945.
[114] DeSilva, A. W., and J. D. Katsouros. "Erratum: Electrical conductivity of dense copper and aluminum plasmas [Phys. Rev. E 57, 5945 (1998)]." *Physical Review E* 59.3 (1999): 3774.
[115] DeSilva, A. W., and J. D. Katsouros. "Measurement of the electrical conductivity of metals in the vicinity of the critical point." *International journal of thermophysics* 20.4 (1999): 1267-1277.